

Internal wave attractors : from geometrical focusing to non-linear energy cascade and mixing

Christophe Brouzet

▶ **To cite this version:**

Christophe Brouzet. Internal wave attractors : from geometrical focusing to non-linear energy cascade and mixing. Fluid Dynamics [physics.flu-dyn]. Université de Lyon, 2016. English. ⟨NNT : 2016LYSEN012⟩. ⟨tel-01361201⟩

HAL Id: tel-01361201

https://theses.hal.science/tel-01361201v1

Submitted on 6 Sep 2016

HAL is a multi-disciplinary open access archive for the deposit and dissemination of scientific research documents, whether they are published or not. The documents may come from teaching and research institutions in France or abroad, or from public or private research centers.

L'archive ouverte pluridisciplinaire **HAL**, est destinée au dépôt et à la diffusion de documents scientifiques de niveau recherche, publiés ou non, émanant des établissements d'enseignement et de recherche français ou étrangers, des laboratoires publics ou privés.



HAL Authorization



Numéro National de Thèse : 2016LYSEN012

THÈSE de DOCTORAT DE L'UNIVERSITÉ DE LYON

opérée par

l'École Normale Supérieure de Lyon

École Doctorale N°52
Physique et Astrophysique de Lyon (PHAST)

Spécialité de doctorat : Physique

Soutenue publiquement le 01/07/2016, par :

Christophe BROUZET

Internal wave attractors: from geometrical focusing to non-linear energy cascade and mixing.

Attracteurs d'ondes internes : de la focalisation géométrique à la cascade d'énergie non-linéaire et au mélange.

Devant le jury composé de :

Le Bars, Michael	Chargé de recherche au CNRS	IRPHE	Rapporteur
Maas, Leo	Professeur	NIOZ, Pays-Bas	Rapporteur
Ermanyuk, Evgeny	Professeur	LIH, Russie	Examinateur
Falcon, Éric	Directeur de recherche au CNRS	MSC	Examinateur
Fauve, Stéphan	Professeur	LPS	Examinateur
Godeferd, Fabien	Directeur de recherche au CNRS	LMFA	Examinateur
Dauxois, Thierry	Directeur de recherche au CNRS	ENS de Lyon	Directeur de thèse
Joubaud, Sylvain	Maître de conférence	ENS de Lyon	Co-encadrant de thèse

Contents

Introduction **1**

1 Internal gravity waves **5**
1.1 Internal waves in theory . . . 6
1.1.1 Physics of a stratified fluid . . . 6
1.1.2 Linear internal waves . . . 7
1.1.3 Vertical modes . . . 11
1.1.4 Reflection of internal waves . . . 12
1.2 Internal waves in the oceans and in the atmosphere . . . 15
1.2.1 Stratification of the oceans and the atmosphere . . . 15
1.2.2 Internal wave generation . . . 16
1.2.3 Internal wave propagation in the ocean . . . 18
1.3 Internal waves in the laboratory . . . 19
1.3.1 Set-ups . . . 20
1.3.2 Density stratification . . . 21
1.3.3 Density measurements . . . 23
1.3.4 Generation of internal waves . . . 24
1.3.5 Visualization techniques . . . 27
1.3.6 Hilbert filtering in time and in space . . . 29

2 Pendulum oscillating horizontally in a stratified fluid **33**
2.1 Theoretical preliminaries . . . 35
2.1.1 Added mass in homogeneous and stratified fluids . . . 35
2.1.2 Affine similitude in a linearly stratified fluid . . . 35
2.1.3 Vertical flat plate in a linearly stratified fluid of finite depth . . . 38
2.2 Pendulum experiments . . . 39
2.2.1 Set-up . . . 40
2.2.2 Equation of motions . . . 44
2.2.3 Impulse response function analysis . . . 47
2.3 Square cylinder: infinite depth . . . 52
2.3.1 Affine similitude prediction . . . 52
2.3.2 Large Square . . . 53
2.3.3 Small square . . . 55
2.4 Small disk cylinder: finite depth effects . . . 56
2.4.1 Homogeneous fluid prediction . . . 57

2.4.2 Stratified fluid . . . 59
2.5 Flattop hill: topography lacking of tidal conversion . . . 61
2.5.1 The shape of the object and theoretical prediction . . . 61
2.5.2 Experimental results . . . 62

3 Internal wave attractors: a geometric and linear construction 67
3.1 An internal wave billiard . . . 69
3.1.1 Ray tracing in a trapezoidal domain . . . 69
3.1.2 The (d, τ) diagram . . . 71
3.1.3 Ray tracing for the $(1, 1)$ attractor . . . 74
3.1.4 Theoretical stream function fields . . . 76
3.2 Exploring the (d, τ) diagram experimentally . . . 80
3.2.1 With constant d . . . 81
3.2.2 A typical $(1, 1)$ attractor . . . 84
3.2.3 The $(1, 1)$ Arnold tongue . . . 86
3.3 Steady state of the $(1, 1)$ attractor . . . 89
3.3.1 Models for the steady state . . . 89
3.3.2 Branch separation . . . 93
3.3.3 Branch profiles . . . 95
3.3.4 Branch wave length and width . . . 97
3.4 Growth and decay of the $(1, 1)$ attractor . . . 100
3.4.1 Typical growth and decay . . . 101
3.4.2 Wave length and amplitude evolution in time . . . 102
3.4.3 Attractor width evolution in time . . . 104
3.5 Exploring different forcings . . . 105
3.5.1 Forcing on all the height . . . 105
3.5.2 Forcing on fundamental intervals . . . 108
3.6 Comparison with numerical simulations . . . 111
3.6.1 Attractors in numerical simulations . . . 111
3.6.2 Numerical set-up . . . 112
3.6.3 Comparison with a stable $(1, 1)$ attractor . . . 114

4 Triadic resonance instability in internal wave attractors 117
4.1 Triadic resonance instability on the most energetic branch . . . 119
4.1.1 Observations of the triadic resonance instability . . . 119
4.1.2 Consequences on the size and the amplitude of the branches . . . 123
4.1.3 Comparison with numerical simulations . . . 126
4.2 An other type of triadic resonance instability . . . 129
4.2.1 Different cases of TRI. . . . 129
4.2.2 TRI in weakly-focused $(1, 1)$ attractors . . . 132
4.3 Wave structure in the transversal direction: 3D effects and role of lateral walls 136
4.3.1 2D visualizations in vertical plane xz at different transversal locations 137
4.3.2 Velocity profiles in transverse y direction . . . 138
4.3.3 Generation of mean-flows . . . 139
4.3.4 Dissipation in the bulk and in the boundary layers . . . 141
4.3.5 Synthetic Schlieren test . . . 142

5 Non-linear energy cascade and mixing in internal wave attractors 145
5.1 Discrete TRI cascade . . . 150
5.1.1 Time-frequency diagram . . . 150

5.1.2 Bispectrum and bicoherence . . . 152
5.1.3 Frequency resonant condition . . . 154
5.1.4 Energy-spectrum . . . 157
5.1.5 Spatial spectrum . . . 160
5.2 Mixing induced by TRI cascade . . . 163
5.2.1 Time-frequency diagram and bicoherence . . . 163
5.2.2 Energy and spatial Spectra . . . 164
5.2.3 Mixing inferred from vorticity distribution . . . 167
5.3 Comparison with other long-term experiments . . . 169
5.3.1 Other discrete TRI cascade experiments . . . 170
5.3.2 Other mixing experiments . . . 172
5.3.3 Probability density functions of the horizontal vorticity . . . 174

Conclusion **177**

Bibliography **183**

Introduction

Internal waves are ubiquitous in the oceans. Indeed, these waves propagate through stably density stratified fluids using buoyancy as a restoring force and the oceans are one of the natural examples of stratified media. In the deep ocean, internal waves are generated essentially by the tides [55, 56, 123] at large scales [91, 92]. They can travel through long distances, interacting with other oceanic structures [137] and with the topography [30, 84]. They may also be unstable [101, 25] and break. All these processes are responsible for an energy cascade [57] from large to small scales, inducing irreversible mixing in the ocean stratification [55, 76]. This converts a fraction of the energetic input to potential energy rise and contributes to sustain the global oceanic circulation [124, 120]. Nevertheless, the different mechanisms bringing the tidal large-scale mostly monochromatic input to multi-scale internal wave motion are not well understood [76, 135] and the cascade process remains one of the fundamental problems of physical oceanography.

Another possible mechanism connecting the large and small scales in the ocean may be the coupling of the ocean with the boundaries of its domain [65]. Indeed, when internal waves reflect at the topography and at the surface of a basin, they can form closed orbits or loops, called wave attractors. This is possible only if the topography presents some super-critical slopes, meaning that the topography has a slope angle larger than the one of the internal waves. These attractors lead to energy transfer toward smaller scales, due to linear focusing effects. This is the beginning of the cascade. Then, regions of high density gradients are induced, leading to high energy dissipation and possible mixing. This corresponds to the non-linear part of the cascade.

Tang and Peacock [145] have investigated the possibility of wave attractors in realistic ridge topographies in closed basins and pointed that the northern portion of the Luzon ridge can support internal wave attractors. An experiment reported by Echeverri *et al.* [38], in a double-ridge geometry, similar to the ones investigated by Tang and Peacock [145], has shown that this configuration may lead to focusing and wave attractors. More recently, Guo and Holmes-Cerfon [65] used a typical bi-dimensional oceanic bathymetry to evaluate the possibility of presence of wave attractors in an open basin. They have found that wave attractors are likely to be present, with a non negligible probability of 10 attractors per 1000 km.

Nevertheless, there is no evidence of observed wave attractors despite the identification of possible configurations [38, 145, 65]. Manders *et al.* [106] have reported that wave attractors cannot be present in the Mozambique channel with the stratification they have measured. However, the configuration of the channel may allow wave attractors for different stratification and different tidal frequencies. Thus, it seems that natural systems present such diversity that attractors may exist. It is of course necessary to take into account

the differences between idealized systems and the oceanic reality [38, 145, 65]. First, the ocean is not bi-dimensional but three-dimensional. Nevertheless, some three-dimensional configurations may possibly exhibit wave attractors [35, 105]. Secondly, the ocean floor is not smooth and the roughness may diffuse and destabilize possible structures. However, the robustness of wave attractors has been tested experimentally by Hazewinkel *et al.* [69].

Even if no attractor has been observed directly in nature, a very large number of works on wave attractors in closed and geometrically well-controlled basins can be found in the literature. The first theoretical aspects of wave attractors have been developed by Maas and Lam [98] and the first experimental attractor has been reported in [97]. Following these studies, several articles have described the linear state of wave attractors, experimentally [70, 68], numerically [64, 79] and theoretically [86, 125]. More recently, non-linear or unstable wave attractors have been investigated. Indeed, as the attractor is defined as a closed loop of waves, a large part of the energy injected in the system is focused along the path of the attractor. If this energy quantity is too large, the attractor becomes unstable via triadic resonant instability [139] and may induce some mixing [64]. This instability causes a higher dissipation of the energy in the attractor [79] and may partially destroy this structure.

In this manuscript, we propose to study the linear and non-linear cascades in internal wave attractors, using laboratory experiments. These experiments are very precisely controlled and idealized from the oceanic point of view. We utilize a tank with a simple trapezoidal geometry, much used in the literature [68, 70, 64, 139, 105]. The fluid inside the tank is initially linearly stratified, with a constant buoyancy frequency. The forcing is made using the wave-maker described by Gostiaux *et al.* [63] and Mercier *et al.* [115]. It gives us a precise control on the frequency, the amplitude and the shape of the forcing. Tuning the geometry of the basin and the amplitude of the forcing allows us to vary the importance of the non-linearities in the cascade induced by internal wave attractors. In addition to the attractor experiments, I have also performed added mass measurements of an horizontally oscillating object in a linearly stratified fluid. This has strong applications for tidal conversion and forcing, which are necessary to understand. Indeed, tidal forcing is expected to be the main forcing for wave attractors in the oceans [38]. This manuscript is organized as follows.

1. Chapter 1 introduces internal waves in a stratified fluid. First, the main features of internal wave physics are presented. Then, these waves are described in natural systems such as oceans and the atmosphere. Their generation, propagation and effects in these systems are pointed out and the main fundamental questions presented. Finally, as this manuscript deals with laboratory experiments, the experimental techniques used to obtain a stratified fluid, generate internal waves and observe them are described.

2. The added mass experiments on tidal conversion are reported in Chapter 2. The concept of added mass in homogeneous and stratified fluid is first introduced. The affine similitude theory, developed in the literature and allowing the analogy between homogeneous and stratified fluid, is explained. Then, the results obtained for a square-shaped cylinder oscillating horizontally in a stratified fluid of infinite depth are presented. The added mass measurements are in good agreement with the theoretical predictions. Finally, the results for a circular-shaped cylinder oscillating in a stratified fluid of finite depth are described. They are not in total agreement with the

theoretical predictions but they exhibit a very interesting feature, at low frequency of oscillations and at very small depth. This feature is relevant for tidal conversion.

3. The linear internal wave attractors are presented in Chapter 3. The ray tracing method is detailed in the trapezoidal geometry and experimental internal wave attractors are shown. Their main characteristics such as wave length, width and amplitude are discussed as a function of the geometry of the basin for the steady state. The scaling of the attractor width is investigated and we show that, at the ocean scale, the focusing may lead to instability. Investigations on the growth and the decay of attractors are also presented. This shows the strong influence of the basin geometry on the attractor characteristics. Different forcings are tested, in order to observe the influence of the forcing on the structure of internal wave attractors. Numerically simulated attractors, using a code developed by Ilias Sibgatullin, are compared to the experimental ones. The comparison is not only qualitatively but also quantitatively very good for attractors in the linear regime.

4. Chapters 4 and 5 deal with unstable attractors. Chapter 4 focuses on the start of the triadic resonant instability, which is strongly influenced by the geometry of the basin. We show that two kinds of triadic resonance instabilities are possible, one which is local while the other one is global. Numerical simulations of unstable internal wave attractors are found to be in excellent agreement with the experiments. The three-dimensional aspects of the flow are investigated using both experiments and numerical simulations. The flow is proved to be quasi bi-dimensional, with small variations in the third direction.

5. Chapter 5 describes long-term experiments at high forcing amplitude. Unstable internal wave attractors lead to a triadic energy cascade with convincing signatures of internal wave turbulence. When the forcing is sufficiently strong, this cascade induces partial mixing of the fluid. One shows that the intensity of the cascade is also controlled by the geometry of the trapezoid. This may imply that wave attractors are locally responsible for the energy cascade and the mixing processes in the oceans, a possible role of paramount importance for the ocean dynamics.

This PhD has lead to several articles, published, submitted or in preparation:

- Reference [22]: this letter explains the main characteristics obtained on the energy cascade in the attractors, via long-term experiments. This can be found in Chapter 5.
  Energy cascade in internal wave attractors.
  C. Brouzet, E. V. Ermanyuk, S. Joubaud, I. N. Sibgatullin and T. Dauxois
  Published in *Europhysics Letters* (2016), vol. 113:44001

- Reference [23]: this article focuses on the validation of the numerical code using the experiments. It also investigates the three-dimensional effects in the tank, from both experimental and numerical points of view. The content of this article is presented in Chapters 3 and 4.
  Internal wave attractors examined using laboratory experiments and 3D numerical simulations.
  C. Brouzet, I. N. Sibgatullin, H. Scolan, E. V. Ermanyuk and T. Dauxois
  Published in *Journal of Fluid Mechanics* (2016), vol. 793:109-131

- Reference [21]: this article concerns the geometry of the simplest attractor. We show that the shape of the trapezoidal domain plays an important role in the focusing

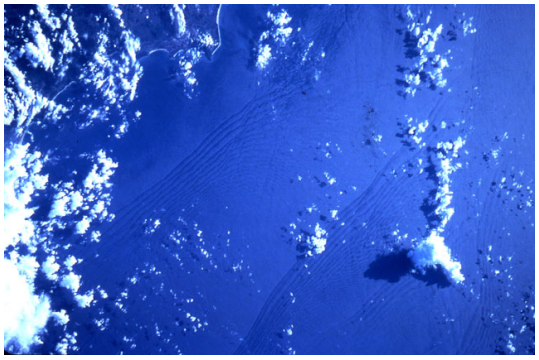
process of internal wave attractors. This has some strong consequences on the triadic resonance instability that may appear if the forcing is sufficiently large. The content of this article is described in Chapters 3, 4 and 5.
Internal wave attractors: Arnold tongue's structure and its implications for the instability scenario.
C. Brouzet, E. V. Ermanyuk, S. Joubaud, G. Pillet and T. Dauxois
Submitted to *Journal of Fluid Mechanics* (April 2016)

- This article will contain the added mass results presented in Chapter 2 and additional results expected to be obtained in future experiments.
  Added mass: a sidekick to tidal conversion.
  C. Brouzet, E. V. Ermanyuk, M. Moulin, and T. Dauxois
  In preparation.

- This article will describe the results concerning the influence of the basin scale on the width of the attractor, which is presented in Chapters 3 and 4. Numerical simulations are expected to complete the experiments.
  Internal wave attractors at different laboratory scales.
  C. Brouzet, E. V. Ermanyuk, S. Joubaud and T. Dauxois
  In preparation.

Chapter 1

Internal gravity waves



Signatures at the sea surface of internal waves observed in South China Sea. From NASA, June 1983.

Internal gravity waves are waves propagating within a stably stratified fluid. The stratification may be due to temperature, salinity, density, concentration or momentum variations. Examples of such fluids on Earth are oceans, lakes and atmosphere [129]. One can also find stratified fluids in stars and in astrophysical objects [131]. Internal waves are thus naturally present and play an important role in these stratified mediums. In the oceans, generated by the internal tides [55, 56], they may allow energy cascade between different scales [57] and through large distances. Moreover, they may be responsible for partial mixing of the stratified fluid [76], contributing to the global ocean circulation [120, 123]. Note that in a majority of systems where internal waves are found, rotation plays also an important role. When rotation only matters, this leads to another type of waves, inertial waves. They have some common features with internal waves. In natural systems, one has a combination of inertial and internal waves, called gravito-inertial waves. Nevertheless, in this manuscript, I essentially focus on internal waves, without any rotation.

In this Chapter, I introduce internal waves in a density stratified fluid and I derive the fundamental characteristics of these waves. Then, I discuss their generation, propagation and role in the oceans and atmosphere. Finally, I describe the experimental set-up used to study these waves in an idealized laboratory ocean, less than 1 meter deep. I present the experimental techniques to obtain a stratified fluid, generate the waves and observe them in the laboratory frame.

1.1 Internal waves in theory

In this section, I introduce the basic physics of internal waves propagating in a stratified fluid. First, I show qualitatively that oscillations can exist in a stably stratified fluid. Then, more quantitatively, I discuss the equations of linear internal waves propagating in an inviscid or viscous stratified fluid. The dispersion relation and the phase and group velocities are derived. Finally, the specific reflection of internal waves at a tilted boundary is introduced.

1.1.1 Physics of a stratified fluid

Let consider a density stratified fluid, where the density changes with the altitude or depth. This is an anisotropic medium, where the vertical direction is different from the other ones. To be stable, the density has to increase with depth or decrease with altitude. The mechanical static equilibrium is given by the balance between the gravity and the pressure forces. This leads to

$$\frac{\partial P}{\partial z} = -\bar{\rho}(z)g, \tag{1.1}$$

where g is the gravity acceleration, $\bar{\rho}$ the local density and P the pressure in the fluid. The vertical axis (z-coordinate) is here defined pointing upward, opposite to the gravity acceleration $\vec{g}$.

We focus now on a parcel of fluid in this stratification. One assumes that the parcel is small enough to have only one density, called ρ_p, and one considers its vertical displacement within the stratification. Its initial vertical position is named z_p. Because the stratification is stable and since the z-axis points upward, one has $\bar{\rho}(z) > \rho_p$ for $z < z_p$ and $\bar{\rho}(z) < \rho_p$ for $z > z_p$. This parcel undergoes the Archimedes force given, in units of volume, by

$$\overrightarrow{\Pi} = \bar{\rho}(z)g\vec{e}_z, \tag{1.2}$$

and its own gravity volumic force $-\rho_p g\vec{e}_z$. The sum $\overrightarrow{R}$ of these two forces can be written

$$\overrightarrow{R} = (\bar{\rho}(z) - \rho_p)g\vec{e}_z. \tag{1.3}$$

This equation shows that the parcel undergoes a force pointing downward if it is surrounded by lighter fluid, so for $z > z_p$. The force is pointing upward if the parcel is surrounded by heavier fluid, so for $z < z_p$. Of course, when $z = z_p$, no force is exerted on the parcel. Thus, one can note that a restoring force is exerted on the parcel when it is displaced in a stratified fluid. The force tends to bring back the parcel at its initial position.

The dynamics is given by the Newton law

$$\rho_p\vec{a} = (\bar{\rho}(z) - \rho_p)g\vec{e}_z, \tag{1.4}$$

where $\vec{a}$ is the acceleration of the fluid parcel. Considering small displacements δz of the parcel around z_p, equation (1.4) leads to

$$\begin{aligned}
\frac{\mathrm{d}^2\delta z}{\mathrm{d}t^2} &= \frac{\bar{\rho}(z_p + \delta z) - \rho_p}{\rho_p}g, &(1.5)\\
&= \frac{\bar{\rho}(z_p) + \delta z \left.\frac{\mathrm{d}\bar{\rho}}{\mathrm{d}z}\right|_{z_p} - \bar{\rho}(z_p)}{\bar{\rho}(z_p)}g + o\left((\delta z)^2\right), &(1.6)\\
&= \frac{g}{\bar{\rho}(z_p)}\left.\frac{\mathrm{d}\bar{\rho}}{\mathrm{d}z}\right|_{z_p}\delta z + o\left((\delta z)^2\right), &(1.7)\\
&\approx -N^2(z_p)\delta z. &(1.8)
\end{aligned}$$

One can note that equation (1.8) is equivalent to an harmonic oscillator equation of pulsation N. The parcel oscillates around its initial position z_p with a pulsation which depends on the density gradient around this position. N is called the buoyancy frequency, defined as

$$N(z_p) = \sqrt{-\frac{g}{\bar{\rho}(z_p)} \left.\frac{\mathrm{d}\bar{\rho}}{\mathrm{d}z}\right|_{z_p}}. \tag{1.9}$$

Note that N is defined only for stable stratifications as they have negative vertical density gradients: the z-axis points upward while the density decreases with z. For an homogeneous fluid, there is no density gradient and $N = 0$ rad/s. For a stratified fluid, the buoyancy frequency exhibits the strength of the density gradients: the higher N, the higher the gradients.

This section shows that a small perturbation of a stably stratified fluid can generate some oscillating motions. In real fluid, these motions are damped by viscosity. Nevertheless, one can see that waves can propagate through stably density stratified fluids with the buoyancy (combination of gravity and Archimedes forces) as the restoring force. These waves are named internal gravity waves and very often abbreviated in internal waves. The label "internal" is given to highlight the difference with surface waves, that propagate only at the surface of the fluid. Indeed, internal waves propagate in the bulk of the stratified fluid.

It worth to note that, in a homogeneous rotating fluid, one can have very similar waves, with the Coriolis force as the restoring force. These waves are called inertial waves. Internal and inertial waves have a lot of properties in common. Nevertheless, I study only internal waves in this manuscript, in order to simplify the problem at the maximum. Thus, I mainly describe them in this Chapter.

1.1.2 Linear internal waves

In the previous section, one considered a parcel of fluid in a density stable stratification. This allowed us to define the buoyancy frequency N and to obtain qualitatively that such medium can support the propagation of waves, named internal waves. In order to describe quantitatively these waves, let us consider an incompressible stably stratified fluid, with a buoyancy frequency $N(z)$. The dynamics of the flow is given by the Navier-Stokes equation

$$\rho \left(\frac{\partial \vec{v}}{\partial t} + (\vec{v} \cdot \vec{\nabla})\vec{v} \right) = \left(\rho - \overline{\rho}(z)\right) \vec{g} - \vec{\nabla} P + \nu \rho \Delta \vec{v}, \tag{1.10}$$

the volume conservation

$$\vec{\nabla} \cdot \vec{v} = 0, \tag{1.11}$$

and the mass conservation

$$\frac{\partial \rho}{\partial t} + \vec{v} \cdot \vec{\nabla} \rho = \kappa \Delta \rho. \tag{1.12}$$

$\vec{v} = (v_x, v_y, v_z)$ is the velocity of the fluid, ν stands for the kinematic viscosity of the fluid and κ for the diffusive coefficient of the stratifying agent. The total density $\rho(x, y, z, t) = \bar{\rho}(z) + \rho'(x, y, z, t)$ is equal to the background stratification $\overline{\rho}(z)$ added with one term corresponding to the density perturbations $\rho'(x, y, z, t)$ due to the internal waves. These 5 equations concern 5 unknown quantities.

To simplify the problem, one can assume that the flow is bi-dimensional and contained in the xOz plane, with no variation along the y-direction. In this framework, using the volume conservation (1.11), one can introduce the stream function ψ defined as

$$\frac{\partial \psi}{\partial x} = -v_z \qquad \text{and} \qquad \frac{\partial \psi}{\partial z} = v_x. \tag{1.13}$$

One can then rewrite equations (1.10) and (1.12) as

$$\partial_{tz}\psi + J(\partial_z\psi, \psi) = -\frac{1}{\rho}\partial_x P + \nu\partial_z\Delta\psi, \tag{1.14}$$

$$\partial_{tx}\psi + J(\partial_x\psi, \psi) = \frac{\rho'}{\rho}g + \frac{1}{\rho}\partial_z P + \nu\partial_x\Delta\psi\ , \tag{1.15}$$

$$\partial_t\rho' + J(\rho', \psi) = \kappa\Delta\rho' + \frac{\mathrm{d}\bar{\rho}}{\mathrm{d}z}\partial_x\psi\ , \tag{1.16}$$

where J is the jacobian defined as $J(f, g) = \partial_x f\partial_z g - \partial_z f\partial_x g$. Note that one uses the convention $\partial_j\psi = \partial\psi/\partial j$, where j stands for x, z or t.

One considers in the following that the density perturbations $\rho'(x, z, t)$ are small in comparison with the background stratification $\bar{\rho}(z)$. This assumption is fully true in our experiments because we use only density stratification between 1000 g/L and 1080 g/L. Thus, the density perturbations are limited to less than 10% of the average stratification. One defines $\rho_0 = \langle\bar{\rho}\rangle$ as the spatial density average of the stratification. Consequently, one can apply Boussinesq approximation in equations (1.14) and (1.15). It consists in approximating the total density ρ everywhere by ρ_0 except in the buoyancy terms. Thus, the buoyancy frequency is now defined by

$$N(z) = \sqrt{-\frac{g}{\rho_0}\frac{\mathrm{d}\bar{\rho}}{\mathrm{d}z}(z)}. \tag{1.17}$$

By differentiating equation (1.14) with respect to z and equation (1.15) with respect to x and combining them, one gets

$$\partial_t\left(\Delta\psi\right) + J(\Delta\psi, \psi) - \nu\Delta\left(\Delta\psi\right) = \frac{g}{\rho_0}\partial_x\rho', \tag{1.18}$$

$$\partial_t\rho' + J(\rho', \psi) - \kappa\Delta\rho' = -N^2\frac{\rho_0}{g}\partial_x\psi. \tag{1.19}$$

Equations (1.18) and (1.19) describe the non-linear dynamics of a viscous stratified fluid, with the stratifying agent diffusing with time. Note that the buoyancy frequency N may depend on the vertical coordinate z. The linear dynamics is obtained by neglecting the non-linear terms, given by the jacobians. This leads to

$$\partial_t\left(\Delta\psi\right) - \nu\Delta\left(\Delta\psi\right) = \frac{g}{\rho_0}\partial_x\rho', \tag{1.20}$$

$$\partial_t\rho' - \kappa\Delta\rho' = -N^2\frac{\rho_0}{g}\partial_x\psi. \tag{1.21}$$

One considers plane wave solutions to the linear system: $\psi = \psi_0\exp(i\omega t - i\vec{k}\cdot\vec{r})$ and $\rho' = \rho'_0\exp(i\omega t - i\vec{k}\cdot\vec{r})$. The wave vector is $\vec{k} = k_x\vec{e}_x + k_z\vec{e}_z$ and its modulus is noted k.

The linear system can thus be written using a matrix

$$\begin{pmatrix} -k^2(i\omega + \nu k^2) & i\dfrac{g}{\rho_0}k_x \\ iN^2\dfrac{\rho_0}{g}k_x & i\omega + \kappa k^2 \end{pmatrix}\begin{pmatrix}\psi \\ \rho'\end{pmatrix} = \begin{pmatrix}0 \\ 0\end{pmatrix}. \tag{1.22}$$

One has non trivial solutions only if the determinant of the matrix is equal to zero. This leads to the relation

$$k^2\left(i\omega + \nu k^2\right)\left(i\omega + \kappa k^2\right) + N^2k_x^2 = 0. \tag{1.23}$$

Equation (1.23) contains the linear physics of the propagation of a plane wave in a viscous stratified fluid. One can make several assumptions on the fluid in order to simplify this equation. Note that plane waves are also solutions of the non-linear problem described by equations (1.18) and (1.19), as $J(\Delta\psi, \psi) = J(\rho', \psi) = 0$.

Inviscid fluid

Let us consider an inviscid and non-diffusive fluid. Thus, ν and κ vanish. Equation (1.23) becomes

$$\left(\frac{\omega}{N}\right)^2 = \frac{k_x^2}{k^2} \qquad \text{or} \qquad \frac{\omega}{N} = \pm\frac{|k_x|}{k}. \tag{1.24}$$

This is the dispersion relation of linear internal waves in a inviscid and non-diffusive fluid. This can be written using the angle θ, between the vertical z-axis and the wave-vector $\vec{k}$

$$\frac{\omega}{N} = \pm\sin\theta. \tag{1.25}$$

This relation is anisotropic and purely geometric. Indeed, the angle θ is determined only by the buoyancy frequency and the pulsation of the waves, if $\omega < N$. Thus, for given N and ω, four different couples $(\pm k_x, \pm k_z)$ are possible to fulfill equation (1.25). Each couple corresponds to one beam in one quadrant, shown in figure 1.1. Moreover, the buoyancy frequency N may depend on z. This defines a local θ angle: when the internal wave propagates through a stratified fluid with non-constant but continuous N, its trajectory

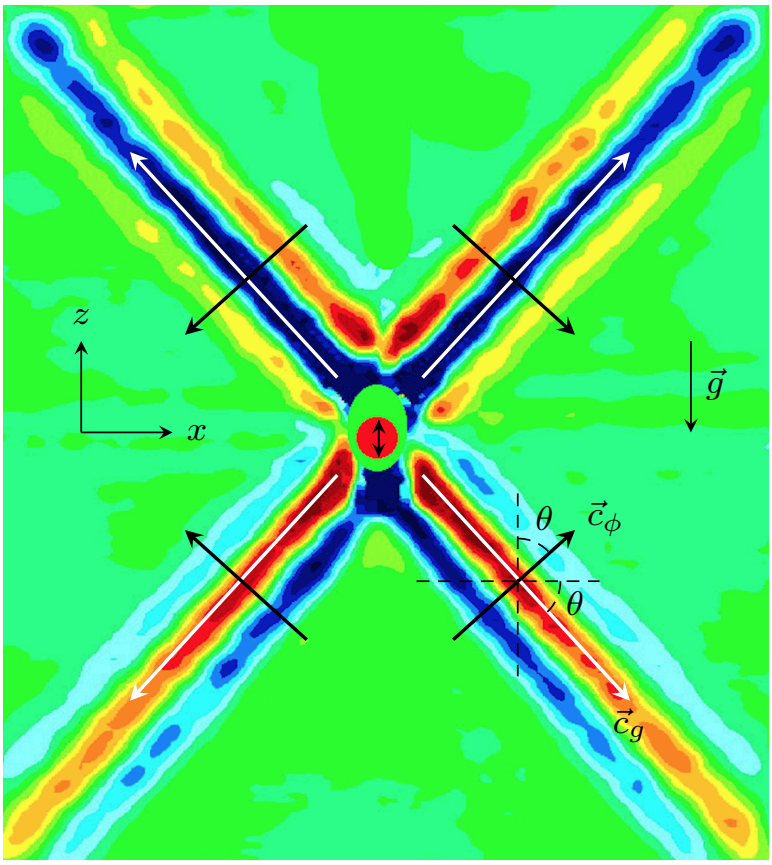


Figure 1.1: Internal waves propagating in a linearly stratified fluid and emitted by a vertically oscillating cylinder, in red in the center of the figure. The group velocity vectors are in white while the phase velocity vectors are in black. The angle θ is defined for one beam. The colors indicate the horizontal density gradient fields, obtained experimentally by Evgeny Ermanyuk using the SyS technique described further in this Chapter.

is bent. Note that θ does not exist for ω larger than N. In this case, the waves are evanescent. Finally, it worths to note that the dispersion relation does not exhibit any characteristic length scale. Thus, the wave length of the internal waves is fixed by the boundary conditions, so the source of the waves only.

From equation (1.24), one can derive the phase and group velocities

$$\vec{c}_\phi = N\frac{|k_x|}{k^3}\left(k_x\vec{e}_x + k_z\vec{e}_z\right), \tag{1.26}$$

$$\vec{c}_g = N\frac{\mathrm{sign}(k_x)k_z}{k^3}\left(k_z\vec{e}_x - k_x\vec{e}_z\right), \tag{1.27}$$

where $\mathrm{sign}(k_x)$ is equal to $+1$ if $k_x > 0$ and -1 if $k_x < 0$. These two velocities bring two interesting properties of internal waves: the group and phase velocities are perpendicular and their vertical components have opposite signs. These two properties are illustrated in figure 1.1. Moreover, as θ is defined between the vertical axis and the wave vector, one can also define it as the angle between the horizontal axis and the group velocity. Thus, the energy propagates at a fixed angle θ with respect to the horizontal for given ω and N. One can see this property in figure 1.1 where the four emitted beams have the same angle of propagation θ. One can define a new coordinate system, attached to a wave beam. The group velocity direction is called the ξ direction and the phase velocity direction is defined as η direction. Note that ξ and η are perpendicular. This system is used in the next paragraph about the viscous attenuation and to describe more precisely the attractor in Chapter 3.

Viscous fluid

Let us consider a non-diffusive ($\kappa = 0$) viscous fluid. Equation (1.23) becomes

$$\left(\frac{\omega}{N}\right)^2 - i\nu\frac{k^2}{N}\left(\frac{\omega}{N}\right) - \frac{k_x^2}{k^2} = 0. \tag{1.28}$$

This is a second order polynomial of the variable ω/N and its discriminant is equal to

$$\Delta = -\nu^2\frac{k^4}{N^2} + 4\frac{k_x^2}{k^2}. \tag{1.29}$$

The sign of Δ depends on the viscosity, the buoyancy frequency and the wave vector. For positive Δ, the roots (ω/N values) of equation (1.28) are complex while for negative Δ, the roots are purely imaginary and the waves are evanescent. For positive Δ, one can write $\omega = \omega_r + i\omega_i$ where

$$\omega_r = \pm N\sqrt{\frac{k_x^2}{k^2} - \frac{\nu^2k^4}{4N^2}} \qquad \text{and} \qquad \omega_i = \frac{\nu k^2}{2}. \tag{1.30}$$

The real part ω_r of the pulsation of the wave is modified by the viscosity. If ν vanishes, one finds the inviscid dispersion relation of equation (1.25). Nevertheless, the modification of the dispersion relation due to viscosity is very small for the values used in the experiments described in this manuscript and in the oceans. For the experiments, $N \approx 1$ rad/s and wave lengths are of the order of 10 cm while in the oceans, $N \approx 10^{-4} - 10^{-3}$ rad/s and the wave lengths are in the range of $100 - 1000$ m. This implies a difference with the inviscid dispersion relation of much less than 1%, in both cases.

The imaginary part ω_i gives the viscous attenuation of the wave. In the (η, ξ) frame introduced before, one has

$$\begin{aligned} \psi(\eta, \xi, t) &= \psi_0 \exp(i\omega t - ik\xi), & (1.31) \\ &= \psi_0 \exp(i\omega_r t - ik\xi) \exp(-\nu k^2 t/2). & (1.32) \end{aligned}$$

Equation (1.32) gives the viscous attenuation of the wave in time. To obtain this attenuation in function of the traveling distance ξ, one has to relate the time t with ξ by $\xi = c_g t = Nt|k_z|/k^2$, using the inviscid group velocity. Thus, this leads to

$$\psi(\eta, \xi, t) = \psi_0 \exp(i\omega_r t - ik\xi) \exp(-\beta\xi), \tag{1.33}$$

where

$$\beta = \frac{\nu k^3}{2\sqrt{N^2 - \omega^2}}. \tag{1.34}$$

Thus, the waves are damped with the wave number to the power 3 as they travel through the distance ξ. The shorter the wave length or the closer ω to N, the more the waves are damped.

Let us consider now that κ no longer vanishes. The polynomial on ω/N in equation (1.23) becomes

$$\left(\frac{\omega}{N}\right)^2 - i(\nu + \kappa)\frac{k^2}{N}\left(\frac{\omega}{N}\right) - \left(\nu\kappa\frac{k^4}{N^2} + \frac{k_x^2}{k^2}\right) = 0. \tag{1.35}$$

The discriminant of this polynomial is thus

$$\Delta = -\nu^2\left(1 - \frac{1}{\mathrm{Sc}}\right)^2 \frac{k^4}{N^2} + 4\frac{k_x^2}{k^2}, \tag{1.36}$$

with $\mathrm{Sc} = \nu/\kappa$ the Schmidt number. This number compares the effects of viscosity with the ones of salt diffusion. For water and salt, ones has $\mathrm{Sc} \approx 700$ that allows us to neglect the ratio $1/\mathrm{Sc}$ in front of 1. Thus, the discriminant in equation (1.36) can be considered equal to the one of a viscous but non-diffusive fluid, presented in equation (1.29).

As the viscous dispersion relation is very close to the inviscid one, one can consider that the waves propagate with the inviscid dispersion relation but with a viscous damping along the trajectory of the waves.

1.1.3 Vertical modes

In the previous section, we investigate the linear dynamics of a stratified fluid using plane waves. Nevertheless, this assumes that the fluid has an infinite extent, which is not true for the experiments and the oceans. Indeed, internal waves are vertically confined as the vertical extent of oceans in much smaller than the horizontal extent. Consequently, it worths to think in terms of vertical modes, of type

$$\psi(x, z, t) = \psi_0 f(z) \exp(i\omega t - ik_x x). \tag{1.37}$$

With these vertical modes, the propagative part is only horizontal. For an inviscid and non-diffusive fluid, equations (1.20) and (1.21) give

$$\frac{\partial^2 \Delta\psi}{\partial t^2} + N^2 \frac{\partial^2 \psi}{\partial x^2} = 0. \tag{1.38}$$

The injection of the vertical mode in equation (1.37) leads to

$$\frac{\mathrm{d}^2 f}{\mathrm{d}z^2} + k_x^2 \left(\frac{N^2}{\omega^2} - 1 \right) f(z) = 0. \tag{1.39}$$

Note that for equations (1.38) and (1.39), the buoyancy frequency N may depend on the vertical coordinate z. Nevertheless, for simplicity, one assume that N is constant in the remainder of this section. To solve equation (1.39), one needs two boundary conditions on f. They are provided by assuming that the fluid does not go through the boundaries at $z = 0$ and $z = H$. This implies that the stream function vanishes for any values of t and x, so $f(0) = f(H) = 0$. The solutions of equation (1.39) are

$$f_p(z) \propto \sin\left(p\pi \frac{z}{H} \right), \tag{1.40}$$

where p is an integer. As the system is linear, the solutions correspond to the sum of all the possible solutions f_p

$$\psi(x, z, t) = \sum_{p=0}^{\infty} A_p \sin(k_{z,p} z) \exp(i\omega t - i k_{x,p} x), \tag{1.41}$$

with $k_{z,p} = p\pi/H$, $k_{x,p}$ the horizontal component of the wave vector obtained using equation (1.24) and A_p integration constants. Note that each p mode can be decomposed into two plane waves propagating with two wave vectors equal to

$$\vec{k}_{p+} = k_{x,p}\vec{e}_x + k_{z,p}\vec{e}_z \qquad \text{and} \qquad \vec{k}_{p-} = k_{x,p}\vec{e}_x - k_{z,p}\vec{e}_z. \tag{1.42}$$

In the remainder of this manuscript, the forcing is made only via a vertical mode 1 (corresponding to $p = 1$) with the wave-maker. The horizontal and vertical velocity components of this mode are given by

$$v_x = v_{x0} \cos\left(\pi \frac{z}{H} \right) \cos\left(\omega t - k_x x \right), \tag{1.43}$$

$$v_z = v_{z0} \sin\left(\pi \frac{z}{H} \right) \sin\left(\omega t - k_x x \right). \tag{1.44}$$

The amplitudes of these two velocity components are linked by the volume conservation equation

$$v_{x0} = v_{z0} \sqrt{\frac{N^2}{\omega^2} - 1}. \tag{1.45}$$

1.1.4 Reflection of internal waves

The dispersion relation of internal waves is very specific because the angle of propagation of such waves is fixed for given N and ω. This leads to a very specific reflection on a sloped boundary, as shown in this section. This non-Descartes reflection is a key process in the existence of internal wave attractors, studied in this manuscript in Chapters 3, 4 and 5.

One considers an inviscid linearly stratified fluid of constant buoyancy frequency N. The sloped boundary is tilted with an angle α with respect to the vertical, as shown in figure 1.2. Note that this configuration does not seem natural for the reflection of internal waves on the topography at the bottom of the ocean. Nevertheless, this is the configuration used in the set-up of this manuscript. For the sake of clarity, in this section only, the origin

of the coordinates is taken at the bottom of the slope, also shown in figure 1.2. It worths to note that, as the salt flux through the boundary vanishes, the lines of constant density must be bent very close to the boundary in order to be perpendicular to it [133, 30, 150]. This distortion of the stratification is caused by salt diffusion and is limited to a given distance to the boundary. Following Phillips [133], this distance in our experiments is less than 0.5 mm. Thus, one can consider that the wave propagation and reflection are not disturbed by this phenomena.

The linear theory of internal wave reflection has been developed first by Phillips [132] and is based on a well-known incident wave reflecting at a sloped boundary [129]. Let assume that the incident wave is bi-dimensional and can be described by the stream function

$$\psi_{\mathrm{i}}(x,z,t) = \psi_{0,\mathrm{i}} \exp(i\omega_{\mathrm{i}} t - i\vec{k}_{\mathrm{i}} \cdot \vec{r}). \tag{1.46}$$

The index i refers to the incident wave field and ω_{i} and $\vec{k}_{\mathrm{i}}$ are the pulsation and wave vector of the incident wave. They verify the dispersion relation. The energy density is defined as

$$\begin{aligned} E_{c,\mathrm{i}} &= \frac{1}{2}\left(|v_x|^2 + |v_z|^2\right), & (1.47)\\ &= \frac{1}{2}\left(|\partial_z \psi_{\mathrm{i}}|^2 + |\partial_x \psi_{\mathrm{i}}|^2\right), & (1.48)\\ &= \frac{1}{2} k_{\mathrm{i}}^2 |\psi_{0,\mathrm{i}}|^2. & (1.49) \end{aligned}$$

When the incident wave hits the sloped boundary, a reflected wave is created and can be expressed as follows

$$\psi_{\mathrm{r}}(x,z,t) = \psi_{0,\mathrm{r}} \exp(i\omega_{\mathrm{r}} t - i\vec{k}_{\mathrm{r}} \cdot \vec{r}), \tag{1.50}$$

where the index r refers to the reflected wave field. Thus, the energy density of the reflected wave is

$$E_{c,\mathrm{r}} = \frac{1}{2} k_{\mathrm{r}}^2 |\psi_{0,\mathrm{r}}|^2. \tag{1.51}$$

The complete wave field is therefore $\psi = \psi_{\mathrm{i}} + \psi_{\mathrm{r}}$. As the flow does not penetrate the sloped boundary, the total stream function field must vanish at the boundary, where $x = -z \tan\alpha$.

In order to simplify the boundary condition, one defines the coordinates attached to the slope (x_s, z_s), as shown in figure 1.2. The velocity fields in the slope coordinate system are $(v_{x_s}, v_{z_s}) = (-\partial\psi/\partial z_s, \partial\psi/\partial x_s)$ and the wave number is noted $\vec{k}_s = (k_{x_s}, k_{z_s})$. The non-penetration condition can be expressed as $v_{x_s} = 0$ at $x_s = 0$ and for all z_s and time t. On the total stream function field, this becomes

$$k_{z_s,\mathrm{i}} \psi_{0,\mathrm{i}} \exp(i\omega_{\mathrm{i}} t - i\vec{k}_{s,\mathrm{i}} \cdot \vec{r}_s) + k_{z_s,\mathrm{r}} \psi_{0,\mathrm{r}} \exp(i\omega_{\mathrm{r}} t - i\vec{k}_{s,\mathrm{r}} \cdot \vec{r}_s) = 0, \tag{1.52}$$

at $x_s = 0$ and for all z_s and time t. This leads to

$$\begin{aligned} \omega_{\mathrm{i}} &= \omega_{\mathrm{r}} \equiv \omega, & (1.53)\\ k_{z_s,\mathrm{i}} &= k_{z_s,\mathrm{r}} \quad \text{and} & (1.54)\\ \psi_{0,\mathrm{i}} &= \psi_{0,\mathrm{r}} \equiv \psi_0. & (1.55) \end{aligned}$$

Thus, the frequency and the wave vector component parallel to the sloped boundary are conserved during the reflection. The normal component of the wave vector can be determined using geometrical construction and the dispersion relation

$$\begin{aligned} k_{x_s,\mathrm{i}} &= k_{z_s,\mathrm{i}} \tan(\theta - \alpha), & (1.56)\\ k_{x_s,\mathrm{r}} &= k_{z_s,\mathrm{r}} \tan(\theta + \alpha). & (1.57) \end{aligned}$$

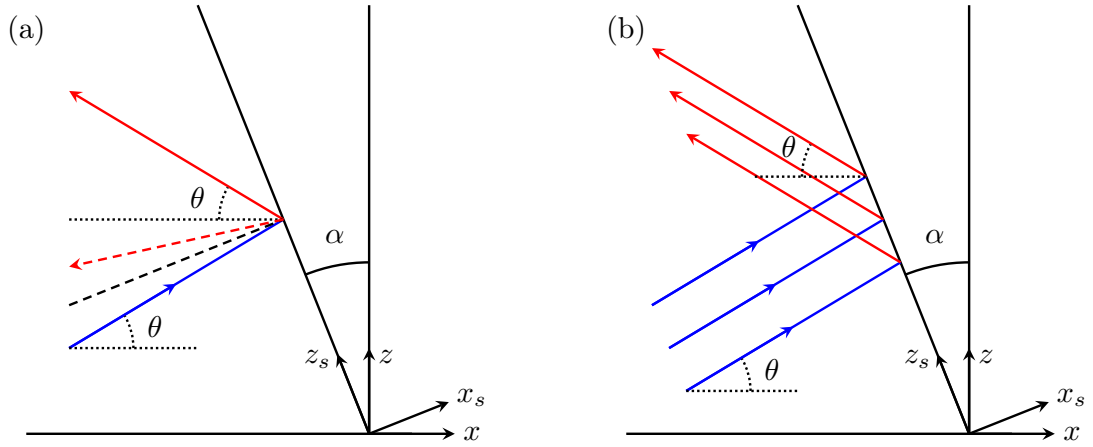


Figure 1.2: (a): Reflection of an incident blue ray on the sloped boundary inclined with an angle α with respect to the vertical. In optics or acoustics, the reflected ray is the dashed red line. For internal waves, the reflected ray is the red solid line. (b): Reflection of an incident internal wave beam in blue on a sloped boundary. The reflected wave beam is in red. The slope coordinates (x_s, z_s) are shown on both panels.

Thus, the ratio between the norms of the two wave vectors is given by

$$\frac{k_\mathrm{r}}{k_\mathrm{i}} = \left|\frac{\cos(\theta-\alpha)}{\cos(\theta+\alpha)}\right| \equiv \gamma. \tag{1.58}$$

This defines the focusing parameter γ, which is greater than 1 in figure 1.2. This parameter diverges for $\theta+\gamma \to 90°$. This corresponds to the case where the waves have a propagation angle very close to the slope of the boundary. This situation is called critical reflection. Indeed, it is critical because γ diverges and thus, the wave length of the reflected wave tends to 0.

As the pulsation of the wave is conserved, both the incident and reflected waves propagate with the same angle θ, defined as $\sin\theta = \omega/N$. It worths to note that this is very different from reflection in optics or acoustics where the electromagnetic or sound waves conserve the angle with respect to the normal to the sloped boundary (dashed black line in figure 1.2(a)). This is a classical Descartes reflection. The difference with internal waves is illustrated in figure 1.2(a). The incident ray is in blue. The reflected ray for optics or acoustics is the dashed red line while the one for internal waves is the solid red line.

One can see in figure 1.2(b) that the blue incident beam is reflected into the red one. The width of the reflected beam is thus reduced by the factor γ, defined in equation (1.58). Thus, this is a focusing reflection. The energy in the incident beam is concentrated into the red one. Indeed, equation (1.58) leads to $E_{c,\mathrm{r}} = \gamma^2 E_{c,\mathrm{i}}$ showing that the energy density is increased by a factor $\gamma^2 > 1$. One can also have a defocusing reflection if the incident beam is the red one in figure 1.2(b) while the reflected beam is the blue one.

Finally, note that a reflection on a slope which is horizontal or vertical does not lead to focusing or defocusing. Indeed, for this kind of slopes, α is equal to 0 or π. Thus, $\gamma = 1$ and everything is conserved.

In this section, I have shown the fundamental properties of internal waves propagating in a stably stratified fluid. As oceans, lakes and atmosphere are naturally stably stratified

systems, such waves can propagate through them. In the next section, I present internal waves in these systems.

1.2 Internal waves in the oceans and in the atmosphere

Oceans and atmosphere are natural systems which can be partly stratified and thus, the support of internal waves. I give in this section the main characteristics of the internal waves in the oceans and atmosphere. It worths to note that, in reality, the waves observed in the ocean and in the atmosphere are gravito-inertial waves.

1.2.1 Stratification of the oceans and the atmosphere

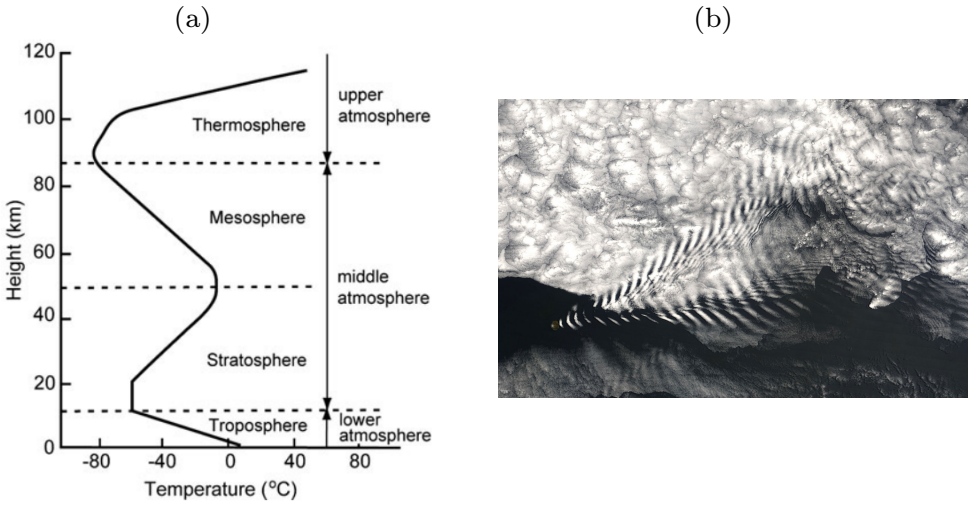


Figure 1.3: (a): Vertical structure of the atmosphere in temperature. (b): Atmospheric internal waves behind the Amsterdam island, located in the south of Indian Ocean.

Figure 1.3(a) shows a typical temperature evolution as a function of the altitude in the atmosphere. This kind of stratification can be measured using weather balloons for example. One can identify different regions with approximately constant temperature gradient: troposphere, stratosphere, mesosphere and thermosphere. These regions are separated by different turning points in temperature, marked as horizontal dashed lines. The boundaries between the regions are named tropopause, stratopause and mesopause (from low to high altitude). This temperature profile does not define a stable stratification. Nevertheless, the density in the atmosphere depends on the temperature and on the pressure, which vary strongly with the altitude. Indeed, the pressure decays by three orders of magnitude between the ground ($z = 0$ km) and the stratopause ($z = 50$ km) and by six orders of magnitude between the ground and the upper atmosphere ($z = 100$ km). Thus, it it necessary to define a potential temperature, which is a temperature of the atmosphere at the same pressure. This potential temperature defines a stable stratification. The buoyancy frequency in the atmosphere is around 10^{-2} rad/s. In figure 1.3(b), one can distinguish internal waves in the atmosphere using the clouds close to an island in the Indian Ocean.

The ocean is stratified in temperature and salinity, as shown in figures 1.4(a) and (b). This induces a stratification in density presented in figure 1.4(c). From this, one can

compute the buoyancy frequency profile, shown in figure 1.4(d). Although the stratification depends on the geographical location on the Earth, one can identify three main layers in the ocean:

- a mixed layer, located just below the surface. This layer is approximately 100 m thick and is homogeneous in temperature and salinity. The mixing is due to the different interactions with the atmosphere. Indeed, there are some momentum exchanges with the wind in the atmosphere and also thermal transfers

- an abyssal region, below the mixed layer. In this layer, the density varies quasi-linearly with the depth on several kilometers. The buoyancy frequency in this layer is typically of $10^{-4} - 10^{-3}$ rad/s

- a pycnocline, where the density varies strongly. This layer is located in between the mixed layer and the abyssal region and is very thin. Thus, it exhibits strong density gradients and the buoyancy frequency in this layer is typically of 10^{-2} rad/s. The pycnocline limits the exchanges between the mixed layer and the abyssal region because of strong density gradients.

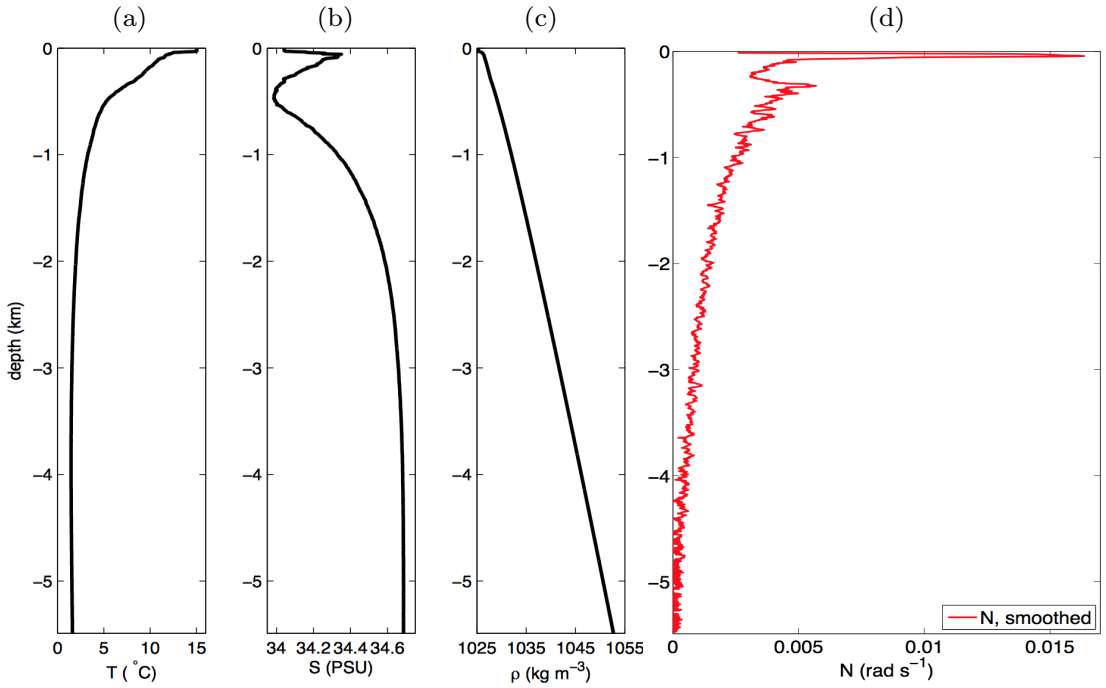


Figure 1.4: Profiles of temperature (a), salinity (b), density (c) and buoyancy frequency (d) as a function of the depth, extracted from [60]. Theses profiles have been measured at 40°N in the Pacific Ocean.

1.2.2 Internal wave generation

In the atmosphere, internal waves are essentially generated by the interactions between a mean-flow and a topography. One can characterize this wave emission by the Froude

number Fr, defined as

$$\mathrm{Fr} = \frac{U}{Nh}, \tag{1.59}$$

where N is the buoyancy frequency, h the height of the obstacle and U a typical velocity of the wind. This dimensionless number measures the importance of the kinetic energy of the flow with respect to the stratification density. If $\mathrm{Fr} < 1$, the kinetic energy of the flow is too low to break the stratification: when a parcel of fluid encounters the obstacle, it contours it instead of going above. Thus, no waves are generated. When $\mathrm{Fr} > 1$, the flow has enough energy to break the stratification. When a parcel a fluid encounters the obstacle, its altitude is changed and it causes a density perturbation. Thus, internal waves are created. Let $h = 1000$ m and $N = 10^{-2}$ rad/s. To generate internal waves, one should have a typical wind of 40 km/h, on the topography.

In the ocean, there are two mechanisms responsible for the generation of internal waves. The first one is internal wave emission by a topography. Indeed, when the water is moved upon a topography by the tides or a current, this can create internal waves. The Froude number Fr is also important here. For example, let us consider a tidal or an oceanic current on a 100 m high topography, with $N \approx 10^{-3}$ rad/s. This leads to internal wave generation when the speed of the current is greater than 40 cm/s. Figure 1.5, extracted from [55], illustrates this phenomena for tidal forcing. Note that it is not necessary to have a very deep ocean to generate internal waves, as one can see on the left of the figure where waves are generated by the interactions between the tides and the continental shelf.

The other internal wave generation mechanism is the pycnocline forcing by the atmosphere. Indeed, the atmosphere can generate motions in the pycnocline, due to storms, winds or surface waves. Then, the pycnocline can emit internal waves, that propagate along the pycnocline or in the abyssal region.

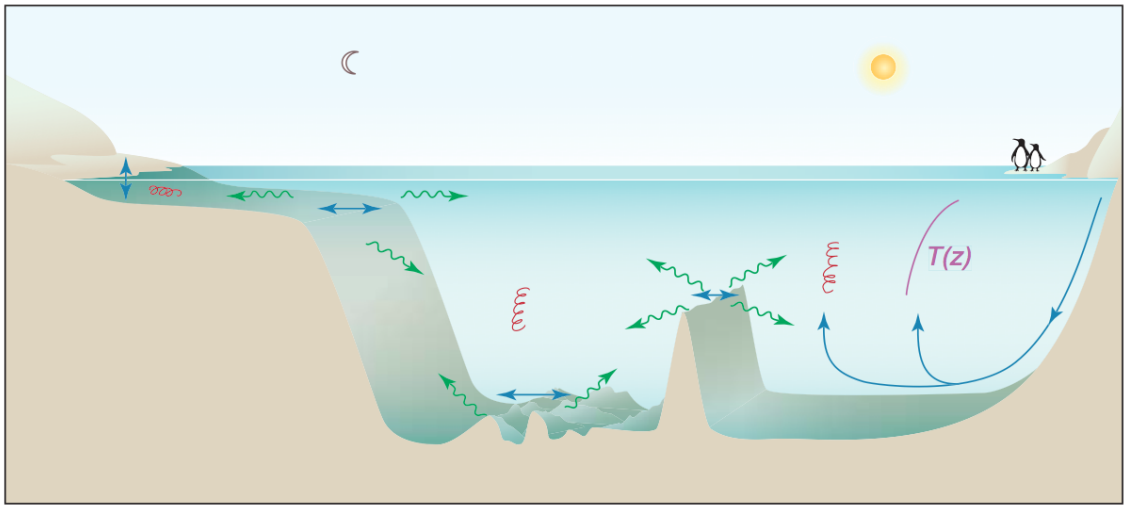


Figure 1.5: Internal wave generation by tidal forcing, extracted from [55]. In the center, waves are forced by the tides on topographies at the bottom of the ocean. On the left, waves are forced by the tides close to a continental shelf. The waves contribute to turbulence and mixing in the ocean: they have an effect on the density profile (here tuned by the temperature), as shown on the right.

1.2.3 Internal wave propagation in the ocean

The purpose of this manuscript is more adapted to internal waves in the ocean than in the atmosphere. Indeed, we study the behavior of internal waves in closed domains, which are more likely to be found in the oceans thanks to the topography than in the atmosphere. Thus, I mainly discuss in this section the internal wave propagation in the ocean. Nevertheless, in the atmosphere, internal waves are also important and responsible for different phenomena. For example, the quasi-biennial oscillation (QBO) is an atmospheric periodic zonal-flow induced by internal waves [3]. Some laboratory experiments have been performed on this phenomena by Plumb and McEwan [134], by Otobe *et al.* [128] and more recently by Semin *et al.* [140].

In the ocean, internal waves have a typical wave length varying between 100 m and several kilometers. Thus, their wave number is very small and the viscous attenuation is vanishing, according to equation (1.34). The typical damping distance is around 50000 km. This means that internal waves can visit the entire ocean and have global effects on the stratification, despite they are created at a more local scale.

As viscosity does not play an important role, non-linear effects can be significative. This can lead to partial mixing of the stratification. A way to measure the mixing in the ocean is to observe the turbulent diffusivity. This quantity is related to the average vertical flow of mass. The larger the diffusivity, the larger the mixing. Polzin *et al.* [135] measured this quantity in the Brazil basin above two kinds of topography. The results are shown in figure 1.6. Above the smooth topography on the left, the values of the diffusivity are small while the diffusivity is high above the sharp topography on the right. As internal waves are generated by the topography, one can guess that more waves are present above the sharp topography. This can explain the high values of diffusivity.

Thus, internal waves can generate mixing of the oceanic stratification and play a role in the oceanographic circulation. Indeed, mixing is of paramount importance for global circulation. The ocean is not a heat engine [73], and, therefore, sustainable global circulation requires an input of mechanical energy and efficient mixing. In the upper ocean, wind stress produces a significant input of mechanical energy inducing surface waves, geostrophic currents and Eckman drift. The energy cascades in the upper ocean are described, for instance, in flourishing literature on wave turbulence [121, 151], wave breaking [130] and stratified turbulence and mixing in shear flows [47]. Globally, about 90% of the roughly 60 TW of the energy input from the wind to the Ocean is dissipated within the upper 100 m from the water surface [48]. Energy cascade in the abyssal ocean is less clear. Existing oceanographic data suggest that order 1TW source of energy is needed to maintain the abyssal mixing [120]. The sustainable energy input to the ocean abyss comes from the interaction of global tides with the bottom topography yielding the global rate of energy conversion to internal tides order 1TW [56]. An efficient energy cascade must exist to ensure the energy transfer from the internal tides to complex multi-scale internal wave motion in the interior of the ocean and, ultimately, to abyssal mixing and dissipation [120].

There is no unified viewpoint on the dominance of a particular mechanism of abyssal mixing under natural conditions [76]. The existing literature describes isolated events which are likely to be at play in the energy cascade: wave focusing [25], critical and nearly-critical reflection of internal waves at a slope [30], refraction of waves at layers of high density gradient [108], positive interference of waves emitted by complex multi-ridge topography [38], internal Lee waves [123, 100]. Possible scenarios of instability include triadic resonant instability [16], hydrostatic instability [108], shear and bottom layer instabilities at slopes [58, 87], etc.

Thus, severals questions remain to be addressed, in particular, about the mixing and

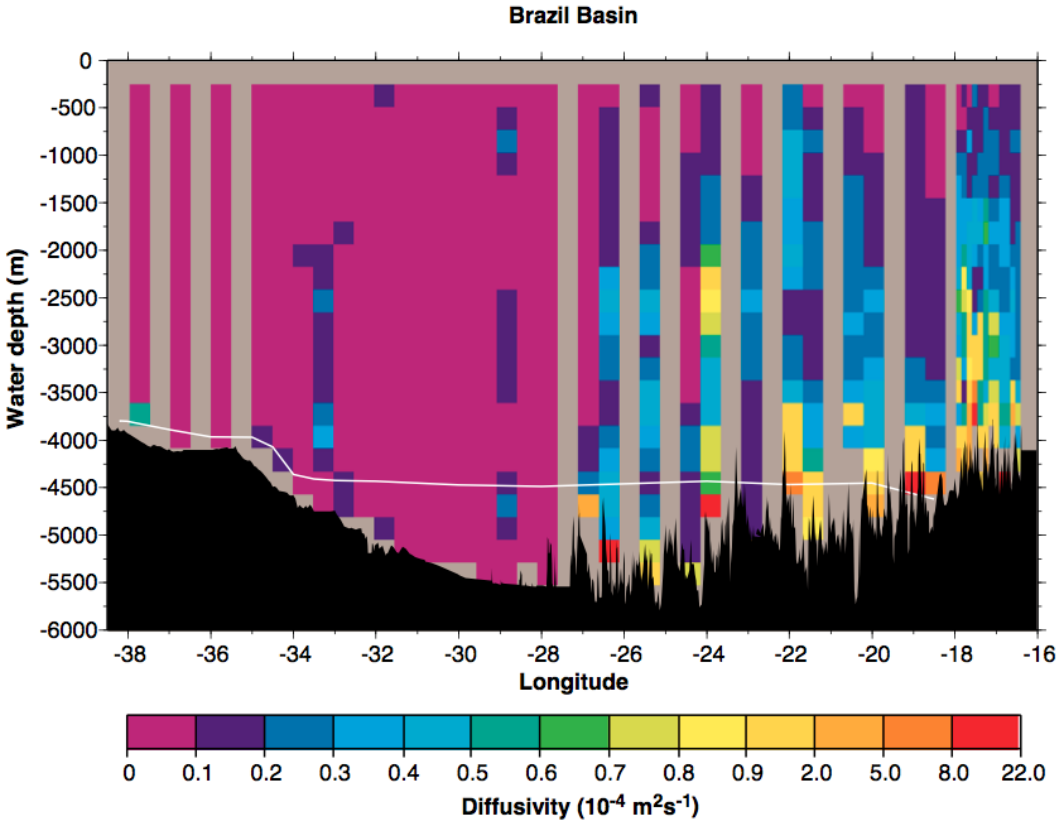


Figure 1.6: Turbulent diffusivity coefficient in a depth-longitude section measured in the Brazil basin, upon two different topographies. On the left, the topography is smooth and the diffusivity remains small while on the right, the topography is very sharped and the diffusivity takes large values. Extracted from [135].

the energy cascade processes. This manuscript studies the possibly that these processes are due to internal wave attractors. It worths to examine these questions in idealized laboratory experiments to simplify the problems. As the ocean exhibits very complex features such as rotation, non-linear stratification, different wave forcings, very diversified topography, one can try to model the ocean by using its fundamental characteristics but simplified: linear stratification in a tank where both forcing and the geometry are well-controlled. The next section deals with how internal waves are generated and observed at the laboratory scale.

1.3 Internal waves in the laboratory

In this section, I present the frame of the experiments in laboratory. As the ocean is very complicated to model, we consider in this manuscript idealized experiments in a tank much smaller than the ocean. This tank is filled with linearly stratified fluid and the waves are generated by a wave-maker.

1.3.1 Set-ups

In this section, I describe the set-up used for the attractor experiments of this manuscript, discussed in Chapters 3, 4 and 5. The set-up used for Chapter 2 is presented in section 2.2.

Figure 1.7 shows the attractor set-up. The tank is filled by a linearly stratified fluid using the double bucket method, described in section 1.3.2. On the left side, a wave-maker, described in section 1.3.4, generates the internal waves at a pulsation ω_0. On the right, there is a sliding sloping side wall, inclined at an angle α. This wall is slowly inserted into the fluid after the end of the filling procedure. This set-up delimits a trapezoidal domain of length L (at the bottom), of height H and with an angle α. The width of the tank in the transverse direction is named W.

The different axes are indicated in figure 1.7. z is the vertical direction while x and y are the horizontal directions. x lies within the plane of the schema and y is the direction perpendicular to this plane. The origin is taken at the bottom of the wave-maker in the $x - z$ plane and in the middle of tank for the y direction.

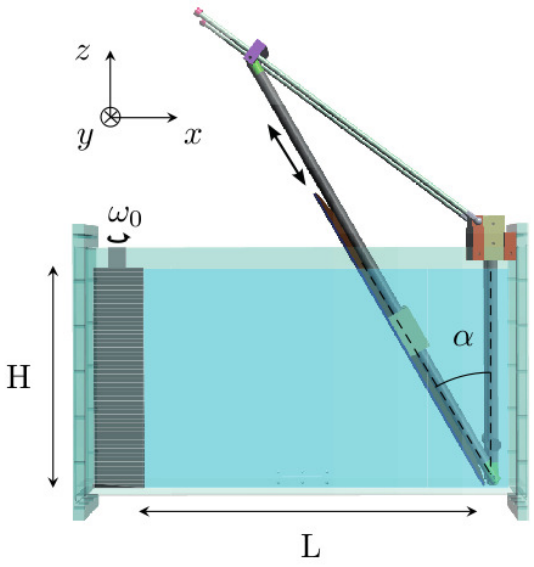


Figure 1.7: Schema of the set-up used in all the attractor experiments described in this manuscript. The tank is filled with a linearly stratified fluid. The wave-maker is on the left vertical side. The different axes are defined above the tank.

In reality, we used two set-ups. Both of them have the same geometrical configuration described in figure 1.7, but they have different scales. Indeed, I started my PhD using a small tank, with $H \times L \times W = 40 \times 80 \times 17$ cm^3. This kind of tank has been used in our group for a long time [15, 71]. This allows us to perform experiments with $L \approx 45$ cm and $H \approx 30$ cm. During my PhD, we built a new tank, named large tank in this manuscript by opposition to the small one. This has been done working with Denis Le Tourneau, from the mechanical workshop of the laboratory. The dimensions of this tank are $H \times L \times W = 100 \times 200 \times 17.4$ cm^3. Thus, the width is unchanged while the height and the length are more than doubled. The experiments performed in this tank are typically carried out with $L \approx 150$ cm and $H \approx 90$ cm. Thus, the scale of the experiments is increased by a factor of 3. The idea to have a larger tank is to perform experiments with larger scales, less dissipated by the viscosity (see equation (1.34)). The large tank is made with PMMA while the small tank is made with PETg.

The construction of this new large tank faces different major problems. The first one is related to the size of the experiment. As both H and L have been multiplied by 3, the volume is approximately increased by a factor of 10. The filling procedure is thus longer and involves larger quantities of salt and water than for the small tank. Then, one had to develop a new wave-maker, of 90 cm height. Indeed, the maximum height accessible with the standard wave-maker presented in section 1.3.4 is 40 cm. Thus, it was unable to force on all the height of the fluid. We worked with the mechanical workshop to create a new wave-maker, also described in section 1.3.4. Finally, the visualization technique has to be adapted to the large tank. In the small one, one can perform Particle Image Velocimetry or Synthetic Schlieren, described in section 1.3.5. During this PhD, I only performed Synthetic Schlieren in the large tank experiment.

1.3.2 Density stratification

In order to support internal-wave propagation, the fluid in the tank must be stratified in density. In the oceans, the stratification is made using both temperature and salinity, as shown in figure 1.4. In the laboratory, for the experiments made in this manuscript, we used only salt as the stratifying agent for two reasons. The first one is that salt concentration is much easier to control than the temperature, which can be changed by the environment. The second one is that the salt diffusivity is smaller than temperature diffusivity. Indeed, the Schmidt number Sc, equal to the ratio between the water kinematic viscosity and the diffusion coefficient of salt or temperature, is 700 for salt while the one for temperature is equal to 7. Thus, the stratification is more stable with salt than with temperature.

We use salt water with densities ranging between 1000 g/L and 1030 g/L for the small tank and between 1000 g/L and 1080 g/L for the large tank. Consequently, the largest variation of density is less than 10% of the mean density. Thus, the average of density in the tank ρ_0 is close to the fresh water density. Moreover, the range of densities gives the buoyancy frequency N of the order of 1 rad/s in the small tank and 0.8 rad/s in the large tank. As internal waves propagate only with a pulsation ω_0 smaller than N, the shortest period of the waves is around 6 s. Thus, acquisition techniques giving two fields per second allow a very good time sampling of the waves. One also can perform long experiments with hundreds of periods of the waves within few hours.

The experimental tank is filled with linearly stratified fluid using the double bucket method [127, 54], illustrated in figure 1.8. A bucket A of fixed density ρ_A is discharged in a bucket B with a flow rate Q_1. The fluid of density $\rho_B(t)$ in the bucket B, always in agitation, is discharged in the experimental tank with a flow rate Q_2.

The mass and the volume are conserved. This leads to

$$\frac{\mathrm{d}(\rho_B(t)V_B(t))}{\mathrm{d}t} = \rho_A Q_1 - \rho_B(t)Q_2, \tag{1.60}$$

$$\frac{\mathrm{d}(V_B(t))}{\mathrm{d}t} = Q_1 - Q_2. \tag{1.61}$$

We derive from equation (1.61)

$$V_B(t) = (Q_1 - Q_2)t + V_B(0), \tag{1.62}$$

and, by combining equations (1.60) and (1.62), we obtain a differential equation for $\rho_B(t)$

$$\frac{\mathrm{d}(\rho_B(t))}{\mathrm{d}t} = Q_1 \frac{\rho_A - \rho_B(t)}{(Q_1 - Q_2)t + V_B(0)}. \tag{1.63}$$

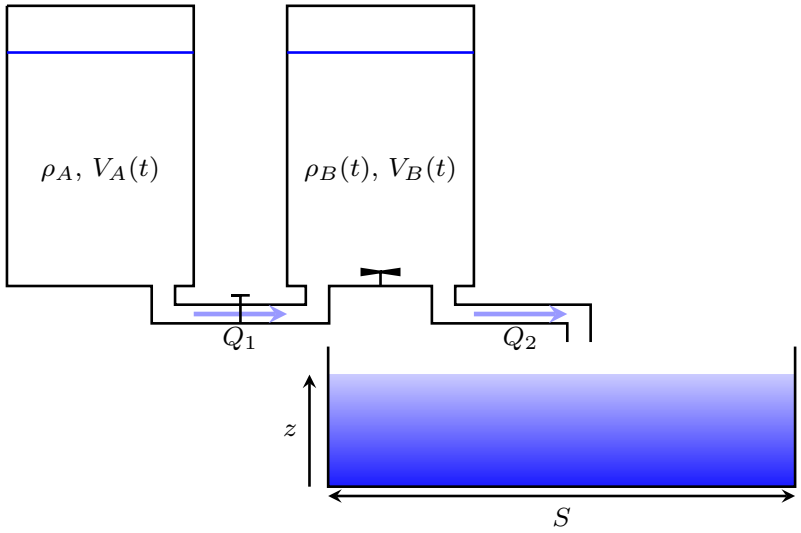


Figure 1.8: Sketch of the double bucket method for the generation of a stratified density fluid, extracted from [15].

By integrating this differential equation, we extract the evolution of $\rho_B(t)$

$$\rho_B(t) = \rho_A - (\rho_A - \rho_B(0)) \left(1 + \frac{(Q_1 - Q_2)}{V_B(0)} t\right)^{Q_1/(Q_2 - Q_1)}. \tag{1.64}$$

The experimental tank can be filled from the bottom or from the top of the free surface. Consequently, a fluid injected at time t is positioned at a height

$$z(t) = \frac{Q_2}{S_H} t, \tag{1.65}$$

when filled from above, and at a height

$$z(t) = H - \frac{Q_2}{S_H} t, \tag{1.66}$$

when filled from below. S_H is the horizontal section of the experimental tank, and H its height. Combining these results to equation (1.64), we obtain the density in the experimental tank as a function of the height,

$$\rho_B(z) = \rho_A - (\rho_A - \rho_B(0)) \left(1 + \frac{(Q_1 - Q_2)}{Q_2} \frac{S_H}{V_B(0)} z\right)^{Q_1/(Q_2 - Q_1)}, \tag{1.67}$$

when filling from the top, and

$$\rho_B(z) = \rho_A - (\rho_A - \rho_B(0)) \left(1 + \frac{(Q_1 - Q_2)}{Q_2} \frac{S_H}{V_B(0)} (H - z)\right)^{Q_1/(Q_2 - Q_1)}. \tag{1.68}$$

when filling from above the tank. From equations (1.67) and (1.68), we can notice that the stratification is linear only when $Q_1/(Q_2 - Q_1) = 1$, so when $Q_1 = Q_2/2$. Two different methods allow to achieve this specific relation between flow rates: the flow rates can be controlled independently thanks to two peristaltic pumps, or one can only impose Q_2 and obtain Q_1 by communicating both buckets from below. This last method requires equal section of the base of both buckets.

For $Q_1 = Q_2/2$, the density profiles are

$$\rho_B(z) = \rho_B(0) + (\rho_A - \rho_B(0))\frac{S_H}{2V_B(0)}z, \tag{1.69}$$

$$\rho_B(z) = \rho_A + (\rho_A - \rho_B(0))\frac{S_H}{2V_B(0)}z, \tag{1.70}$$

for the filling from above and below respectively.

The densities are selected depending if one fills from above or from below. In order to obtain a stratification that increases density with depth, one has to choose $\rho_B(0) < \rho_A$ when we fill from below and $\rho_A < \rho_B(0)$ when we fill from above.

In a large majority of experiments presented in this manuscript, the filling of the experimental tank is done from below. For the small tank, a typical flow rate Q_2 is 300 mL/min while for the large tank, this flow rate is around 1 L/min. This leads to typical filling time of 2 hours for the small tank and 5 hours for the large tank. These flow rates are chosen to be sufficiently slow to avoid mixing during the filling and enough high to fill the tank in a reasonable time. The relevant quantity to prevent mixing is the vertical speed of the surface during the filling

$$\frac{\mathrm{d}z(t)}{\mathrm{d}t} = \frac{Q_2}{S_H}, \tag{1.71}$$

Thus, the flow rate can be larger for the large tank than the one for the small tank because the section S_H is greater for the large tank.

To obtain a linear profile, note that the horizontal section S_H has to be independent of z. In order to get a constant section S_H, one carefully inserts the sloping wall at the end of the filling procedure only.

1.3.3 Density measurements

To measure the stratification in the tank and the associated buoyancy frequency N, one uses a conductivity probe. It measures both the electric resistivity of the fluid between two conductive plates and the temperature. The resistivity of the fluid depends on the ions present in the solution, and a calibration allows the association of the resistivity and temperature values with the density. The calibration is made by measuring with the probe the resistivity and the temperature of different homogeneous samples. These samples have well known densities and temperatures, measured by an AntonPaar DMA 35 densimeter. This device consists in a capillary filled with the fluid to be studied. An electro-mechanic system vibrates the capillary and measures the resonant frequency of the capillary-fluid system. This frequency depends on the mass of both, the known capillary mass and the fluid mass, which allows us to extract the fluid density. This equipment measures densities between 0 and 3 kg/L with an accuracy of 0.001 kg/L. The samples are chosen to get densities and temperatures varying in the range of the ones of the stratification.

The probe attached to a stainless steel bar is moved in the stratified fluid by a stepper motor. The resistivity and temperature are measured continuously as the probe moves. The probe descends slowly in order to generate the least possible change in the stratification. An example of the measure of the density is shown in figure 1.9, by the solid black line. The buoyancy frequency is obtained by modeling this measurement by a linear fit, as shown by the dashed red line. One can observe at the top of the profile, just below the dashed dotted black line representing the surface, that the fluid is close to be homogeneous. This homogenization can be due to convective motion of the air close to the free surface. It

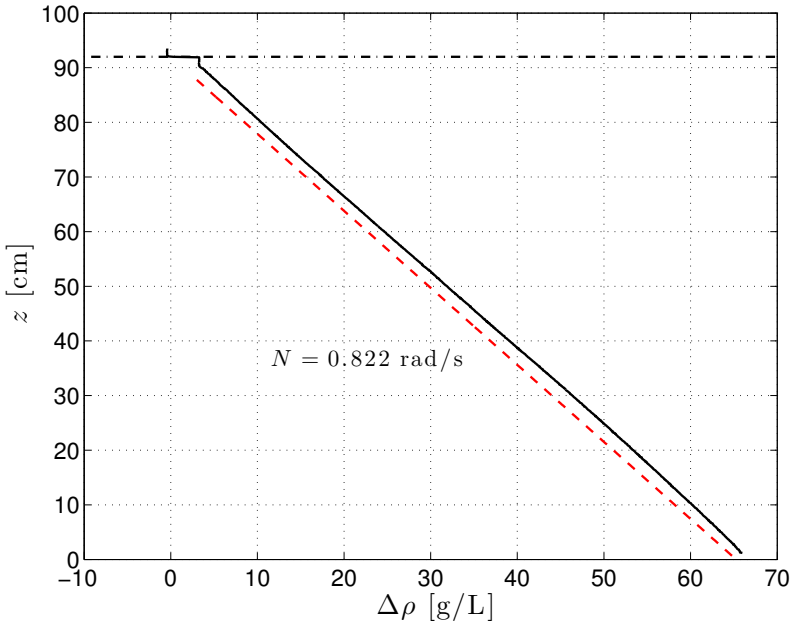


Figure 1.9: Example of a density profile obtained in the large tank. The measured profile is plotted as the solid black line while the dashed red line shows a linear fit of the profile, slightly shifted for the sake of clarity. The horizontal dashed dotted line represents the free surface.

is possible to pump away this layer at the end of the filling procedure in order to get only a linear profile. Other effects, such as filling effects and large temperatures change can also influence the density profile, especially at the top and the bottom of the stratification.

Note that the stratification is very stable in time: it remains linear during several weeks without any mixing caused by the waves. Nevertheless, the thickness of the homogeneous layer close to the free surface increases with time, around half of a centimeter a day.

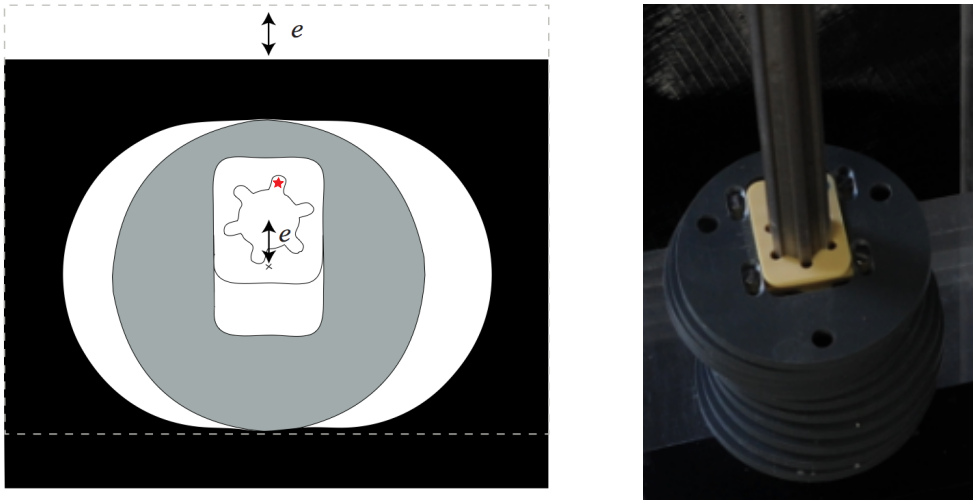
1.3.4 Generation of internal waves

The internal waves are generated in the tank, filled with linearly stratified fluid, using a wave-maker, which is different for the small and large tanks. Historically, internal waves have been produced in the laboratory by oscillating a cylinder in a stratified fluid. The cylinder creates four wave beams in the four quadrants, as in figure 1.1. This is how the internal wave dispersion relation has been measured for the first time [62, 119].

All the attractor experiments reported in this manuscript have been performed with a mode 1 forcing, defined by the horizontal displacement of the wave-maker

$$\zeta(z,t) = a\sin(\omega_0 t)\cos\left(\frac{\pi z}{H}\right), \tag{1.72}$$

where a the amplitude of the maximum displacement, H the height of the fluid and ω_0 the forcing frequency. The profile is thus half of a cosine modulated in time. The aim is to impose the horizontal velocity v_x, defined in equation (1.43), with $p = 1$. Then, as the horizontal and vertical components of the wave fields are linked by the volume conservation, a wave is emitted. Nevertheless, the wave-maker is not 100% efficient. Indeed, it imposes only the horizontal velocity and the vertical one is supposed to be given by the volume conservation, using equation (1.45).



(a) (b)

Figure 1.10: (a): Representation of the disc and plate system which allows to transform the rotation motion in a unidirectional translation. The white piece within the disc can be displaced to change the eccentricity e, and therefore, the translation amplitude of the black plate. (b): Image of discs piled over the camshaft (the discs are continuously shifted in phase). These two images are extracted from [71, 15, 12].

The wave-maker used in the experiments performed in the small tank is the one developed by Gostiaux *et al.* [63], studied by Mercier *et al.* [115] and improved by Bordes [12]. This allows a very accurate control on the shape, the amplitude and on the frequency of the waves generated. The working principle of this wave-maker is to transform a rotation of a vertical camshaft of plates in an oscillatory horizontal movement. The rotation of the camshaft is generated by a motor, and perforated discs within the plates allow the selection of the amplitude and phase of oscillation. A disc is shown in grey in figure 1.10(a). The position of the white piece of the inside can be set in a way that the axle does not necessarily coincide with the center of the disc. When rotated, the black plate allows to obtain an unidirectional oscillation, where the amplitude corresponds to the distance between the axle and the center of the disc. The system allows the generation of horizontal displacements of amplitude e, between 0 and 15 mm. This set-up also has the possibility of changing the relative phase between two contiguous discs, in order to create profiles with the same amplitude but different phases (see figure 1.10(b)). This typically leads to plane waves. Nevertheless, in this manuscript, all experiments have been performed generating a vertical mode. For these modes, all discs have the same phase but different amplitudes. Thus, there is no need to change the phases. Practically, in the small tank, the wave-maker is composed of 47 plates having the following horizontal displacements given in equation (1.72). The wave-maker is built outside the tank and then inserted on the left of the tank before the filling procedure. Once the tank is filled, one can only change the frequency ω_0 of the waves. The shape and the amplitude are fixed until one empties the tank and changes them.

The wave-maker used in the experiments performed in the large tank is different. As we built the large tank, we developed a new wave-maker with Marc Moulin, from the mechanical workshop of the laboratory. The idea is to get a mode 1 shape by deforming a flexible plate. Figure 1.11(a) shows a schema of this wave-maker. The assembly, the

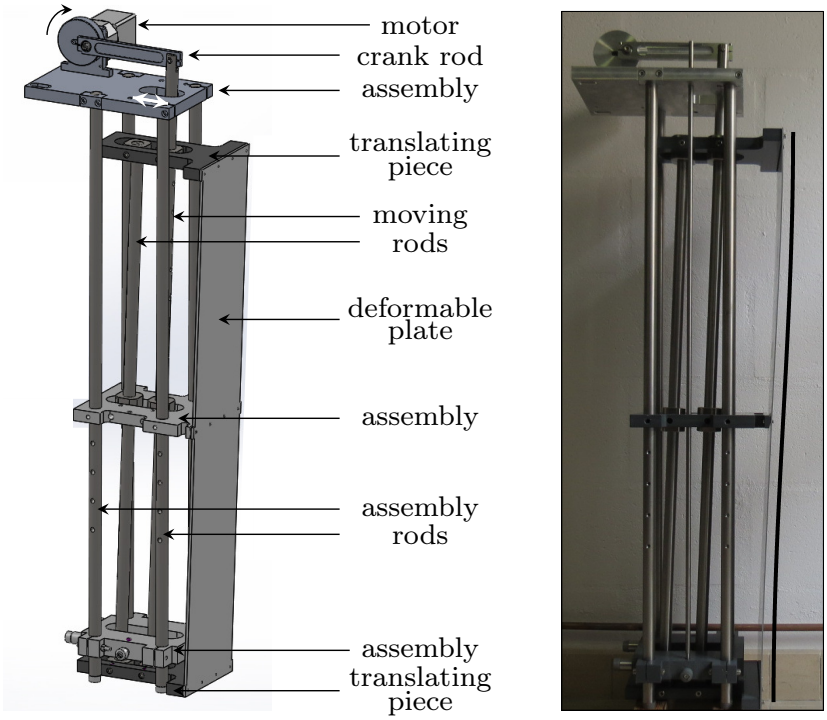


Figure 1.11: (a): Schema of the wave-maker used in the large tank. The different pieces are shown by the arrows. (b): Picture of the wave-maker from the side with an high amplitude a. The phase of the plate is chosen to get the maximal horizontal distance between the bottom and the top of the plate. The dashed black line has the shape of half a cosine, expected for the bended plate with reasonable accuracy.

fixed part of the wave-maker, is composed of three different horizontal pieces, located at the bottom, the middle and the top of the wave-maker. These pieces are linked by four vertical assembly rods. The deformable plate is attached at its top and bottom to horizontally translating pieces. They move in opposition of phase, thanks to two moving rods, using the principle of a deformable parallelogram. Moreover, the middle of the plate is horizontally fixed to the assembly in order to get a pivot point with $\zeta = 0$ for $z = H/2$. Note that the plate is fixed at its top and bottom on the translating pieces for few centimeters, in order to ensure that the ends of the plate remain vertical (in other words, clamped), as for the mode 1 shape. The translating pieces are moved using a motor, fixed at the top of the assembly. The rotating motion of the motor is converted into a horizontally translating motion using a crank rod. The plate has the same width W as the tank and is sealed on its sides to avoid water exchanges between the two faces of the plate. A picture of the wave-maker viewed from the side is shown in figure 1.11(b). The position of the plate has been chosen to have $\sin(\omega_0 t) = -1$ in equation (1.72). The solid line, having a shape of half a cosine, shows that the deformation of the plate is very close to a mode 1 shape, as expected. The shape of the wave-maker is thus fixed in a mode 1 shape. Nevertheless, one can change the amplitude of the wave-maker by modifying the crank rod once the tank is filled. This allows us to perform different experiments varying the forcing amplitude only. This is not possible with the small wave-maker. Note that the forcing frequency is also easily tunable by controlling the motor.

1.3.5 Visualization techniques

Two different techniques have been used to visualize the internal waves propagating in the tank: Particule Image Velocimetry (PIV) and Synthetic Schlieren (SyS). Both are well-known techniques used to observe internal waves in laboratory experiments [147].

Synthetic Schlieren

This technique is based on the fact that the optical index of water changes with the salt concentration. Thus, the stratification in salt induces a stratification in optical index. When an internal wave passes through a stratified fluid, it causes density perturbations and consequently optical index perturbations. Moreover, when a light ray passes through an inhomogeneous refractive index medium, it is spatially bent. The bending angle in one direction is directly linked with the density gradient in this direction. Thus, one can measure the density gradients caused by an internal wave by measuring the ray deflections due to this wave.

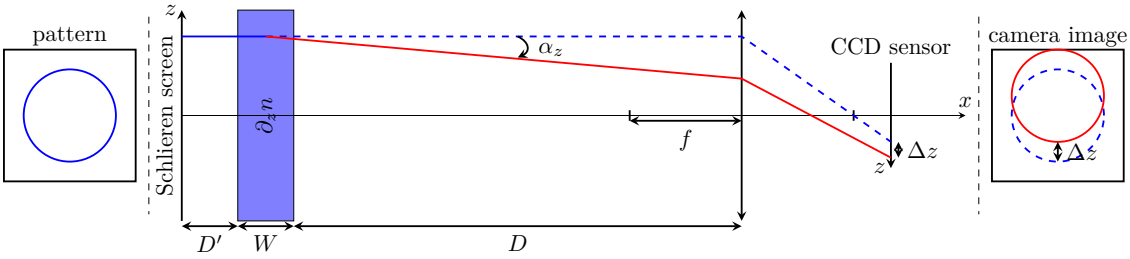


Figure 1.12: Sketch of the Synthetic Schlieren visualization set-up, extracted from [71, 15]. A blue light ray (solid line on the left) is emitted from the Schlieren screen and is collected by the CCD sensor of the camera, using a length of focal length f. The dashed blue line represents the trajectory of this ray without the density gradient while the red line shows the trajectory of this ray with the density gradient.

A camera with a lens of focal depth f measures in time a pattern placed over a luminous screen (Schlieren screen) with a CCD sensor. A tank is located between the screen and the camera. When this tank is filled with an homogeneous fluid, there is no density gradient and the ray is not deflected, as shown by the dashed blue line in figure 1.12. However, the light ray is bent by an angle α_z, as shown by the solid red line in figure 1.12, when the tank is filled with a fluid that is stratified in density and, therefore, in refractive index. The angle α_z is related to the spatial gradient of the refractive index through the relation

$$\alpha_z = \frac{W}{n}\frac{\mathrm{d}n}{\mathrm{d}z} = \frac{W}{n}\frac{\mathrm{d}n}{\mathrm{d}\rho}\frac{\mathrm{d}\rho}{\mathrm{d}z}. \tag{1.73}$$

In the salt concentration range used in this work, the variation of the density as a function of the refractive index is linear and the slope is equal to $\mathrm{d}\rho/\mathrm{d}n = 4.1 \times 10^3$ kg/m^3.

The deviation of the ray of light generates a displacement of the pattern over the CCD sensor. This is shown on the right of figure 1.12. Note that the image recorded by the camera is reversed as the CCD is located at a larger distance than f from the lens. Thus, the image shown on the right of figure 1.12 has been reversed, to have it in a normal way. In the approximation of small angles, the deviation of the pattern with respect to the

homogenous medium case is

$$\Delta z = \alpha_z f \frac{D' + W/2}{D' + W + D - f}. \tag{1.74}$$

We can translate the spatial displacement of the detected pattern to pixel displacement through the relation $\Delta p = \Delta z / r$, where r is the physical size of a pixel.

The density gradient can be therefore written as

$$\frac{\partial \rho}{\partial z} = r \Delta p \frac{\mathrm{d}\rho}{\mathrm{d}n} \frac{n}{W} \frac{(D' + W + D - f)}{f(D' + W/2)}. \tag{1.75}$$

When internal waves propagate, the density gradient is locally modified. Consequently, the refractive index is locally modified and therefore the pattern on the camera is also changed. The comparison of an image of the fluid with and without waves allows to determine the local variations of the refractive index caused by the internal waves. Considering that no waves are present in the fluid at $t = 0$, we directly have access to the perturbations of the refractive index

$$\frac{\partial \rho'}{\partial x} = \frac{\partial \rho(t)}{\partial x} - \frac{\partial \rho(0)}{\partial x} \qquad \text{and} \qquad \frac{\partial \rho'}{\partial z} = \frac{\partial \rho(t)}{\partial z} - \frac{\partial \rho(0)}{\partial z}. \tag{1.76}$$

In order to get a good resolution in the density gradients, one needs a good spatial resolution in the displacements of the pattern located behind the tank. Thus, one uses a pattern made of random black dots on a white background which gives good results with sub-pixel accuracy. The typical frame rate used for SyS is 2 Hz. Thus, as ω_0 is usually around 0.6 rad/s, this allows a very good temporal sampling of 20 density gradient fields per wave period.

If vertical mixing occurs, the average density profile is changed and the measure of the wave is distorted, as the mixing and the wave perturbation both contribute in the term $\partial \rho(t)/\partial z$. In order to have reliable measurements, mixing and long experiments should be avoided. It is also important to note that this technique is developed for flows with specific features: they have to be two-dimensional flows or they must have some know symmetries [126].

This technique has been used for experiments performed in both small and large tanks.

Particle Image Velocimetry

Particle Image Velocimetry (PIV) is a technique that allows to measure the velocity field of a flow. The fluid is seeded with light-reflecting hollow glass spheres of size 8 μm and density 1100 kg/m^3. Because of their small size, the particles are dragged by the flow, and their motion represent the flow. Even if the particles are slightly denser than the fluid, the time-scale of particle sedimentation is very low (typically several days), with negligible effect on results of velocity measurements. The longitudinal mid-plane of the test section is illuminated by a vertical laser sheet coming through the transparent side of the tank, at the right of the slope (which is also transparent). The laser sheet is made using a cylindrical lens or an oscillating mirror. The light pattern emitted by the particles is recorded by a camera at different times. Two successive images are compared in order to obtain the displacement of the light pattern, and estimate the fluid velocity. Typically, 4 frames are taken per second, with a regular sampling or a burst mode. The burst mode is performed for high forcing experiments where the velocity fields is expected to have a strong amplitude. This mode consists in taking 2 frames very close in time, in order to

reduce the displacements of the particles between the two images. Then, the camera waits for a given time in order to avoid to get too large data and takes 2 more pictures. The regular and the burst mode sampling allow to get 2 velocity fields per second and thus, give us a good temporal resolution of around 20 fields per wave period, as SyS.

This technique has been used only for experiments performed in the small tank. Indeed, in the large tank, as the laser sheet comes through the transparent side of the tank, the light has to go through 2 m of water, and is drastically damped by the water. Thus, the particles located close to the wave-maker are not lighted correctly and are not detectable by the algorithm. Therefore, I did not perform PIV in the large tank. Nevertheless, with coated particles reflecting better the laser light and maybe a stronger laser or a oscillating mirror, one should be able to drive PIV experiments in the large tank.

Image correlation algorithm

The velocity or the density gradient fields are calculated with the help of the cross-correlation technique [49], which is visualized in the *uvmat* graphic interface [141]. The aim is to measure the displacements of the light pattern between two successive images for PIV or to measure the displacements of the dot pattern between one image and an image at $t = 0$ for SyS. Each image is divided in boxes of a selected size. The size of the box is chosen such that a recognizable pattern can be observed within the box, but the box must remain small enough to present little perturbation of the shape of the pattern between two images, when the fluid is moving. The algorithm determines the position of the pattern in the successive image by calculating the correlation coefficients, the maximal correlation defining the position of the pattern in the successive image. This algorithm allows to estimate the displacement of the pattern in a time Δt defined by the acquisition frequency, at a resolution of a tenth of a pixel.

For PIV in the small tank, this algorithm typically leads to a resolution of 1 velocity vector per area of about 3×3 mm^2. For SyS, the spatial resolution is around 3×3 mm^2 for the small tank and 5×5 mm^2 for the large tank.

These two techniques have their own assets and drawbacks. SyS is better to observe small wavelength so it is very efficient to detect triadic resonance instability (see Chapter 4). However, if the instability is too strong or if there is some mixing, this technique becomes inefficient because it is based on optical index variations. Moreover, the observed field is integrated on all the width of the tank. PIV is less sensitive to small scales but it is also useful to detect triadic resonant instability. It can be used even in case of strong instability or mixing. In this cases, index matching in the tank increases the precision of the PIV measurements. Moreover, PIV is related to energetic quantities and it is more localized than SyS because the measurements are made only within the laser sheet. Finally, both techniques are equivalent in the case of a nominally 2D problem as demonstrated in [68].

1.3.6 Hilbert filtering in time and in space

The two visualization techniques presented in the previous section give us the velocity or the density gradient fields in the tank. As the main motions are due to waves and therefore are periodic, it worths to filter the fields obtained to separate the different components of the wave-field oscillating at different frequencies. It is also possible to filter spatially the fields by keeping only the waves propagating in given directions. Such filtering is named Hilbert filtering (or Hilbert transform) and has been developed and studied for internal waves by Mercier *et al.* [114].

The principle for the time filtering is the following. First, a temporal Fourier transform of the signal is made. This leads to a frequency spectrum, with different peaks associated with the waves having different frequencies. This spectrum is then multiplied by an Hamming window, centered around a working frequency and with a small width in frequency. Thus, one isolates one specific frequency. Then, from this spectrum, one perform an inverse temporal Fourier transform which leads to a signal in the real space. The signal is complex, one can take the real part to get the original signal filtered at the working frequency. One also have access to the modulus of this complex signal and to the phase. There is a similar procedure for a filtering in space. Nevertheless, for space filtering, we are used to select all the positive (or negative) components of the horizontal or vertical wave vectors. Thus, one selects more a quadrant than a specific wave number.

These temporal and spatial filterings are often used in the remainder of this manuscript. For the space filtering, the quadrant selected by the filter will be indicated by a black rectangle in a wave vector space.

Conclusion

In this Chapter, I have introduced internal waves propagating in a stably density stratified fluid, from a theoretical, observational and experimental point of view.

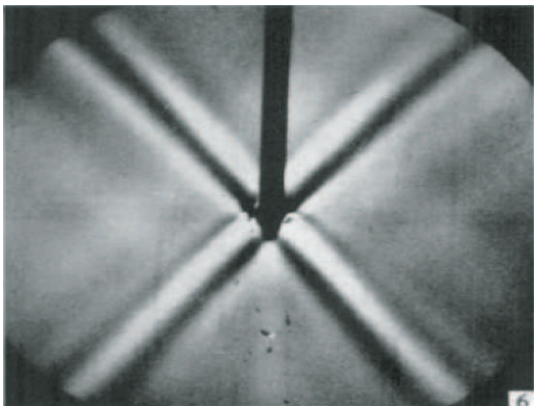
First, I have described the physics of a stably stratified fluid. I have shown that internal waves have very specific features such as an anisotropic and geometric dispersion relation, perpendicular group and phase velocities and specular reflection on a sloped boundary. These properties, unusual, have a strong importance in natural systems.

Then, I have described the main features of these waves in oceans and in the atmosphere, from their generation to their influence on the stratified fluid supporting them. I have presented the main open questions regarding internal waves in the oceans. They concern the processes of energy cascade and mixing induced by internal waves.

Finally, I have discussed the experimental details necessary to investigate internal waves in a laboratory. I have shown how to prepare a stratified fluid, how to generate internal waves and how to measure them using two different techniques. I have presented the attractor set-up used in Chapters 3, 4 and 5 which can be adapted to two tanks of different sizes. This allows us to explore different experimental scales although the ocean remains much larger than the tanks used in the laboratory frame.

Chapter 2

Pendulum oscillating horizontally in a stratified fluid



Object oscillating in a stratified fluid and creating internal waves. Extracted from [119].

The interaction of the tidal motion with the ocean bottom topography is continuously generating internal waves [7, 148, 56]. The global rate of energy conversion from barotropic to baroclinic tide is estimated to be around 1 TW [118, 56]. The generation of internal wave energy has been studied in some details for obstacles in stratified fluid of infinite extent: flat topography [7], elliptic and circular cylinders [74, 75, 143, 144], Gaussian, witch of Agnesi and exponential ridges [91] in two dimensions, and sphere in three dimensions [82, 149, 41].

In the case of fluid of limited depth, the tidal conversion has been estimated [92] for a vertical barrier mimicking a very steep underwater ridge. In particular, Llewelyn Smith and Young [92] show that the tidal conversion is considerably enhanced in a fluid of limited depth as compared to a fluid of infinite extent. Measurements of wave power emitted by an oscillating circular cylinder placed at mid-depth in a horizontal stripe of a uniformly stratified fluid have been performed by Ermanyuk and Gavrilov [42]. This geometry corresponds to the case of a semi-circular mountain. The experimental trends found by Ermanyuk and Gavrilov [42] suggest that the tidal conversion decreases as the ratio of the obstacle height to the fluid depth decreases. A similar trend has been observed in calculations performed by Sturova [142]. However, Ermanyuk and Gavrilov [42] experimentally and Sturova [142] numerically were unable to obtain precise information on the low-frequency limit of tidal conversion, the quantity discussed by Llewelyn Smith and Young [92]. Therefore, the cross-comparison of the mentioned results seems to be inconclusive.

In this chapter, we re-visit the problem of tidal conversion by an isolated bi-dimensional bottom topography in a uniformly stratified fluid of limited or infinite depth, using the concepts of added mass and affine similitude. Recently the importance of added mass in the context of emission of internal waves by oscillating bodies has been discussed in [149].

The rule of affine similitude relating the added masses of affinely similar bodies in uniformly stratified and homogeneous fluids has been proposed in [40]. This rule provides a simple tool for evaluation of force coefficients of oscillating bodies (and the amount of energy radiated with waves) which proves to be efficient to recover the previously obtained results for an elliptic cylinder [74] and vertically oscillating spheroid [85] and to obtain the estimates for other configurations such as horizontally oscillating spheroids [40], diamond- and square-shaped cylinders [43]. In a geophysical context, the latter cases can be also interpreted as underwater mountain ridges of triangular and rectangular (plateau-shaped) cross-sections. This approach is extended in this chapter to the case of a ridge with square-shaped in a uniformly stratified fluid of infinite depth and to the case of a ridge with circular shape of cross-section in a uniformly stratified fluid of limited depth. In addition, a topography lacking of tidal conversion for given frequencies [96] is tested. Experiments with this kind of topographies have been reported recently [99] but the radiated wave power of such structures has never been measured yet.

First, in section 2.1, I introduce the theoretical preliminaries on added mass in homogeneous and stratified fluids. I briefly explain the concept of affine similitude and take the example of a flat plate in a fluid of finite depth. Then, in section 2.2, I present the experimental set-up and the data analysis. In the two last sections, I show the experimental results that we obtained and compare them to the theoretical predictions. Section 2.3 is dedicated to a cylinder with a square-shaped cross section in a fluid of infinite depth, in order to test the affine similitude predictions. Section 2.4 describes the results for a cylinder with circular cross section in a fluid of finite depth and the possible tidal applications. Finally, section 2.5 presents the results obtained using the topography lacking of tidal conversion in a fluid of finite depth.

Note that this chapter is slightly apart from the remainder of the manuscript, mainly focused on internal wave attractors. Nevertheless, it exhibits interesting features that can be valuable for the generation of internal wave attractors in the ocean. The notations used in this chapter are defined and valid for this chapter only.

2.1 Theoretical preliminaries

2.1.1 Added mass in homogeneous and stratified fluids

When an object moves in an ideal fluid, it has to move the fluid around in order to pass through. As the fluid has a given density, a higher force is necessary to displace the object in the fluid than in the vacuum. Indeed, as both the object and the surrounding fluid have to be accelerated, the necessary force is equal to the acceleration of the object multiplied by the mass of the object and another mass m_A, due to the fluid [152]. This mass is called the added mass and depends on the shape of the object in the fluid. Thus, this mass is generally described using a tensor. In naval architecture, the added mass is very important because it can easily reach a large amount of the total mass of the ship or the sub-marine. This leads to a large number of studies on added masses of different objects in homogeneous fluid [20]. However, it is not necessary to take this mass into account for aircrafts, as the air density is much smaller than the one of the water.

Added mass can be used to investigate the tidal conversion in the oceans [149]. Indeed, the topography at the bottom of the oceanic floor can be viewed as objects moving in a stratified fluid. In reality, the topography is fixed and the fluid moves via tidal forcing but the two problems are totally equivalent for small amplitude oscillations. Thus, it is possible to use the knowledge developed on added mass in homogeneous fluid to explore the problem in stratified fluid. In such fluid, internal waves can be emitted if the body oscillates at a frequency ω smaller than N. In this case, the added mass is complex and depends on the frequency of oscillations ω. It can be decomposed in two parts

$$m_A = \mu(\omega) - i\frac{\lambda_{\mathrm{w}}(\omega)}{\omega}. \tag{2.1}$$

μ is the inertial coefficient, also called added mass and λ_{w} is the damping coefficient. It represents the loss of energy due to wave emission. μ acts on the acceleration of the object while λ_{w} gives an additional term linked with the speed of the object. When $\omega > N$, there is no wave emission and the added mass is real but depends on ω. It is worthwhile to remark that μ and λ_{w} are linked together using Kramers-Kronig relation [42].

Note that we assume an ideal fluid, which is inviscid. In a viscous fluid, as in the experiments, the object undergoes an attenuation of its speed due to the viscosity of the fluid. Thus, when $\omega > N$, there is only a viscous damping. Nevertheless, when $\omega < N$, the attenuation of the speed of the object is due to the viscosity and to the wave emission. As one can see in the experiments, the wave emission damping coefficient is much more important than the viscous one.

2.1.2 Affine similitude in a linearly stratified fluid

Let us consider a two-dimensional object submerged at depth $H/2$ in a channel of full depth H filled with an ideal continuously stratified fluid having a constant buoyancy frequency N. This is sketched on the left panel in figure 2.1. We assume that the horizontal extent of the channel is infinite. The upper and lower boundaries of the channel are assumed to be rigid. A Cartesian coordinate system is introduced with the x-axis located at mid-depth of fluid and pointing left, and z-axis pointing downwards. The y-axis is horizontal and perpendicular to the x-axis. The horizontal and vertical sizes of the object are denoted a and b, respectively. One defines the aspect ratio of the body $p = b/a$ and the aspect ratio of the fluid $q = b/H$. We restrict our consideration to the case of horizontal harmonic oscillations of the object with frequency ω and amplitude A. The non-dimensional

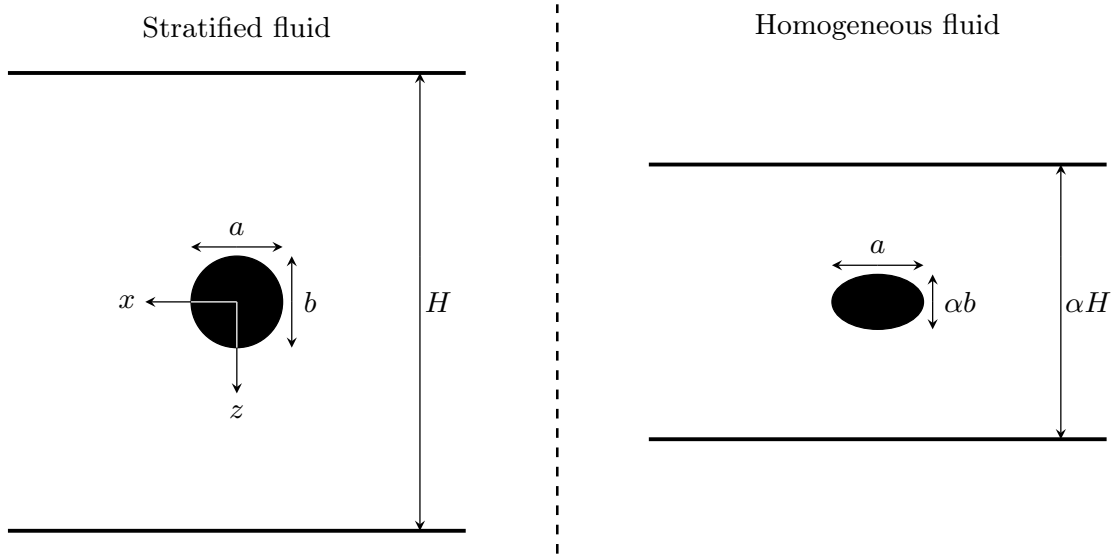


Figure 2.1: Geometries of the real and fictitious problems. Left panel: two-dimensional object in a linearly stratified fluid of depth H. The horizontal and vertical sizes of the object are named a and b, respectively. Right panel: fictitious body in a homogeneous fluid after an affine transformation of the object in the left panel. The transformation changes the vertical scales by a factor α. The horizontal and vertical sizes of the fictitious object are a and $b_* = \alpha b$, respectively. The fluid has a depth of αH.

frequency is introduced as $\Omega = \omega/N$. Note that on the left panel in figure 2.1, the body is a circular disk but the theoretical preliminaries of this section are also valid for other shapes. Below we consider experimentally the cases of objects with cross section being a square or a circular disk. In oceanographic context these geometries correspond to the cases of ridges with triangular and circular cross-sections.

Let us consider first the problem where $\Omega > 1$, i.e. where the added mass is a real quantity. The added mass coefficient K of a body undergoing horizontal oscillations in uniformly stratified fluid of infinite extent ($H \to \infty$) are known [40] to be related with the added mass coefficient K_* of a fictitious affinely similar body oscillating in a homogeneous fluid

$$K = K_*. \tag{2.2}$$

Here, the added mass coefficients are defined as $K = m_A/\rho_c S$ and $K_* = m_{A*}/\rho_c S_*$, where ρ_c is the reference density at the depth corresponding to the center of the body, m_A and m_{A*} are the added masses per unit length, S and S_* are the cross-sections of the initial and fictitious bodies, respectively. The fictitious body is obtained by compressing the initial body in the vertical direction α times, where $\alpha = (\Omega^2 - 1)^{1/2}/\Omega$. Note that equation (2.2) is also valid for finite H. Consequently, it relates also the added mass coefficient K of a body oscillating in a uniformly stratified fluid of limited depth H and the added mass coefficient K_* of the fictitious body oscillating in a homogeneous fluid of depth αH. This is shown in the right panel in figure 2.1 where the fictitious body is an ellipse of major axis a and minor axis $b_* = \alpha b$. Consequently, the surface $S = \pi ab/4$ of the body is transformed in $S_* = \pi a b_*/4 = \alpha S$ for the fictitious body.

In many problems, it is more convenient to normalize the added mass of the oscillating cylinder by the added mass of a flat plate of height b so that $k = m_A/\rho_c \pi b^2$ and $k_* =$

$m_{A*}/\rho_c \pi b_*^2$. This normalization is particularly suitable in geophysical fluid dynamics in view of the scaling used for the tidal conversion [92]. Obviously, with such a normalization, equation (2.2) should be replaced by

$$k = k_* \alpha. \tag{2.3}$$

Equation (2.2) has been obtained in Ermanyuk [40] by considering the integrals of pressure over the body surface and the control surface surrounding the body, and applying the Gauss theorem to the fluid volume comprised between these surfaces. The control surface can be a material surface that undergoes the same affine transformation as the body surface. In this case, equation (2.2) remains valid since the conversion factors relating surface integrals over initial and fictitious bodies as well as over initial and transformed control surfaces are the same. However, if $\Omega < 1$, one should keep in mind that the control surface cannot be a closed one. There must be a possibility for radiation of internal wave energy to infinity. In this chapter, we consider a body oscillating between infinite rigid horizontal planes and the latter requirement is fulfilled.

Now let us suppose that, for a certain family of bodies oscillating in a homogeneous fluid between two horizontal parallel rigid planes, we know the functions, representing the dependence of the added mass coefficients on non-dimensional geometrical parameters $p = b/a$ and $q = b/H$

$$K_* = F_* (p, q) \qquad \text{or} \qquad k_* = f_* (p, q) . \tag{2.4}$$

Note that $q = b/H$ does not change under affine transformation. Then, for $\Omega > 1$, the added mass coefficients of a body in a uniformly stratified fluid at certain given values of p and q can be found as follows

$$K(\Omega) = F_* (p\alpha, q) \qquad \text{or} \qquad k(\Omega) = f_* (p\alpha, q)\, \alpha. \tag{2.5}$$

As discussed in Ermanyuk [40] in context of Hurley [74], $K(\Omega)$ and $k(\Omega)$ at $\Omega < 1$ can be obtained by analytic continuation in frequency. This can be done if the radiation condition formulated in the causal sense does hold true, i.e. the internal waves are radiated from the source to infinity and never return back. For $\Omega < 1$, the analytic continuation for α is $\mathrm{i}\eta$, where $\eta = (1 - \Omega^2)^{1/2}/\Omega$ is the real-value parameter. Accordingly, equation (2.5) becomes

$$K(\Omega) = F_* (p\mathrm{i}\eta, q) \qquad \text{or} \qquad k(\Omega) = f_* (p\mathrm{i}\eta, q)\, \mathrm{i}\eta. \tag{2.6}$$

Thus, knowing the added mass coefficient for a family of bodies in a homogenous fluid, one can deduce the added mass coefficient of related bodies in a linearly stratified fluid, as a function of the frequency. This can be useful because added mass in homogeneous fluid is well studied [20] while the added mass in stratified fluid has been investigated only recently.

For $\Omega > 1$, the added mass is real-valued. Accordingly, there is no wave radiation. When $\Omega < 1$, the added mass is complex-valued, as defined by equation (2.1). The non-dimensional inertial and damping coefficients can be introduced as

$$C^\mu = \mathrm{R}e(K) = \frac{\mu}{\rho_c S}, \tag{2.7}$$

$$C^\lambda = \Omega\, \mathrm{I}m(K) = \frac{\lambda_\mathrm{w}}{\rho_c S N}, \tag{2.8}$$

or as

$$c^{\mu} = \mathrm{Re}(k) = \frac{\mu}{\rho_c \pi b^2}, \tag{2.9}$$

$$c^{\lambda} = \Omega\ \mathrm{Im}(k) = \frac{\lambda_{\mathrm{w}}}{\rho_c \pi b^2 N}. \tag{2.10}$$

The imaginary part of the added mass is related to the radiated wave power

$$P(\omega) = \frac{1}{2}(A\omega)^2 \lambda_{\mathrm{w}}(\omega), \tag{2.11}$$

where A is the amplitude of oscillations. The power radiated with waves is of particular interest since it is directly related to tidal conversion. In such a problem, we can replace $A\omega$ with the amplitude of the tidal velocity U as it is usually done in geophysical hydrodynamics. Using the definition of the added mass coefficient k and equation (2.6), we can express (2.11) as follows

$$P(\omega) = \frac{1}{2}\rho_c \pi b^2 U^2 \omega\ \mathrm{Im}\left(f_*\left(pi\eta, q\right) \mathrm{i}\eta\right), \tag{2.12}$$

The dimensionless form for the radiated wave power is

$$P_{\mathrm{w}} = \frac{1}{2}\Omega^2 C^{\lambda}(\Omega). \tag{2.13}$$

In the case of a fluid of infinite extent, the functions of equations (2.4) are known for a variety of geometrical shapes (see for example Korotkin [83]). As demonstrated in [40], equations (2.5) and (2.6) can be used to re-derive the formulas for hydrodynamic loads acting on an elliptic cylinder [74], and a vertically oscillating spheroid [85]. New solutions can be also obtained. For example, the cases of a horizontally oscillating spheroid and cylinders with square-shaped and rectangular cross-sections are considered in [40] and in [43].

There are only few analytical solutions for the added mass of bodies oscillating in ideal homogeneous fluid of finite depth. The known results are limited to the cases of vertical flat plate [93], an elliptic cylinder [27] and a rectangle [122]. In the next section, one shows a theoretical example of the application of the affine similitude theory for a vertical flat plate oscillating horizontally in a stratified fluid.

2.1.3 Vertical flat plate in a linearly stratified fluid of finite depth

Let us consider the case of a vertical flat plate of height b. This is one of the only examples where one has an analytical formula for the added mass in a homogeneous fluid of finite depth. As the plate is infinitely thin, one has $p = b/a \to \infty$. The added mass of this flat plate oscillating in a homogeneous fluid of infinite depth ($H \to \infty$ and $q = b/H \to 0$) is $m_A = \rho_c \pi b^2$. Therefore for this case, the function given in equation (2.4) is $f_*(\infty, 0) \equiv 1$. Thus, the added mass and damping coefficients in a linearly stratified fluid are given by

$$C^{\mu} = \frac{\left(\Omega^2 - 1\right)^{1/2}}{\Omega} \qquad \text{and} \qquad C^{\lambda} = 0, \tag{2.14}$$

for $\Omega > 1$ and

$$C^{\mu} = 0 \qquad \text{and} \qquad C^{\lambda} = \left(1 - \Omega^2\right)^{1/2}, \tag{2.15}$$

for $\Omega < 1$. For this last case, the wave power radiated by the flat plate in an uniformly stratified fluid of infinite extent amounts to

$$P_\infty(\Omega) = \frac{1}{2}\rho_c \pi b^2 U^2 N (1-\Omega^2)^{1/2}. \tag{2.16}$$

This expression coincides with the solution found by Hurley [74].

Following [93, 122], the added mass coefficient of a vertical flat plate of height b oscillating in a homogeneous fluid of finite depth H is

$$k_* = f_*\left(\infty, \frac{b}{H}\right) = 2 \times \left(\frac{2H}{\pi b}\right)^2 \ln\left[\sec\left(\frac{\pi b}{2H}\right)\right]. \tag{2.17}$$

Thus, when $\Omega < 1$, the wave power radiated by the flat plate in a uniformly stratified fluid of limited depth is

$$P_H(\Omega) = \frac{1}{2}\rho_c \pi b^2 U^2 N (1-\Omega^2)^{1/2} M\left(\frac{b}{H}\right), \tag{2.18}$$

where, following Llewellyn Smith and Young [92], we introduce the enhancement factor

$$M\left(\frac{b}{H}\right) = \frac{P_H(\Omega)}{P_\infty(\Omega)} = \frac{f_*(\infty, \frac{b}{H})}{f_*(\infty, 0)} = f_*\left(\infty, \frac{b}{H}\right). \tag{2.19}$$

Our expression for the enhancement factor is equivalent to the result given by a more complicated formula in [92], with rotation neglected. The power given by equation (2.18) is twice the power calculated by Llewellyn Smith and Young [92] since they consider the upper half of geometry. The added mass and damping coefficients of a vertical plate oscillating horizontally in a fluid on finite depth are equal to the ones for a fluid of infinite depth multiplied by the enhancement factor M.

It worths to note that the expression for the wave power given in [92] is for the low-frequency limit ($\Omega \to 0$). In this limit, the dimensionless damping coefficient is given by

$$C^\lambda(\Omega \to 0) = M\left(\frac{b}{H}\right). \tag{2.20}$$

When $b/H \to 0$, $M \to 1$. Nevertheless, for smaller H/b, M becomes higher than 1, which highlights a more important damping coefficient at finite depth than at infinite depth for the low frequency limit, useful for tidal conversion.

In this chapter, no experiment with a flat plate has been performed. Nevertheless, using the affine similitude theory, we are able to predict the added mass and damping coefficients as functions of the dimensionless frequency Ω for linearly stratified fluid of finite or infinite depth. Moreover, one obtains a interesting result at low frequency which is discussed in section 2.4 in the case of a circular cylinder in a fluid of finite depth. In sections 2.3, one uses the affine similitude theory to predict the added mass and damping coefficients as functions of the dimensionless frequency of a square-shaped cylinder oscillating horizontally in a linearly stratified fluid.

2.2 Pendulum experiments

The experiments are performed to be compared with the theoretical predictions given by the affine similitude, in a fluid of finite or infinite depth. In order to oscillate horizontally the objects in a stratified fluid, they are attached at the lowest end of a pendulum. By

measuring the time history of the angle of the pendulum after an impulse excitation, it is possible to measure the added mass and damping coefficients of the body. This assumes that the interactions between the fluid and the rest of the pendulum are negligible. In this section, I present the set-up of the pendulum experiments and the data analysis used.

2.2.1 Set-up

The set-up is composed of two different apparatus. The first one is the pendulum itself and the assembly supporting it. The second apparatus is the wave-breaker, located at the edges of the tank in order to dissipate the waves emitted by the pendulum when oscillating below the buoyancy frequency.

Pendulum

The set-up of the pendulum experiments is sketched in figure 2.2. This set-up has been built by Marc Moulin, from the mechanical workshop of the laboratory. The set-up is very similar to the one described by Ermayuk [39, 40] and Ermanyuk and Gavrilov [42, 44]. The pendulum has a cross shape, with a massive cylinder attached at the end of the bottom vertical arm. The cylinder has a center of gravity named G' and a mass M' and is invariant in the y-direction. It can have different cross section shapes, a square as in figure 2.2 or a disk. The cross section has a length scale a. Note that, here $a = b$ and $p = 1$ using the definition given in section 2.1. The volume of the immersed streamlined part of the pendulum is less than 1% of the volume of the cylinder. Thus, one can neglect its influence on the fluid-body interactions. The vertical arm opposite to the mass, at the top, is a screw where lies a counter-weight of mass $m' = 704$ g. Changing the position of the counter-weight with respect to the axis of rotation allows to tune the characteristic frequency of the pendulum, defined as ω_c. There are also two long horizontal arms. At the end of the right one, there is a small horizontal circle, covered by a tensioned rubber membrane. A ball, initially hold by an electric magnet, can be dropped on the membrane to excite the pendulum. The ball is supposed to bounce on the membrane once. Thus, the membrane is slightly inclined to eject the ball after the first rebound. As the period of the oscillations of the pendulum is of several seconds, if the membrane is sufficiently tight, the excitation of the pendulum is very close to an instantaneous impulse. Attached to the right arm, one also has a small plateau which can contain one mass m for the calibration procedure, explained in section 2.2.2. On the left horizontal arm, there is a small annulus which can be displaced horizontally. This is to adjust very precisely the horizontality of the pendulum before the beginning of each experiment. The center of mass of the pendulum without the counter-weight is noted G, its mass M and its moment of inertia is defined as J. Note that the mass of the pendulum alone, without the object and the counter-weight is 889 g. All the relevant distances are defined in figure 2.2(a), with respect to the rotation axis. This axis is shown by a white spot in figure 2.2(a) and by a dashed line in figure 2.2(b). L and ℓ are given in Table 2.1 for each cylinder. d is equal to 40 cm while ℓ' varies in the range $[5.1 - 21]$ cm. One notes d' the vertical distance between the axis of rotation and the position of the horizontal arms. $d' = 1$ cm which is small with respect to d. The different masses are also shown in figure 2.2(a). When the pendulum oscillates, it makes an angle θ with respect to the vertical axis z. The coordinates are defined in figure 2.2(a). The origin of the coordinates, O, is taken at the rotation axis.

The pendulum is surrounded by an assembly which is fixed. The rotation is made possible by two wedge-shape supports made of very strong steel, attached to the pendulum. Each wedge is in contact with a horizontal cylinder made of steel, oriented perpendicularly

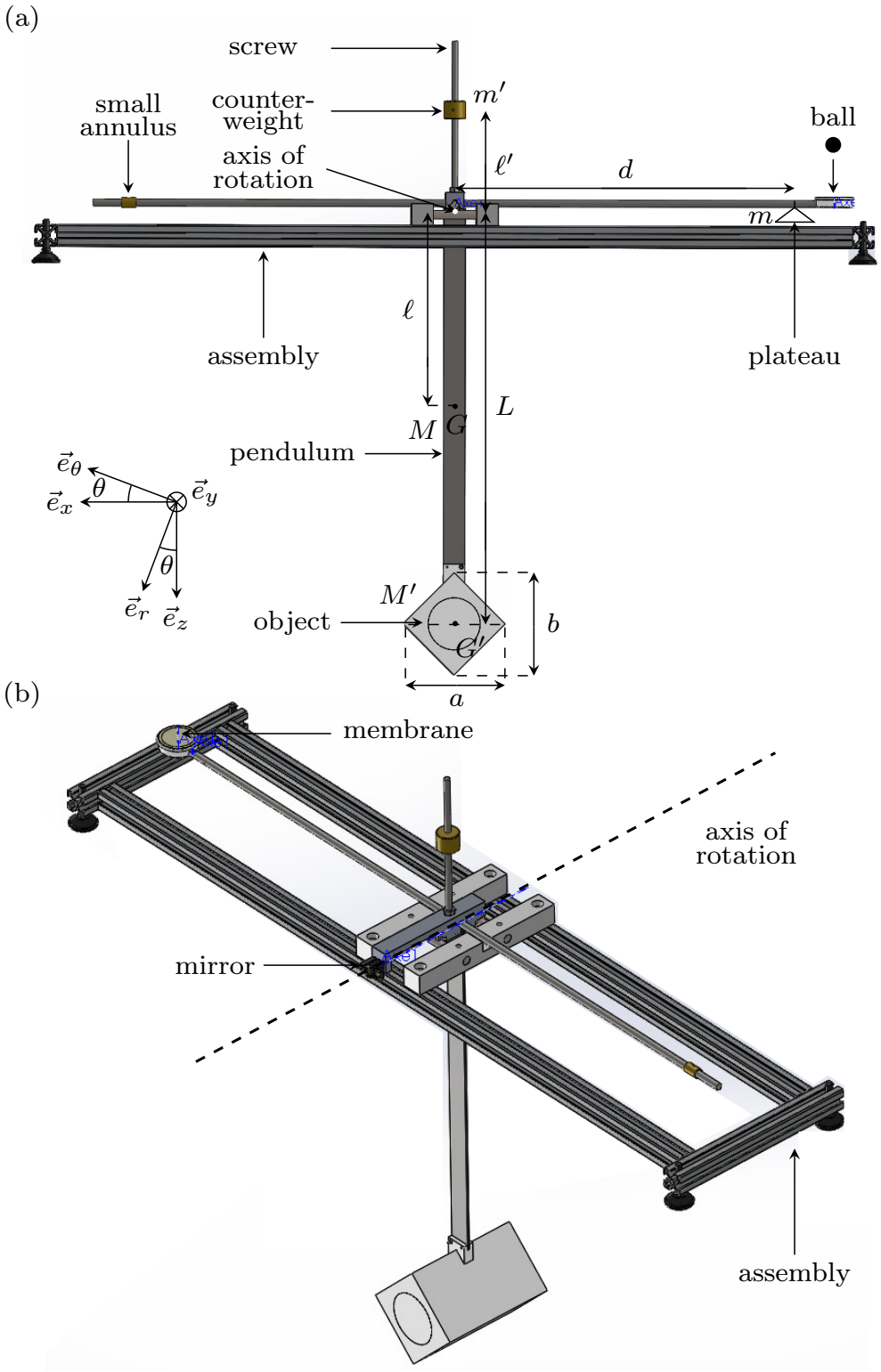


Figure 2.2: Schema of the pendulum set-up viewed from the side (a) and from top and behind (b). The arrows show the different elements of the set-up and the different relevant lengths are labelled. The coordinates are shown in panel (a).

to the rib of the wedge and fixed on the assembly. The two lines of contact between the wedges and the cylinders define the axis of rotation. Using the wedges, the friction between the pendulum and the assembly is very small and can be neglected. For each experiment, the height of the assembly is adjusted in order to have the center of gravity of the mass, named G', in the middle of the stratification. The fluid has a depth of H. Thus, G' is located at $z = H/2$. The angle θ is measured as a function of time using a laser and a position sensor. The laser spot is reflected on a small mirror, fixed on the pendulum and located on the axis of rotation. The mirror is shown in figure 2.2(b) but not the laser neither the position sensor. As the pendulum oscillates, the mirror deflects the laser by an angle twice larger as the angle θ. The deviation is measured via an elongated position sensor, giving a tension proportional to the deviation of the laser spot. The angle θ is deduced from the tension given by the sensor via a calibration. The deflection of the laser is recorded at a frequency of 50 Hz during the experiment. Note that in this chapter, one assumes that the angle θ remains very small and thus the object at the bottom of the pendulum have almost horizontal motions. The quantity x is defined as the horizontal distance between the initial position of the center of mass of the object G' at $\theta = 0$ and its position at a time t. Thus, one has $x = L\theta$ within the small angle approximation. Experimentally, we took care to limit the forcing in order to have a maximal horizontal displacement of 10 mm. For each experiment, the pendulum is excited three times to increase the statistics of our measurements and to reduce the noise-over-signal ratio. Each measurement appears to be very reproducible.

Cross-section shape	Section	a [cm]	W' [cm]	ρ [g/cm^3]	M [g]	L [cm]	ℓ [cm]	J [g·m^2]	H [cm]
Large Square	2.3.2	14	17	1.08	2730	57.5	40.2	655	95
Small Square	2.3.3	7	16	1.41	1453	54	25.5	215	95
Small Disk	2.4	5	16	1.43	1339	56.7	22.3	173	$6-16$
Flattop Hill	2.5	20	16.4	1.21	2833	55.3	39.7	639	$16-20.3$

Table 2.1: Parameters of the four cylinders used in this chapter. The shape indicates the cross section of the cylinder, in the $x-z$ plane. W' is its width in the y-direction and ρ its density. a represents a typical length scale, so the diagonal for the squares and the diameter for the disk. M is the total mass of the pendulum and the cylinder, without the counter-weight. L and ℓ are defined in figure 2.2 while J is the moment of inertia of the whole pendulum (without the counter-weight). Note that J and ℓ are carefully measured. The fluid depth indicates the type of experiments performed with the objects: for the two square shapes, this depth is much greater than a which means than we are close to an infinite depth. For the disk shape and the flattop hill, the depth has the same order of magnitude than a, these are finite depth experiments.

Different experiments have been performed, with different shapes of the body and in a fluid of finite or infinite depth. Four different cylinders have been used for the experiments, with different cross section shapes. For each shape, the position of the center of mass G' and the moment of inertia J have been measured using a method described in the next section. The object has a width W' slightly smaller than W, the width of the tank. Nevertheless, one can assume that the added mass and damping coefficients do not depend on the y coordinate. Table 2.1 summarizes the different characteristics of four cylinders used. The height of the fluid H is given in the last column. When $H = 95$ cm, this means infinite depth and the experiments are performed in the large tank. The finite depth experiments have been performed in the small tank.

Wave-breakers

To prevent the return of the waves after reflection on the edges of the tank, we built two different wave-breakers. They are located at the edges of the tank, to attenuate or to trap the waves before their reflections. Figure 2.3 shows the two types of wave-breakers used. The first one (see panel (a)) is based on a network of grids of different sizes. The green grid has a mesh size of 3 cm while the white one has a mesh size of 1 cm. Five layers of grids are fixed together and placed at the edges of the tank. The space between the grids is around 5 cm. At the bottom of the tank and below the surface, only two layers of grids are present. Both grids have a mesh size smaller than the wave length of the internal waves emitted

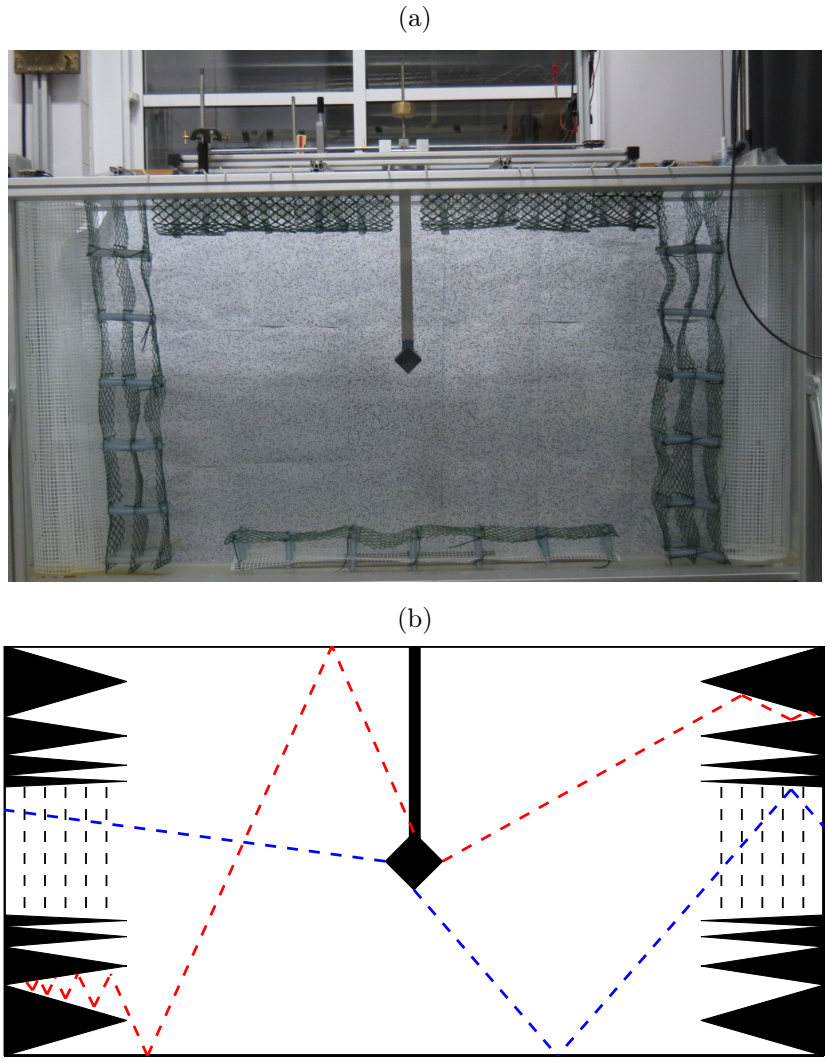


Figure 2.3: (a): Picture of the large tank with the wave-breaker built using grids of different sizes. The object inside is the small square cylinder. (b): Sketch of the anechoic chamber in the large tank, with the large square cylinder. The vertical dashed black lines in the middle of the chamber symbolize the wave-breaker visible on panel (a). Examples of four different rays starting from the four summits of the square are shown. The two red rays are trapped by the anechoic chamber while the two blue rays may come back and perturb the pendulum.

by the pendulum. One expects the waves to be attenuated where they pass throughout. The second wave-breaker is sketched in figure 2.3(b), in the large tank. One can call it an internal wave anechoic chamber, by comparison with the set-ups which absorb sound or electromagnetic waves. Note some similarities with the dissipative structures for sound and for internal waves. This chamber is built for this particular geometry, where the source of the waves is in the center of the tank. As the pendulum oscillates with its characteristic frequency, the waves it emits have one fixed propagation angle. Consequently, it is possible to compute where the waves, emitted by the four submits of the square, hit the structure of the wave-breaker. If the waves hit a slope less steep than their propagation direction, they reflect not in the direction of the pendulum but continue their propagation inside the structure. They are trapped and never return. Of course, the structure has to be adapted to the different angles of propagation: this gives smaller structures close to mid-depth. Waves hitting the edges of the tank approximately at the depth of the pendulum itself propagate almost horizontally. Thus, it is impossible to trap them. The anechoic chamber presents two holes at mid-depth of the tank. These holes have been filled by the wave-breakers built with grids of different sizes, shown in figure 2.3(a). This implies that the almost horizontal waves are not trapped but may be slightly attenuated. It worths noting that it is these waves that cause the major part of the problem of wave reflection. The anechoic chamber is not expected to tackle this problem but can limit drastically the return of high frequency waves. One can compute the minimal angle of the waves which are not trapped in the structure and fall in one of the two holes. For a typical buoyancy frequency of $N = 0.8$ rad/s, this gives that waves with $\Omega > 0.2$ are expected to be trapped by the anechoic chamber. Some rays with higher frequencies can fall in one of the two holes at mid-depth, as shown by the blue ray emitted to the right in figure 2.3(b). These rays can also come back but one can consider that they are attenuated because their trajectories are much longer than the ones of almost horizontal rays.

2.2.2 Equation of motions

For each shape tested, one need three different steps to measure the added mass and the damping coefficients in a stratified fluid of finite or infinite extent. Indeed, it is necessary to perform initial experiments in the air and in homogeneous fluid before attending to carry out an experiment in a stratified fluid. This section presents the different equations of motions of the cylinder in the different fluids.

In the air

Let us first consider that the pendulum is surrounded by air only. It undergoes:

- its own weight, in G: $Mg\vec{e}_z$
- the weight of the counter-weight: $m'g\vec{e}_z$
- the weight of the calibration mass m if it is present: $mg\vec{e}_z$.

We neglect the viscous damping of the air on the pendulum and the friction at the contact between the pendulum and the assembly. Experimentally, this approximation is relevant because the oscillations of the pendulum in the air can last more than 30 minutes. The kinetic momentum theorem in O gives

$$(J + m'\ell'^2)\frac{\mathrm{d}^2\theta}{\mathrm{d}t^2} + \ell Mg\sin\theta = m'g\ell'\sin\theta + mg(d\cos\theta + d'\sin\theta). \tag{2.21}$$

Using the small angle approximation and $x = L\theta$, one has

$$\left(\frac{J + m'\ell'^2}{L}\right)\frac{\mathrm{d}^2x}{\mathrm{d}t^2} + \frac{\ell}{L}Mgx = \frac{\ell'}{L}m'gx + mg\left(d + \frac{d'}{L}x\right). \tag{2.22}$$

This equation uses two unknown quantities: J and ℓ. To determine ℓ, one has to perform a calibration procedure. One considers the pendulum at rest with $m = 0$. Then, one adds a mass m in the plateau to modify the equilibrium position of the pendulum x_{eq}. This position is measured always at rest. Equation (2.22) leads to

$$\ell x_{\mathrm{eq}} = \frac{m'}{M}\ell' x_{\mathrm{eq}} + \frac{m}{M}(dL + d'x_{\mathrm{eq}}) \approx \frac{m'\ell' x_{\mathrm{eq}} + mdL}{M}, \tag{2.23}$$

as d' and x_{eq} are much smaller than d and L, respectively. Plotting the quantity on the right of equation (2.23) as a function of ℓx_{eq} leads to the measure of ℓ using a linear fit.

The only unknown of equation (2.22) is now J, the moment of inertia of the pendulum. One removes the small mass m on the plateau: the equilibrium position is $x = 0$. The pendulum is excited using the ball and then relaxes. This leads to

$$\left(\frac{J + m'\ell'^2}{L}\right)\frac{\mathrm{d}^2x}{\mathrm{d}t^2} + \frac{g}{L}(\ell M - \ell' m')x = 0, \tag{2.24}$$

for small angle oscillations. This is the equation of a harmonic oscillator, of characteristic frequency

$$\omega_c^2 = \frac{g(\ell M - \ell' m')}{J + m'\ell'^2}. \tag{2.25}$$

By measuring ω_c for different positions of the counter-weight ℓ', one can deduce the moment of inertia of the pendulum J. The values of ℓ and J for the three different cylinders discussed in this chapter are shown in Table 2.1.

In homogeneous water

All the characteristics of the pendulum in the air now are known. One needs to perform an experiment in homogeneous water in order to measure the attenuation of the pendulum due to the viscosity of the fluid. The pendulum undergoes the same forces as in the air in addition to

- the Archimedes force. This modifies the apparent weight of the pendulum: $Cg\vec{e}_z$, where C is a constant depending on the mass M of the pendulum and on the Archimedes forces
- the viscous damping. One defines λ_{h} as the water viscous damping coefficient, proportional to the speed of the pendulum: $-\lambda_{\mathrm{h}}\dfrac{\mathrm{d}x}{\mathrm{d}t}\vec{e}_x$. One assumes that this force is applied only on the cylinder and not on the immersed streamline of the pendulum
- the added mass μ, due to the mass of the fluid that the pendulum has to move to go through the fluid. Note that in the case of a homogeneous fluid, the added mass is real and one has $m_A = \mu$. Again, one assumes that the added mass is applied only on the cylinder and negligible for the rest of the pendulum. The force is proportional to the acceleration of the object: $-\mu\dfrac{\mathrm{d}^2x}{\mathrm{d}t^2}\vec{e}_x$.

This leads to

$$\left(\frac{J+m'\ell'^2+\mu L^2}{L}\right)\frac{\mathrm{d}^2x}{\mathrm{d}t^2}+\lambda_\mathrm{h}L\frac{\mathrm{d}x}{\mathrm{d}t}+\left(\frac{C-\ell'm'g}{L}\right)x=mg\left(d+\frac{d'}{L}x\right). \tag{2.26}$$

From the air calibration, one knows J but C and μ are unknown. It is possible to compute the constant C by calculating the Archimedes force for the pendulum. Nevertheless, this constant is measurable by a similar calibration procedure as in the air. One uses the small mass m on the plateau, which is responsible for the right-hand-side of equation (2.26). When the pendulum is at rest, one changes its position of equilibrium by varying the small mass on the plateau and one measures the new equilibrium position x_eq. From equation (2.26), one has

$$(C-\ell'm'g)x_\mathrm{eq}=mg(dL+d'x_\mathrm{eq}). \tag{2.27}$$

This allows us to measure C precisely, by varying the mass m', and thus x_eq.

Then, the masses on the plateau are removed and the equilibrium position is $x=0$. The pendulum is now ruled by the equation

$$\left(\frac{J+m'\ell'^2+\mu L^2}{L^2}\right)\frac{\mathrm{d}^2x}{\mathrm{d}t^2}+\lambda_\mathrm{h}\frac{\mathrm{d}x}{\mathrm{d}t}+\left(\frac{C-\ell'm'g}{L^2}\right)x=0, \tag{2.28}$$

with J and C known. This equation is the equation of a damped harmonic oscillator whose the solution is given by

$$x(t)=x_0\exp\left(-\frac{t}{\tau}\right)\sin(\omega_0 t), \tag{2.29}$$

where

$$\tau = \frac{2}{\lambda_\mathrm{h}}\left(\frac{J+m'\ell'^2+\mu L^2}{L^2}\right), \tag{2.30}$$

$$\omega_0^2 = \frac{C-\ell'm'g}{J+m'\ell'^2+\mu L^2}-\frac{\lambda_\mathrm{h}^2L^4}{4(J+m'\ell'^2+\mu L^2)^2}, \tag{2.31}$$

$$\approx \frac{C-\ell'm'g}{J+m'\ell'^2+\mu L^2}\equiv\omega_c^2, \tag{2.32}$$

if λ is sufficiently small. Equation (2.29) is given for the impulse initial conditions $x(0)=0$ and $\mathrm{d}x/\mathrm{d}t(0)=\omega_0x_0$.

In density stratified water

This is the last step of the measurements. The tank is now filled by a linearly stratified fluid with a constant buoyancy frequency N, using the double bucket method described in section 1.3.2. Note that the tank is filled from below, with the pendulum already present in the tank and fixed at $x=0$ during all the filling procedure to avoid mixing.

The pendulum undergoes the same forces as in homogeneous water except that one has to take into account the density stratification for the Archimedes force. Moreover, as the pendulum oscillates at its characteristic frequency, it can emit waves if ω_c is smaller than N. One introduces the dimensionless characteristic frequency of the pendulum, $\Omega_c=\omega_c/N$. Thus, internal waves are emitted when $\Omega_c<1$. The wave emission leads in a loss of

energy due to wave, which damps the pendulum. Thus, one can define an other damping coefficient λ_{w} and the total damping coefficient is given by

$$\lambda = \lambda_{\mathrm{h}} + \lambda_{\mathrm{w}}, \tag{2.33}$$

where λ_{h} is the damping coefficient measured in homogeneous water. The equation ruling the horizontal displacement of the pendulum x is

$$\left(\frac{J + m'\ell'^2 + \mu L^2}{L^2}\right)\frac{\mathrm{d}^2x}{\mathrm{d}t^2} + (\lambda_{\mathrm{h}} + \lambda_{\mathrm{w}})\frac{\mathrm{d}x}{\mathrm{d}t} + \left(\frac{C - \ell' m' g}{L^2}\right)x = 0. \tag{2.34}$$

Once again, C can be obtained using the calibration procedure already explained for air and homogeneous water. It uses the small mass m on the plateau and it consists in measuring the equilibrium position of the pendulum x_{eq}.

The next section addresses how to measure precisely μ and λ for the cases of homogenous and stratified fluids, using the impulse response function analysis.

2.2.3 Impulse response function analysis

In homogeneous water

Figure 2.4 shows a typical signal recorded in a homogeneous fluid, using the large square cylinder, in the large tank. Before $t = 0$ s, the pendulum is at rest $x = 0$. At $t = 0$ s, the ball hits the membrane and the pendulum starts to oscillate until it comes back to rest, due to viscous attenuation. One wants to use this signal to measure the values of μ and λ_{h}.

It is possible to fit the curve obtained in figure 2.4 by the equation (2.29), for the pendulum motion in a homogeneous fluid. This gives access to μ and λ_{h}, at the characteristic frequency of the pendulum ω_c. Nevertheless, one can also work on the signal in the frequency space, after a Fourier transform. This uses the impulse response function analysis,

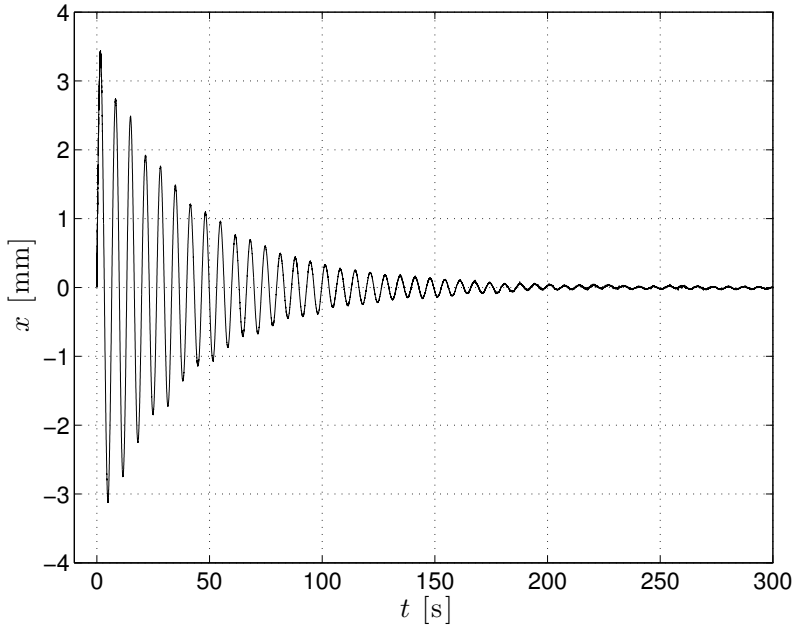


Figure 2.4: Typical oscillations x as a function of time t. This signal has been recorded in homogeneous water for the large square-shaped cylinder and in the large tank.

already described by Ermanyuk [39, 40] and by Ermanyuk and Gavrilov [42, 44]. The idea is to examine the response of equation (2.28) to a forcing proportional to $\exp(i\omega t)$. The response function is defined by

$$R(\omega) = \int_0^\infty x(t') \exp(i\omega t') \mathrm{d}t'. \tag{2.35}$$

Using equations (2.28) and (2.35), one has

$$R(\omega) = \frac{1}{(C - \ell' m' g) + iL^2 \lambda_\mathrm{h} \omega - (J + m'\ell'^2 + \mu L^2)\omega^2}. \tag{2.36}$$

$R(\omega)$ is a complex quantity and one notes $|R(\omega)|$ its modulus and $\phi(\omega)$ its phase. The real and imaginary part of R are respectively

$$\Big((C - \ell' m' g) - (J + m'\ell'^2 + \mu L^2)\omega^2\Big)\,|R|\cos\phi - L^2\lambda_\mathrm{h}\omega|R|\sin\phi = 1, \tag{2.37}$$

$$\Big((C - \ell' m' g) - (J + m'\ell'^2 + \mu L^2)\omega^2\Big)\,|R|\sin\phi + L^2\lambda_\mathrm{h}\omega|R|\cos\phi = 0. \tag{2.38}$$

Thus, this leads to

$$\mu = \frac{(C - \ell' m' g)}{\omega^2 L^2}\left(1 - \frac{|R(0)|}{|R(\omega)|}\cos\phi(\omega)\right) - \frac{J + m'\ell'^2}{L^2}, \tag{2.39}$$

$$\lambda_\mathrm{h} = \frac{(C - \ell' m' g)}{L^2\omega}\frac{|R(0)|}{|R(\omega)|}\sin\phi(\omega), \tag{2.40}$$

$|R(0)|$ stands for the modulus of the impulse response function for $\omega = 0$ rad/s. As the system is linear, the normalization of $|R(\omega)|$ by $|R(0)|$ allows us to use this Fourier transform approach at any value of the impulse excitation. One defines the dimensionless added mass coefficient as

$$C^\mu = \frac{\mu}{\rho_0 V}, \tag{2.41}$$

where V is the volume of the object and ρ_0 the density of the fluid. Note that one can transform λ_h in a dimensionless quantity C^λ but only in the case of a stratified fluid.

Figure 2.5 shows C^μ and λ_h for the signal plotted in figure 2.4. One can note that there is a plateau around the characteristic frequency of the pendulum ω_c (marked by the two vertical dashed lines) for both panels of figure 2.5. In a homogeneous fluid, the added mass coefficient is supposed to be constant while the variations of the damping coefficient should be small. The impulse response function technique allows us to visualize the added mass and damping coefficients in a range of frequencies located around the characteristic frequency of the pendulum. Thus, this technique is better than the simple fit of the signal, using equation (2.29). Indeed, the fit gives the black filled circles, shown in figure 2.5. They are consistent with the impulse response function analysis but they give only access to one value of the coefficients for the characteristic frequency. Consequently, it is more interesting to perform the impulse response function analysis in order to get the added mass and damping coefficients in a range of frequencies. By changing the characteristic frequency of the pendulum using the counter-weight, one can scan a large range of frequencies and thus, by combining the different experiments, get full curves for the coefficients. Note that in an ideal case, the plateau around ω_c should be of infinite length. This is not the case experimentally because of the noise.

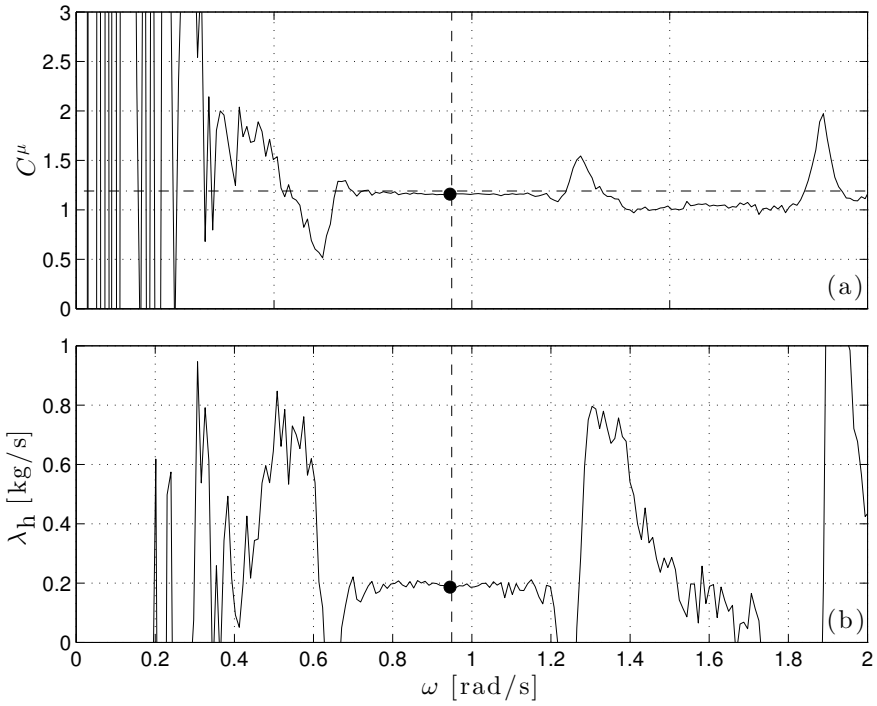


Figure 2.5: Added mass coefficient C^μ (a) and damping coefficient λ_h (b) as a function of ω obtained using the signal shown in figure 2.4. The two vertical dashed lines show the characteristic frequency of the pendulum ω_c. The horizontal dashed dotted line in panel (a) represents the theoretical prediction for the added mass in homogeneous water for the square shape: $C^\mu = 1.19$. The two black filled circles show the values found using a fit of the signal in figure 2.4 by the formula given in equation (2.29).

In a stratified fluid

In a stratified fluid, one can perform exactly the same impulse response function analysis. This leads to μ and $\lambda = \lambda_h + \lambda_w$ as in equations (2.39) and (2.40). In order to get the damping coefficient due to the wave emission λ_w, it is necessary to subtract the damping due to the viscosity of the water, λ_h, measured in homogeneous water. For a stratified fluid, one can define

$$C^\mu = \frac{\mu}{\rho_0 V}, \tag{2.42}$$

$$C^\lambda = \frac{\lambda_w}{\rho_0 V N}, \tag{2.43}$$

$$P_w = \frac{1}{2} C^\lambda \Omega^2, \tag{2.44}$$

where V is the volume of the object, N the buoyancy frequency of the fluid and ρ_0 the density of the fluid at the depth of the center of mass of the object G'. P_w is the radiated wave power coefficient, depending on C^λ and Ω, the dimensionless pulsation of the waves. In section 2.1, the coefficients have been made dimensionless by dividing by S, the section of the cylinder, assuming a bi-dimensional object. In our case, the object is three-dimensional but invariant in one direction. Thus the definitions are equivalent.

Note that in the case of a stratified fluid, C^μ and C^λ depend strongly on the frequency of the pendulum. Thus, at the very beginning of the experiment, just after the ball has hit the

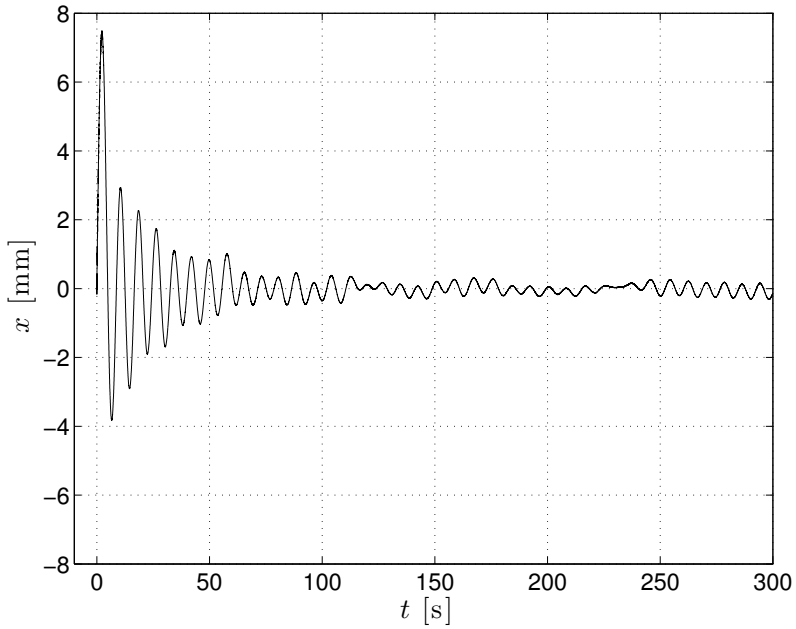


Figure 2.6: Oscillations x as a function of time t. This signal has been recorded in a stratified fluid for the large square-shaped cylinder in the large tank. For this experiment, $\Omega_c = 0.96$. Note the important attenuation during the first oscillation. The signal after $t \approx 50$ s is perturbed by the waves going back to the pendulum after reflecting on the edges of the tank. This shows that the wave-breaker based on grids is not totally efficient.

membrane, all the frequencies are present in the signal, as the forcing can be approximated by a Dirac peak in time. The pendulum emits waves at different frequencies, leading to a very high attenuation in amplitude during the first oscillation. This can be seen in figure 2.6, showing the time history of the horizontal displacement x, for an experiment performed with the large square cylinder in the large tank, linearly stratified. The value of Ω_c for this experiment is slightly less than 1. Thus, the pendulum emits waves and the oscillations are more quickly attenuated than in figure 2.4.

Figure 2.7 shows C^μ and λ for the signal shown in figure 2.6, obtained by the impulse response function analysis. With this analysis, there is still a range of frequencies, located around $\Omega_c = \omega_c/N$, where it is possible to visualize the added mass and damping coefficients. Nevertheless, as the coefficients varies strongly with the frequency, one does not have a plateau any more. Moreover, the impulse response function analysis requires that the system is causal. Indeed, once the waves are emitted, they must not come back to the pendulum. Nevertheless, as the tank is limited in space, some waves are reflected by the edges of the tank and come back to the pendulum. Thus, they act as a source of oscillations and perturb the signal recorded. One can see such wave returns after $t \approx 50$ s in figure 2.6. Consequently, the analysis performed does not work correctly at low frequencies because this creates low frequency noise. This is visible in both panels of figure 2.7 where the signal is very distorted for Ω smaller than 1. However, the signal for $\Omega > 1$ remains clear. Indeed, in this range of frequencies, no wave is emitted and the causality is well-verified. One can note that the dissipation λ is much more important for $\Omega < 1$ than for $\Omega > 1$. For $\Omega > 1$, the dissipation is around λ_h because no wave is emitted by the pendulum. This shows that the dissipation due to wave emission is much more important than the viscous dissipation.

To get the full signal of C^μ and C^λ as a function of the frequency, we combine the

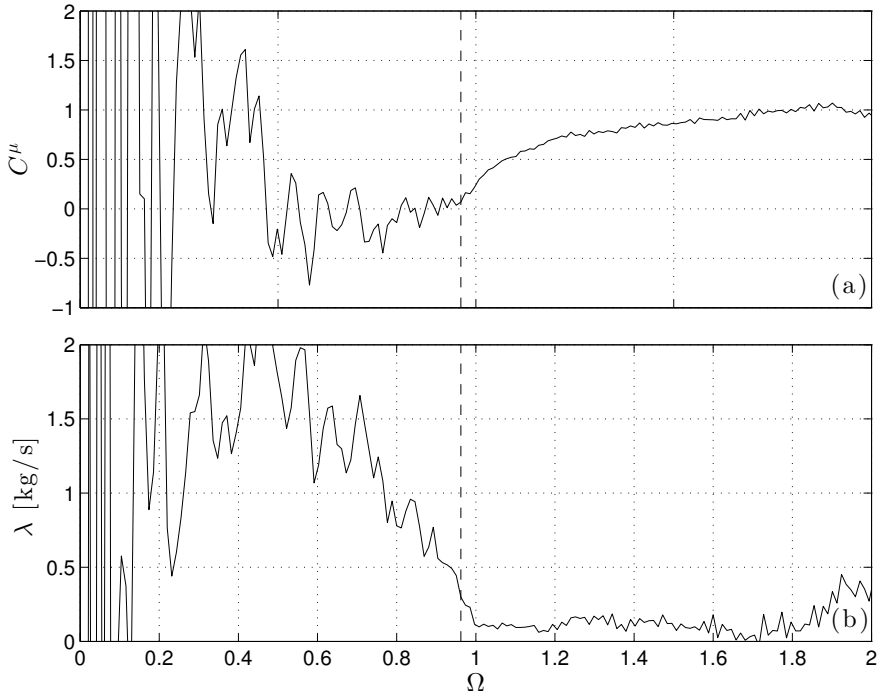


Figure 2.7: Added mass coefficient C^μ (a) and damping coefficient λ (b) as function of $\Omega = \omega/N$ obtained using the signal shown in figure 2.6. The two vertical dashed lines show the dimensionless characteristic frequency of the pendulum Ω_c.

different measurements performed at different positions of the counter-weight, so at different ω_c. Each measurement is weighted by a weight w, centered around the characteristic frequency ω_c of the pendulum. The weight w is defined as

$$w(\omega) = \frac{w_0}{w_0 + (\omega - \omega_c)^\beta}, \tag{2.45}$$

where w_0 and p are arbitrary values. w_0 controls the size of the plateau around ω_c and β acts on the edges of the plateau. Figure 2.8 shows the weight w centered around $\omega_c = 1$ rad/s, for $w_0 = 10^{-6}$ and $\beta = 8$. There is a range around ω_c where the weight is maximal. Then, away from this central region, w vanishes rapidly. Using this kind of weights, one can give more importance to the frequency range where we have reliable information using the impulse response function analysis. Indeed, the plateau obtained using the analysis coincides with the frequency range having the maximal weight. Thus, the different experiments are combined using the most reliable region of each measurement.

Moreover, we applied a median filter to the C^μ and λ spectra in order to smooth slightly the curves. We used the *medfilt1.m* Matlab function. The median filter has been performed on intervals of frequency ω of 0.05 rad/s.

In the next sections, I present the results in terms of added mass and damping coefficients for the three different objects. Sections 2.3.2 and 2.3.3 discuss about the square-shaped cylinder, large and small, in the large tank. This can be viewed as an ocean of infinite depth. Section 2.4 concerns the disk-shaped cylinder in the small tank and addresses the finite-depth effects. Finally, section 2.5 deals with a topography lacking of tidal conversion at finite depth and for a given frequency.

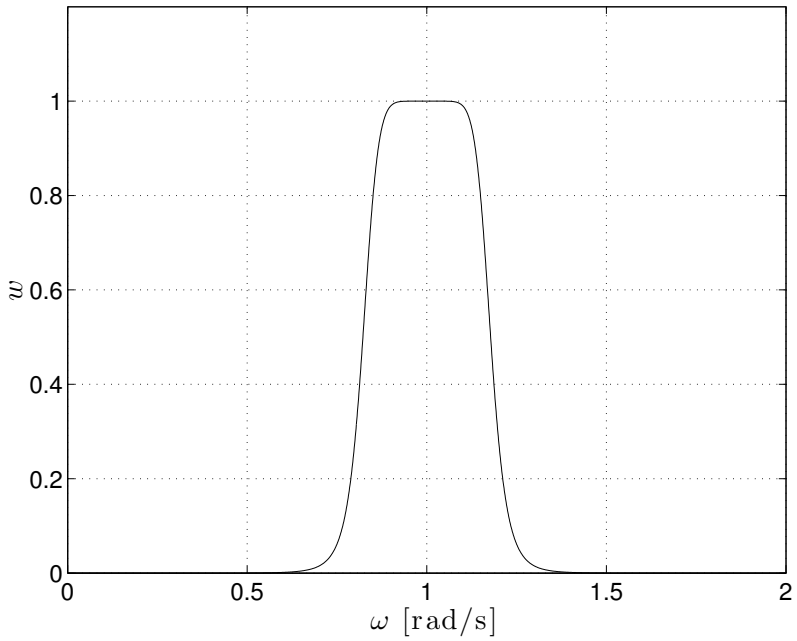


Figure 2.8: Example of a weight w as a function of the frequency ω. The weight is centered around $\omega_c = 1$ rad/s. It corresponds to equation (2.45) with $w_0 = 10^{-6}$ and $\beta = 8$.

2.3 Square cylinder: infinite depth

This section presents the experiments performed in a fluid of infinite depth with a pendulum having a square-shaped cross section. We used two square cylinders: one large with the side of the square equal to 10 cm and one smaller with a side of 5 cm long. As $H = 95$ cm, we are in a good approximation in a fluid of infinite depth.

2.3.1 Affine similitude prediction

For a diamond-shaped cylinder, the added mass in homogeneous fluid of infinite depth is given by

$$F_*(p) = \frac{\Gamma(1.5 - 1/\pi \arctan(1/p))\Gamma(1/\pi \arctan(1/p))}{\Gamma(0.5 + 1/\pi \arctan(1/p))\Gamma(1 - 1/\pi \arctan(1/p))} - 1, \tag{2.46}$$

following Korotkin [83]. Γ is the Euler function and p is equal to the ratio between the vertical and the horizontal diagonals of the diamond. For the squares in our set-up, $p = 1$ which leads to $C^\mu = F_*(p = 1) \approx 1.19$.

Using the affine similitude for a stratified fluid, p is changed by a factor α. Plugging this formula into equations (2.5) and (2.6) and using the complex Euler function for $\Omega < 1$, one can calculate the solution for the square-shaped cylinder in the uniformly stratified fluid of infinite extent. The theoretical dependencies of the added mass, damping and radiated power coefficients on the frequency of oscillations are shown using the black solid line in figures 2.9 and 2.10 together with the experimental points. For $\Omega > 1$, the added mass coefficient describes a curve, asymptotic for large Ω to the added mass value in the homogeneous fluid. The damping and radiated wave power coefficients vanish. For $\Omega < 1$, the solution predicts the drop of all the coefficients at the frequency corresponding to the transition from supercritical to subcritical case, at $\Omega = \sqrt{2}/2$. This frequency corresponds

to an angle of wave propagation θ equal to 45°. Thus, the waves emitted at this frequency have exactly the same angle of propagation than the slope of the sides of the square and this marks the transition between the sub- and super-critical cases. The notion of sub-/super-critical obstacles is commonly used in the studies on tidal conversion to distinguish the obstacles having the slopes smaller/greater than the slope of the wave beam with respect to the horizontal. The extreme cases of the sub-/super-critical obstacles correspond to flat geometry [7] and infinitely thin vertical barrier [92].

The next sections compare the prediction with the experiments performed with the large and small square-shaped cylinders.

2.3.2 Large Square

This section discusses the experiments performed in the large tank with the large square cylinder. Its characteristic parameters obtained in the air are presented in Table 2.1. In homogeneous water, we have found that the added mass coefficient C^{μ} is equal to 1.17 ± 0.1, which is less than 10% of error. This is consistent with the value found from equation (2.46). One can also expect that the viscous damping coefficient λ_{h} is proportional to the square root of the frequency [40]. A linear fit of λ_{h}^2 gives $\lambda_{\mathrm{h}} = 0.2\sqrt{\omega}$, where λ_{h} is in kg/s and ω in rad/s.

We performed two series of experiments with two different wave-breakers. The first series have been done with the wave-breaker composed of different grids, placed at the edges of the tank. The second one has been carried out using the anechoic chamber. The results are shown for the two series of experiments, using figure 2.9.

Figures 2.9(a), (b) and (c) show the damping, radiated power and added mass dimensionless coefficients as a function of the dimensionless frequency Ω, for the first series of experiments while figure 2.9(d), (e) and (f) show the same measured coefficients for the second series. For the first (respectively second) series, the buoyancy frequency N is equal to 0.827 rad/s (resp. 0.87 rad/s). The theoretical prediction is the solid black line. The elliptic part of the coefficients, for $\Omega > 1$, are in a good agreement with the theoretical predictions. Indeed, for panels (a) and (d), the damping coefficients are both very close to zero. For panels (c) and (f), the added mass coefficients follow very precisely the black line. For panels (b) and (e), the radiated power should be null for $\Omega > 1$. This is not totally the case but the defects of the damping coefficients are amplified at high Ω because of the definition of P_{w}. Thus, the slightly negative damping coefficients observed in panels (a) and (d) give a radiated power not totally null. Nevertheless, the agreement is good.

For the hyperbolic part where $\Omega < 1$, the agreement is not completely satisfactory. For panel (a), the black circles follow approximately the theoretical prediction for Ω greater than 0.5. For lower frequencies, the damping coefficient drops down significantly. This is not visible in panel (b), for the radiated power, because the defects of C^{λ} are eliminated at low frequencies, due to its definition. Nevertheless, the points are relatively dispersed and it is impossible to visualize clearly the singularity for $\Omega = \sqrt{2}/2$. This dispersion is due to wave reflections which allow the waves to come back and disrupt the pendulum when it is relaxing. Thus, the temporal signal recorded is deformed and the impulse response function analysis does not lead to correct results. The perturbations of the signal are visible in figure 2.6 and this creates sharp peaks in the spectra of figure 2.7. The signal is more distorted at small frequencies because waves at low frequencies propagate almost horizontally. Thus, these waves have the shortest trajectories before returning to the pendulum. This is why the damping coefficient does not follow the theoretical prediction below $\Omega = 0.5$ in figure 2.9(a). For frequencies in between 0.5 and 1, the median filter and the combination of the different experiments using the weight w smooth the signal better.

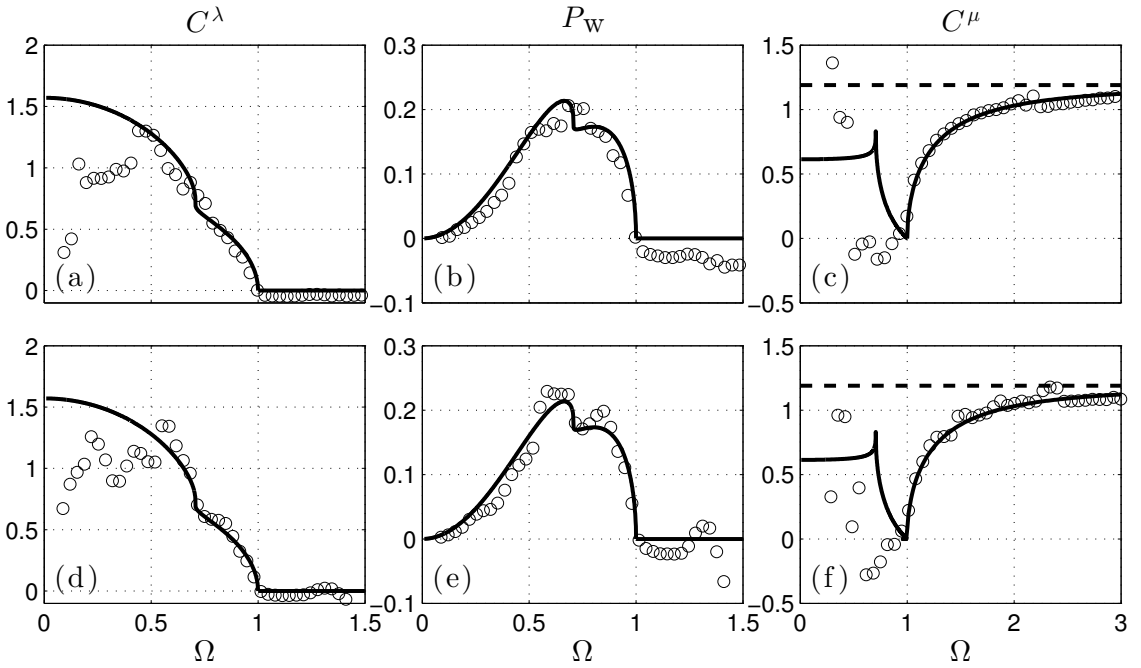


Figure 2.9: Damping (first column), radiated power (second column) and added mass (third column) dimensionless coefficients as a function of the dimensionless frequency Ω, for the large square-shaped cylinder, in infinite depth. The results for the series of experiments performed with the grid network as wave-breaker are in the first line (panels (a), (b) and (c)) while the results for the series carried out with the anechoic chamber as wave-breaker are in the second line (panels (d), (e) and (f)). On the six panels, the theoretical prediction (see equation (2.46)) is plotted as a black line. The dashed lines on panels (c) and (f) show the added mass coefficient for a homogeneous fluid: $C^\mu = 1.19$.

Thus, C^λ follows approximately the theoretical prediction but the singularity is not visible. Nevertheless, with the anechoic chamber as wave-breaker, the singularity is slightly visible in panels (d) and (e). However, in panel (d), below $\Omega = 0.5$, the signal remains away from the theoretical prediction of C^λ, as in panel (a). For the added mass coefficient in panels (c) and (f), the experimental points are totally out of the theoretical prediction for $\Omega < 1$. This is also due to the wave reflections but added mass is more affected, even for dimensionless frequencies in between 0.5 and 1.

To conclude this section, the experimental results are in a good agreement with the prediction for the elliptic part of the frequencies. This shows that the analysis technique is efficient to describe continuously the coefficients as a function of the dimensionless frequency Ω. This range of frequencies is not affected by the wave reflections because the pendulum does not emit waves in this part of the spectrum. For the hyperbolic part, the signal can not be used below $\Omega = 0.5$. In the range of dimensionless frequencies between 0.5 and 1, the experimental results follow reasonably the theoretical prediction. However, in the first series of experiments, the singularity in $\Omega = \sqrt{2}/2$ is not visible while it is distinguishable in the second series. Thus, it seems that the noise caused by the wave returning is less intense in the second series than in the first one. The anechoic chamber is more efficient to prevent wave returnings than the one based on grids of different sizes. Nevertheless, both wave-breakers are not completely efficient and the signal is distorted below $\Omega = 0.5$. For the anechoic chamber, one expects some wave reflection problems only

below $\Omega = 0.2$, which is not the case.

In the next section, we reduce the size of the square edges to $a = 5$ cm. This causes a decrease of the wave length of the waves emitted by the pendulum and increases their viscous attenuation. Thus, one should have less problems due to wave reflections.

2.3.3 Small square

In this section, we show the results obtained for the small square cylinder in the large tank. The characteristic parameters of this object are shown in Table 2.1. We used the wave-breaker based on grid of different sizes only. Indeed, the second wave-breaker, the anechoic chamber, was no built at the time when the experiment has been performed. Nevertheless, as the size of the object is 2 times smaller than the one of the large object, the wave length of the internal wave is decreased by a factor of 2 and the viscous attenuation is multiplied by $2^3 = 8$, according to equation (1.34). Thus, the wave reflections are expected to perturb the signal only weakly or for low frequencies in the spectrum. For this series of experiments, the buoyancy frequency is equal to $N = 0.826$ rad/s. In homogeneous water, the average added mass C^μ has been found equal to 1.32 ± 0.15, which is higher than the expected value of 1.19, predicted by equation (2.46). The damping coefficient λ_h is proportional to the square root of the frequency with $\lambda_\mathrm{h} = 0.1\sqrt{\omega}$.

Figure 2.10 shows the damping, radiated power and added mass dimensionless coefficients obtained. As for the large square experiments, the elliptic part of the spectra is in a good agreement with the theoretical prediction for panels (a) and (b). For panel (c), the measured added mass coefficient seems slightly shifted above the prediction. For the hyperbolic part of the spectrum, the measured damping coefficient follows the black line until $\Omega = 0.7$. Below this value, it escapes slightly before being completely out of the prediction for $\Omega < 0.4$. Nevertheless, one can distinguish a small jump at the singularity in $\Omega = \sqrt{2}/2$. The radiated power in panel (b) shows a similar pattern except that the defects of C^λ are eliminated at low frequencies. As for the large square experiments, the added mass coefficient does not follow the theoretical prediction.

Thus, using a smaller scale object, it is possible to reduce the wave reflection problem and to obtain a better signal-over-noise ratio. Nevertheless, the small size of the object

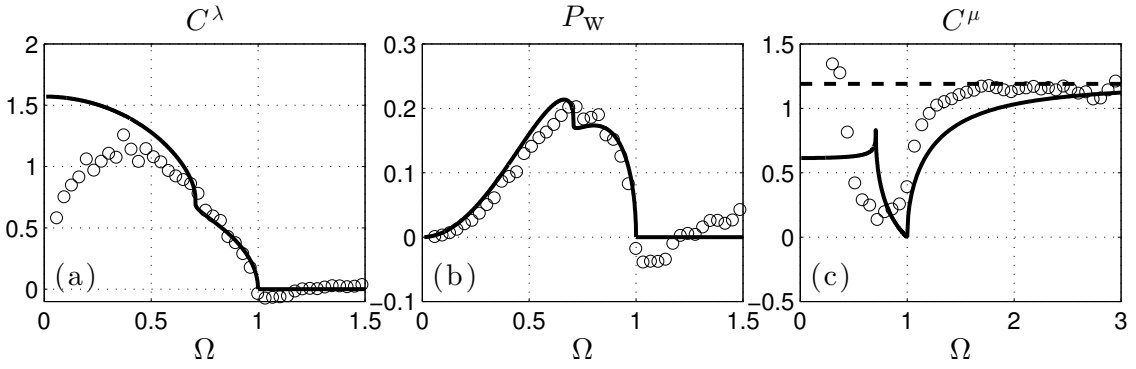


Figure 2.10: Damping (a), radiated power (b) and added mass (c) dimensionless coefficients as a function of the dimensionless frequency Ω, for the small square cylinder, in infinite depth. On the three panels, the theoretical prediction (see equation (2.46)) is plotted as a black line. The dashed line on panel (c) shows the added mass coefficient for a homogeneous fluid: $C^\mu = 1.19$.

presents two main defects. The first one is that the added mass is not fully recovered for $\Omega > 1$. Indeed, the added mass coefficient appears shifted vertically. This can be due to the viscous boundary layers, which increase the effective volume of the cylinder. A typical thickness of the boundary layers is given by $\delta = \sqrt{\nu/\omega}$. For $\omega = 1$ rad/s, this gives $\delta = 1$ mm. Thus, the boundary layers increase the volume of the object by a factor of 10% for the small square cylinder and by a factor of 5% for the large one. As μ has to be normalized by the volume of the cylinder to get C^{μ}, this could lead to higher values of the added mass coefficient if one takes into account the volume of the object only and not the volume of the object with its viscous boundary layers. This boundary layer effect is supposed to be more important for the small cylinder, as the variation of volume is more important for this cylinder. The second defect is that the small details of the theoretical prediction, typically the singularity in $\Omega = \sqrt{2}/2$ are difficult to see with a small scale pendulum. With this present set-up, one has to find a compromise between a large object, which undergoes wave reflection and a distorted signal, and a small object where the viscous boundary layers change the added mass and where the small details of the coefficients are smoothed.

In this section, I have shown that the affine similitude predictions for a square-shaped cylinder in a fluid of infinite extent are in a relatively good agreement with the experiments. Three series of experiments have been performed: two with the large square cylinder and the two different wave-breakers and one with the small square cylinder with the gridded wave-breaker. The main limitation to these experiments is the perturbations caused by the reflections of the waves emitted. Thus, it is difficult to obtain a reliable signal to observe the singularity at $\Omega = \sqrt{2}/2$ of the prediction. Moreover, it is impossible to obtain the damping coefficient at low frequency, where this quantity is relevant for tidal forcing. In the next section, we address the problem of a circular-shaped cylinder at finite depth.

2.4 Small disk cylinder: finite depth effects

In this section, I discuss the finite depth effects on added mass and damping coefficients for a circular-shaped cylinder oscillating horizontally in a stratified fluid. As it has a circular cross section, the diameter is given by $a = b$ and $p = 1$. Ermanyuk [39] has already investigated these coefficients in the approximation of infinite depth ($H/a = 7.57$). Then, Ermanyuk and Gavrilov [42] have also considered these coefficients for the same body but in a fluid of finite depth, with H/a equals to 4.32, 3.24, 2.19 and 1.65. In this section, four series of experiments performed at finite depth are discussed. The body used is also a cylinder but with a slightly larger diameter $a = 5$ cm instead of $a = 3.7$ cm [39, 42]. The ratio H/a for our experiments is equal to 3.2, 2, 1.5 and 1.2. Thus, we complete the series performed by Ermanyuk and Gavrilov [42]. The two first series at $H = 3.2$ and 2 have to be compared with the series already obtained in [42]. Then, the two last series concern low values of H/a, never carried out before.

The characteristics of the cylinder used are given in Table 2.1. For the four series, the pendulum has been calibrated only once in the air, in order to obtain the position of G and J. These experiments have been carried out in two small tanks, connected between each other. Thus, the length of the tank is 160 cm. For experiments in homogeneous or stratified fluid, a rigid lid has been placed at the surface, to avoid that the surface modes appear in the spectrum. Indeed, as the depth is small, the frequency of the surface wave modes can be close to the characteristic frequency of the pendulum ω_c. Thus, it is possible to have a energy transfer from the pendulum to the surface wave modes. The rigid lid on the surface avoids surface wave propagation. Moreover, small wave-breakers have been

made using the grids of different sizes. In the case of finite depth, almost all the waves reflect a large number of times at the bottom and at the surface before reaching the edges of the tank and coming back to the pendulum. Thus, their trajectories can be long and the wave reflection problem is expected to be small.

It is necessary to calibrate the pendulum in homogeneous water for the four different depths, as the viscous dissipation changes with H. Table 2.2 summarizes the different parameters for the four series. The measurements of C^{μ} and λ_{h} are detailed in the next section.

Series	H [cm]	H/a	N [rad/s]	C^{μ}	$\lambda_{\mathrm{h}}/\sqrt{\omega}$ [kg/s$^{3/2}$]	Symbols (filled)
1	16	3.2	1.24	1.39	0.07	Green diamonds
2	10	2	1.41	1.75	0.10	Blue pentagrams
3	7.5	1.5	1.34	2.46	0.17	Red squares
4	6	1.2	1.4	5.12	0.67	Black circles

Table 2.2: Parameters and measured quantities for the four series of experiments at finite depth and using the small disk cylinder. The symbols mentioned in the last column are used in figures 2.11, 2.12 and 2.13.

2.4.1 Homogeneous fluid prediction

The solution for the added mass coefficient of an elliptic cylinder submerged at mid-depth of a stripe of homogeneous fluid has been obtained by Clarke [27]

$$k_*\left(\frac{a}{H},\xi\right) = 2\frac{\ln\left[\sec\left(\frac{\pi a}{2H}\frac{1}{1-\xi}\right)\right]}{\left(\frac{\pi a}{2H}\frac{1}{1-\xi}\right)^2}, \tag{2.47}$$

where the parameter ξ is to be determined from the following equation

$$\frac{2\xi H}{\pi a}\ln\left[\sec\left(\frac{\pi a}{2H}\frac{1}{1-\xi}\right)+\tan\left(\frac{\pi a}{2H}\frac{1}{1-\xi}\right)\right] = \frac{1}{p}. \tag{2.48}$$

In our case, the cross section of the cylinder is not elliptic but is perfectly circular. Thus, one has $p = 1$. Using equations (2.47) and (2.48), it is thus possible to compute the added mass coefficients for different depths H. Table 2.3 gives the measured and predicted added mass coefficients for our four series of experiments and the five ones available in Ermanyuk [39] and in Ermanyuk and Gavrilov [42]. First, one can see that all the experiments are in a good agreement. Indeed, the added mass follows the same evolution when H/a decreases. Moreover, the values obtained for $H/a = 3.24$ in [42] and $H/a = 3$ with our set-up are close. Secondly, the prediction of Clarke [27] is very good for high values of H/a and remains of the same order of magnitude when H/a decreases. Note that the calculations of Sturova [142] lead to added mass values close to the ones predicted by equations (2.47) and (2.48).

Using affine similitude, it may also be possible to use the equations (2.47) and (2.48) to predict the added mass and damping coefficients for the stratified fluid, as for the square shape, in section 2.3. Nevertheless, the added mass in a homogeneous fluid given by equations (2.47) and (2.48) is not determined completely analytically. Thus, it is not

possible to use the affine similitude theory, contrary to the cases of vertical flat plate or square-shaped cylinder. Note that a prediction for damping coefficients has been given by Gorodtsov and Teodorovich [61] but it works only for high values of H/a, as shown by Ermanyuk and Gavrilov [42].

H/a	Reported in	C^μ measured	C^μ predicted [27]
7.57	[39]	1.05	1.029
4.32	[42]	1.12	1.093
3.24	[42]	1.24	1.173
3.2	present section	1.39	1.178
2.19	[42]	1.54	1.438
2	present section	1.75	1.558
1.65	[42]	2.25	1.999
1.5	present section	2.46	2.418
1.2	present section	5.12	5.825

Table 2.3: Measured (third column) and predicted (fourth column) added mass coefficients C^μ in a homogeneous fluid for the different H/a ratios shown in the first column. The second column shows where the data are extracted from: references [39, 42] or present section.

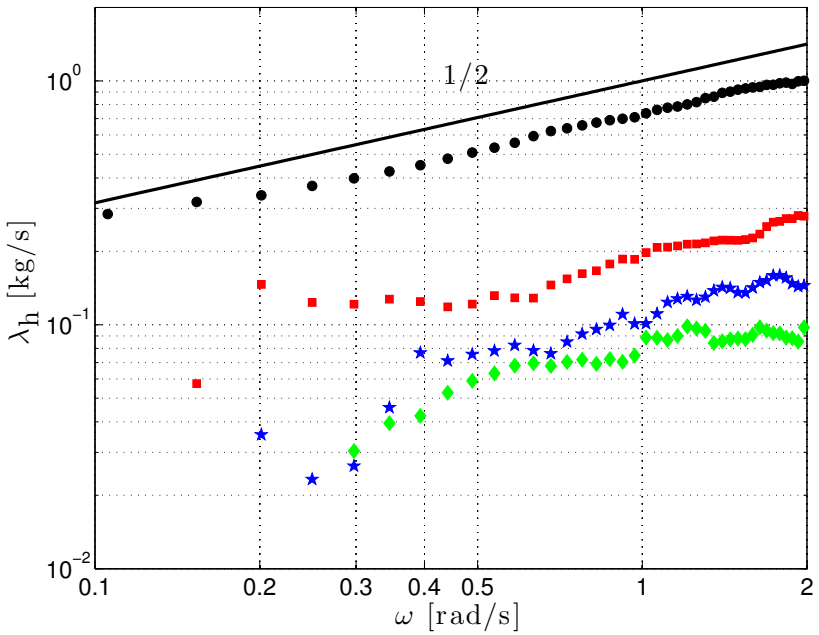


Figure 2.11: Damping coefficient λ_h as a function of frequency ω for the four series of experiments performed with our pendulum set-up in log-log scale. H/a is equal to 1.2 (black circles), 1.5 (red squares), 2 (blue pentagrams) and 3.2 (green diamonds). The solid black line shows the power law $\lambda_h \propto \sqrt{\omega}$.

For the damping coefficient λ_h in homogeneous fluid, one expect that $\lambda_h \propto \sqrt{\omega}$ as in [42]. Figure 2.11 shows the damping coefficients for the four series of experiments

performed with our pendulum set-up as a function of the frequency ω, in log-log scales. One can see that for frequencies higher than $\omega = 0.5$ rad/s, the damping coefficient λ_h depends reasonably on the square root of the frequency ω. Below $\omega = 0.5$ rad/s, the signal is noisy except for the smallest value of H/a (black filled circles).

2.4.2 Stratified fluid

Figure 2.12 shows the added mass coefficients for the four series of experiments. The value of H/a is equal to 1.2 for the black circles, 1.5 for the red squares, 2 for the blue pentagrams and 3.2 for the green diamonds, as indicated in Table 2.2. The added mass prediction [74] for a fluid of infinite depth is represented by the solid black line. Note that for $\Omega < 1$, the added mass coefficient vanishes. This is a special feature of the circular cylinder. In figure 2.12, one can see that the different added mass coefficients reach some asymptotic values for $\Omega > 1$, except for the smallest H/a ratio (black circles). Theses asymptotic values are close to the added mass values measured in homogeneous water, indicated by dashed lines. This is consistent with the prediction that, at high frequencies, the added mass coefficients are not different from the homogeneous case. One can note that as H/a decreases, the added mass coefficient increases. Thus, the deeper, the smaller the added mass, at any frequency. This is consistent with the measurements made by Ermanyuk and Gavrilov [42]. At low frequency, one can guess that the results are more perturbed. This

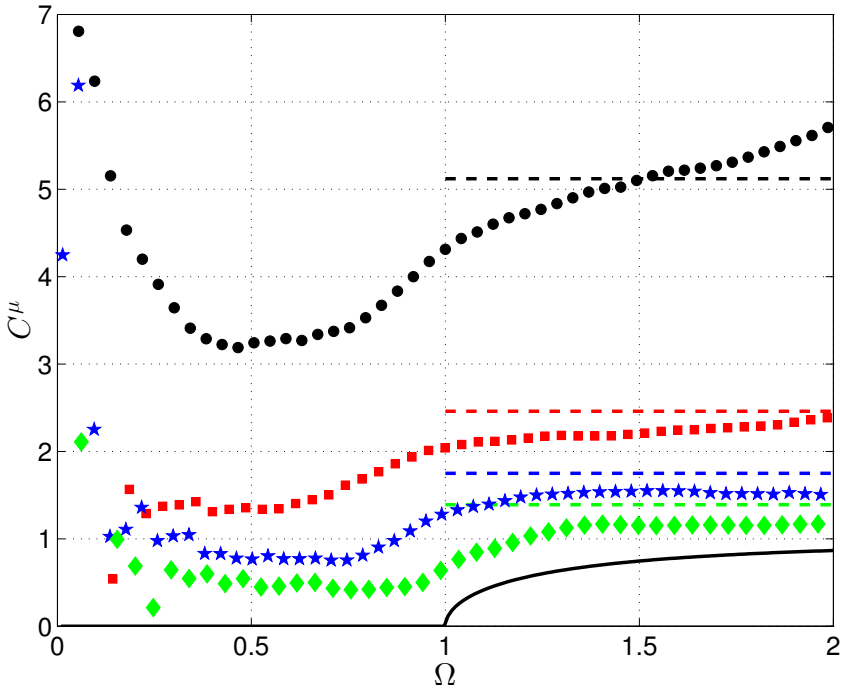


Figure 2.12: Added mass coefficient C^μ as a function of the dimensionless frequency Ω for the four different series of experiments at different depths. H/a is equal to 1.2 (black circles), 1.5 (red squares), 2 (blue pentagrams) and 3.2 (green diamonds). The horizontal dashed lines correspond to the added mass measured in homogeneous water for the different depths. The colors are the same than the ones for the symbols. The solid black line corresponds to the theoretical prediction at infinite depth made by Hurley [74] and verified experimentally by Ermanyuk [39].

is due to wave reflections. Note that the range of frequency where the signal is noisy is reduced when one decreases the depth. Indeed, a small depth imposes to almost all waves to reflect a given number of times at the top and bottom of the tank before reaching the edges of the tank. This is more noticeable in figure 2.13.

Figure 2.13 shows the damping and radiated power coefficients for the four series of experiments. The symbols used are the same as in figure 2.12 and are described in Table 2.2. The prediction for a fluid of infinite depth [74] is plotted as solid black line, on both panels. For the elliptic part, one can see that no wave is emitted as C^λ vanishes, for the four series of experiments. For the hyperbolic part, the symbols are further and further from the infinite depth prediction as one decreases the depth of the fluid H. This can be nicely seen in figure 2.13(b). In panel (a), one can see the signatures of wave reflections at low frequency. The results are distorted before $\Omega = 0.3$ for the largest depth (green diamonds), before $\Omega \approx 0.2$ for the two intermediate depths (blue pentagrams and red squares) while no distortion of the signal is visible for the smallest depth (black circles). This shows that the values of C^λ at $\Omega = 0$ is greater than 1 for very small aspect ratios H/a in qualitative agreement with predictions for the vertical ridge by Llewellyn Smith and Young [92].

The low-frequency limit of the damping coefficient is a measure of efficiency of tidal

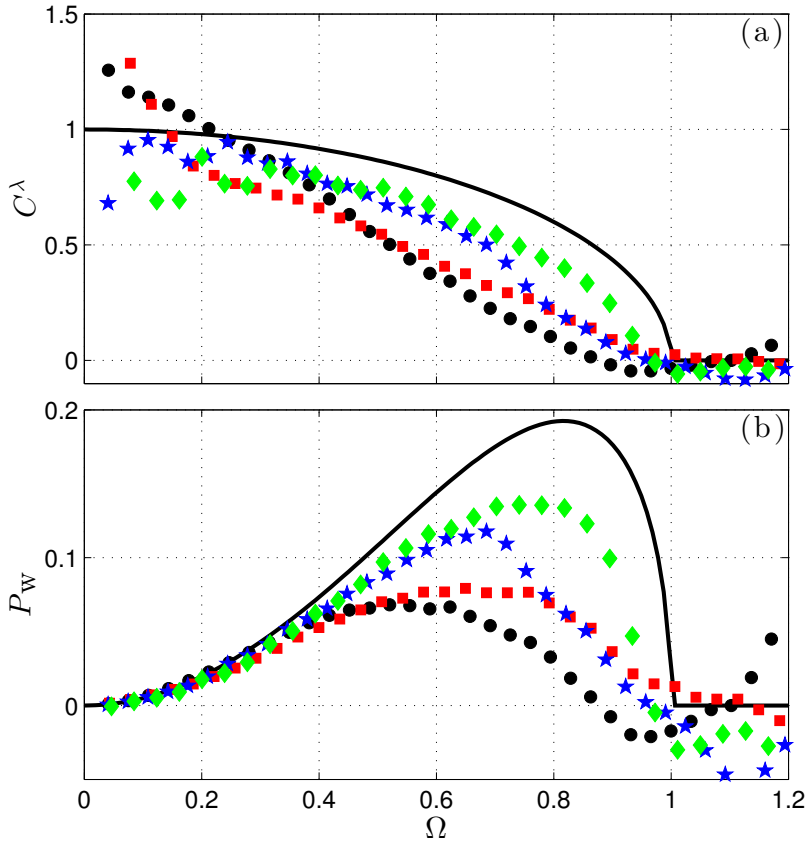


Figure 2.13: Damping coefficient C^λ (a) and radiated power P_w (b) as a function of the dimensionless frequency Ω for the four different series of experiments at different depths. As in figure 2.12, H/a is equal to 1.2 (black circles), 1.5 (red squares), 2 (blue pentagrams) and 3.2 (green diamonds). The solid black line corresponds to the theoretical prediction at infinite depth made by Hurley [74] and verified experimentally by Ermanyuk [39].

conversion in terms of the scaling adopted in [92]. For example, equation (2.17) predicts that, for a vertical flat plate in a fluid of finite depth, as H/a becomes smaller and smaller, the dimensionless damping coefficient takes values higher than 1. In figure 2.13(a), the black circles, corresponding to the smallest ratio H/a and having a good reliability at low frequencies, take values higher than 1 for low frequencies, below $\Omega < 0.2$. The prediction of equation (2.17) for such H/a gives $C^{\lambda}(\Omega \to 0) \approx 1.58$. For the black circles in figure 2.13(a), it seems that $C^{\lambda}(\Omega \to 0) \approx 1.4$. Nevertheless, this predicted value is for a vertical flat plate and not a cylinder. Thus, it is difficult to compare the measured value with the prediction, even if both are higher than 1. It it encouraging that a very small aspect ratio H/a, one finds $C^{\lambda}(\Omega \to 0) > 1$, as expected by Llewellyn Smith and Young [92]. This is of crucial importance for tidal conversion.

2.5 Flattop hill: topography lacking of tidal conversion

In this section, we present experiments performed with an object having a specific shape. This object has been designed thanks to Leo Maas in order to exhibit that, at finite depth and for a given frequency, no tidal conversion is observed. Topographies lacking of tidal conversion have already been exhibited theoretically by Maas [96] and a series of experiments have been reported recently showing such lack of tidal conversion [99]. By measuring the radiated wave power, we can expect to find a significant decay of this power at a given frequency, depending on the total height of the fluid.

2.5.1 The shape of the object and theoretical prediction

Figure 2.14 shows the shape of the object in the $x - z$ plane. Its height is equal to 8 cm and it has a horizontal length of 20 cm. The object is invariant in the y-direction. As the shape is symmetric with respect to the x and z axes, it is composed of one specific curve shown in figure 2.14(b). The curve has a flat part for small x and then a decay with an inflexion point. The point is marked using a blue circle in figure 2.14(b). At this inflexion point, the slope has an angle of 36.6° which corresponds to a dimensionless frequency of $\Omega_s = 0.596$ for internal waves. This slope is shown by a blue dashed line in figure 2.14(b). The inflexion point has, by definition, the steepest slope of the curve.

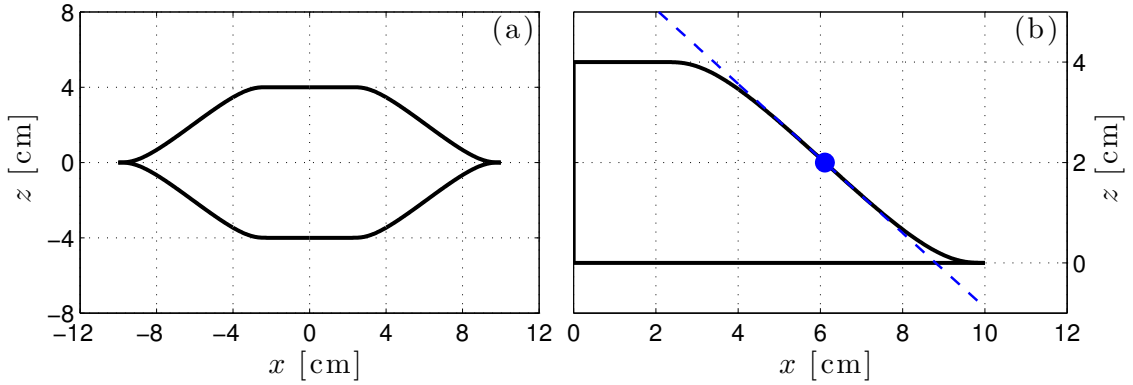


Figure 2.14: (a): Shape of the object in the $x - z$ plane. The object is symmetric with respect to the x and z axes. (b): Zoom on the upper right quarter of the object. The inflexion point is marked by the blue point. The slope of the shape at this point is shown by the dashed blue line.

According to Maas [96], it is possible to predict the frequency where the topography does not emit internal waves. This frequency can be found by connecting two inflexions point by internal wave rays reflecting on the surface or at the bottom of the tank. This connects the frequency lacking of tidal conversion Ω_ℓ with the depth of the fluid H. Figure 2.15 shows the height of the fluid as a function of the frequency Ω_ℓ. This frequency is much smaller than 1 for small depth. When $H \to \infty$, the dimensionless frequency Ω_ℓ shifts towards 1, i.e. the limit of the wave emission frequency range. Note that this is valid only for frequency higher than Ω_s, i.e. when the shape is subcritical. Indeed, one can easily understand that for Ω smaller than Ω_s, the internal wave rays should go through the object to connect the two inflexion points. Thus, we should not observe a lack of wave emission for very small depth, for H below 13 cm. Note that the height of the object is 8 cm.

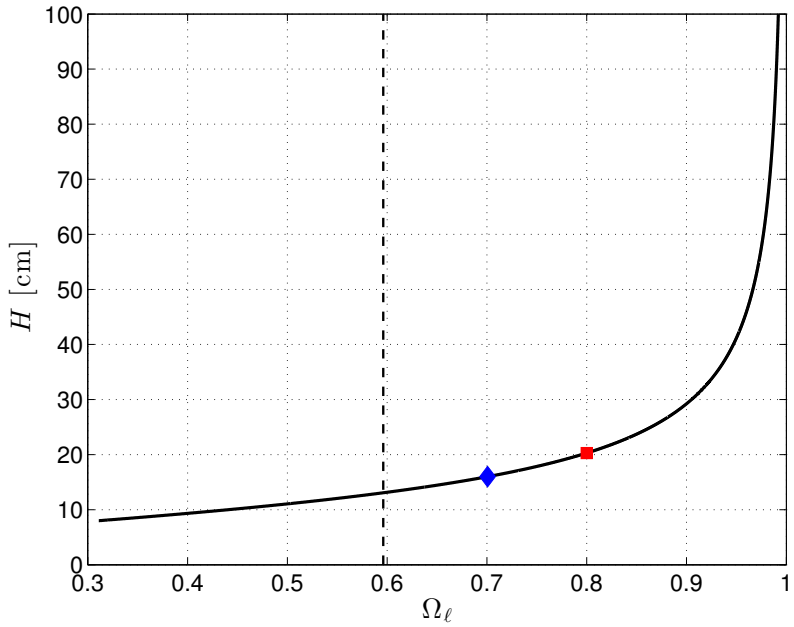


Figure 2.15: Correspondence between the height of the fluid H and the frequency where the topography lacks of tidal conversion Ω_ℓ. The vertical dashed line shows the frequency $\Omega_s = 0.596$. The two symbols represent the two different fluid depths tested during this PhD and reported in the remainder of this section.

In the next sections, I discussed two series of experiments performed at $H = 20.3$ cm and 16 cm. These experiments are shown by the red square and the blue diamond in figure 2.15, respectively. The prediction gives Ω_ℓ equal to 0.8 and 0.7 for the two depths. Before performing these two series of experiments, the pendulum with this shape has been calibrated in the air. The main characteristics are gathered in Table 2.1.

2.5.2 Experimental results

In homogeneous fluid

Experiments have been first carried out in a homogeneous fluid of depth H equal to 20.3 and 16 cm. The added mass and viscous damping coefficients have been measured using the impulse response function analysis. As expected, the added mass has been found constant

for all frequencies and the viscous damping coefficient depends on the square root of the frequency. The results are shown in Table 2.4.

Series	H [cm]	C^{μ}	$\lambda_{\mathrm{h}}/\sqrt{\omega}$ [kg/s$^{3/2}$]	Symbols (filled)
1	20.3	0.92	0.20	Red squares
2	16	1.16	0.28	Blue diamonds

Table 2.4: Parameters and measured quantities for the two series of experiments at finite depth and using the cylinder with the flattop hill cross section. The symbols mentioned in the last column are used in figures 2.16 and 2.17.

In stratified fluid

Figure 2.16 shows the wave damping and radiated wave power coefficients, for the two series of experiments. The red squares represent the experiments performed at $H = 20.3$ cm while the blue diamonds show the ones carried out at $H = 16$ cm. One can see a significant minimum in this coefficient, at $\Omega = 0.8$ for $H = 20.3$ cm (red squares) and at $\Omega = 0.7$ for $H = 16$ cm (blue diamonds). Thus, this is fully consistent with the theoretical prediction,

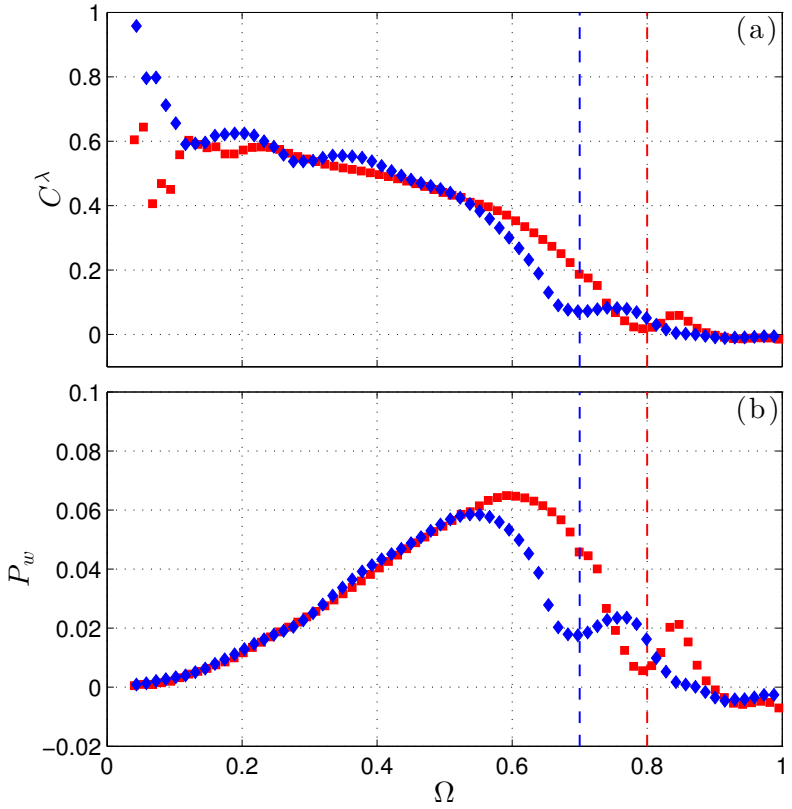


Figure 2.16: Damping coefficient C^{λ} (a) and radiated wave power P_{w} (b) as a function of the dimensionless frequency Ω for the two different series of experiments at different depths. The symbols are indicated in Table 2.4. The two vertical dashed lines show the prediction for Ω_{ℓ} using figure 2.15.

given in figure 2.15. Below $\Omega = 0.5$, the two curves collapse well. Note that the wave reflection disrupts the signal for Ω smaller than 0.2 for $H = 20.3$ cm and for Ω smaller than 0.4 for $H = 16$ cm.

Figure 2.17 shows the added mass coefficients, for the two series of experiments. As for the damping and wave power in figure 2.16, the red squares represent the experiments performed at $H = 20.3$ cm while the blue diamonds show the ones carried out at $H = 16$ cm. As in section 2.4, the added mass at smaller fluid depth is higher. Moreover, for large frequency, the added mass coefficients tend to reach the asymptotic value found in the homogeneous water. These values are represented by horizontal dashed lines in figure 2.17.

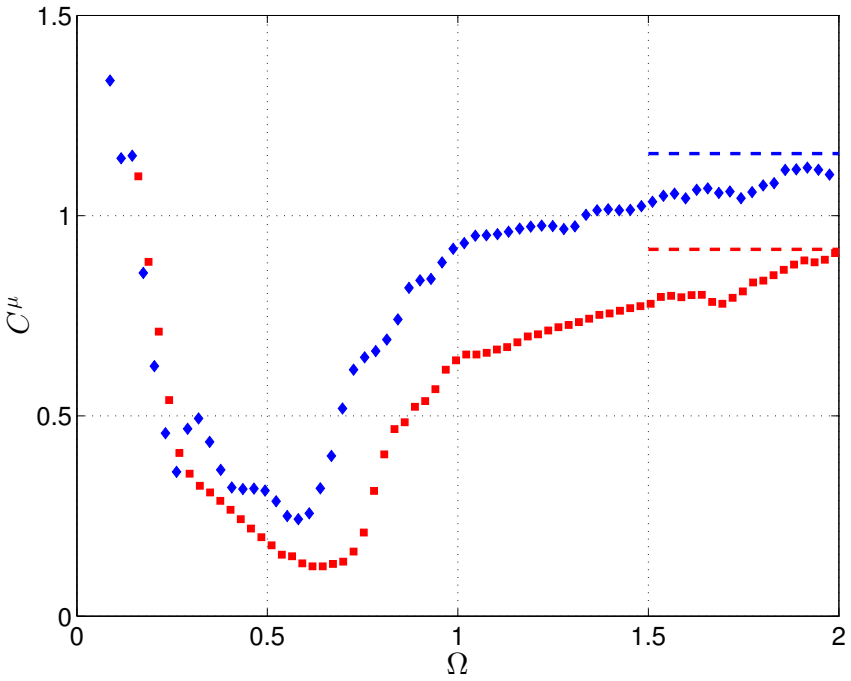


Figure 2.17: Added mass coefficient C^μ as a function of the dimensionless frequency Ω for the two different series of experiments at different depths. The symbols are indicated in Table 2.4. The horizontal dashed lines correspond to the added mass measured in homogeneous water for the different depths. The colors are the same than the ones for the symbols.

In this section, only two different fluid depths have been tested. We have found that the wave emission is much lower for some frequencies, in agreement with the theoretical prediction. It can be worthwhile to perform other experiments to explore the full range of depths. At least, one can carry out one series of experiments at very large depth in the large tank ($H = 95$ cm) to obtain the radiated wave power when $H \to \infty$. It can be also interesting to perform another series of experiments at very small depth ($H = 12$ cm) to check that there is no lack of tidal conversion at small frequency. I expect to carry out these experiments during the month of June 2016, before the defense.

Conclusions

In this chapter, the added mass and damping coefficients of three different bodies have been measured in infinite or finite depth experiments. This allows us to test the affine similitude theory, developed in Ermanyuk [40], for square- and circular-shaped cylinders and to visualize a lack of tidal conversion for given frequencies.

First, the added mass and damping coefficients have been measured for square-shaped cylinders in a stratified fluid of infinite depth. For $\Omega > 1$, when no wave is emitted, the theoretical prediction given by the affine similitude is well satisfied. For $\Omega < 1$, the cylinder emits waves which come back to it, despite the experimental wave-breakers set-up at the edges of the tank. This leads to a high experimental noise, especially at low frequency. Nevertheless, we were able to verify the theoretical prediction, at least for $\Omega > 0.5$. Two different sizes of cylinder have been tested in order to limit the wave emission and reflection. The largest cylinder undergoes more wave reflections but the measurements are more sensitive to the singularities in the coefficient variations with frequency.

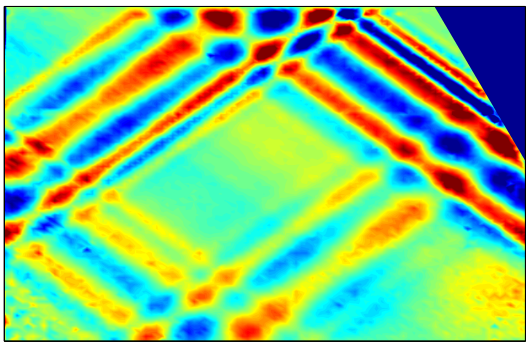
Secondly, we measured the added mass and damping coefficients of a circular cylinder in a stratified fluid of finite extent, with different depths. The results obtained are in a good agreement with the ones reported in [39, 42]. Moreover, some experiments were carried out at smaller depths than Ermanyuk and Gavrilov [42], leading to a very good reliability of the signal, even at low frequency. This shows that for small depths and $\Omega \to 0$, the damping coefficient is larger than 1, the value of this coefficient for infinite depth. Thus, in the low frequency limit which is relevant to tidal conversion, the damping coefficient is more important at small depth than at infinite depth. Theoretically, this is proved for a vertical flat plate by equation (2.17) and for a steep ridge by Llewellyn Smith and Young [92]: this has not been measured yet.

Finally, we measured the damping coefficient and the radiated wave power of an object with a specific cross section, inspired by Maas [96]. We show that it exhibits a lack of tidal conversion for a given frequency Ω_ℓ, as expected. This frequency depends on the height of the fluid and the results are consistent with the theoretical prediction. This can have some consequences in the ocean because it exists a large variety of such topography.

All these results have been obtained before the submission of this PhD manuscript or during the review process of this manuscript (for section 2.5). Nevertheless, more experiments would be welcome to fully investigate the added mass of objects oscillating in a stratified fluid and its applications with tidal conversion. For example, experiments on a vertical flat plate oscillating in a stratified fluid of finite depth seem relevant to perform, in order to verify the prediction of equation (2.17) in the low-frequency limit for a large range of depths. Moreover, for topographies lacking of tidal conversion, it is worthwhile to explore the extreme cases when H tends to infinity or to the height of the object. I expect to be able to perform these experiments before the PhD defense.

Chapter 3

Internal wave attractors: a geometric and linear construction



Internal wave rays converging towards an attractor in an experiment reported in this chapter.

Internal waves are very specific because their dispersion relation can lead to focusing or defocusing while the waves reflect on a slope. In natural cases, the slope can be typically the bottom topography of the oceans. In closed basins of several shapes [98] or on the topography of an ocean [65], the focusing of internal waves can form internal wave attractors. These attractors are periodic orbits where, due to the specificity of the geometry, the internal waves form closed loops.

Twenty years ago, Maas and Lam [98] studied for the first time internal wave attractors theoretically, using ray tracing in closed domains. Few years later, Maas *et al.* [97] obtained the first experimental attractor in a trapezoidal domain. Then, inertial wave attractors have been observed in numerical simulations [138] or in laboratory experiments [104], and also described theoretically [125]. Few years ago, several studies characterized precisely the geometry of internal wave attractors, using laboratory experiments [70, 69, 68], numerical simulations [64] or theory [86]. More recently, unstable attractors have been discussed using both experiments and numerical simulations [79, 139].

In the ocean, to our knowledge, no attractor has been measured yet [106]. Nevertheless, Guo and Holmes-Cerfon [65] have considered the probability to find an attractor with a typical topography of a two-dimensional ocean. The probability, about 10 attractors per 1000 km, is small but non negligible. Moreover, they may be responsible for the energy cascade from large to small scales in oceans. Thus, it worths to study the different properties of the internal wave attractors using idealized experiments, with a linearly stratified fluid in a trapezoidal domain. The main difference with the previous experiments performed on wave attractors [70, 69, 68, 104] is the generation of the waves by the wave-maker [115, 63], described in section 1.3.4. This allows us a very accurate control on the forcing and gives us the possibility to vary it while all the other parameters remain constant.

This Chapter describes the linear regime of internal wave attractors. First, a review is made on the internal wave ray tracing in a trapezoidal domain. The different possible

shapes of the attractor are discussed, depending on the geometry. Then, experimental internal wave attractors are exhibited. The remainder of the Chapter is focused on the simplest attractor, called $(1, 1)$ attractor, which has one reflection on each wall of the basin. The region of existence of the $(1, 1)$ attractors is explored and the different characteristics of the attractors are examined via the geometry. Different forcings are also explored, using the wave-maker. Finally, a comparison is made between attractors obtained in experiments and in numerical simulations.

3.1 An internal wave billiard

Internal wave ray tracing in different closed basin shapes has been essentially studied by Leo Maas over the last past twenty years. This can be viewed as an internal wave billiard [98]. The classical billiard studies the trajectories in a closed domain of a particle reflecting elastically and following the standard Descartes reflection. It can exhibit periodic motion, motion along an invariant curve or chaos [9]. For the internal wave billiard, the reflections are ruled by the geometric dispersion relation, conserving the angle of propagation with respect to the horizontal. This leads to attractive (focusing) or neutral trajectories, but not to chaotic motion.

In this section, I discuss internal wave ray tracing in a trapezoidal domain using the literature. I explain first that, depending on the geometry, rays can converge towards periodic orbits called attractors. One can draw a map of the attractors as a function of the geometry, as reported by Maas *et al.* [97]. Then, I focus particularly on the ray tracing for specific attractors, named $(1,1)$. Finally, I explain how to compute theoretically the stream function for this kind of attractors.

3.1.1 Ray tracing in a trapezoidal domain

As shown in Chapter 1 (see equation (1.38)), the linear inviscid 2D hyperbolic equation of propagation of internal waves is

$$\frac{\partial^2}{\partial t^2}\Delta\Psi + N^2(z)\frac{\partial^2\Psi}{\partial x^2} = 0, \tag{3.1}$$

where $N(z) = \sqrt{\dfrac{-g}{\rho_0}\dfrac{\partial\bar{\rho}}{\partial z}}$ and Ψ the stream function. For monochromatic waves of frequency ω_0, this gives

$$\left(1 - \frac{\omega_0^2}{N^2(z)}\right)\frac{\partial^2\psi}{\partial x^2} - \frac{\omega_0^2}{N^2(z)}\frac{\partial^2\psi}{\partial z^2} = 0, \tag{3.2}$$

by taking $\Psi(x,z,t) = \psi(x,z)\exp(i\omega_0 t)$. Here, if the buoyancy frequency N is constant, internal waves propagate at the angle $\theta = \arcsin(\omega_0/N)$ with respect to the horizontal.

One considers here the propagation of internal waves in a trapezoidal basin, defined by figure 3.1(a). This basin has a height H, a length at the bottom L and a slope on the right side with an angle α with respect to the vertical. To study easily the propagation of internal waves in such a basin, one can do the change of variables

$$x' = \frac{2x}{L} - 1, \tag{3.3}$$

$$z' = \frac{2z}{L}\sqrt{\frac{N^2}{\omega_0^2} - 1}. \tag{3.4}$$

This leads equation (3.2) to

$$\frac{\partial^2\psi}{\partial x'^2} - \frac{\partial^2\psi}{\partial z'^2} = 0. \tag{3.5}$$

Time is removed from this hyperbolic wave-equation, it has spatial coordinates only. The change of variables rescales the geometry of the trapezoidal basin as shown in figure 3.1(b). The rescaled height of the basin is defined as $\tau = \dfrac{2H}{L}\sqrt{\dfrac{N^2}{\omega_0^2} - 1}$ and x' is in

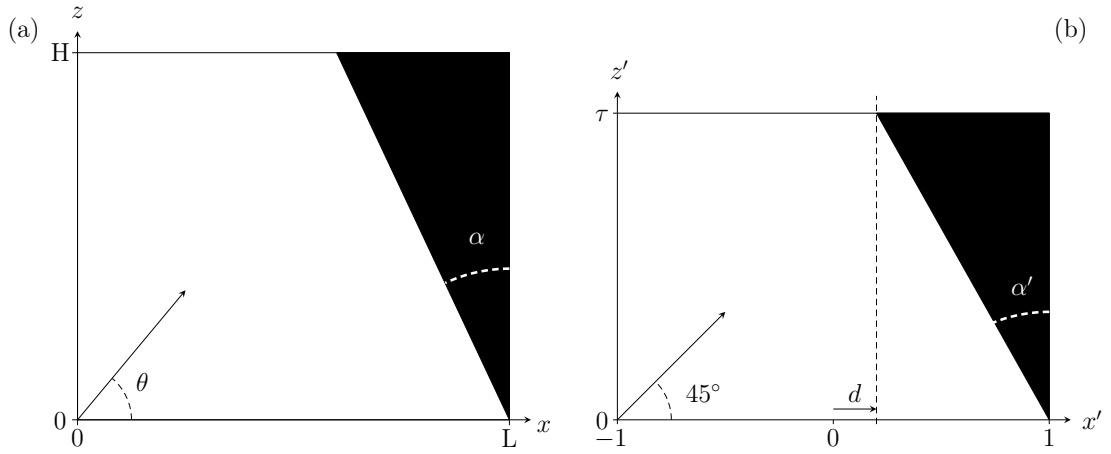


Figure 3.1: (a): Drawing of the trapezoidal basin with the different geometrical characteristics. Here, $H/L = 0.85$ and $\alpha = 25.2°$. One internal wave ray, starting from the bottom left corner, is propagating upward at an angle $\theta = 50.2°$ here. (b): Rescaled trapezoidal basin using equations (3.3) and (3.4). Here, $d = 0.2$ and $\tau = 1.41$. The ray, starting from the left bottom corner, is propagating upward at an angle of 45°.

the range $[-1; 1]$. One can define d as the x-coordinate of the upper corner of the slope, as shown in figure 3.1(b). With such a definition, $d = 1 - \frac{2H}{L} \tan\alpha$. The angle α is transformed in α' by $\tan\alpha' = \tan\alpha \tan\theta$. After this rescaling, internal waves propagate at 45° with respect to the horizontal. It worths to note that the origin is defined in the middle of the bottom of the basin for the rescaled geometry while the origin is in the bottom left corner of the basin for the real geometry. In previous works [97, 70, 64, 86], the geometry used was also a trapezoid but the slope was located differently. Nevertheless, a simple symmetry with respect to the horizontal line located at $z = H/2$ transforms our geometry into the geometry used in [97, 70, 64, 86]. The change of variables, given by equations (3.3) and (3.4), and the (d, τ) diagram presented in the next section are not affected by this slight difference, due to the symmetry.

It is much easier to perform ray tracing in the rescaled geometry because the rays are always propagating at an angle of 45°, with respect to the horizontal. Changing ω_0 or θ in the real space is equivalent to change τ in the rescaled geometry. However, one rescaled geometry can be obtained from an infinite number of different geometries. For example, the d and τ parameters are invariant through dilation or compression of both horizontal and vertical axes of the geometry in real space. Geometries with very different aspect ratios could also have the same dimensionless parameters d and τ by tuning the angles α and θ.

Defining $\xi' = x' + z'$ and $\eta' = x' - z'$, equation (3.5) becomes

$$\frac{\partial^2 \psi}{\partial \eta' \partial \xi'} = 0. \tag{3.6}$$

This leads to the solution

$$\psi(x', z') = f_-(x' - z') + f_+(x' + z'). \tag{3.7}$$

As rays propagate with an angle of 45°, the quantities $x' - z'$ and $x' + z'$ are constant along rays. Thus the values of $f_\pm$ are transported by the rays [102, 103]. The boundaries of the

basin are assumed to be rigid and there is no fluid penetration through them. This implies that boundary conditions are $\psi = 0$ except on the vertical left wall where forcing can be applied. This connects the two functions f_- and f_+. At the bottom, $z' = 0$ and thus $f_-(x') = -f_+(x')$. Consequently, $\psi(x', z') = f(x' - z') - f(x' + z')$. The other boundary conditions on the surface and on the slope are less obvious to use.

Magaard [102, 103] and Maas [98, 97] computed the stream function in any point of different basin shapes using f-value propagation along rays. This method is presented in section 3.1.4 to obtain the theoretical stream function into a trapezoid, with the geometry defined above and with the same forcing as in the experiments described below in this manuscript.

3.1.2 The (d, τ) diagram

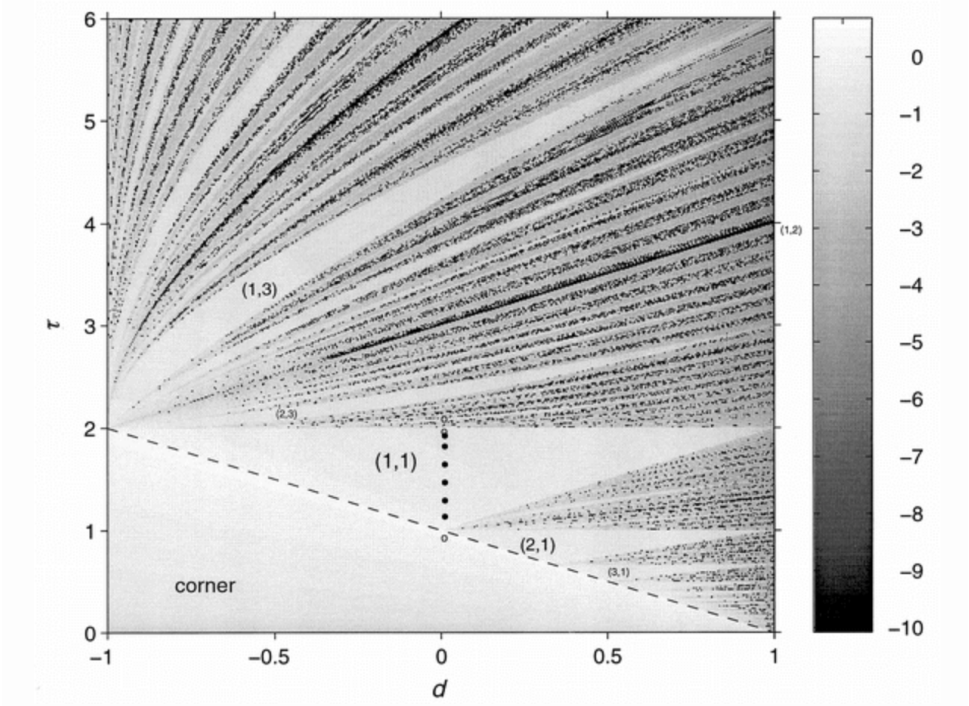


Figure 3.2: (d, τ) diagram extracted from [97]. The greyscale shows $\log_{10}(-\Lambda)$, where Λ is the Lyapunov exponent of the trajectories. The white regions are regions where Λ is very negative, so attractive regions. The darker regions are regions where Λ is too close to 0 and no pattern emerge from the ray tracing. The black dots located at $d = 0$ and between $\tau = 1$ and $\tau = 2$ correspond to the different experiments performed in [97]. The names of the different attractive regions $(1, 1)$, $(2, 3)$, $(2, 1)$, etc... are explained in the text.

In a trapezoidal domain, Maas *et al.* [97] used the dimensionless parameters d and τ to build a map of the different patterns that can be obtained when internal wave rays propagate in the basin. In the remainder of the manuscript, this map is named as the (d, τ) diagram. This diagram is shown in figure 3.2. The greyscale represents $\log_{10}(-\Lambda)$, where Λ is the Lyapunov exponent of the wave rays. Λ is defined in [98] and measures the rate of convergence or divergence of the rays propagating in the trapezoidal domain. Maas *et al.* [98, 97] have shown that this Lyapunov exponent is generally negative or null but never positive. Thus, almost all wave rays converge. There is no chaos here, in opposition

to a classical billiard with Descartes reflections [9]. White regions in figure 3.2 are regions where $|\Lambda|$ is relatively large: these regions are attractor regions and mathematically, they correspond to Arnold tongues. Any wave ray starting from any point in the basin converges toward a limit cycle, called attractor. This attractor is the same for all the rays and there is only one type of attractor per region. Only one ray is periodic, the one following the attractor. Note that this ray has at least one focusing reflection on the slope during this orbit. Then, the darker the regions in figure 3.2, the smaller $|\Lambda|$. Thus, in the darker regions, no pattern emerge from the ray tracing, $|\Lambda|$ being too small to obtain a simple pattern after a few number of reflections.

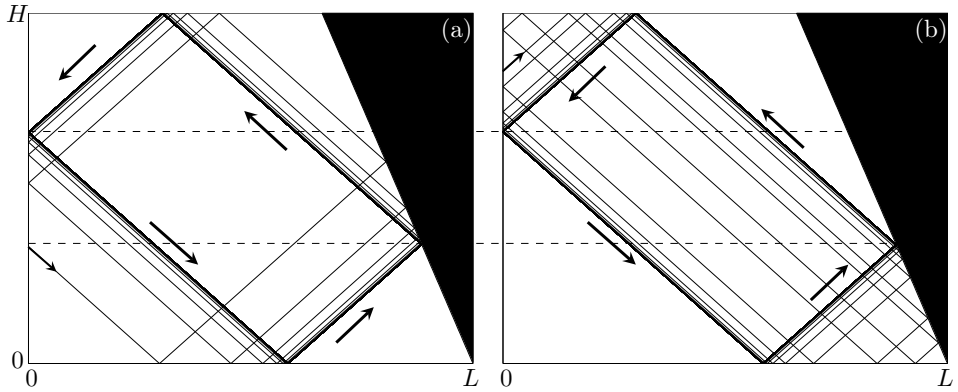


Figure 3.3: Convergence towards the same $(1,1)$ attractor of two rays starting from two different points in the same geometry. Here, $H/L = 2/3$, $\alpha = 27°$ and $\theta = 37°$. Thus, $(d,\tau) = (0.32, 1.77)$. The small arrows indicate the two positions where the rays start, while the large arrows show the direction of propagation of the periodic ray on the attractor. The two horizontal dashed lines shows that the two attractors reached are exactly identical.

The different regions where attractors exist are labelled using two indices m and n: (m,n). m describes the number of reflections at the surface (or at the bottom) and n the number of reflections on the vertical side wall (or on the slope). For example, in the largest white region named $(1,1)$, attractors have only one reflection on the surface and on the vertical wall. In fact, they have one reflection on each side of the basin. An example of $(1,1)$ attractors is shown in figure 3.3. The reflection on the slope is focusing (see section 1.1.4), as the periodic ray on the attractor propagates anti-clockwise. Figure 3.4 shows two examples of attractors from different white regions, the $(2,1)$ (a) and the $(1,3)$ (b) ones. The $(2,1)$ attractor has only one reflection on the slope, which is focusing. The $(1,3)$ attractor has three reflections on the slope, two which are focusing and one which is defocusing. The attractors always exhibit an odd number of reflections on the slope (n), in order to have always more focusing reflections than defocusing ones. As the (d,τ) parameters are displaced in attractor regions, the position of the attractor in the basin changes but it keeps the same number of reflections on each side. The region below the dashed line at the bottom of the (d,τ) diagram and named "corner" presents point attractors. All the wave rays end in the bottom right corner of the basin, trapped by the reflection law for internal waves. This is shown in figure 3.4(c). The ray tracing from a darker region is shown in figure 3.4(d). No specific pattern emerge here, the Lyapunov exponent being very small in absolute value.

There are also lines on the diagram where there is global resonance, or seiche modes. For these geometric configurations, there is no attractor. All rays are periodic but there

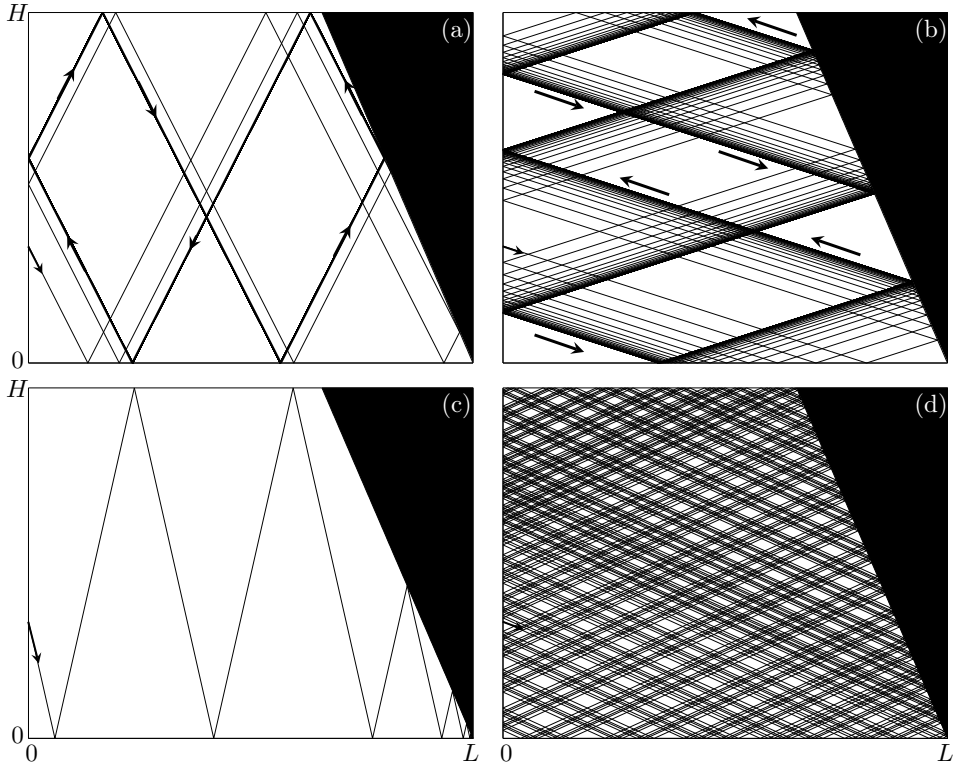


Figure 3.4: Convergence towards different attractors: $(2,1)$ attractor (a), $(1,3)$ attractor (b), point attractor (c) and no attractor (d). As in figure 3.3, $H/L = 2/3$ and $\alpha = 27°$ so $d = 0.32$. θ (respectively τ) is equal to 58° (resp. 0.83) (a), 15.2° (resp. 4.91) (b), 75° (resp. 0.36) (c) and 21° (resp. 3.47) (d). The small arrows indicate the positions where the ray starts while the large arrows show the direction of propagation of the wave rays on the attractor. Note that for cases (a) and (b), the number of reflections on the slope is odd.

is no convergence at all: the Lyapunov exponent is strictly equal to zero. For these global resonances, all the rays have an even number of reflection on the slope (n). Thus, there is always the same number of focusing and defocusing reflections. One of these lines is identified on the (d,τ) diagram in figure 3.2 by $(1,2)$. Such a seiche is also plotted in figure 3.5. Each ray has two reflections on the slope, one which is focusing and one which is defocusing. The examples of rays are shown, as solid and dashed thick lines in figure 3.5. The seiche modes appear when both the bottom corners are connected to the top ones by rays. This is illustrated by the red and blue rays in figure 3.5.

The skeleton of the (d,τ) diagram is composed of lines delimiting the different attractor regions. It is possible to calculate this skeleton by considering the geometries where rays connect different corners of the basin. These geometries do not give seiche modes because in these geometries, only one top corner is connected to one bottom corner. For a seiche mode, both top corners are connected to both bottom ones. For example, the line $\tau = 2$ in the diagram represents all the geometries where the ray emitted from the bottom right corner connects directly the top left one. This line delimits the top of the $(1,1)$ region. Thus, $(1,1)$ attractors with τ close but smaller than 2 are located in the diagonal formed between the right bottom and left top corners. The line $\tau = d + 1$ on the (d,τ) diagram represents geometries where the top right corner is connected to the bottom left one. This

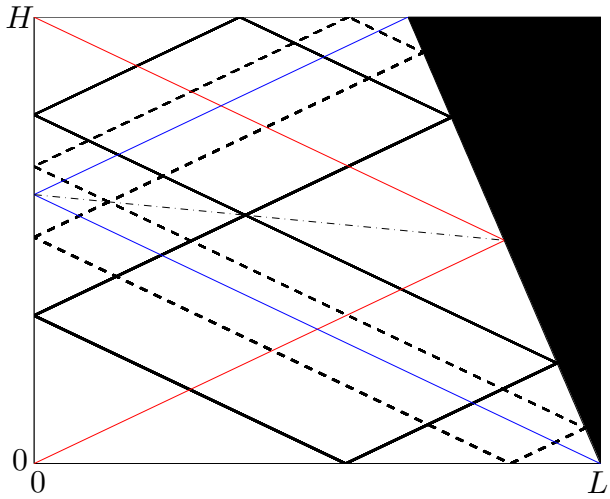


Figure 3.5: Example of a seiche or a global resonance $(1, 2)$, where each ray is periodic. Here, $H/L = 2/3$, $\alpha = 27°$ and $\theta = 21.88°$. Thus $(d, \tau) = (0.32, 3.32)$. Two examples of rays are shown with the dashed and solid black lines. The red and the blue solid lines are rays connecting the different corners of the basin. The dashed dotted black line connects the reflection of the red line on the slope and the reflection of the blue line on the vertical wall. All the wave rays cross themselves along this line. Note that the number of reflections on the slope is 2, which is an even number.

line is the line below the $(1, 1)$ region for positive d. Thus, $(1, 1)$ attractors with τ close but larger than $d + 1$ are located in the diagonal formed by the bottom left and top right corners. Consequently, travelling at constant d in the (d, τ) diagram through the $(1, 1)$ region changes the pattern of the $(1, 1)$ attractors, from one diagonal to the other. This is illustrated in section 3.2.1. Last example for skeleton lines: the dashed line above the corner region is the line where the slope is critical. Thus one ray connects the top left and bottom right corners, after a reflection on the slope. This can be done for all the attractor regions, by looking for corner connections after a different number of lateral reflections.

My work during this PhD is mainly focused on $(1, 1)$ attractors, from their linear behavior to their non-linear dynamics. The next section addresses the different geometrical properties of $(1, 1)$ attractors, giving more details about the specificity of ray tracing in the $(1, 1)$ attractor Arnold tongue.

3.1.3 Ray tracing for the $(1, 1)$ attractor

In this section, the main results of [97, 86] are recalled to describe more precisely the behavior of the wave rays in the $(1, 1)$ region. By simplicity, we consider a given rescaled geometry, with $(d, \tau) = (0.32, 1.77)$. As mentioned before, in a rescaled basin, the rays propagate at an angle of 45°. All definitions presented in this section are valid for any geometry of the $(1, 1)$ attractor region.

The left vertical wall is divided into different fundamental intervals. These intervals are set by the series of reflections on the left vertical wall of the two rays emitted from the top and bottom right corners. Figure 3.6 shows how these fundamental intervals are defined. In figure 3.6(a), the first reflection on the left vertical wall of the ray emitted from the top right corner defines the bottom primary fundamental interval. It is represented by a black rectangle and lies between 0 and the altitude of the first reflection. Then, when the

ray reaches the left vertical wall a second time, it defines the first secondary fundamental interval, drawn as a gray rectangle in figure 3.6(a). It lies between the first and the second reflections of the ray on the vertical wall. The ray converges towards the attractor, so the altitude of its reflections on the vertical wall is higher and higher, converging also towards the altitude of the reflection of the attractor itself on the vertical wall. This defines other secondary fundamental intervals (second, third, ...) which are smaller and smaller but closer and closer to the attractor reflection on the vertical wall. Thus, the number of fundamental intervals is infinite. The four first fundamental secondary intervals are represented by lighter and lighter gray rectangles, in figure 3.6(a). The ray emitted from the top right corner thus defines the bottom (primary and secondary) fundamental intervals. The top (primary and secondary) fundamental intervals are defined by the ray starting from the bottom right corner, as shown in figure 3.6(b). The process is very similar except that the reflections of this ray converge towards the reflection of the attractor from the top to the bottom. The five first intervals are shown as black and gray rectangles in figure 3.6(b).

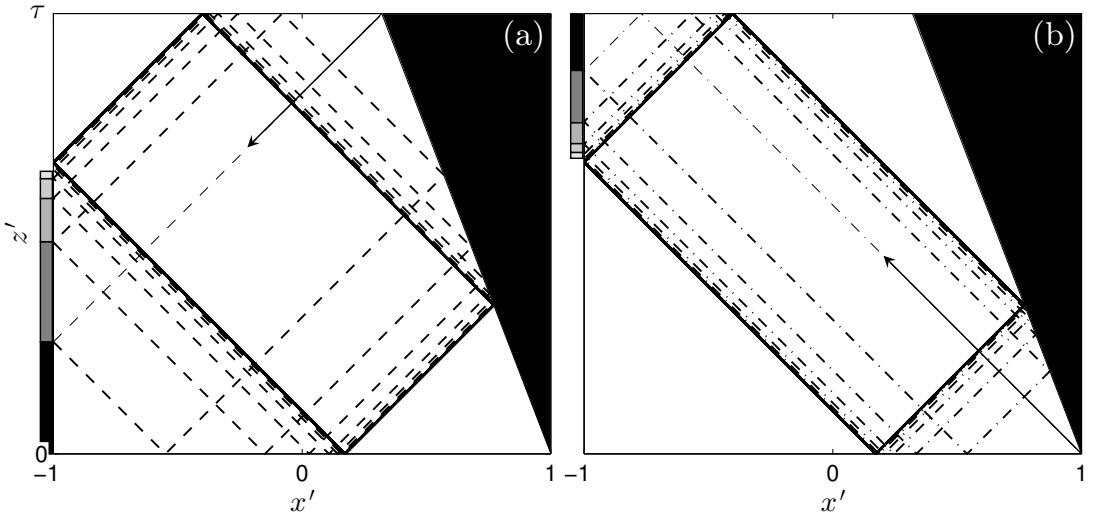


Figure 3.6: Definition of the primary (black rectangles) and secondary (rectangles with shades of grey) fundamental intervals, on the vertical left wall. The solid line shows the attractor corresponding to this geometry. (a): the dashed line is the wave ray emitted from the top right corner. It defines the bottom fundamental intervals. (b): the dashed-dotted line is the wave ray emitted from the bottom right corner. It defines the top fundamental intervals.

These intervals are very important for the geometry of the attractor. As shown in figure 3.7, any point in the basin can be reached by one ray starting from one of the two primary fundamental intervals. The attractor divides the trapezoidal basin into five regions. There is a central region, surrounded by the attractor and there is also four triangles in the four corners of the basin, delimited by the walls of the basin and by the attractor. Rays emitted by the bottom primary fundamental interval propagate only in the central region and in the two top right and bottom left triangles. By symmetry, rays emitted by the top primary fundamental interval propagate only in the central region and in the two top left and bottom right triangles. This is summarized in figure 3.7. Rays starting from the primary fundamental intervals reach all the secondary fundamental

intervals converging towards the attractor. One secondary fundamental interval is simply connected with its neighbors (previous and next secondary fundamental intervals) by rays doing one tour of the basin, with one reflection on each side. As a consequence, any point in the basin which is inside the attractor is traversed by two rays coming from the two different primary fundamental intervals. For a basin point located outside of the attractor, the two rays passing through this point are emitted by the same (top or bottom) primary fundamental interval.

From these considerations, one can now imagine the trajectory of any ray starting propagating upward or downward from any z-coordinate of the vertical left wall. We can consider only the bottom fundamental intervals, located between 0 and the z-coordinate of the attractor reflection on the vertical wall, because the case for the top fundamental interval is similar by symmetry. If the ray starts propagating upward or downward from the bottom primary fundamental interval, it will reach all the secondary fundamental intervals as it converges towards the attractor. If the ray starts propagating downward from one of the secondary fundamental intervals, it will go to the next secondary fundamental interval and converge towards the attractor. If the ray starts propagating upward, it will reach all the previous secondary fundamental intervals until it hits the primary fundamental interval. After that, it behaves like rays emitted from this interval and reaches all the other secondary fundamental intervals converging towards the attractor.

One can use the word "web" to define one ray trajectory. The webs are infinite and converge towards the attractor. It worths to note that the webs are spatial structures ruled by the equation (3.5). Thus, time does not appear directly and, despite the vocabulary used to describe the trajectories, the way the ray tracing is done should not be considered as a process evolving in time.

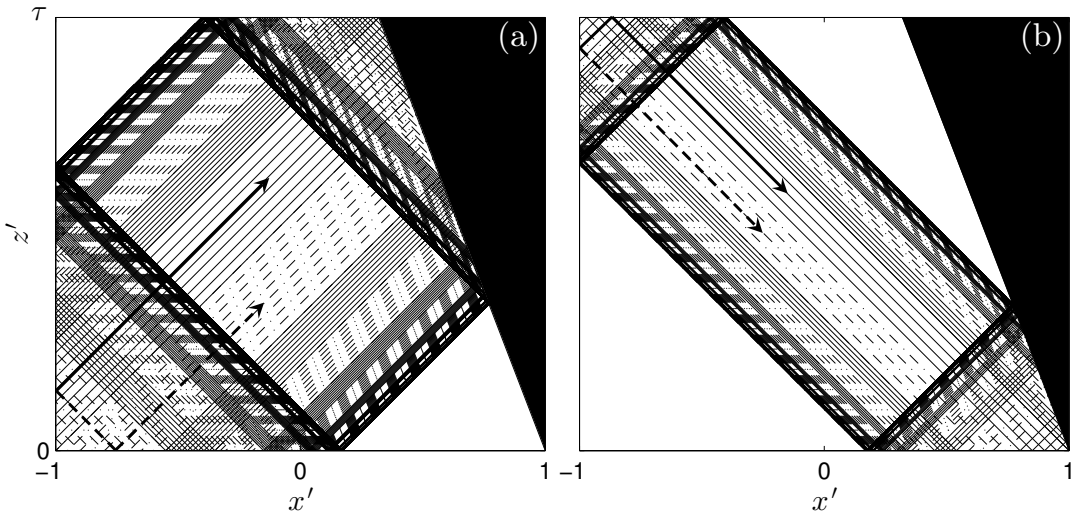


Figure 3.7: Ray propagation from the bottom (a) and the top (b) primary fundamental intervals. Ray starting propagating upward are in solid lines, ray starting propagating downward are in dashed-dotted lines.

3.1.4 Theoretical stream function fields

Following [98, 97, 86] and section 3.1.1, one can find the theoretical stream function $\Psi(x', z', t') = \psi(x', z')\exp(it')$ for our geometry and the forcing applied by the wave-

maker. Here, t' is the dimensionless time defined as $t' = \omega_0 t$. ψ is given by $\psi(x', z') = f(x' - z') - f(x' + z')$, where f is prescribed by the forcing. The stream functions obtained in this section are computed with a geometry at $(d, \tau) = (0.32, 1.77)$, as in previous section. Nevertheless, the stream functions can be computed for any geometry located in the $(1, 1)$ region on the (d, τ) diagram.

To determine the theoretical stream function ψ in any point of the trapezoidal basin, one considers that the function f is first prescribed arbitrarily only on the two primary fundamental intervals, on the left vertical wall of the basin. These intervals are delimited by the two horizontal dashed lines on the left of figure 3.8 and the prescribed f function is in bold. Then, the f-values are propagated by the rays towards the secondary fundamental intervals, fixing f-values on all the left vertical wall. Finally, it is possible to compute the theoretical stream function at any point in the basin: one simply has to make the difference between the f-values carried by the two rays that go through this point [102, 103]. An example of solution is represented in figure 3.8, where the stream function $\psi(x', z')$ is computed for each point in the basin. This stream function has real values only, because the f-values are real. Thus, $\Psi(x', z', t') = \mathrm{Re}\left(\psi(x', z')\exp(it')\right)$ is only a standing pattern, which is "blinking". Maas *et al.* [98, 97] introduced this "blinking" term because there is no time propagation along rays. As experiments shown in [97] and in this manuscript exhibit that the waves in the basin propagate, this "blinking" stream function is not consistent with the observations.

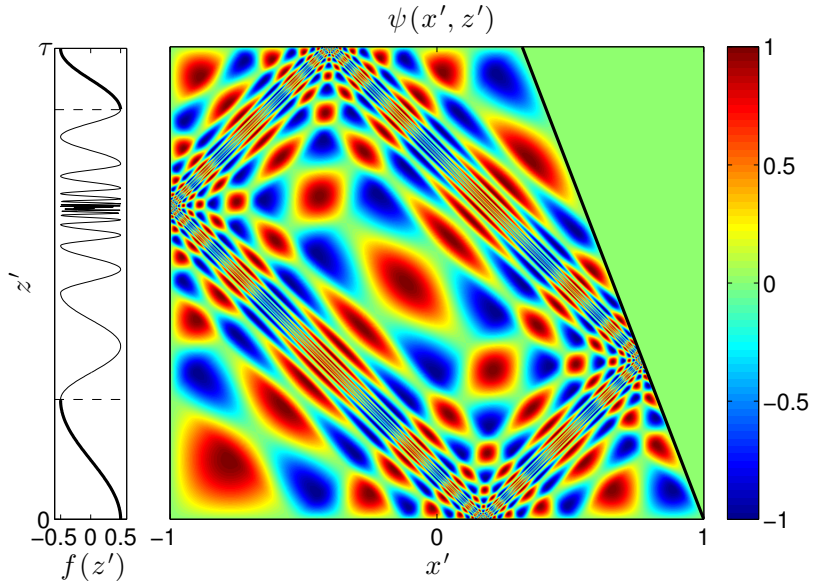


Figure 3.8: Stream function $\psi(x', z')$ in a trapezoidal basin computed using one arbitrary function f prescribed on the two primary fundamental intervals. On the left, the function f is shown on all the z-axis. The two horizontal dashed lines show the limit of the top and bottom primary fundamental intervals. The prescribed f function is in bold on the left.

Moreover, in the experiments, the wave-maker prescribes a boundary condition for $\psi(x', z')$, on the vertical left wall. This imposes the f function for each fundamental interval and leads to an other issue. Indeed, if f is constant along rays, as rays connect the different fundamental intervals, f would be multi-valued.

Lam *et al.* [86] revisits both these problems of standing "blinking" wave and forcing.

These two problems are treated separately and the solutions are then combined. First, let consider the "blinking" problem. In order to get propagative waves, f should be complex. Indeed, one can decompose the prescribed stream function of the primary fundamental intervals into Fourier modes. For example,

$$\cos(z') = \frac{1}{2}\exp(iz') + \frac{1}{2}\exp(-iz') = f_U(z') + f_D(z'). \tag{3.8}$$

Thus, this splits the rays in two categories: rays which start propagating upward and rays which start propagating downward from these intervals. The complex f value associated to these different rays are different and named f_U (upward) and f_D (downward). This leads to two semi-infinite webs with constant f_U or f_D instead of one infinite web of constant f. In order to compute the stream function ψ in the bulk of the basin, some bookkeeping is needed to know if the rays going through this point were upward or downward rays when they start from the primary fundamental intervals. After that, a complex stream function value is computed to each point, by doing the difference between the f values of the two rays going through this point, as before. In order to get a time evolution, one needs to

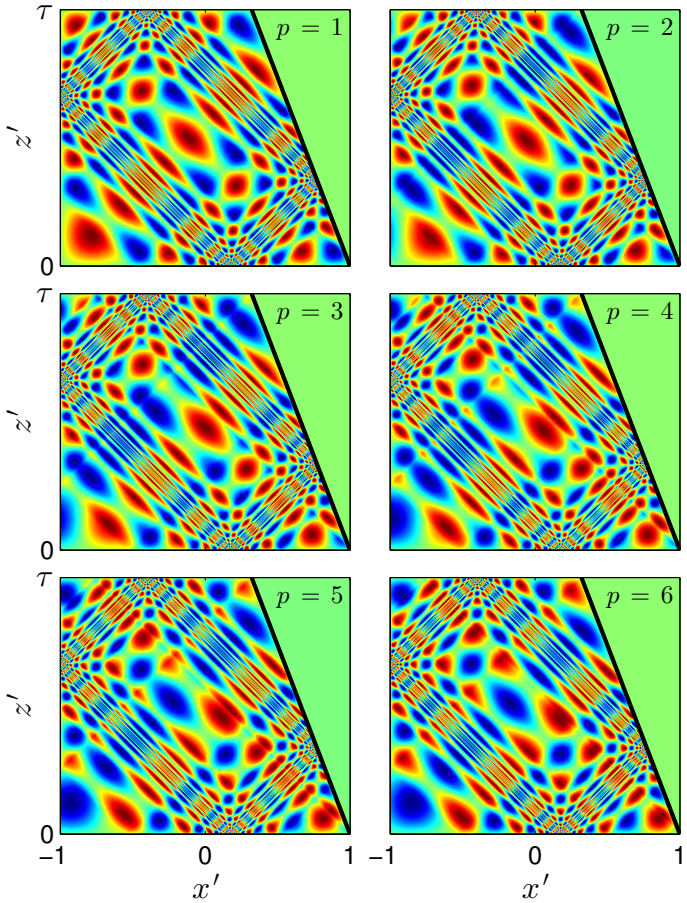


Figure 3.9: Example of stream function fields $\Psi(x', z', t')$ of an attractor with one arbitrary function prescribed on the two primary fundamental intervals, at different times during the period. The indices p indicate the different dimensionless times: $t' = 2(p-1)\pi/12$. The colorbar is the same as the one in figure 3.8 and the $p = 1$ image is the same than the one in figure 3.8.

evaluate $\Psi(x', z', t') = \mathrm{Re}\left(\psi(x', z')\exp(it')\right)$, where t' is the dimensionless time. This gives the series of images, in figure 3.9. One can see a propagation of the waves emitted from the two primary fundamental intervals. The image at the top left corner, with $p = 1$, is similar to the one in figure 3.8.

Now, once the "blinking" problem has been solved, one considers the forcing problem. In the experiments, the forcing is made on all the height of the tank. In order to mimic the forcing of the wave-maker, Lam *et al.* [86] suggests to superpose partial solutions from the different fundamental intervals. It is possible to superpose all the solutions because the stream functions are solution of a linear problem. The two primary fundamental intervals supply the two first solutions, ψ_1 and ψ_{-1}. Then the two first secondary fundamental intervals supply the stream functions ψ_2 and ψ_{-2} and so on. Thus, the two n-th secondary fundamental intervals supply the stream functions ψ_{n+1} and $\psi_{-(n+1)}$. The total stream function is

$$\psi = \sum_{n=1}^{\infty}(\psi_n + \psi_{-n}). \tag{3.9}$$

This assumes that for each contribution ψ_n, the external forcing is applied once and then it is reflected on all the sides of the basin. This means that the boundary condition $\psi(x' = -1, z')$ is imposed on the left vertical wall but that the reflection nature of this left vertical wall stays the same. This is fully possible in the experiments because the amplitude of the wave maker is very small, few millimeters, in comparison to the size of the tank. Thus, the reflection properties are not altered by the slight changes of shape.

To compute the stream function in any point (x', z') of the basin, one still has to consider the two rays going through that point. For an easier computation, Lam *et al.* [86] redefines the stream functions ψ_n as follows. ψ_1 is defined as the forcing on the first left wall reflections of the two leftward rays that pass to the point (x', z'). ψ_{-1} is defined as the forcing on the first left wall reflections of the two rightward rays that pass to the point (x', z'), after reflections on the surface, on the bottom or on the slope. Then following these different rays, one can define the other stream functions ψ_n using the n-th reflections on these rays on the left vertical wall. When n becomes large, the rays are close the attractor. Thus the forcing is very close for the two rays and the difference vanishes. So this method converges. ψ is obtained by adding all these contributions, and it is bounded.

It is possible to implement this method for a forcing with real f-values. A "blinking" attractor is found, but with a forcing on all the height of the fluid. Nevertheless, it is also possible to apply this method for the propagating case, where the forcing is splitted into two complex parts, propagating upward and downward. Thus, some bookkeeping is also needed following the rays passing through the point (x', z') and their reflections on the left vertical wall. Using this method, one obtains the series of images presented in figure 3.10. The propagation is very visible and the stream function field is smooth, except on the attractor.

In section 3.5.1, a comparison between the theoretical stream function fields obtained here and the experimental ones is made. To obtain the theoretical stream function fields, the inviscid equation of propagation of internal waves has been used. In the experiments, the viscosity is always present and plays a role, modifying the patterns of the attractors and the stream function fields. Moreover, the focusing present in the attractors can lead to non-linear effects when too much energy is focused into the attractor. These non-linearities are discussed in Chapters 4 and 5.

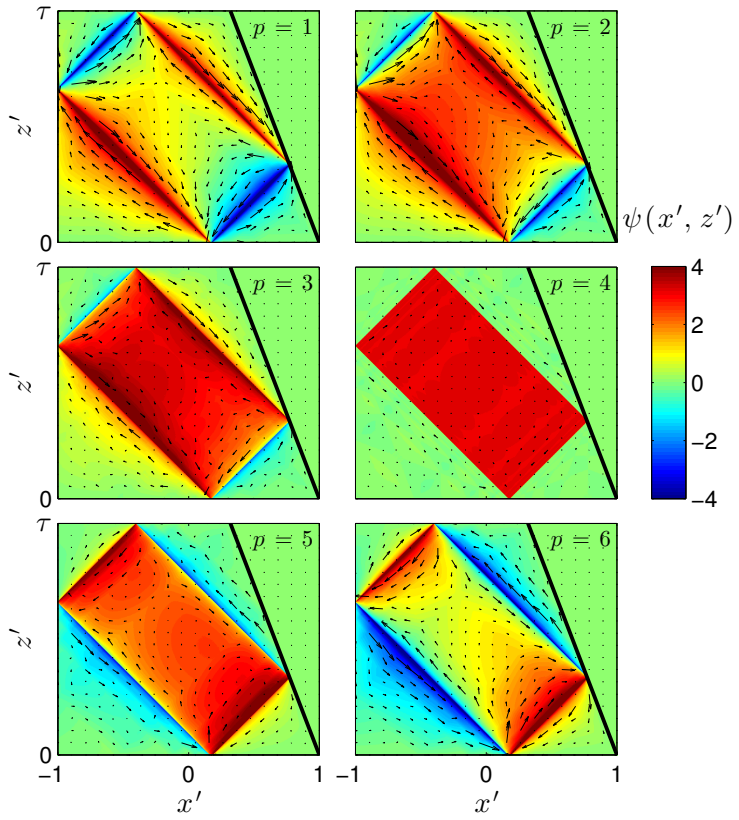


Figure 3.10: Example of stream function fields $\Psi(x', z', t')$ of an attractor with dimensionless mode 1 forcing on all the height of the basin, at different times during the period. The indices p indicate the different dimensionless times: $t' = 2(p-1)\pi/12$. Arrows indicates the velocity fields computed from the stream function. They all have the same dimensionless scale.

3.2 Exploring the (d, τ) diagram experimentally

The first experimental attractor has been obtained in [97], in a $(1, 1)$ configuration. Then, several articles [70, 69, 68, 139] have reported on experimental internal wave attractors. Manders and Maas [104] have also observed attractors in a trapezoidal basin but in the case of inertial waves. Most of these articles, except [139], studied stable attractors. In this Chapter, we consider only stable attractors. Instabilities in internal wave attractors are presented in Chapters 4 and 5.

To illustrate the large variety of patterns that are accessible with the attractors, experiments have been performed through the (d, τ) diagram. This diagram has been explored using two different ways. First, the diagram is explored with experiments at constant d. This means that the geometrical parameters setting d are fixed and only the frequency of the waves, ω_0, and consequently τ, is changed. Different regions in the (d, τ) diagram can be investigated and the different patterns observed are presented in section 3.2.1. Then, the (d, τ) diagram is explored in the $(1, 1)$ Arnold tongue. First, a typical experimental $(1, 1)$ attractor is shown and described in section 3.2.2. Then, experiments carried on to scan a large part of the $(1, 1)$ region are reported in section 3.2.3. This has been done by changing both the geometry, the d parameter, and the frequency of the waves, the τ

parameter.

Experiments presented in sections 3.2.1 and 3.2.3 have been performed in partnership with Grimaud Pillet, who started his PhD in September 2015.

3.2.1 With constant d

In this section, experiments have been performed with a fixed geometry, in the large tank. The visualization technique is the SyS. For these experiments, $H = 92$ cm, $L = 155$ cm and $\alpha = 22.2°$. Thus, $d = 0.52$. The τ parameter has been varied from 0.21 to 5.49, in order to visit the different regions of the (d, τ) diagram. As one can see in figure 3.2, regions which are accessible are, from small to large τ:

- the corner or point attractor region
- the $(2, 1)$ region
- the $(1, 1)$ region
- the $(1, 3)$ region
- other very small regions like $(3, 1)$ or $(2, 3)$
- all black and grey regions in between the attractor regions.

One has to pay attention that this diagram is made using the (d, τ) parameters. Experimentally, once the geometry is set, d is fixed. The only mean to change τ is by changing ω_0. Nevertheless, the relation between τ and ω_0 (or $\theta = \arcsin(\omega_0/N)$) is nonlinear. This means that attractor regions that appears large in terms of τ could be narrow in term of frequency (or angle θ), which is the parameter we set for the experiments. If one has to rescale the (d, τ) diagram in terms of (d, ω_0) diagram, the top (high τ) would be compressed and the bottom (low τ) would be stretched. Thus, for $d = 0.5$, the $(1, 3)$ and $(2, 3)$ are in reality thiner to our experimental control parameter than they appear on the (d, τ) diagram. Moreover, the aspect ratio of the tank is also important. For example, $(1, 3)$ attractors can be seen more easily with H much greater than L in order to distinguish clearly the three reflections on the side and $(2, 1)$ attractors are better to visualize in a tank whose L is much greater than H. Nevertheless, changing the aspect ratio leads to changing the d parameter.

In addition to that, there is some experimental uncertainty on the value of τ. Indeed, τ depends on the geometry and on the frequency of the waves. These parameters can be slightly modified for example if the stratification is not perfectly linear or if there is a mixed layer on the top of the stratification. This changes locally the ray trajectories and shifts the value of τ. Thus, this increases the experimental challenges to visualize attractors located in very small regions on the (d, τ) diagram. For example, we were unable to visualize attractors located in the $(3, 1)$, $(2, 3)$ and $(1, 3)$ regions. Indeed, with the geometrical parameters used for the experiments presented in this section, the width of the range of frequencies covering the $(3, 1)$ attractor region is 0.03 rad/s. This width is 0.006 rad/s for the $(1, 3)$ attractors while it is 0.1 rad/s for the $(1, 1)$ attractors and 0.06 rad/s for the $(2, 1)$ attractors.

Figure 3.11 shows different attractors belonging to the $(1, 1)$ region, after filtering in frequency to get the amplitude of the waves. All have the same $d = 0.5$ but τ varies from 1.62 in panel (a) to 1.98 panel (f), changing the ray tracing prediction, plotted as a dashed black line on each panel. One can see clearly that the energy is focused along

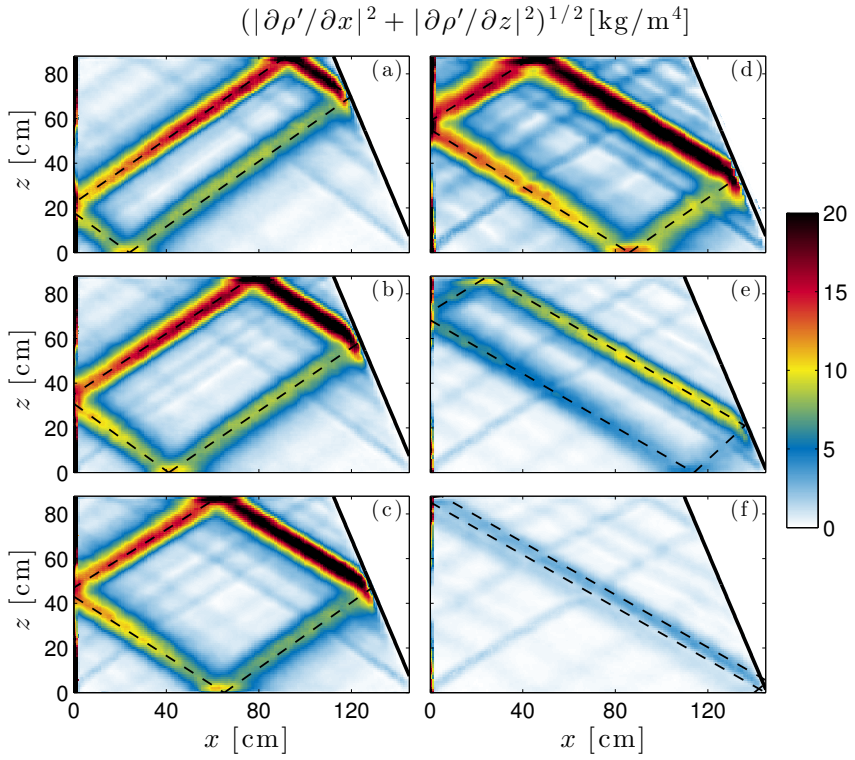


Figure 3.11: Amplitude of the density gradient fields of different $(1, 1)$ attractors, after Hilbert filtering in frequency. They have the same d parameter but different τ parameter. τ is increasing with the order of the letters designing the panels and is equal to 1.62(a), 1.70(b), 1.76(c), 1.83(d), 1.90(e) and 1.98(f). d is equal to 0.5. The ray tracing predictions are indicated by the dashed black lines.

the ray tracing prediction, showing that all rays converge towards the attractor. Contrary to the ray tracing prediction, the attractor has a given thickness, due to viscosity. The direction of propagation appears here to be clearly anti-clockwise. Indeed, one can see that the amplitude of the density gradient fields decreases as one follows the ray tracing prediction in the anti-clockwise way. This is also due to viscosity, which damps the waves during their propagation. The colorbar, which is the same for all the panels, shows that the amplitude decays as attractors are close to the boundaries of the $(1, 1)$ region, so in one of the diagonals of the basin.

Figures 3.12 shows attractors belonging to the $(2, 1)$ region, with the same d but different τ. The images have been filtered in frequency to get the amplitude of the waves. Here also, almost all the energy injected converges towards the attractor. It is also possible to guess the direction of propagation of the waves, paying attention to the decrease of the amplitude. This is consistent with the ray tracing prediction because the $(2, 1)$ attractors exhibit one focusing reflection on the slope.

Figure 3.13 shows snapshots of the horizontal density gradient fields for a point attractor. Panel (a) has been filtered in frequency and in space, to keep only the waves propagating from left to right ($k_x > 0$), while panel (b) has also been filtered in frequency and in space, but to keep only the waves propagating from right to left ($k_x < 0$). In that geometrical configuration, the waves are supposed to be focused into the corner of the slope, at the bottom of the tank. It is here difficult to see what happens in this part of

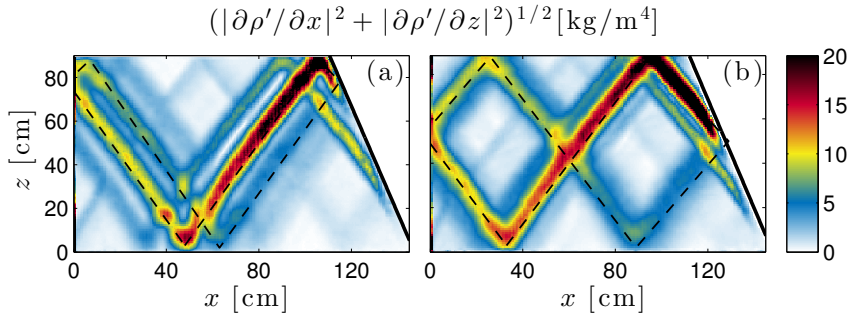


Figure 3.12: Amplitude of the density gradient fields of two $(2, 1)$ attractors, after Hilbert filtering. Both have the same d parameter, equal to 0.5. For panel (a), $\tau = 0.86$ while for panel (b), $\tau = 0.93$. The ray tracing predictions are indicated by the dashed black lines.

the tank but one can clearly see that there is no wave propagating from right to left. This demonstrates that all waves are trapped by the slope, in the corner, at the point attractor. Note that the mode 1 shown in figure 3.13(a) is not perfect. This could be due to the stratification, which is slightly nonlinear at the bottom. Thus, the buoyancy frequency could be slightly smaller and, as the frequency of the waves is close to this frequency, the waves are reflected before reaching the bottom of the tank.

For the experiments located in the black or grey regions in the (d, τ) diagram, no specific pattern is supposed to emerge. The images obtained using SyS give only a signal which is close to noise. Motions should be present in the tank but they are probably disorganized motions, meaning that no specific path is created. The SyS is here unable to see the motions in the fluid because it is more sensitive to patterns with a short wave length. If no attractor is created, there is no pattern with a small wave length and thus, this is invisible to SyS visualization. One should perform experiments in PIV in order to see all the motions in the tank, even if they are disorganized.

$(1, 1)$, $(2, 1)$ and point attractors have been observed exploring the (d, τ) diagram at a constant d. Qualitatively, these attractors exhibit the characteristics predicted by the ray tracing, described in section 3.1. Indeed, all the energy injected by the wave-maker is

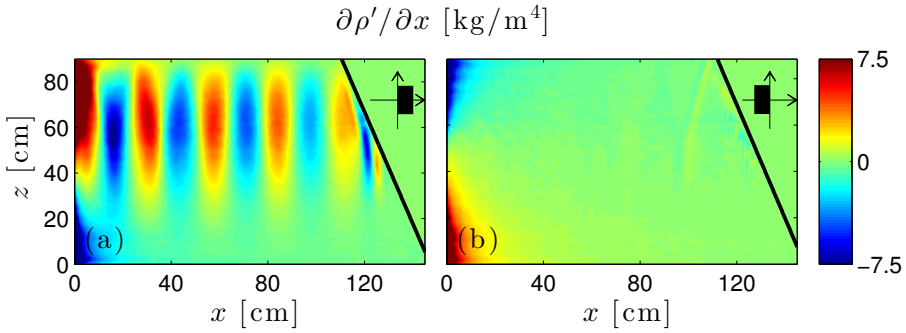


Figure 3.13: Snapshots of the horizontal density gradient fields for a point attractor, after Hilbert filtering in frequency and in space. Only the horizontal component of the wave vectors have been filtered, keeping the positive part (a) or negative part (b) of the wave vectors. The black rectangles at the right of the slope indicate where the space filtering in wave vectors is performed.

focused along the ray tracing prediction and the waves seem to propagate anti-clockwise. Nevertheless, the viscosity, inherent for experiments, has effects on the thickness of the attractor, which is finite in the experiments. After this qualitative introduction on experimental internal wave attractors, I will essentially focus on $(1,1)$ attractors in the remainder of this manuscript.

3.2.2 A typical $(1,1)$ attractor

$(1,1)$ attractors have already been shown in figure 3.11. These attractors have been obtained in the large tank, with the SyS visualization technique. This section shows typical $(1,1)$ attractors obtained in the small tank, using SyS or PIV. These attractors are used to define the different branches and their geometry properly.

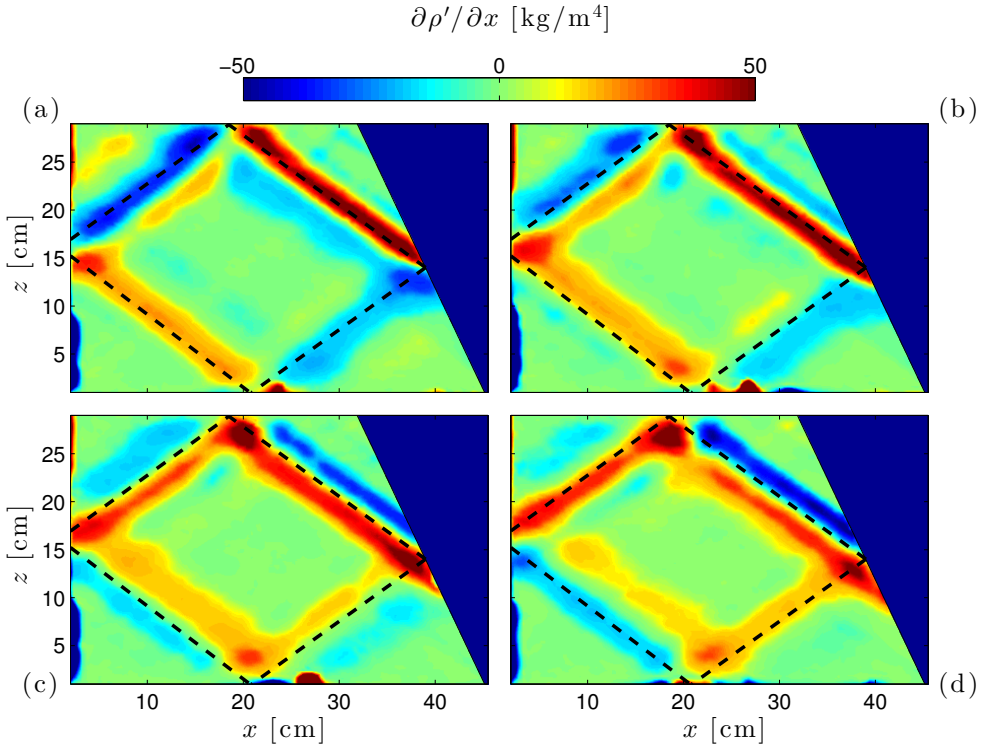


Figure 3.14: Snapshots of the horizontal density gradient fields of an attractor. Each snapshot is separated by approximately one tenth of an attractor period, T_0, and the snapshots are taken around $t = 65\ T_0$. The dashed black line indicates the ray tracing prediction for the geometry. $(d, \tau) = (0.38, 1.85)$.

Figures 3.14 and 3.15 show two $(1,1)$ internal wave attractors, using the two different techniques of SyS and PIV. The images do not come from the same experiment, but geometries of the attractors are close. As the attractor as a small wavelength, the different branches of the attractor appear more clearly in figure 3.14 with SyS than in figure 3.15 with PIV. Nevertheless, on the two figures, one can also clearly see that all the energy injected by the wave-maker is focused along the attractor. This energy oscillates around the theoretical ray tracing prediction corresponding to the geometry, plotted as a dashed black line in figures 3.14 and 3.15. To confirm that the energy is really focused along the attractor, as in section 3.2.1, it is necessary to filter the experimental images around the frequency of the wave-attractor, ω_0. Then, one can take the modulus of this field to get

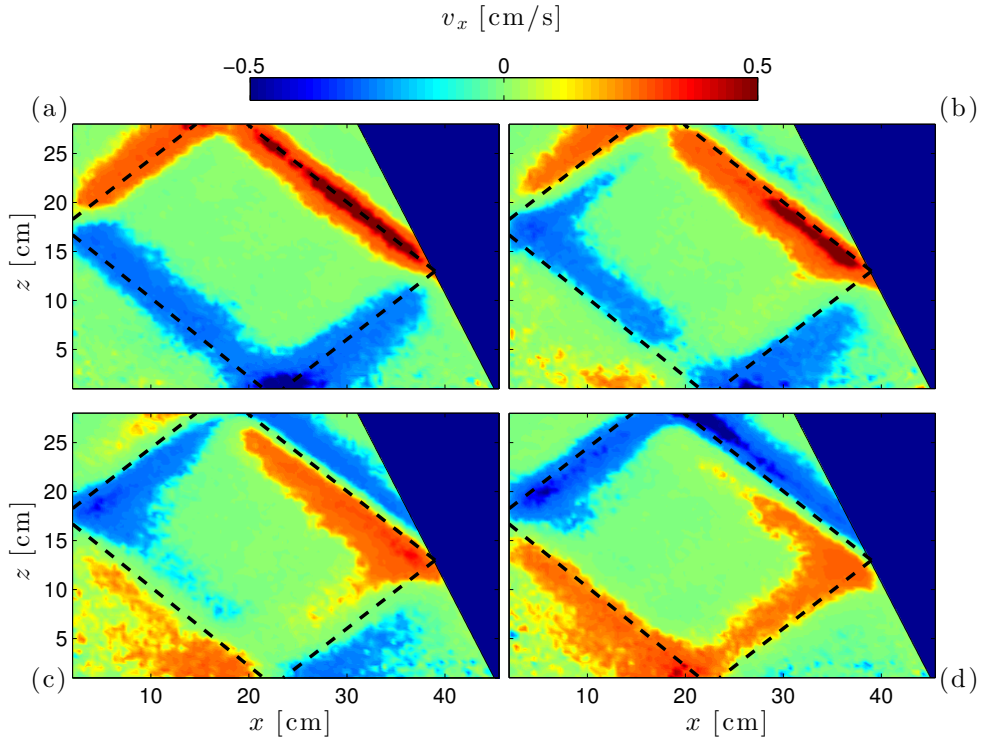


Figure 3.15: Snapshots of the horizontal velocity fields of an attractor. Each snapshot is separated by approximately one tenth of the period, T_0, and the snapshots are taken around $t = 65\ T_0$. The dashed black line indicates the ray tracing prediction for the geometry. $(d, \tau) = (0.31, 1.84)$.

the amplitude. This is shown in figure 3.16, for PIV measurements. Similar results are obtained using Hilbert filtering on SyS measurements, as in figure 3.11. It appears that all the energy is focused around the ray tracing prediction.

From figure 3.16, one can defined the geometry of a $(1, 1)$ attractor. As it has four reflections, the attractor exhibits four branches, one between each reflection. The branches are labelled anti-clockwise from 1 to 4, from the focusing reflection on the slope. For each branch, two specific directions, ξ and η, are defined. ξ is along the branch, positive anti-clockwise. η is normal to ξ, oriented towards the outside of the attractor.

Here again, as in figure 3.11, it is possible to see that the waves propagate anti-clockwise. In figure 3.16, the energy is the most intense on branch 1 and then is less and less intense from branches 2 to 4. As the waves propagate anti-clockwise, the water viscosity damps them and the amplitude decreases. This is balanced by the focusing reflection on the slope, between branches 1 and 4. Thus, the attractor reaches an equilibrium state where the viscous damping all along the perimeter of the attractor (which is around 1 m) is balanced by the focusing of the energy at the specific reflection, at one particular point. With the definitions of ξ and η for each branch, this means that the group velocity is in the ξ direction while the phase velocity and the wave-vectors are in the η direction. For example, on branch 1, wave energy propagates from the slope to the surface, so leftward and upward. As the wave-vector is normal to the group velocity, phase propagates leftward and downward. Thus, the wave vector points towards negative η. For branches 2 and 4, the wave-vectors point towards the positive η. For branch 3, as for branch 1, the wave

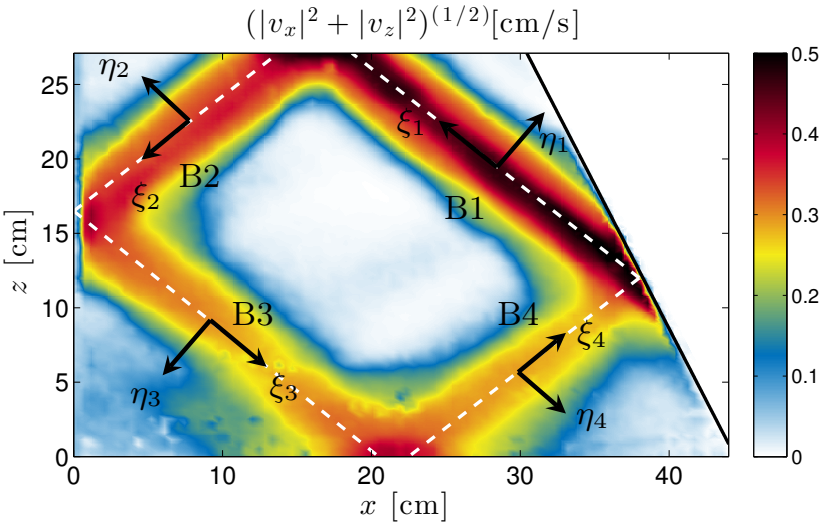


Figure 3.16: Amplitude of the velocity fields after Hilbert filtering of the attractor presented in figure 3.15. The ray tracing prediction is plotted in white dashed line. The different branches and their geometrical coordinates are defined. $(d, \tau) = (0.31, 1.84)$.

vector points towards the negative η. This can be seen in figures 3.14 and 3.15. This is an other proof that waves propagate anti-clockwise.

3.2.3 The $(1, 1)$ Arnold tongue

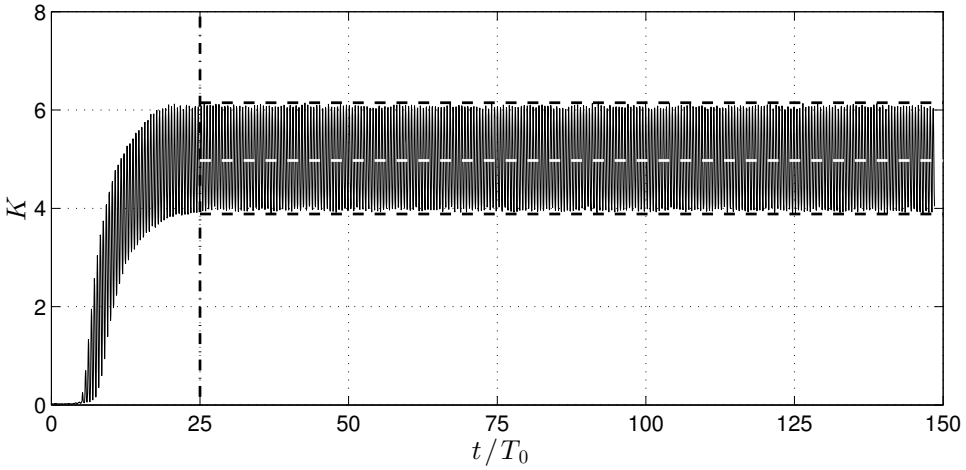


Figure 3.17: Typical experimental time-history of the dimensionless kinetic energy. The vertical dotted dashed line indicates the instant where the kinetic energy saturates. The average of the signal, computed from this instant and to the end of the experiment, is represented by the dashed white line. The two horizontal dashed black lines represent K_{min} and K_{max}, the minimal and maximal values bounding the oscillations of the kinetic energy during the saturated state. The parameters for this experiment are: Ω_0=0.59, H=30 cm, L=45 cm, $\alpha = 27.3°$, $\tau = 1.84$, $d = 0.31$ and $a = 1.5$ mm. For this experiment, $\langle K \rangle = 5$ and $R = 0.65$.

To reveal the structure of the Arnold tongue of $(1,1)$ attractors, we consider the total dimensionless kinetic energy of the fluid confined in the trapezoidal domain. Experimentally, this quantity is measured in the vertical longitudinal mid-plane and defined as follows

$$K = \frac{\int_S \mathrm{d}x\mathrm{d}z \, \frac{1}{2}(v_x^2 + v_z^2)}{\frac{1}{2}(a\omega_0)^2 S}, \tag{3.10}$$

where v_x and v_z are the horizontal and vertical velocity components and S is the area of the trapezoidal domain. Section 4.3 shows that the internal wave pattern in the experimental set-up is reasonably two-dimensional. Thus, the measurements performed in the vertical mid-plane are representative for the whole volume except thin near-wall boundary layers.

Figure 3.17 presents a typical experimental time-history of K. It can be seen that after a transient, which has a typical duration of about 25 periods, the process reaches saturation and kinetic energy oscillates between certain well-defined minimum and maximum values. We denote its corresponding time-averaged value as $\langle K \rangle$, performed in the saturated regime. This quantity $\langle K \rangle$ can be interpreted as a susceptibility of the system to the prescribed forcing of unit amplitude a. In addition, one can introduce $R = K_{min}/K_{max}$, the ratio of minimum to maximum kinetic energy as a measure characterizing a particular wave regime as standing or propagative waves. Similar to $\langle K \rangle$, this quantity is defined for the saturated regime. For purely standing waves, $R = 0$, while for purely propagative waves with vanishingly thin wave beams $R \to 1$. In realistic systems with wave beams of finite thickness, we observe $0 < R < 1$.

Using $\langle K \rangle$ and R as variables, we performed a series of 50 *short-term* experiments (parameters are given in Table 3.1) with stable $(1,1)$ attractors to study the structure of their domain of existence, the so-called Arnold tongue, as a function of the two parameters (d, τ) controlling the convergence of wave rays. The limiting case of triangle geometry $(d = -1)$ is typically characterized by the presence of a point attractor at a vertex of the triangle, while the case of rectangular geometry $(d = 1)$ corresponds to classic normal modes [110] for a discrete set of τ. The plot of the Lyapunov exponents as a function of (d, τ) is shown in figures 3.2 and 3.18 in greyscale. It can be seen that the domain of existence of $(1,1)$

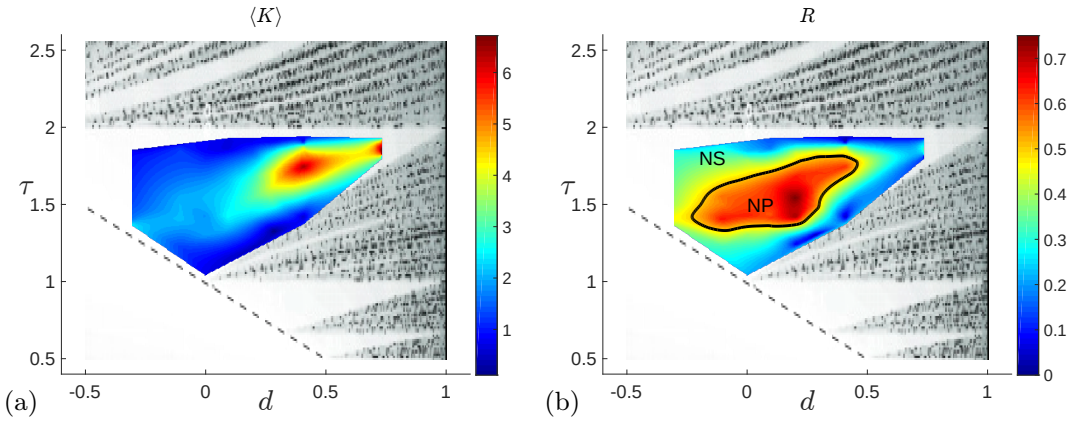


Figure 3.18: Structure of Arnold tongue of a stable $(1,1)$ attractor in terms of the mean normalized kinetic energy $\langle K \rangle$ (a) and the ratio of minimum to maximum kinetic energy R (b). The results are plotted from the 50 *short-term* experiments described in Table 3.1. The solid black line shows the contour at the value $R = 0.5$, enclosing the region with nearly propagating waves (NP), while nearly standing waves (NS) are outside this region.

#	α	Ω_0	d	τ	#	α	Ω_0	d	τ
1	11.3	0.552	0.73	1.93	26	31.2	0.719	0.20	1.24
2	11.3	0.554	0.73	1.90	27	31.2	0.731	0.20	1.22
3	11.3	0.574	0.73	1.86	38	34.6	0.530	0.09	1.93
4	11.3	0.588	0.73	1.83	39	34.6	0.545	0.09	1.85
5	11.3	0.602	0.73	1.81	30	34.6	0.588	0.09	1.61
6	11.3	0.609	0.73	1.79	31	34.6	0.643	0.09	1.43
7	24.2	0.551	0.41	1.94	32	34.6	0.643	0.09	1.41
8	24.2	0.559	0.41	1.89	33	34.6	0.669	0.09	1.34
9	24.2	0.587	0.41	1.85	34	34.6	0.707	0.09	1.15
10	24.2	0.615	0.41	1.74	35	37.5	0.673	0.00	1.85
11	24.2	0.642	0.41	1.42	36	37.5	0.707	0.00	1.78
12	24.2	0.668	0.41	1.37	37	37.5	0.743	0.00	1.42
13	28.5	0.554	0.28	1.90	38	37.5	0.755	0.00	1.30
14	28.5	0.574	0.28	1.83	39	37.5	0.766	0.00	1.04
15	28.5	0.602	0.28	1.71	40	40.3	0.552	-0.10	1.88
16	28.5	0.622	0.28	1.62	41	40.3	0.559	-0.10	1.85
17	28.5	0.656	0.28	1.49	42	40.3	0.602	-0.10	1.55
18	28.5	0.695	0.28	1.32	43	40.3	0.616	-0.10	1.50
19	28.5	0.707	0.28	1.30	44	40.3	0.643	-0.10	1.40
20	31.2	0.554	0.20	1.90	45	40.3	0.731	-0.10	1.22
21	31.2	0.574	0.20	1.83	46	45.0	0.530	-0.30	1.86
22	31.2	0.602	0.20	1.68	47	45.0	0.559	-0.30	1.85
23	31.2	0.636	0.20	1.54	48	45.0	0.602	-0.30	1.50
24	31.2	0.669	0.20	1.42	49	45.0	0.629	-0.30	1.40
25	31.2	0.707	0.20	1.24	50	45.0	0.669	-0.30	1.36

Table 3.1: Parameters for the series of experiments represented in figure 3.18. For all these experiments, the working depth is 30 cm, the working bottom length is 45.5±1 cm, and the amplitude of the wave-maker is $a = 1.5$ mm. # is the number of the experiment (from 1 to 50), α the angle (in $\circ$) of the slope, Ω_0 the dimensionlesss forcing frequency, d and τ the dimensionless parameters of the geometry.

attractor has triangular shape. Its structure is revealed by plotting $\langle K \rangle$ and R as shown in colourfigure 3.18. Combining the information presented in terms of $\langle K \rangle$ and R, we can conclude that there are two distinct regions with different regimes for R:

i) the central part of the Arnold tongue, with high values of R: it is indicating a propagative wave system (denoted NP in the remainder of the text) corresponding to a classic case of wave attractor with thin well-defined branches. It is clearly seen in the left panel of figure 3.18 that there exists an optimum range of $\langle K \rangle$ in (d, τ)-space, with maximum transfer of energy to the attractor. As the focusing increases (negative d), the excitation of high-energy attractors is hindered by increased dissipation in narrow wave beams

ii) the border regions of the Arnold tongue are typically characterized by low values of R due to geometric degeneration of the attractor. In that domain referred as NS, waves are nearly standing. In the right tip of the Arnold tongue, we observed high values of $\langle K \rangle$ and low values of R, typical features for standing waves. Indeed, the

right corner of the Arnold tongue corresponds to $d \to 1$, i.e. to the limiting case of a rectangular domain where standing waves are generic.

3.3 Steady state of the $(1,1)$ attractor

In figure 3.17, one can see that the attractor reaches a steady state, after 25 periods of growth. In this section, we study the influence of the geometry on the $(1,1)$ attractor main features, in the steady state. Different theoretical models developed to explain the characteristics of the attractors are reminded. Then, these models are compared with the different experiments performed during this PhD.

3.3.1 Models for the steady state

Different models have been developed in the literature to explain the different geometrical characteristics of the attractors: branch profiles, wave length and width of the branches. This section presents the main results of these different models in order to compare the experiments performed with their predictions, further in this Chapter.

Virtual point source and beam width

The beam formed by the branches of the attractor can be seen as a beam emitted by a point virtual source, located behind the focusing reflection [64, 79]. Figure 3.19 illustrates this idea. One assumes that the thickness of the beam depends on the distance from the virtual source to the power 1/3. This scaling is the same as the one provided by Thomas and Stevenson [146] and is typical for self-similar internal/inertial wave beams. The distance c between the focusing reflection and the virtual point source is set by this scaling law

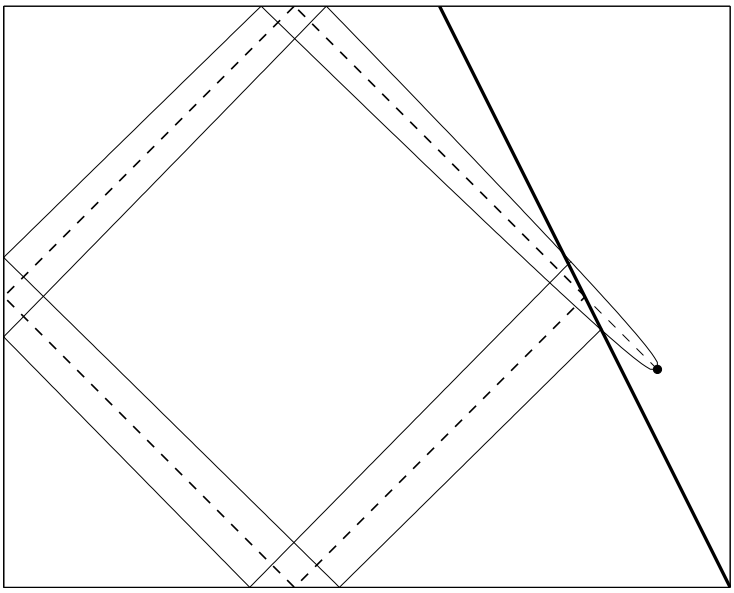


Figure 3.19: Ray tracing prediction (dashed line) for an attractor with $(d,\tau) = (0.2, 1.6)$. The slope is represented by the thick solid black line. The virtual point source is indicated by the black dot, at the right of the slope. It emits a beam, whose the width scales to the power 1/3 with the distance from the source. Branches are larger and larger until the focusing reflection on the slope.

and the geometry of the attractor. Indeed, the thickness of the beam is controlled by the focusing parameter γ and the length of the branches in [79] or the perimeter of the attractor L_p in our case. Note that γ is a function of the angle of the waves θ and the angle of the slope α (see equation (1.58)). Let's call $\sigma(\xi)$ the thickness or the width of the beam. It depends on ξ, the distance along the attractor with the 1/3 scaling. The width of the beam just after the focusing reflection is $\sigma(0)$. After propagating all along the perimeter of the attractor, the thickness of the attractor is $\sigma(L_p)$ and is related to $\sigma(0)$ by the focusing parameter γ

$$\gamma = \frac{\sigma(L_p)}{\sigma(0)}. \tag{3.11}$$

Now, one can write σ as a function of the distance ξ

$$\sigma(\xi) \propto (\xi + c)^{1/3}, \tag{3.12}$$

where c is the distance between the focusing reflection and the virtual point source. Thus, using equations (3.11) and (3.12), one has

$$\gamma = \left(\frac{L_p + c}{c}\right)^{1/3}, \tag{3.13}$$

which leads to

$$c = \frac{L_p}{\gamma^3 - 1}. \tag{3.14}$$

Thus, the distance between the virtual source depends on the perimeter of the attractor L_p and on the focusing parameter γ. One defines $\Xi = \xi + c$ as the total distance along the attractor, from the virtual point source. In [79], the beam is focused at each reflection. Thus, there is four virtual point sources behind each reflecting wall. In our experimental set-up, the beam is focused only once, on the focusing slope and therefore there is only one virtual point source, located behind the focusing slope.

A more quantitative model for the width (or the thickness) of the attractor is developed in [64], for the steady state of the attractor. This model gives the evolution of the width of the branches all along the perimeter of the attractor

$$\sigma(\xi) = C'\left(\frac{\nu}{\sqrt{N^2 - \omega_0^2}}\right)^{1/3}\left(\xi + \frac{L_p}{\gamma^3 - 1}\right)^{1/3} = C'\left(\frac{\nu}{\sqrt{N^2 - \omega_0^2}}\right)^{1/3}\Xi^{1/3}, \tag{3.15}$$

using the notations of this manuscript. C' is a constant and ν the viscosity of the fluid. The 1/3 scaling is observed for the distance Ξ but a similar scaling appears for the viscosity. If one normalizes the width by the perimeter of the attractor, one gets

$$\frac{\sigma(\xi)}{L_p} = C'\left(1 - \Omega_0^2\right)^{-1/6}\left(\frac{\nu}{NL_p^2}\right)^{1/3}\left(\frac{\xi}{L_p} + \frac{1}{\gamma^3 - 1}\right)^{1/3}, \tag{3.16}$$

$$= C'\left(1 - \Omega_0^2\right)^{-1/6}\left(\frac{\nu}{NL_p^2}\right)^{1/3}\left(\frac{\xi + c}{L_p}\right)^{1/3}. \tag{3.17}$$

This shows that the ratio between the width of the attractor and its perimeter scales as $(\nu/NL_p^2)^{1/3}$. In the experiment, it is impossible to change the viscosity of water but one can change the perimeter of the attractor. Indeed, using the two tanks available, one can realize two different experiments with the same (d, τ) parameters but with two different perimeters. In the small tank, the perimeter is around 1 m while in the large tank it is more than 3 m. Thus, the aspect ratio σ/L_p should be larger of a factor $(3^2)^{1/3} \approx 2$ in the small tank than in the large tank. This is explored in section 3.3.4.

Velocity profiles

As the width scales with the distance to the power $1/3$, it is normal to observe this scaling in the branch profiles of inertial wave attractors [79]. Jouve and Ogilvie [79] performed numerical simulations of wave attractors which are slightly different from the configuration studied in this manuscript or in several papers cited within. Attractors are obtained simulating inertial waves in a square. This square is rotated around an axis which is tilted with respect to the sides of the square. Thus, each side of the tank acts as a focusing reflection and inertial wave attractors are observed, both in a linear and non-linear regime. In this part, only the linear regime is discussed. Adapting equations developed in [125] to the square geometry, Jouve and Ogilvie [79] are able to predict and verify numerically the shape of the velocity profiles of the branches. Formulas for longitudinal and normal (in the plane normal to the attractor plane) velocity fields have been derived. As inertial and internal waves are very similar, one can test the theoretical prediction of [79, 125] on the velocity fields measured in our experimental configuration. Nevertheless, inertial waves are always three-dimensional while internal waves can be two-dimensional. In our configuration, measurements have been done to verify the two-dimensional character of the flow. The results are presented in section 4.3 of this manuscript and show that the waves in the tank are quasi-independant of the y component. Thus, there is no normal velocity for internal wave attractors produced by our set-up. So, one can only test the prediction for the longitudinal velocity field. This field, given in [79] and adapted to the notations introduced in this manuscript, is

$$v_\xi = \mathrm{Re}\left(U(\eta,\Xi)\exp(i\omega_0 t)\right), \tag{3.18}$$

where ω_0 is the frequency of the wave and $U(\eta,\Xi)$ the complex velocity profile. Ξ is here defined as the distance between the profile and a virtual source, which could mimic the same inertial/internal wave beam, if it has been placed behind a reflecting focusing wall. The expression of U is

$$U(\eta,\Xi) = \left(\frac{\omega_0}{\nu\Xi}\right)^{1/3} a_0 \int_0^\infty i\exp(-ip\tilde{\eta} - p^3)\mathrm{d}p, \tag{3.19}$$

where a_0 depends on the forcing, ν is the viscosity, and $\tilde{\eta}$ is the dimensionless version of η, given by

$$\tilde{\eta} = \left(\frac{\omega_0}{\nu\Xi}\right)^{1/3} \eta. \tag{3.20}$$

One has here a self-similar profile for the longitudinal velocity fields. This profile depends on the transverse dimensionless coordinate $\tilde{\eta}$ and its amplitude varies with respect to the forcing (a_0) and to the longitudinal distance ξ to the power $-1/3$. The same $1/3$ scaling is used to normalize the transverse coordinate η. This velocity profile is compared with the one obtained experimentally in section 3.3.3.

Wave length of branches

Hazewinkel *et al.* [70] have developed a model to explain the spectrum of the wave profiles, during the steady state. This model considers a wave-packet propagating in the tank. Energy is injected in the tank at a low wave number k_{inj}. Then, as the energy propagates, the injected wave number k_{inj} is transformed into larger wave numbers by the focusing reflection and, consequently, higher wave numbers appear. First, due to focusing, the energy of these higher wave numbers is amplified. Nevertheless, this process is limited

by viscosity. As higher and higher wave numbers are created, they are more and more dissipated by viscosity which attenuates more the smaller scales. Thus, at the end, an equilibrium is reached between the injected wave number, focused and amplified, and the viscous damping. The spectrum exhibits a maximum, at a value $k_{\text{peak}} = k_{\text{inj}}/\Gamma^{1/3}$, where

$$\Gamma = \frac{2\nu L_p}{\sqrt{N^2 - \omega_0^2(\gamma^3 - 1)}} \left(\frac{2\pi}{H}\right)^3. \tag{3.21}$$

Let assume that the injection is made by a vertical mode p. Thus, one has $k_{\text{inj}} = p\pi/H$. This leads to

$$k_{\text{peak}} = p \left(\frac{\gamma^3 - 1}{16}\right)^{1/3} \left(\frac{\sqrt{N^2 - \omega_0^2}}{\nu L_p}\right)^{1/3} \propto p\gamma \left(\frac{\sqrt{N^2 - \omega_0^2}}{\nu L_p}\right)^{1/3}, \tag{3.22}$$

for γ sufficiently greater than 1. This shows the main dependance of k_{peak} in term of the different parameters of the problem: the number p of the mode, the focusing parameter γ, the perimeter L_p, the viscosity ν and the frequencies N and ω_0. With a typical value $\gamma = 2$ for our experimental $(1, 1)$ attractors, ones has

$$k_{\text{peak}} \approx \left(\frac{\sqrt{N^2 - \omega_0^2}}{L_p \nu}\right)^{1/3}. \tag{3.23}$$

This model is illustrated by the spectrum in figure 3.20, taken from [70] and annotated to highlight the main ideas. The experiments and the model related in [70] present a good quantitative agreement and Grisouard *et al.* [64] show very similar spectra.

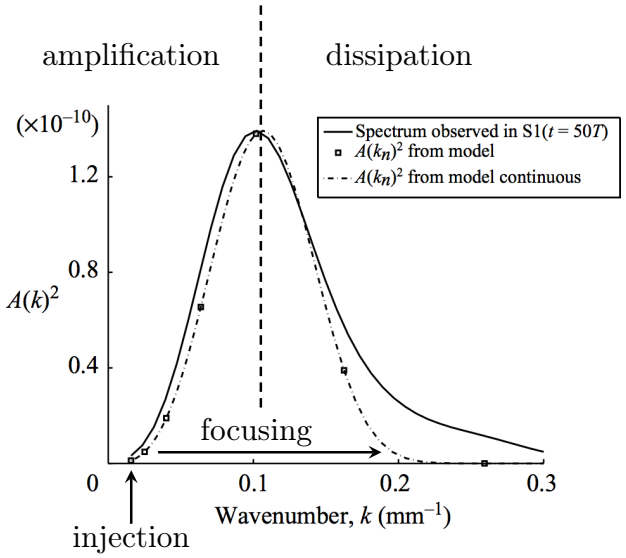


Figure 3.20: Theoretical and experimental spectra of a cut through branch 1, extracted from [70]. The energy is injected at the scale of the basin, at a low wave number. The focusing drives the wave numbers from low (left) to high (right) values with time. The vertical dashed line shows the maximum of the spectra and splits the figure in two parts: the left part where amplification dominates and the right part where viscous dissipation is more important.

In order to use these models with the data collected during the experiments, one has to measure the profiles of the branches of the attractor. The velocity profiles can be directly compared with the model given by Jouve and Ogilvie [79] while the width and the spectrum of the branches can be compared with the models developed by Grisouard *et al.* [64] and Hazewinkel *et al.* [70]. This is the point of the next section.

3.3.2 Branch separation

To study in details the branches of the attractor, it can be comfortable to separate them. It is possible to separate the four branches of the attractor using Hilbert filtering in space, for experiments performed in SyS or PIV. As phase and group velocities are orthogonal and as the wave vector and the group velocity have z-component opposite in sign, each branch is associated to a quadrant into the 2D wave vector space. Table 3.2 shows the signs of the horizontal and vertical components of the wave vector, for each branch. Thus, keeping only the positive (or negative) horizontal and vertical components of the wave vector allows us to separate the four different branches.

Branch	1	2	3	4
k_x	< 0	< 0	> 0	> 0
k_z	< 0	> 0	> 0	< 0

Table 3.2: Signs of the horizontal and vertical components of the wave vector for each branch.

This is what has been done in figure 3.21. The four panels present the four different isolated branches of an attractor. The panels are arranged to keep qualitatively the same relative position for the branches. Thus, panel (a) is for branch 2, panel (b) is for branch 1, panel (c) is for branch 3 and panel (d) is for branch 4. This is very convenient because, using Hilbert filtering in space, one can look at branch profiles without interference of the other branches. Figure 3.21 shows also that, except on the four branches, the motions of the fluid are very weak.

Once each branch has been isolated, one can combine the different measured fields into more appropriate fields for the branches, the transverse or longitudinal fields. This has been done for SyS in [70, 64] but one can also do the same thing for PIV, as Jouve and Ogilvie [79] give predictions on the longitudinal velocity fields for a inertial wave attractor branch. For each branch, the group velocity is in the ξ direction while the phase propagates in η direction. These two directions have been defined for each branch in section 3.2.2 in figure 3.16. Thus, for SyS, one can expect the strongest density gradient fields in the transverse (η) direction and the weakest fields in the longitudinal (ξ) direction, because the phase propagates along the transverse direction. Thus, the density gradients are stronger in the transverse direction than in the longitudinal direction. On the other hand, for PIV, one can expect the strongest velocity fields in the longitudinal (ξ) direction while the weakest should be in the transverse (η) direction for the same reason. The velocity fields is mainly oriented along the ξ direction and not in the η direction. Thus, it worths to combine the measured fields, the horizontal and vertical density gradient or velocity fields into more appropriate density gradient or velocity fields, depending on the visualization technique employed. Hazewinkel *et al.* [70] have introduced for the first time the transverse density gradient fields, $\partial\rho'/\partial\eta$, for SyS. This transverse gradient has been used to perform a cut through branch 1 and analyse the Fourier spectrum of this cut. One can introduce

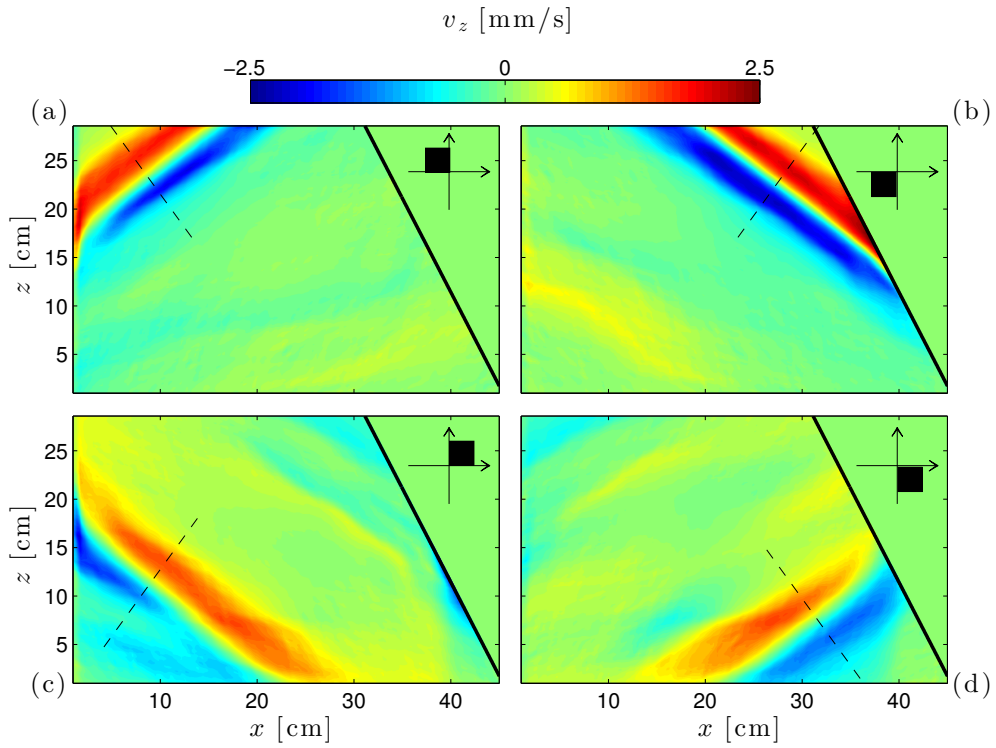


Figure 3.21: Snapshots of the real part of the vertical velocity fields filtered around ω_0 in frequency and around each sign of k_x and k_z in space. (a): branch 2; (b): branch 1; (c): branch 3; (d): branch 4. The location of the images is chosen to conserve qualitatively the relative position of the four branches of the attractor. The experiments is the same as the one used in figures 3.15 and 3.16. The dashed black lines indicate the cuts made through the branches, in figures 3.22 and 3.23. The black squares at the right of the slope indicate where the space filtering in wave vectors is performed for each panel.

here the longitudinal velocity fields, v_ξ. The quantities $\partial\rho'/\partial\eta_1$, $\partial\rho'/\partial\xi_1$, v_{η_1} and v_{ξ_1} for branch 1 are given by

$$\frac{\partial\rho'}{\partial\eta_1} = \frac{\partial\rho'}{\partial x}\sin\theta + \frac{\partial\rho'}{\partial z}\cos\theta, \tag{3.24}$$

$$\frac{\partial\rho'}{\partial\xi_1} = -\frac{\partial\rho'}{\partial x}\cos\theta + \frac{\partial\rho'}{\partial z}\sin\theta, \tag{3.25}$$

$$v_{\eta_1} = v_x\sin\theta + v_z\cos\theta, \tag{3.26}$$

$$v_{\xi_1} = -v_x\cos\theta + v_z\sin\theta. \tag{3.27}$$

The computation of the transverse and longitudinal fields for the other branches are similar, paying attention to the orientation of ξ and η with respect to the horizontal and vertical axis.

Figure 3.22 shows snapshots of the different velocity components along a cut through branch 1 for an attractor, after Hilbert filtering in frequency and space. Panels (a) and (b) show the measured horizontal and vertical velocity components, v_x and v_z while panels (c) and (d) exhibit the transverse and longitudinal components, v_{η_1} and v_{ξ_1}, computed using the measured velocity fields. As expected, v_{ξ_1} is slightly more intense than v_x and v_z while v_{η_1} is close to zero. Similar features can be obtained for the other branches. For

SyS, the figure is not presented in this manuscript but it exhibits the same characteristics except that the transverse density gradient field is relevant and the longitudinal density gradient field vanishes. Thus, one can verify that the longitudinal density gradient field or the transverse velocity field are negligible with respect to the other fields. The relevant fields are longitudinal velocity fields for PIV and transverse density gradient fields for SyS.

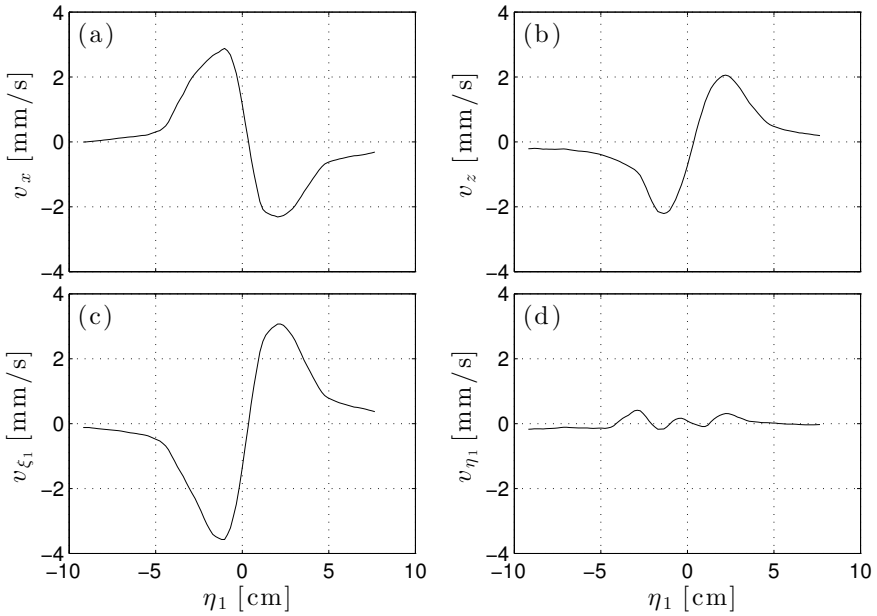


Figure 3.22: Snapshots of the real part of the different velocity components along a cut made through branch 1, after Hilbert filtering in frequency and space. (a): v_x, horizontal velocity component; (b): v_z, vertical velocity component; (c): v_{ξ_1}, longitudinal velocity component; (d): v_{η_1}, transverse velocity component. The locations of the cut made through branch 1 is shown in figure 3.21(b), as a dashed black line.

One can use the branch separation and the relevant fields to characterize the different branches, in term of phase propagation, width and wave length.

3.3.3 Branch profiles

As the phase is normal to the group velocity for internal waves, the cuts made through the branches are a good way to observe the phase propagation. Figure 3.23 shows this phase propagation of the four branches, after Hilbert filtering in frequency and space. For each branch, a black thick line represents the amplitude of the branch or the envelop and four phases are plotted with different colors. As the wave vector is pointing towards the negative (respectively positive) η for branches 1 and 3 (resp. for branches 2 and 4), the phase propagates from right to left on panels (b) and (c) (resp. from left to right on panels (a) and (d)).

Looking to the amplitude (or envelop) of the branches, it seems that the black curves are more or less symmetric with respect to $\eta = 0$ cm. Panel (b) for branch 1 is well symmetric with respect to $\eta = 0$ cm but for the other branches on the other panels, the

asymmetry is more and more important. Nevertheless, the different phases exhibit the same characteristics. Moreover, one can see that the maximum of the amplitude of the cut decreases as one follows the trajectory of the waves. The maximum is reached for branch 1 and then is smaller and smaller for branch 2, 3 and 4. As the amplitude goes down, the envelop is slightly broadened. This confirms that waves propagate anti-clockwise: the amplitude is damped by viscosity and the envelop is larger and larger because of momentum diffusion. This has been seen by [70, 64] using Fourier spectra of cuts made through the different branches.

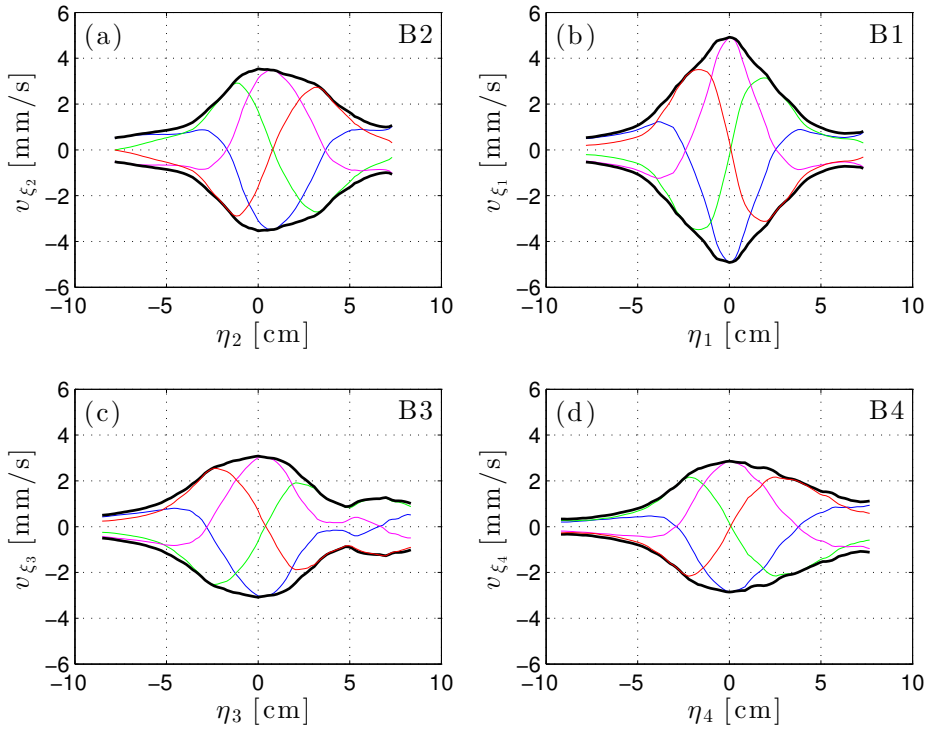


Figure 3.23: Longitudinal velocity fields along cuts made through the four branches of the attractor at four instants. (a): branch 2; (b): branch 1; (c): branch 3; (d): branch 4. The location of the cuts are indicated by the dashed black lines in figure 3.21. On each panel, the thick black line shows the amplitude (modulus) and the four lines of different colors represent the profiles at different instants. The four instants are separated by a quarter of a period and are ordered as follows: blue, green, magenta and red.

For the experiment presented in this section, one has $c \approx 0.1 L_p \approx 10$ cm, meaning that the virtual source is distant to the focusing reflection around a tenth of the perimeter behind the slope.

To compare the predictions of [125, 79] (see equations (3.19) and (3.20)) with our measurements, one focuses on branch 1 which exhibits the best results in term of signal-over-noise ratio. The signal has to be normalized because the a_0 term in the amplitude depends on the numerical forcing of [79], which is different for us. Indeed, the numerical forcing of [79] is a bulk forcing. Thus, one can compare only the normalized signals. The dimensionless profile of [79] is normalized and its width is scaled using equation (3.20) and the distance Ξ between the profile and the point source. Figure 3.24 shows the comparison between the longitudinal velocity profiles measured in our configuration and the prediction made by [125, 79] and given in equation (3.19). Experimental (solid lines) and theoretical

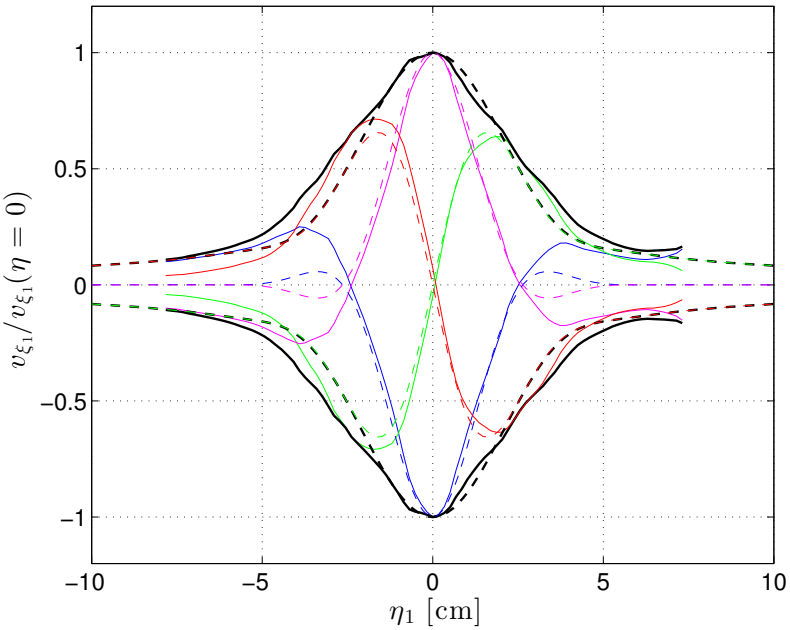


Figure 3.24: Comparison between normalized experimental (solid lines) and theoretical (dashed lines) longitudinal velocity profiles. The theoretical profiles are given by equation (3.19).The black lines represent the envelop and four different phases are shown, from blue, green, magenta to red. The experiment used here is the same as the one in figures 3.15 and 3.16.

(dashed lines) profiles are in a good agreement. Close to $\eta_1 = 0$ cm, where the amplitude of the attractor is the highest, theory and experiments are quantitatively consistent. The difference between them becomes more important away from the center region $\eta_1 = 0$ cm but the profiles remain qualitatively similar. This discrepancy could be due to two reasons. The first one is that the geometry of [79] is different from the trapezoidal geometry we used. Thus, the rays may have a different way to converge towards the attractor and therefore do not contribute to the attractor in the same manner as they do for the trapezoid geometry. Moreover, the forcing is here different because it is a bulk forcing. Thus, the trajectories of the rays converging towards the attractor are different than the ones in our set-up.

3.3.4 Branch wave length and width

We have shown in the previous section that the model for the velocity profiles developed by Jouve and Ogilvie [79] is in good agreement with the experimental results. In this section, we focus on the wave length and the width of the attractor branches in order to compare them with the ones predicted by the models of Grisouard *et al.* [64] and Hazewinkel *et al.* [70].

The peak wave number and the width of the attractor are measured using experiments performed in the large tank with SyS as a visualization technique. The different branches have to be separated using Hilbert filtering in frequency and in space. The results obtained for branch 1 are similar for the other branches except that the others are slightly broader and less intense than the first branch. The filtered horizontal and vertical gradient density fields are combined to the transverse density gradient field, $\partial\rho'/\partial\eta_1$. This field is plotted in figure 3.25(a). A cut, plotted as a dashed black line, is made through branch 1. From

this cut, one can have the real signal, the modulus (amplitude) and also the phase, along the cut. These quantities are plotted as a function of the distance η_1, in figures 3.25(b) and (d). The phase is related to the wave-vector by $\vec{k} = -\vec{\nabla}\phi$. When unwrapping the phase, one can fit it by a linear profile where the amplitude of the wave is high and get the slope. One obtains the norm of the peak wave vector and thus, the peak wave number k_{peak}. This value is consistent with the Fourier spectrum of the real part of the signal, shown on panel (c). The maximum of the spectrum is close to the value found with the phase. The width of the branches is defined as the width at half maximum. Consequently, the width is the distance between the two vertical dashed black lines, surrounding the maximum of the amplitude in $\eta_1 = 0$ cm, on panels (b) and (d). The width depends of course of the definition taken. Changing half in one third or one quarter will certainly increase the width. Nevertheless, we are interested in the variation of the width as a function of the distance ξ and the definition taken for the width only changes the constant C' in equation (3.15). Moreover, the same definition is used in all this manuscript and this definition is more easily applicable to the branches than the one proposed in [64].

The Fourier spectrum in figure 3.25(c) is similar to the one described in the model of [70]. Equation (3.16) has been verified by [64] numerically, for an attractor in a steady

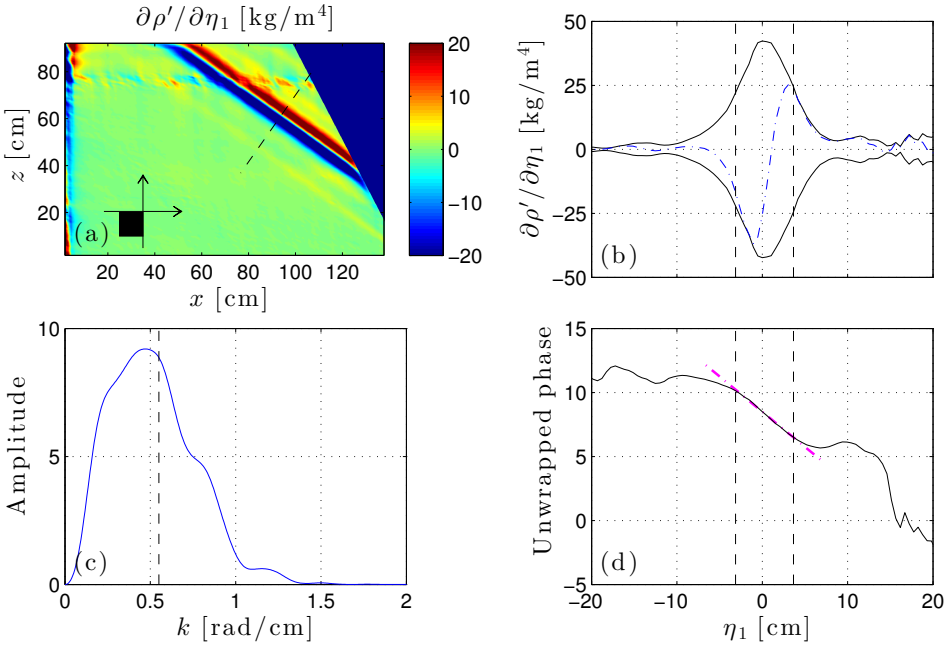


Figure 3.25: (a): $\partial\rho'/\partial\eta_1$ of a stable attractor observed with SyS during the steady state, after Hilbert filtering in frequency and space. The black square indicates where the space filtering in wave vectors is performed. The cut made through branch 1 is plotted as a dashed black line. (b): $\partial\rho'/\partial\eta_1$ along the cut through branch 1. The real part is represented by a dashed dotted blue line and the modulus by the two black lines. (c): Fourier spectrum of the real part of $\partial\rho'/\partial\eta_1$ shown on panel (b). The vertical dashed line shows the peak wave number found using the phase on panel (d). (d): Unwrapped phase (black solid line) and fit of the central part (magenta dashed dotted line). The part were the fit is done is in between by the two vertical dashed lines, on both panels (b) and (c). The distance between these two lines defines the width σ of branch 1.

state. Nevertheless, the definition of the width has been changed from [64]. To verify that the definition given in that manuscript is similar to the one proposed in [64], the width of the attractor has been measured all along the perimeter. Several cuts have been made through the branches 1 to 4 and the width at half maximum has been measured. The width is plotted as a function of the distance ξ, in figure 3.26. The agreement is relatively good with the power law predicted by equation (3.16) and is similar to the results reported in [64]. A linear fit gives a slope of 0.43, similar to the one found in [64]. Thus, the definition taken for the width of the branch seems valid and gives results similar to numerical simulations reported in [64].

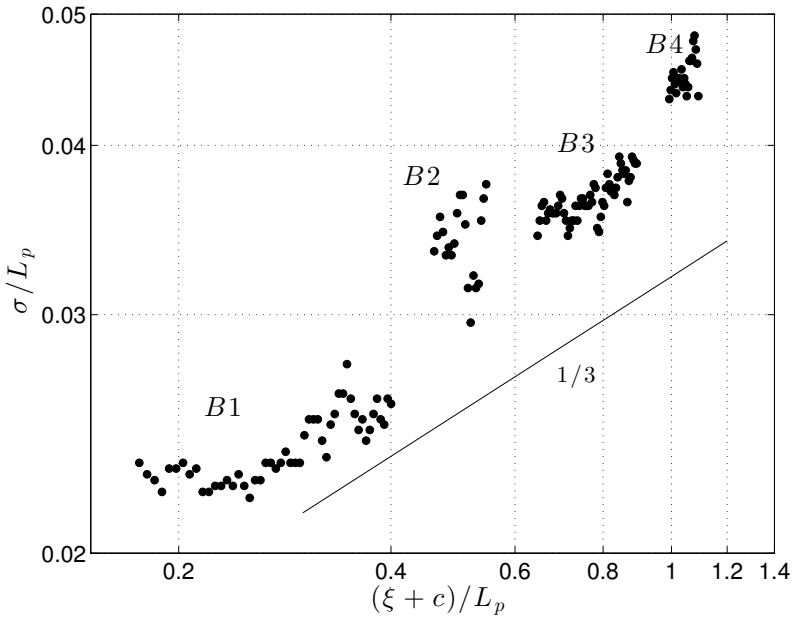


Figure 3.26: Width-over-perimeter ratio as a function of the normalized distance (black dots) in log-log scales. The black line shows the predicted power law, 1/3. The points come from the four branches, indicated on the figure. The dispersion of neighbor points gives an estimate of the error bar of this measure.

It is now possible to check the scaling for the width of the attractor as a function of the perimeter given by equation (3.16). Figure 3.27 shows a comparison between two attractors, one in the small tank and the other one in the large tank, both observed using SyS. The two attractors have very close (d, τ) parameters but different scales. The horizontal and vertical scales of the trapezoid in panel (a) are approximately 3 times smaller than the ones in panel (b). Thus, plotting these two attractors with the same dimension is equivalent to normalize them. The horizontal density gradient fields are represented after a filter in frequency around ω_0 and a normalization by the maximal amplitude of the branch 1. Thus the color bar is the same for the two attractors and lies in the range $[0 - 1]$. According to equation (3.16), the width of the small tank attractor (panel (a)) appears larger than the width of the large tank attractor (panel (b)). The width measurements made cutting branch 1 of both attractors, at the same Ξ/L_p, show that the ratio σ/L_p is 4.55×10^{-2} for the small tank attractor and 2.25×10^{-2} for the large tank attractor. There is a factor 2 between these ratios. The model described in [64] and given in equation (3.16) claims that the ratio $\sigma/L_p \propto L_p^{-2/3}$. Thus, the ratio between σ/L_p of the large and small attractors should be equal to the ratio of the perimeters, equal to 3, to the power 2/3: $3^{2/3} \approx 2$.

Thus, the width measurements are in good agreement with the model described in [64]. We took care of measuring the width of branch 1 at the equivalent location in both attractors. Moreover, section 3.4 demonstrates that, for stable attractors, the width of the attractor does not depend on the amplitude of the forcing. Thus, the measured widths in the two attractors of figure 3.27 do not depend on their amplitude.

To validate completely this scaling for the width given in equation (3.16), one should vary the perimeter L_p or the viscosity ν on large ranges of order of magnitude. It is difficult to do this experimentally. However, if one can imagine attractors in oceans or lakes, this scaling shows us that, in natural structures, where the scales are kilometers or more, the attractor width is very small in comparison to the perimeter. For example, if one considers the experimental set-up scaled with the ocean depth, which is around 4000 m, the perimeter L_p is approximately equal to 10000 m. In the ocean, the buoyancy frequency is in between 10^{-4} and 10^{-3} rad/s. The scaling for the width σ gives an attractor of few meter thick, which is unrealistically thin. For a lake of 100 m depth and a buoyancy frequency of 10^{-3} rad/s, the width is less than one meter. It is impossible to confine all the energy is such narrow beams. Thus, one can assume that stable attractors can not be present in oceans or lakes as they are in the experimental set-up. Non-linearities play surely an important role, as highlighted in Chapters 4 and 5.

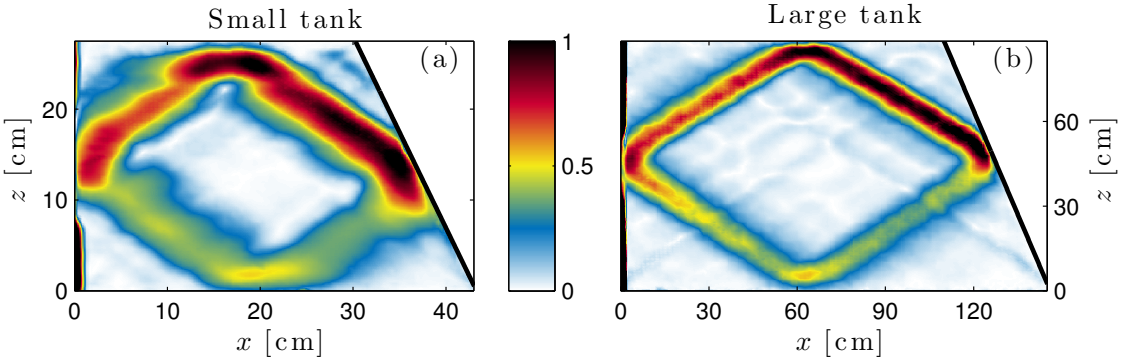


Figure 3.27: $|\partial\rho'/\partial x|$ filtered around ω_0 and normalized by the amplitude of the branch 1 for attractors made in the small (a) and large (b) tanks. $(d, \tau) = (0.38, 1.85)$ for (a) and $(d, \tau) = (0.52, 1.83)$ for (b).

3.4 Growth and decay of the $(1, 1)$ attractor

Experiments [70] and numerical simulations [64] have already studied the evolution of the wave number of the branches of the attractor as a function of time, using spectra made from a cut through branch 1. These studies have been done during the decay of the attractor, once the forcing has been stopped. During the decay, there is no more low wave number injection and, due to focusing, all wave numbers become higher and higher and are damped by viscosity. Thus, the k_{peak} value shifts more and more to high wave number values and the amplitude of the peak decreases [70, 64]. In this section, the wave length, the width and the amplitude of the attractor branch 1 are followed in time, from the growth to the decay of an internal wave attractor.

3.4.1 Typical growth and decay

Experiments have been performed in the large tank in order to follow the branch 1 of an attractor during the growth, the stationary state and the decay of the attractor. Moreover, the amplitude of the wave-maker has been changed between the different experiments, to study the effect of the forcing on the evolution of the branches. Because these experiments were done in the large tank, the technique used was SyS. Two series of experiments have been performed, using the same filling of the tank. The second series has been carried on the next day of the first series. This ensures that all the experiments have exactly the same geometry, the same stratification and the same forcing frequency. Thus, $(d, \tau) = (0.34, 1.81)$ for all the experiments presented in this section. Experiments of the first series are growth and decay experiments, with different amplitudes of forcing. This means that the wave-maker is started at the beginning of the experiment, the attractor grows until it reaches the steady state and then the wave-maker is stopped. Data are collected continuously during the three phases, until the fluid in the tank comes back to rest. Experiments of the second series are only growth experiments, with different forcing amplitudes. Thus, the decay phase is not recorded. In this section, only experiments where the attractor is stable are presented. This corresponds to experiments where the amplitude of the wave-maker is small. Experiments with unstable attractors at large forcing amplitudes are presented in next chapter, section 4.1.2.

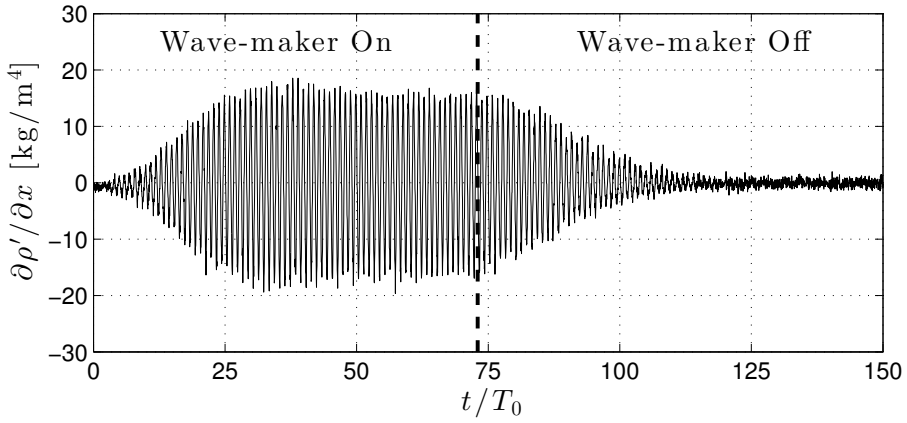


Figure 3.28: Time history of the horizontal density gradient fields in a point located at $x = 85$ cm and $y = 63$ cm, on branch 1. The wave-maker is started at $t = 0\ T_0$ and is stopped at $t = 73\ T_0$. The position of the attractor in the tank is shown in figure 3.29.

Typical growth, steady state and decay are shown in figure 3.28, using the time-history of the horizontal density gradient field in a point located on branch 1. The amplitude starts to grow until the attractor reaches a stationary state around $40\,T_0$. Then this stationary state is maintained, until the wave-maker is stopped at $t = 73\,T_0$. Then, the attractor decays and no motion is observed after $t = 115\,T_0$. The part of the figure between $t = 125$ and $150\,T_0$ gives the noise amplitude of the signal. Although this amplitude is quite small in comparison to the maximum amplitude of the attractor, this can lead to small fluctuations in the amplitude of the stationary state that are visible in figure 3.28, between $t = 30$ and $73\,T_0$.

Figure 3.29 shows four different snapshots of an attractor, filtered around ω_0 in frequency. The experiment is the same as the one used in figure 3.28. Panels (a) and (b) of figure 3.29 are during the growth and the stationary state while panels (c) and (d) are

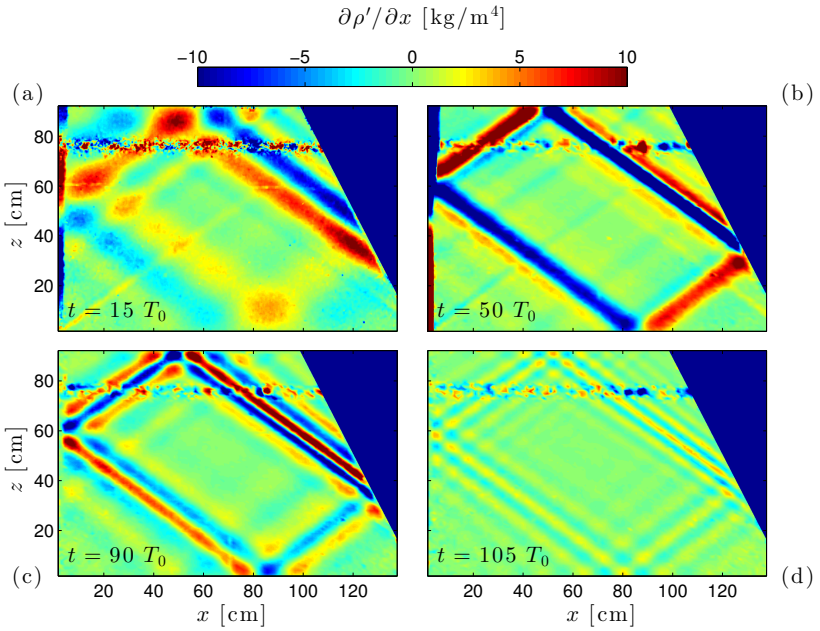


Figure 3.29: Horizontal density gradient fields for $t = 15\,T_0$ (a), $t = 50\,T_0$ (b), $t = 90\,T_0$ (c) and $t = 105\,T_0$ (d). (a) corresponds to growth, (b) to steady state and (c) and (d) to decay. The images have been filtered around ω_0 in frequency. The horizontal line around $z = 80$ cm which presents artificial defects is due to PIV particles that converged towards their iso-density line.

during the decay of the attractor, after the wave-maker has been stopped. One can clearly see an evolution in the peak wave number (the peak value k_{peak}), in the amplitude and in the width of the branches, as in [70, 64]. Panel (a) has the smallest wave number. Then panels (b), (c) and (d) have larger and larger ones. This is consistent with the model developed in [70] and illustrated in figure 3.20. The peak wave number of panel (a) is in the left part of the steady state spectrum, the amplification part. Panel (b) corresponds to the steady state, while peak wave numbers of panels (c) and (d) are in the right part, the dissipation one. The amplitude of the branches grows until its stabilizes during the steady state and then decays slowly. This is consistent with figure 3.28. Peak wave number and amplitude of branch 1 will be investigated as a function of time in section 3.4.2.

Regarding the width of the branches, it seems that during growth and stationary state, the width has a similar behavior as the wave length since one can see only approximately one wave length into the branches of the attractor. Nevertheless, during the decay, it seems that the width of the attractor remains approximately constant and therefore more wave lengths appear into the width because the wave length is reduced during the decay. Results about the width of the attractor are presented in section 3.4.3.

3.4.2 Wave length and amplitude evolution in time

In order to measure the peak wave number and width of branch 1 as a function of time, the analysis presented in figure 3.25 has been done on several images, using always the same cut location. The complete evolution in time of the wave length λ, defined as $\lambda = 2\pi/k_{\text{peak}}$, is shown in figure 3.30(a), for three experiments with different amplitudes of the wave-maker. The amplitudes are $a = 0.7$ (green), 1.5 (magenta) and 2.1 mm (blue). The attractors are

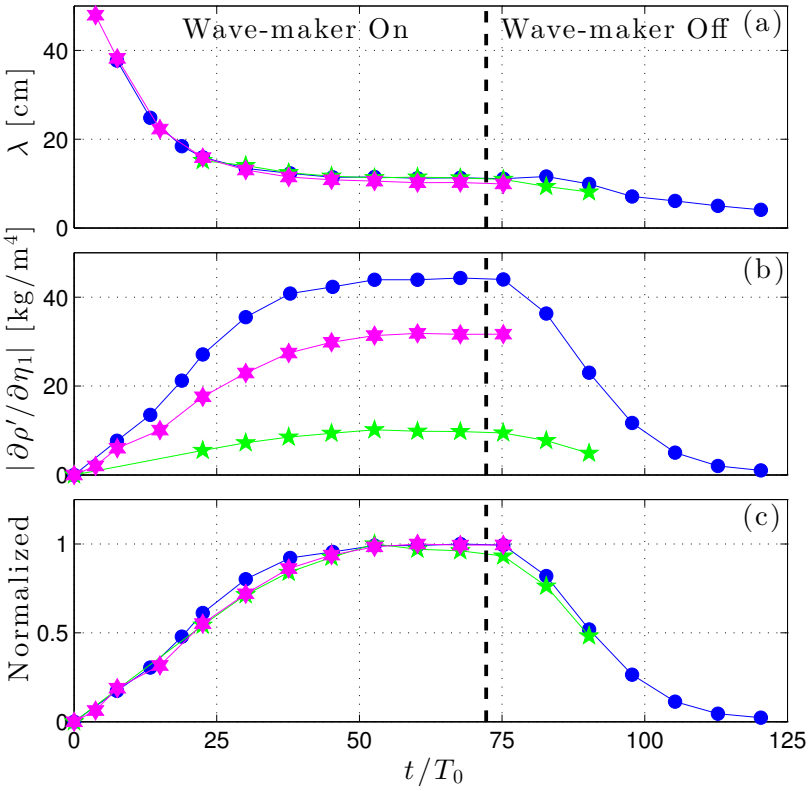


Figure 3.30: (a): Wave length of the attractor branch 1 as a function of time. (b): Transverse density gradient fields amplitude of the attractor branch 1 as a function of time. (c): Normalized transverse density gradient fields amplitude, with respect to the steady state, as a function of time. The different symbols and colors indicate experiments of different amplitudes: green pentagons for $a = 0.7$ mm, magenta hexagons for $a = 1.5$ mm and blue dots for $a = 2.2$ mm. The symbols show the instants where the wavelength and the amplitude have been measured. There are two growth and decay experiments (green and blue points) and one growth experiment (magenta points). The vertical dashed line represents the moment when the wave-maker was stopped.

stable for these amplitudes. One can first note that the attractor wave length is totally independent of the amplitude of the wave-maker at any time, because all the three curves are superimposed. Secondly, one can see how the attractor set-up is a machine to decrease the wave lengths. Indeed, the wave-maker injects a very large wave length, typically of 184 cm, which is equal to two times the height of the large tank. While the waves reflect on the slope, the energy is focused and the wave lengths are smaller and smaller until a steady state is reached. In this state, the focusing is balanced by the viscous broadening. The ratio between the injected scale and the scale of the attractor in the steady state is around 13.5. This value is larger than 9, which is the value of the same ratio reported for a small tank attractor experiment [139], for linear focusing. Thus, the large tank allows an energy transfer through a larger range of scales than the small tank. Once the wave-maker has been stopped, there is no more large injected wave length and the slope focuses the waves into smaller and smaller wave length until all the energy is damped by viscosity.

The influence of the amplitude of the wave-maker can be seen in figure 3.30(b), showing the transverse density gradient field amplitude as a function of time, for the same three

different experiments as in figure 3.30(a). The higher the amplitude of the wave-maker, the higher the amplitude reached by the steady state. Thus, for stable attractors, all the energy emitted by the wave-maker is focused into an attractor with the same geometrical characteristics. The only difference is that the amplitude varies with the one of the wave-maker. Figure 3.30(c) shows the normalized version of the curves presented in figure 3.30(b). Each curve is now divided by the maximum of amplitude, reached during the steady state. All curves collapse well, showing that only geometry matters in the attractor process, the amplitude of the wave-maker giving only the amplitude of the branches. This shows that the creation of stable attractors is a purely linear process, evolving only through geometrical focusing.

3.4.3 Attractor width evolution in time

One can also study the evolution of the width of the branches of the attractor as a function of time, during the growth, stationary state and decay of the attractor. As for the wave length and the amplitude, different images have been analyzed and the width of branch 1 has been measured always at the same location. These images come from the three different experiments of the previous section, with exactly the same geometry but with different amplitudes. Results are presented in figure 3.31. Figure 3.31(a) shows the evolution of the width as a function of time. All the curves from the three experiments collapse well as for the wave length evolution in time. During the growth and the steady state of the attractor, the behavior of the width is very similar to the one of the wave length, presented in figure 3.30(a). Nevertheless, after the stop of the wave-maker, the width of branch 1 increases slightly while the wave length decreases. The width-over-wave length ratio gives

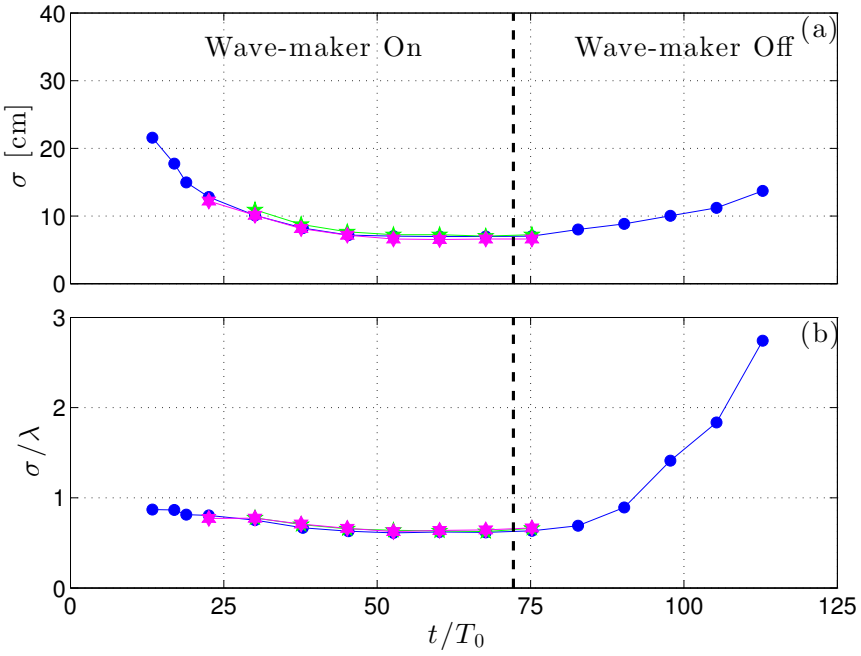


Figure 3.31: (a): Width σ of branch 1 as a function of time, for the same three experiments as in figure 3.28. (b): Ratio between the width σ and the wave length λ of branch 1 as a function of time. The dashed black lines show the time where the wave-maker has been stopped. The symbols are the same than the ones in figure 3.28.

an idea of the number of wave lengths that are present in the width of the branch. This ratio is plotted, as a function of time, in figure 3.31(b). During the growth, this ratio slightly decays but one can consider that the ratio is more or less constant during the growth and the steady state. This means that there is only one wave length in the width of the branch during this two phases. This is consistent with the snapshots in figures 3.29(a) and (b). Once the wave-maker has been stopped, this ratio increases drastically. Indeed, the wave length decreases a lot, due to focusing and the width of the beam slightly increases. On the snapshots presented in figure 3.28, the width of the beam does not seem to increase. The increase in figure 3.31(a) is probably due to the damping of the waves. Thus, the amplitude of the beam is smaller and the envelop is flatter. Nevertheless, this shows that there is more wave lengths that are present in the width of the branch, as the attractor decays. This is also consistent with what it is observed in figure 3.29.

To conclude this section, one can pay attention to the scaling of both the peak wave number and the width of the attractor, given by [70, 64] and by equation (3.16). For the width, one has $\sigma \propto (\nu L_p/\sqrt{N^2-\omega_0^2})^{1/3}$ while the scaling for the wave length is $\lambda \propto (\nu L_p/\sqrt{N^2-\omega_0^2})^{1/3}$ for a forcing at large scales, with a vertical mode 1. The ratio between the two is equal to 1. This explains why one can only see one wave length per branch in the steady state. Nevertheless, the scaling for the wave length depends on k_{inj}, the wave number where energy is injected. With $k_{\text{inj}} \approx 1/H$, one gets the previous scaling. So it could be interesting to force the tank with a larger wave number, like a mode 2 or 3 for example. The wave length should be smaller and one should see more wave lengths than only one in the width of the branch. Doing that, one has to be careful to remember that the smaller scales are more attenuated by viscosity.

3.5 Exploring different forcings

In this section, different forcings are explored experimentally, from the forcing on all the height of the basin to a more local forcing, on primary fundamental intervals only. The results are compared to the theoretical stream function fields (see section 3.1.4), obtained for the same type forcing.

3.5.1 Forcing on all the height

The experimental stream function of an attractor can be obtained by measuring the velocity fields. This has already been done in [68], but, without comparison with the theoretical stream function. In [86], the theoretical displacements computed from the theoretical stream function were compared to the observed displacements in the first experiments on internal wave attractors [97]. Moreover, in [97, 68], the forcing was different.

Using section 3.1.4, it is possible to compare the stream function obtained using this method to the one obtained experimentally. The main difference is that the theoretical method is inviscid (the rays and the attractor are infinitely thin) while viscosity is not negligible in the experiments. Moreover, the theoretical method exhibits only the stationary state of the attractor while it is also possible to observe transition states (growth or decay) of the attractor experimentally. To compare with one experiment, it is easy to transform the dimensionless stream function field into a stream function field with dimensions. The basin has to be rescaled and the stream function must be multiplied by the amplitude a of the wave-maker. However, the wave-maker is not 100% efficient and this overestimates slightly the stream function.

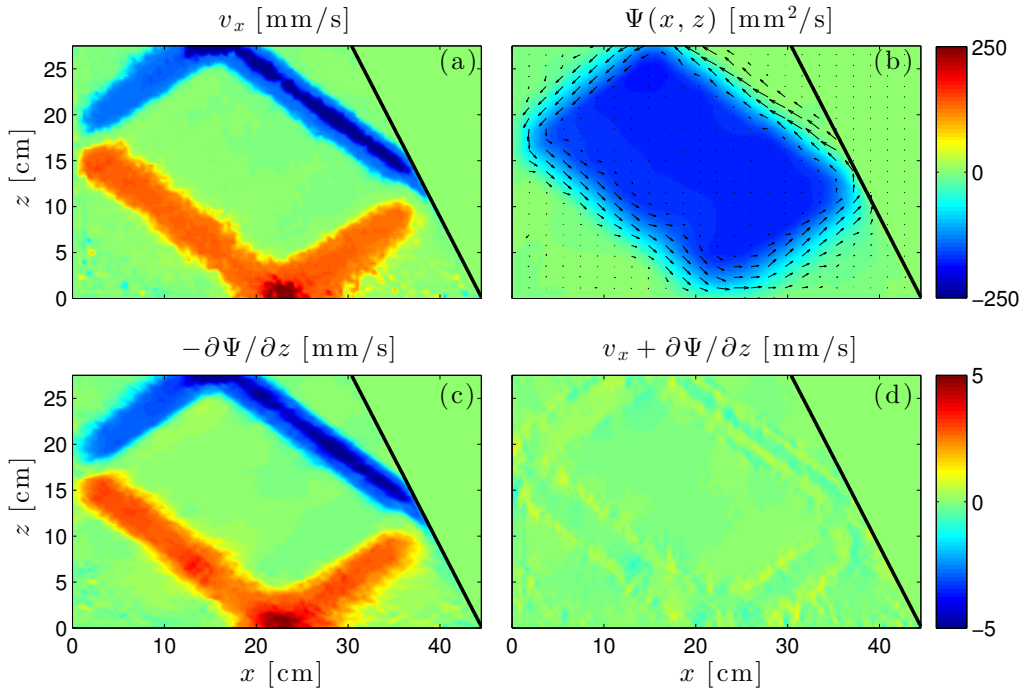


Figure 3.32: (a): Snapshot of the measured horizontal velocity field, v_x. (b): Stream function obtained using the Matlab function *intgrad2.m* and the measured horizontal (a) and vertical velocity fields. The arrows show the velocity fields. (c): Horizontal velocity field, $-\partial\Psi/\partial z$, differentiated from the stream function (b). (d): Difference field between the measured and the differentiated horizontal velocity fields. The colorbar is the same for panels (a), (c) and (d) and is presented on the right of panel (d). The colorbar for panel (b) is plotted to its right.

Experimentally, the stream function is obtained by integrating the measured velocity fields with the Matlab function *intgrad2.m*. This function has been tested by Hazewinkel *et al.* [68] in a similar context, for SyS and PIV data. Figure 3.32(a) shows a snapshot of the measured horizontal velocity field, v_x. Using this field and the measured vertical one, the Matlab function *intgrad2.m* gives the stream function field, $\Psi(x,z)$, in figure 3.32(b). To determine the constant of integration, one makes the average of the stream function at the right of the slope. This value is non zero because the integration is made on the whole rectangle, with the velocity fields equal to zero at the right of the slope. The average value, which is non-zero but small compared to the stream function amplitude, is subtracted to the stream function.

To estimate the error made by the integration, one can take the gradient of the stream function field obtained, which leads to differentiated horizontal and vertical velocity fields, $-\partial\Psi/\partial z$ and $\partial\Psi/\partial x$. The corresponding horizontal velocity field, $-\partial\Psi/\partial z$, is shown in figure 3.32(c). Then, one can make the difference between the original horizontal velocity field, v_x, and the differentiated one, $-\partial\Psi/\partial z$. This is done in figure 3.32(d). Figures 3.32(a), (c) and (d) have the same color bar, plotted at the right of figure 3.32(d). One can clearly see that figures 3.32(a) and (c) are very similar. Thus, the error made by the integration and the differentiation is quite small. This is confirmed by figure 3.32(d), where the amplitude of the difference between figures 3.32(a) and (c) is very small in comparison of the amplitude observed in figures 3.32(a) or (c). The difference is smaller than 5% everywhere in the

tank. The same order of magnitude for the error made by integration and differentiation has also been observed in [68].

Figure 3.33 shows the comparison between experimental (left column) and theoretical (right column) stream functions, for four different times within half a period. The agreement is qualitatively excellent, the different phases of the images being very similar. Nevertheless, the color bar needs to be adapted. This is due to viscous effects that are present in the experiments. Moreover, for the theoretical stream function, motions are more localized around the attractor than in the experiment. This is also due to viscosity, branches of the experimental attractor having a given thickness.

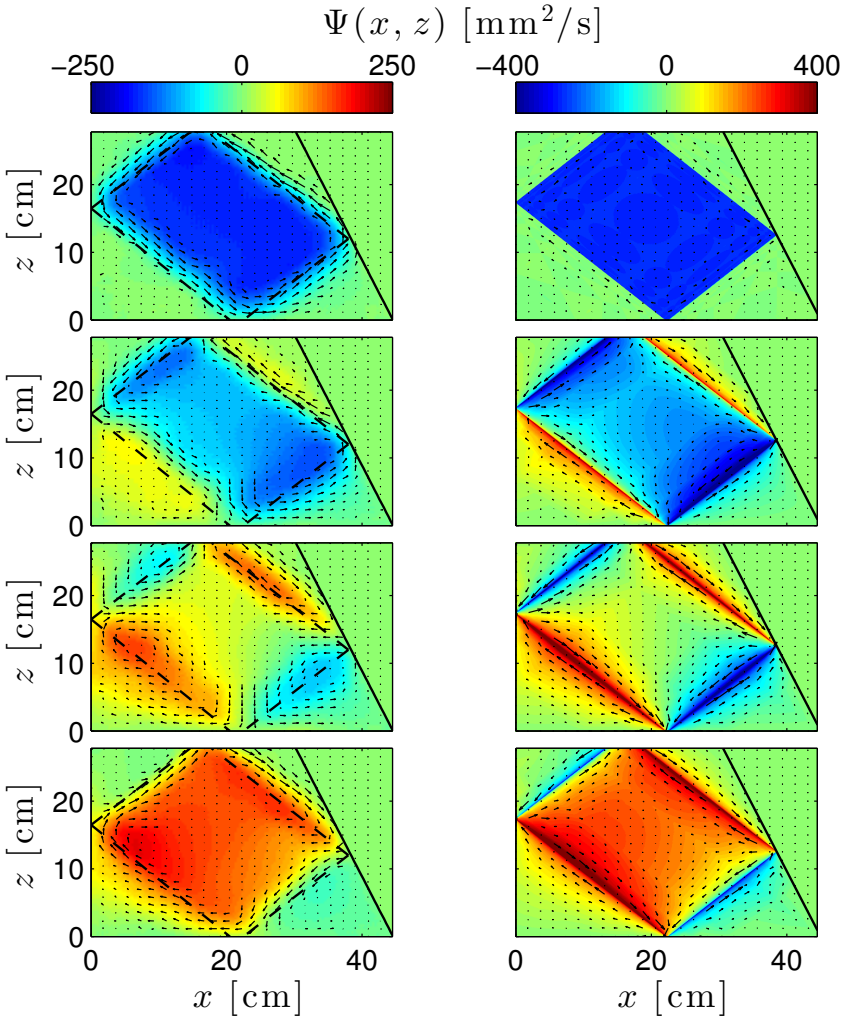


Figure 3.33: Comparison between the experimental stream function (left column) and the theoretical stream function (right column) for the same geometry. The dashed black line on the images of the left column shows the ray tracing prediction for this geometry. The color bars are adapted to have the same visual impression. The arrows indicate the velocity fields. The arrows very close to the attractor in the theoretical case are not represented because they are too large.

With the wave-maker, it is also possible to force locally with different shapes. Such set-up is also very easy to mimic in order to obtain the theoretical stream function. In particular, forcing on primary fundamental intervals seems to be very interesting regarding

the importance of these intervals for the geometry of the attractor. This is done in the next section.

3.5.2 Forcing on fundamental intervals

Regarding the importance of the primary fundamental intervals for the geometry of the attractor as it has been shown in section 3.1.3, experiments have been performed with a forcing only on one of the primary fundamental intervals. The formation of an attractor is expected, but only with a part of the webs. In particular, points inside the attractor are reached by webs coming from the two primary fundamental intervals. Here, one web is missing. Outside the attractor, the points are reached by webs coming from the same primary fundamental interval. Thus, one can expect no motion in some regions. An example of a theoretical stream function obtained with a forcing on the top primary fundamental interval is shown in figure 3.34. Here, the top right and bottom left corners outside the attractor do not exhibit any motion. The stream function pattern appears to be very different than the one obtained with forcing on all the height, as in figure 3.10 in section 3.1.3.

Experiments have been performed in both small and large tanks. In the small tank, the

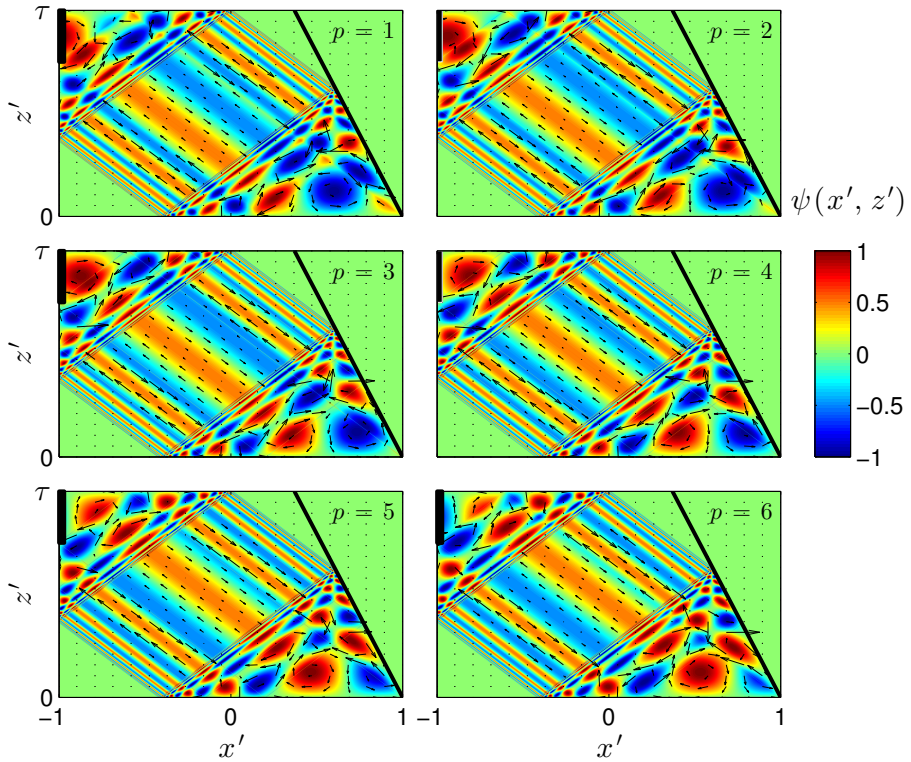


Figure 3.34: Example of stream function fields $\Psi(x', z', t')$ of an attractor with dimensionless mode 1 forcing on the top primary fundamental interval, at different times during the period. The indices p indicate the different dimensionless times: $t' = 2(p-1)\pi/12$. Arrows indicates the velocity fields computed from the stream function. Large arrows close to the attractor are not represented. A black rectangle on each image shows the region where the forcing is made on the left vertical wall.

forcing has been done on the bottom primary fundamental interval, with a mode 1 shape of 7.5 cm height and an amplitude of 3 mm. The other cams were set to zero amplitude. The velocity fields were measured using PIV. Nevertheless, due to viscosity, the waves never reach the ray tracing prediction. We were able to see only few reflections of the internal waves on the basin: the wave were damped before they converge towards the attractor. Thus, in the small tank experiments, it is impossible to observe an attractor forced locally because of the viscosity and the size of the experiments. The wave length injected by the wave-maker is too small.

In the large tank, the forcing has been done on the top primary fundamental interval, using the small wave-maker raised in order to have its top at the surface of the water. The forcing was here also a mode 1 shape, with an amplitude of 3 mm and a total height of 30 cm. The experiments have been performed using SyS technique. During these experiments with a fixed geometry, different frequencies of the wave maker have been tested. Changing the frequency of the waves induces a change in the τ parameter and, of course, in the location of the primary fundamental intervals. Thus, the forcing was not only restricted to the top primary fundamental interval but could be smaller or larger in height than this interval. Moreover, as the height of the mode 1 shape is 30 cm, the wave length injected is larger than the one in the small tank. Consequently, the viscous attenuation is reduced and the waves can reach the attractor.

Figure 3.35 shows snapshots of the horizontal density gradient fields for six different experiments performed in the large tank. All have the same values of $d = 0.37$ but τ is different, varying from 1.92 for panel (a) to 1.40 for panel (f). The forcing is applied on the top of the vertical wall, as signaled by the black rectangles. Here, we do not have access directly to the stream function, because the technique used is SyS. In figures 3.35(a) and (b), one can see using the ray tracing prediction (dashed line) that the attractor reflects on the left wall in the black rectangle, so on the wave-maker. This means that all the top fundamental intervals are forced, but also some bottom secondary fundamental intervals. Thus, we obtain something very close to an attractor forced on all the height. In figures 3.35(c), (d), (e) and (f), as the reflection on the left wall is not in the black rectangle, only some top fundamental intervals are forced. In these experiments, one can clearly see the convergence of the rays towards the attractor. This limit cycle, plotted as a dashed black line, is reached by the rays. As the rays propagate, they exhibit smaller and smaller scales. In the large tank, the wave length of the forcing is thus large enough to limit the viscous damping and to reach the attractor. As the colorbar is the same for all panels in figure 3.35, one can see that the amplitude of the waves is very different between the experiments. The amplitude is high in panels (a), (e) and (f), intermediate in panel (d) and small in panels (b) and (c). The discrepancy of amplitude in panels (a) and (b) can be explained by the fact that the attractor reflects in the middle of the wave-maker for panel (a) while it reflects on the edge of the wave-maker in panel (b). Indeed, the wave-maker imposes a stream function on the left wall, which is maximum in the center of the wave-maker and null at its edges. Let us consider the periodic wave ray, the one corresponding to the attractor. This ray is directly on the attractor, so this is the ray with the shortest trajectory to reach the attractor. Thus, this ray contributes more to the attractor than others, which are damped by viscosity while converging towards the attractor. This periodic ray is forced at the maximum amplitude by the wave-maker for panel (a) while its amplitude is close to zero for panel (b). This can explain why the amplitude is low for panel (b). For the other panels, the ray tracing prediction reflection on the left wall is not in the black rectangle. Thus, the periodic ray is not forced directly and all the waves generated by the wave-maker have to converge towards the attractor.

One can see that the general amplitude of the waves raises from panels (c) to (f), so when τ decreases. This can be due to an increase of the focusing parameter γ, which concentrates more the energy emitted by the wave-maker.

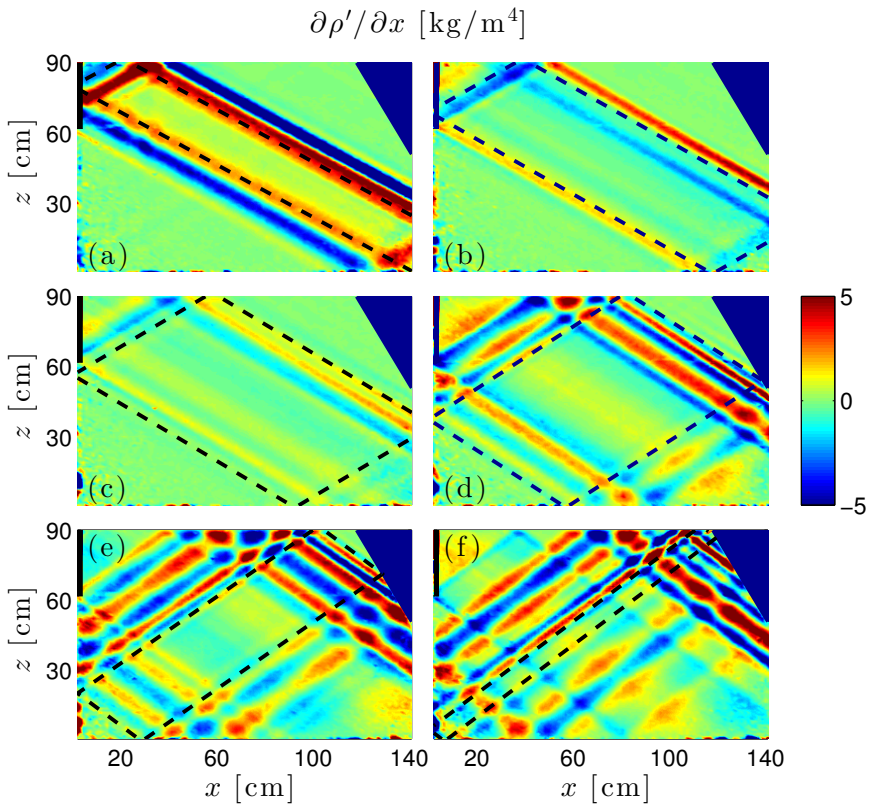


Figure 3.35: Snapshots of the horizontal density gradient fields of different attractors forced by a mode 1, only on the top of the tank. The fields are filtered around ω_0, to reduce the noise on the image. On each panel, the wave-maker is marked as a black rectangle while the dashed black line is the ray tracing prediction. For all these experiments, $d = 0.37$ and τ is equal to 1.92 (a), 1.84 (b), 1.76 (c), 1.63 (d), 1.51 (e) and 1.40 (f).

Let us focus on the experiment in figure 3.35(e). In the geometry of this experiment, the wave-maker coincides exactly with the top primary fundamental interval. One can isolate the attractor branch 1 by doing Hilbert filtering in frequency, around ω_0, and in space, by keeping only the negative horizontal and vertical components of the wave vector. One then can combine the horizontal and vertical density gradients to obtain the density gradient along η_1, the direction normal to the propagation of the wave. A snapshot of this gradient is plotted in figure 3.36(a). One only can see the branch 1. Figure 3.36(b) shows a cut of this branch, along the dashed black line indicated in figure 3.36(a). ℓ is the distance along the cut, starting from the top left corner. The amplitude of the wave is in black solid line, while the real value is in dashed blue line. The location of the attractor, following the ray tracing prediction, is shown by the dashed dotted black line. One can notice first that the wave length is shorter and shorter, approaching the ray tracing prediction. The waves are more and more focused as they converge towards the attractor. Secondly, one can see that the amplitude of the waves is not the highest on the ray tracing prediction. Indeed, as the waves are focused, the viscosity damps more the wave with a smaller wave

length. Thus, an equilibrium is found by the system, between the damping of small wave length and the amplification of the waves due to focusing. These experiments allow us to decompose the process of ray convergence toward the attractor.

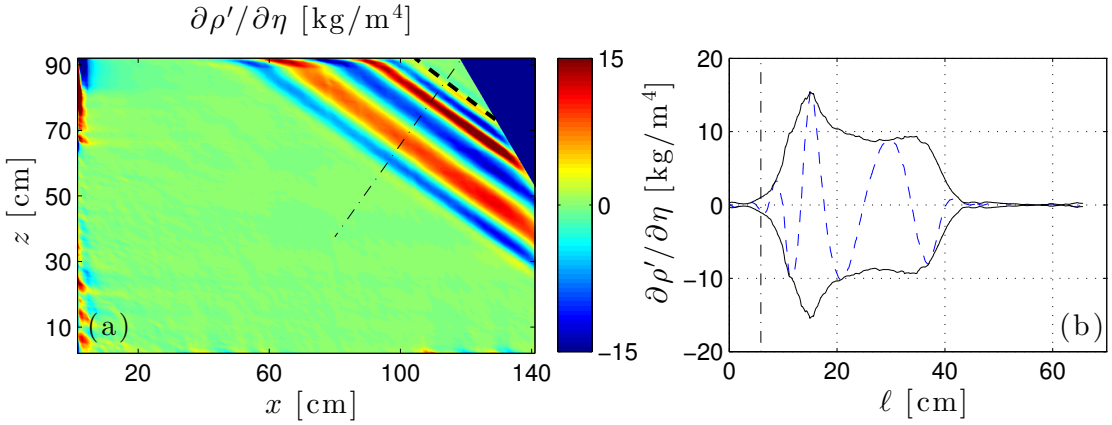


Figure 3.36: (a): Branch 1 of the attractor presented in figure 3.35(e) after Hilbert filtering in frequency around ω_0 and in space to conserve branch 1 (k_x and k_z negative). The dashed dotted line indicates the transversal cut made through the branch while the thick dashed line indicates the location of branch 1 using ray tracing. (b): Amplitude (black solid line) and real value (dashed blue line) of the density gradient fields along the cut presented in (a). The black dashed dotted line indicates where the ray tracing prediction is located on this cut. ℓ is the distance along the cut, varying from 0 (top left corner) to 65 cm (bottom left).

3.6 Comparison with numerical simulations

During my PhD, we collaborated with Ilias Sibgatullin, from the Institute of Mechanics and the Department of Mechanics and Mathematics, at Moscow State University, in Russia. He developed a spectral element method code, especially to reproduce our experimental set-up, and performed all the numerical simulations present in the manuscript. I was not involved in the development of the code, but I performed almost all the analysis of the data: Hilbert transform, time-frequency diagrams, PDFs of the wave-vectors, mean-flow decomposition, drawing of the pictures, ... We compared the numerical simulations to the experiments done by Hélène Scolan and reported in [139], for both stable and unstable cases. We also used the numerics to investigate the 3D effects and the influence of the lateral walls of the tank, in comparison with the experiments I performed. Finally, the numerical simulations were very useful to investigate the gain of potential energy due to mixing for unstable attractors. This is reported in the Chapter 5.

In this section, the code used is described and a comparison with a stable attractor is made. The comparison with an unstable attractor is shown in section 4.1.3, while the 3D effects and the influence of the lateral walls are presented in section 4.3.

3.6.1 Attractors in numerical simulations

Summing up the literature survey, we note that there are only few studies reporting direct numerical simulations of internal [64, 68] and inertial [79] wave attractors. Apart in [35]

in a more oceanographic context, all these studies were performed in two-dimensional settings. Grisouard *et al.* [64] used a trapezoidal geometry, with one horizontal boundary representing a free surface, and free-slip conditions at rigid boundaries of the fluid volume, except at the vertical wall, where barotropic forcing was applied in the form of a uniform horizontal flow of small amplitude oscillating at a chosen forcing frequency. The implementation of free-slip conditions avoid resolving viscous boundary layers. Hazewinkel *et al.* [68] used a similar geometrical set-up but forced the system via a progressive first-mode internal wave. In both cases, Grisouard *et al.* [64] and Hazewinkel *et al.* [68] took advantage of the 2D version of MITgcm, the general circulation model developed by [107] based on finite volume method. The Prandtl-Schmidt number (the ratio of the fluid viscosity to the salt diffusivity) was taken equal to 100 in [64] and 770 in [68]. In their study of inertial waves, Jouve and Ogilvie [79] used a different geometry: a tilted square. They carried out direct numerical simulations using a two-dimensional version of the 3D spectral code SNOOPY [88, 89, 90]. No-slip boundary conditions were imposed via a fictitious absorbing layer outside the fluid domain where the velocity components were forced to vanish, ensuring the global energy conservation with an accuracy of a few per cent.

To our knowledge, there have been no attempts of 3D simulations for direct comparison with experimentally generated attractors. In rectangular domains where normal modes are of primary interest, the dissipation at rigid walls (boundary friction) can dominate the dissipation in the bulk by a factor of 100 [8, 86]. The importance of boundary friction for triadic resonance instability in the case of normal modes in a rectangular domain has already been emphasized by McEwan in [110]. His experimental results of the amplitude threshold for triadic resonance instability of normal modes are indeed in good agreement with theoretical predictions when the sum of a bulk-internal term and a boundary-layer term is taken into account in the calculated energy dissipation. Moreover, he noticed that, on a laboratory scale, internal dissipation becomes comparable with wall dissipation only from a vertical modal number of the order of 10. In the case of the normal modes, an analytical expression for the energy dissipation can be found and reveals that the bulk dissipation depends on the wavelength of the wave while the boundary dissipation is only related to the direction of the wavenumber vector. In contrast to normal modes, attractors are strongly dissipative structures which adapt their typical wavelength (and, therefore, shear and associated dissipation rate) to reach a global balance between the injected and the dissipated energy [125]. Thus, the role of the dissipation at rigid boundaries as compared with the dissipation by shearing in the bulk of fluid is less clear for attractors than for normal modes. It is also not obvious to what extent 3D simulations are necessary to reproduce the experimental results quantitatively. The present paper aims at addressing these questions about dissipation and 3D effects by performing cross-comparisons of the available experimental data against the results of three-dimensional direct numerical simulations of internal wave attractors using a spectral element method based on the code Nek5000 [52].

3.6.2 Numerical set-up

The numerical simulation of wave attractors faces two major challenges. First, the fluid motion is highly nonlinear, and accounting for nonlinear interactions is crucial for the dynamics, even for weak interactions. Second, the Schmidt number (Sc), defined as the ratio of water kinematic viscosity and salt diffusivity, is close to 700 in a salt-stratified fluid. So the spatial scale of the density perturbations can be much smaller than the scale of the velocity perturbations and more demanding in terms of spatial resolution. The scale under which no scalar gradient remains because of diffusion effect is very small and

smaller than the usual Kolmogorov scale L_K used as a mesh criterion for direct simulations where $L_K = \mathrm{Re}^{-3/4} \times L$ with L the integral scale and Re the large scale Reynolds number. Strictly speaking, this small scale where scalar diffusion takes place can be estimated with the Batchelor scale $L_B = L_K \times \mathrm{Sc}^{-1/2}$ [5, 24, 136].

The first numerical simulation of the formation of internal wave attractors [64] used finite volume method, one of the most popular state-of-the-art tools in computational fluid dynamics. However, as noted by these authors, the numerical simulation could only reproduce the dynamics of the attractors for Schmidt number less than 100. In addition, the discretization of convective terms produces a numerical viscosity, which acts similarly to a real viscosity. This numerical artefact blurs the fine-scale structures arising due to the high value of the Schmidt number and it may also introduce substantial errors in calculations of the long-term dynamics of attractors (at time scales of tens or hundreds of periods). However, for the current study, the long time intervals are precisely of particular interest to study the growth, saturation and cascades of secondary instabilities.

As an alternative, the Galerkin method represents a highly efficient approach to tackle the nonlinear interactions if a full system of basis functions subject to boundary conditions can be used. A pseudospectral approach offers an efficient realization of the Galerkin method. In [79], this approach has been used to study nonlinear interactions in attractors of inertial waves. In the present work we have chosen the method of spectral elements which combines the accuracy and high resolution of spectral methods with geometric flexibility of finite element methods, and what is particularly suitable for simulation of long-term evolution of fine-scale flows in globally forced geophysical systems [46]. The computational domain is divided into a finite number of quadrilateral (in two dimensions) or hexahedral (in three dimensions) elements and a Galerkin approach is applied to each element. For the numerical realization, we use the open code Nek5000, developed by Paul Fischer and colleagues [52], [50] and [51]. In each element, the Lagrange polynomial decomposition is used and applied at Gauss-Lobatto-Legendre points for the sake of stability (to avoid ill-conditioning). The full resulting mesh, consisting of the elements and the Gauss-Lobatto-Legendre points, is highly nonuniform, adding a bit more complexity in post-processing data treatment. However, the efficiency of the code fully justifies such a nuisance. In other words, the approach used weighted residual techniques employing tensor-product polynomial bases. Besides other benefits, it allows “analytical" computation of the derivatives through matrix-matrix products or matrix-matrix-based evaluation

$$u(x,y,z,t) = \sum_{i,j,k} u_{i,j,k}(t)\chi_i(x)\chi_j(y)\chi_k(z), \tag{3.28}$$

$$\frac{\partial}{\partial x}u(x,y,z,t) = \sum_{i,j,k} u_{i,j,k}(t)\chi_i^{'}(x)\chi_j(y)\chi_k(z), \tag{3.29}$$

in which u represents any of the unknown variables, for instance, velocity components, density, etc. χ is a Lagrangian interpolant through the Gauss-Lobatto-Legendre points.

The implementation of a high-order filter in Nek5000 allows to stabilize the method for convection-dominated flows [51]. The time advancement is based on second-order semi-implicit operator splitting methods and stable backward-difference scheme. The additive overlapping Schwarz method is used as a pre-conditioner [50].

The most difficult regions from a computational viewpoint are located in the vicinity of the rigid walls since, in these regions, intense folding of high-gradient density layers may occur, especially in the case of a high-amplitude wave motion. For this reason, a non uniform element mesh in the near-wall regions is preferable for simulations of the

nonlinear dynamics of wave attractors. Typically, we have used meshes with up to 0.5 million elements, with eighth to tenth order polynomial decomposition within each element.

The full system of equations being solved consists of the Navier-Stokes equation in the Boussinesq approximation

$$\rho_m \left(\frac{\partial \vec{v}}{\partial t} + (\vec{v} \cdot \vec{\nabla})\vec{v} \right) = -\vec{\nabla} P + \rho \nu \Delta \vec{v} + \rho_s \vec{g}, \tag{3.30}$$

the continuity equation

$$\vec{\nabla} \cdot \vec{v} = 0 \tag{3.31}$$

and the equation for the transport of salt

$$\frac{\partial \rho_s}{\partial t} + (\vec{v} \cdot \vec{\nabla})\rho_s = \kappa \Delta \rho_s, \tag{3.32}$$

where ρ_m is the density of solution with the constant minimal reference salinity, ρ_s the density perturbation in a unit volume due to local salinity (the full density is $\rho = \rho_m + \rho_s$), ν the kinematic viscosity and κ the diffusivity of salt. Dynamical viscosity and diffusivity are assumed to be constant. We impose no-slip boundary conditions on the rigid surfaces and stress-free condition on the upper surface. The boundary conditions on ρ_s are isolation: $\partial \rho_s / \partial n = 0$ where n is the normal to the wall. Forcing is applied at the vertical wall by prescribing the profile of the horizontal velocity which reproduces the motion of the wave-maker in the vertical direction and takes into account the difference between the width of the wave-maker W' and the width of the tank W. The transverse profile of the forcing is prescribed by stepwise or piecewise linear function. At the central segment of the width W', the horizontal velocity is uniformly distributed in the transverse direction in both cases. At the side segments of width $(W - W')/2$, we prescribe either i) zero velocity or ii) a linear decrease of the velocity from the uniform value to zero. These two versions of transverse profiles of forcing give essentially the same results, with a small quantitative difference in the second version where forcing gives a higher horizontal impulse to the system. Both versions can be implemented in calculations, but the second version of the forcing is found to be much less expensive computationally and the major part of computations was performed with it. The efficiency of the wave-maker used in experiments is not 100%. For this reason, the amplitude of forcing in computations with the piecewise linear case is intentionally reduced by 10% compared to the experimental value, thereby providing a good match between numerical and experimental results.

The comparison between numerical and experimental results is typically complicated by the presence of a thin mixed layer close to the free surface of the stratified fluid in the test tank. Because of this layer, the internal wave beam is not reflected precisely at the free surface. Instead the wave beam undergoes a complex reflection, partially at the interface between the mixed layer and the linearly stratified fluid and partially at the free surface. This complex reflection affects the shape of the attractor [64] and the shape of envelopes of wave motions in the wave beams. To take this layer into account in the numerical model, we introduce a model density distribution where the full depth is denoted H as in experiments, the thickness of the thin mixed upper layer is δ, and the depth of the linearly stratified fluid is $H' = H - \delta$.

3.6.3 Comparison with a stable $(1, 1)$ attractor

A comparison has been made between experiments published in [139] and the numerical simulations, using the same geometrical parameters. 2D and 3D simulations were performed. Both were able to capture the dynamics of stable internal wave attractors. Nevertheless, the amplitude of the attractor in 2D numerical simulations is higher than the

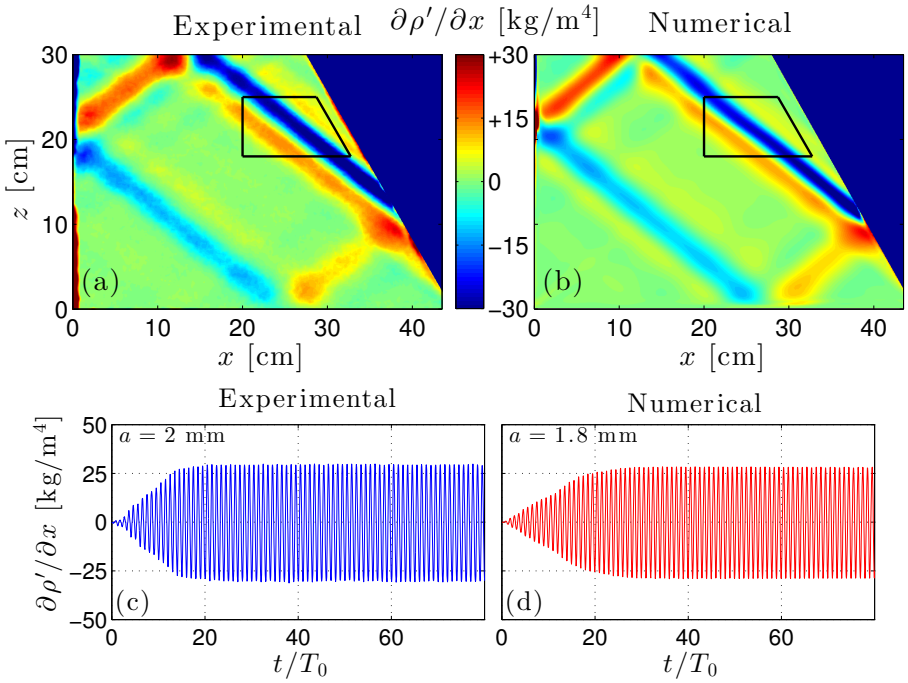


Figure 3.37: Experimental (a) and numerical (b) snapshots of the horizontal density gradient at $t = 50\ T_0$. The amplitude of the wave maker is $a = 2$ mm for the experiment and $a = 1.8$ mm for the simulation. Both attractors are stable. Note that the shade (color online) scale is the same in both panels. The small black quadrilateral defines the acquisition region used for computing the time-frequency spectrum presented in figure 4.8. The wave frequency is $\Omega_0 = 0.62 \pm 0.01$. Experimental (c) and numerical (d) horizontal density gradients as a function of the time, for a point located on the most energetic branch within the black trapezoid depicted in panels (a) and (b). In the calculation we take a piecewise linear approximation of the experimental density profile, with the lower layer of depth $H' = 30.8$ cm and buoyancy frequency N, and the upper layer of depth $\delta = 1.8$ cm with a density gradient 8 times smaller. The total depth of fluid $H = H' + \delta = 32.6$ cm.

amplitude in 3D simulations. This is related to the lack of dissipation, due to the absence of the side walls, present in the 3D set-up, which fully reproduces the experimental set-up. Thus, for a better comparison with the experiments, only 3D simulations have been used. The 2D simulations were performed to follow the mixing caused by unstable attractors. Indeed, simulations of mixing experiments should be very long and 2D simulations are shorter to perform than 3D simulations.

We observe a very good quantitative agreement in our 3D simulations once we introduce a small correction for non-perfect efficiency of the wave generator. Typical snapshots of the computed and measured fields of the horizontal density gradient are shown in figure 3.37, emphasizing a very good qualitative and quantitative agreement between the numerical and experimental data. This good agreement is further confirmed with the time-series of the horizontal density gradient at a point located in the most energetic branch of the attractor as illustrated in figure 3.37. Note that the numerical value of the density gradient is computed at the vertical mid-plane xOz of the test tank. With this comparison, we tacitly assume that the flow is approximately two-dimensional and the standard schlieren technique is applicable [29]. The effects of three-dimensionality are discussed further in the next chapter, in section 4.3.

Conclusion

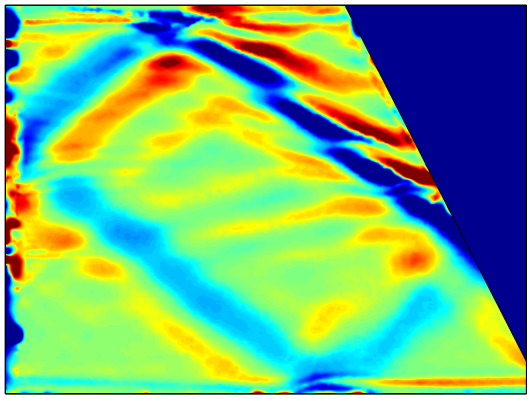
In this chapter, I discussed the linear behavior of internal wave attractors. I started this chapter by reminding the different works of Leo Maas and others who contribute to study this linear regime, which is very rich. Then, I described the different results that I obtained on:

- the Arnold tongues of the (d, τ) diagram and especially the one for the $(1, 1)$ attractors. This allows us to quantify the susceptibility of the geometry with respect to the forcing and also to quantify the nature of the wave attractors: nearly standing (NS) or nearly propagating (NP)
- the wave length and the width of the attractor branches. I have shown their dependance as a function of the different geometrical parameters of the system and I compared the different models in [79, 70, 64] with the experiments. This leads to the conclusion that the linear regime is unlikely in oceanic basins and thus emphasizes that the non-linear regime seems more relevant for the natural cases
- the evolution in time of the wave length, width and amplitude of the attractor branches. This highlights the importance of the geometry, which controls totally the focusing of the energy injected, despite the amplitude of the forcing (in the linear regime)
- the importance of the forcing which highlights the role of the primary fundamental intervals in the establishment of the attractor
- the comparison between experiments and numerical simulations. A spectral element code, adapted to the experimental geometry, has been tested and compared with stable attractor in the linear regime. We found a very good quantitative agreement between the numerics and the experiments.

All these different results emphasize that the geometry and the choice of the operating point in the (d, τ) diagram are determinant for the internal wave attractors in the linear regime. However, attractors in the oceans may not be stable due to focusing until very small scales. Experimentally, Scolan *et al.* have shown that attractors are prone to a triadic resonance instability [139]. This instability is discussed in the Chapter 4 and can be, in certain cases, also controlled by the geometry and the choice of the operating point in the Arnold tongue.

Chapter 4

Triadic resonance instability in internal wave attractors



The triadic resonance instability, abbreviated as TRI in the remainder of this manuscript, is a resonant mechanism involving three waves. One can also talk of three-wave interactions. A primary wave becomes unstable and transfers a part of its energy to two secondary waves, which grow from infinitesimal perturbations. This energy transfer is possible thanks to the quadratic non-linear term of the Navier-Stokes equation. The three waves satisfy the two following temporal and spatial resonant conditions

$$\Omega_0 = \Omega_1 \pm \Omega_2, \tag{4.1}$$
$$\vec{k}_0 = \vec{k}_1 \pm \vec{k}_2. \tag{4.2}$$

Ω_i is the dimensionless frequency and $\vec{k}_i$ is the wave vector of each wave. The index i can be 0, for the primary wave, and 1 or 2 for the secondary waves.

TRI in internal-waves has been first investigated experimentally and theoretically by Davis and Acrivos [31] and Hasselmann [67] in 1967, in a configuration with two layers of different densities. For a linearly stratified fluid, McEwan [110, 111, 112] is the first one to study these three wave interactions, also experimentally and theoretically, and in a rectangular basin. The visualization technique was shadowgraphy and the forcing was made by a moving vertical boundary, which created a vertical mode. The frequency of this mode is set to obtain standing waves in the basin. For forcing with high amplitude, this mode is destabilized and leads to two secondary waves. Benielli and Sommeria [8] have performed similar experiments later, forcing the waves by vibrating the tank. They measured the density using dye lines and a local conductivity probe. These experiments have shown that TRI appears only above a given threshold. Approximately at the same period, Bouruet-Aubert *et al.* [19] performed the first numerical simulations of the temporal evolution of a vertical mode in a linearly stratified fluid. They measured the growth rate of the instability and the wave vectors of the different waves, to compare with the inviscid theory. This work has been continued by [26], to see the transfer of energy between scales.

Few years ago, experiments on well controlled vertical modes and beams have been carried out after the development of a new wave-maker [115]. This powerful tool allows to generate beams with precisely controlled properties. Consequently, experiments on unstable vertical modes have been made by [78], using SyS as a visualization technique. The wave-maker was also used to observe TRI into inertial wave beams [13] or into internal wave beams [16]. Bourget *et al.* [16] verified the TRI theory for plane waves, by measuring the growth rate and the wave vectors of the three waves. Effects on TRI due to the size of the beam have been reported in [17]. Indeed, if the primary wave is contained in a narrow beam, as the secondary waves have different frequencies and consequently different propagation angles, these secondary waves may escape very quickly from the primary beam and thus from the source of TRI. Thus, this could limit the TRI. Karimi and Akylas [80] and Bourget *et al.* [17] have developed a theory to explain such effects on TRI.

TRI in internal wave attractors has been reported only recently by Scolan *et al.* [139]. If the amplitude of the wave-maker and thus, the amplitude of the attractor, is higher than a given threshold, the most energetic branch is destabilized via TRI and creates two secondary frequencies. The resonant conditions are fulfilled by the measured frequencies and wave vectors [139]. TRI has also been suggested in numerical simulations of inertial wave attractors by Jouve and Ogilvie in [79]. Grisouard *et al.* [64] have observed an instability in their numerical simulations of internal wave attractors but the secondary frequencies are super-harmonics of the forcing frequency while Scolan *et al.* [139] reported that the secondary frequencies are smaller than the forcing frequency.

To be complete, TRI has also been observed in the oceans as reported in [2, 1, 101]. In the oceanographic context, the instability is named parametrical subharmonic instability and abbreviated as PSI. This is a particular case of TRI where the two secondary waves created have a frequency equal to the half of the forcing frequency. Indeed, in the ocean, due to the large scales, viscosity does not play a role and the instability leads to two subharmonic secondary waves with the same frequency. Gayen and Sarkar [59] also observed PSI in their realistic numerical simulations of oceanic waves. The limitation of TRI in the ocean is essentially due to the width of the beam instead of the viscosity. Moreover, the rotation of the Earth is an important parameter to take into account as the waves are gravito-inertial waves. The f parameter, controlling the rotation effects, increases the level of complexity of TRI [109].

Three-wave interactions are not limited to internal or inertial waves. Indeed, these interactions between waves have been first studied in the context of capillarity-gravity waves [113]. These waves propagate only at the surface of the water and experience three- or four-wave interactions. Ball [4] has shown that these wave interactions for surface waves can lead to the creation of an internal wave propagating at the interface between the layers of difference densities, under the surface. Non-linear interactions between waves have also been observed for elastic plate waves [28, 14] or plasma waves. Wave interactions are a key ingredient of wave-turbulence, because energy transfers and cascades are done via these interactions. These processes are described in details in chapter 5, on the TRI cascade due to unstable attractors.

This chapter is dedicated to the initial growth of the TRI and its consequences on the size of the attractor branch 1 and on the flow in the tank. First, the TRI as described in [139] is discussed. Then, an other type of TRI is exhibited. Indeed, the TRI can appear directly as a *global* instability, instead of being localized. In the last part of this chapter, both numerical simulations and experiments are used to investigate the wave structure in the transversal y direction, for stable and unstable attractors.

4.1 Triadic resonance instability on the most energetic branch

In this section, the TRI growing from branch 1 is investigated in a experiment performed in a large tank using SyS. Then, the evolution in time of the wave length and amplitude of branch 1 are followed for unstable attractors. Finally, a comparison between experiments reported in [139] and numerical simulations described in section 3.6 is done when TRI is present.

4.1.1 Observations of the triadic resonance instability

Experiments performed in [139] have been performed in the small tank described in section 1.3.1 of this manuscript and using the SyS visualization technique. During my PhD, I performed unstable attractor experiments in the small tank, with PIV or SyS as visualization technique, and in the large tank using only SyS. As Chapter 5 is mainly focused on energy cascade in unstable attractors obtained in the small tank and using PIV, I exhibit in this chapter the case of a TRI in the large tank observed with SyS.

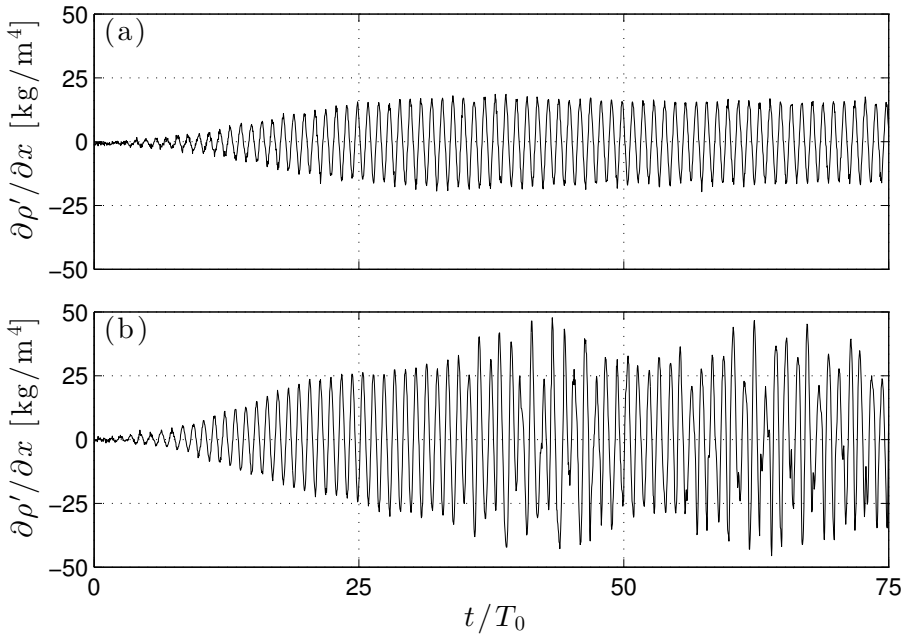


Figure 4.1: Horizontal density gradient fields at a point located on branch 1 as a function of time for two attractors with exactly the same geometry but different forcing amplitudes. (a): $a = 2.2$ mm and the attractor is stable. (b): $a = 2.9$ mm and the attractor is unstable. $(d, \tau) = (0.34, 1.81)$.

TRI is obtained by increasing the amplitude of the wave-maker and thus, the amplitude of the attractor itself. Indeed, the previous chapter has shown that all the energy injected is concentrated into a beam of same width, without any dependance of the forcing amplitude, in the linear regime. Thus, in this regime, the amount of energy of the beam increases with the amplitude of the wave-maker. Benielli and Sommeria [8] and later Bourget *et al.* [17] have shown that TRI starts once the primary wave is above a certain threshold. Consequently, if the amplitude of the attractor is higher than this threshold, TRI starts.

This is illustrated in figure 4.1 where two horizontal density gradient fields at a point located on branch 1 as a function of time are shown for two attractors with exactly the same geometry but different forcing amplitudes. The amplitude of the forcing is slightly higher for panel (b) than the one for panel (a). The instability is clearly visible in panel (b), after $35\,T_0$ while the amplitude is very stable in panel (a).

As in [16, 17, 139], the TRI can be investigated using time-frequency diagrams. Time-frequency diagrams are calculated with the formula

$$S_r(\Omega,t) = \left\langle \left| \int_{-\infty}^{+\infty} \frac{\partial \rho'}{\partial r}(x,z,\tau) e^{i\Omega N\tau} h(t-\tau)\, d\tau \right|^2 \right\rangle_{xz}, \tag{4.3}$$

where h is an Hamming window and r the direction of the density gradient field along x or z, i.e. S_x or S_z. The $\langle\rangle_{x,z}$ symbol means that the quantity is spatially averaged to reduce the noise-to-signal ratio. Typically, this spatial average is made on a region located on branch 1. The calculations are performed with the Matlab toolbox described in [53]. The appropriate choice of the length of the Hamming window allows us to tune the resolution in frequency and time. The resolution is similar to the Heisenberg uncertainty principle in quantum mechanics: one cannot know the position and the momentum of a quantum particle as precise as we want. Thus, the larger the length of the Hamming window, the better the resolution in frequency and the lower the resolution in time. A compromise has to be found between a good accuracy in time and a sufficient frequency resolution to split the different secondary frequencies.

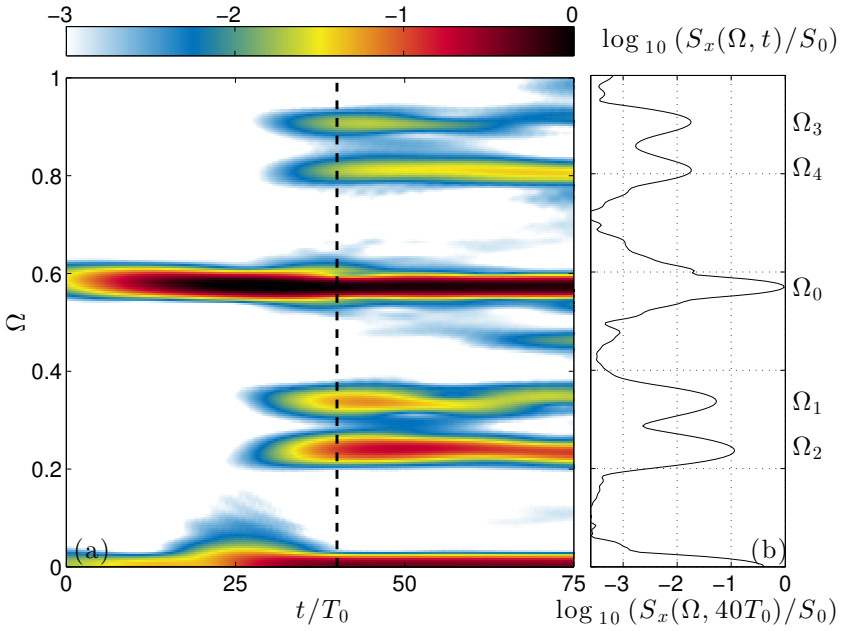


Figure 4.2: (a): Typical time-frequency diagram obtained for an unstable attractor. The experiment used is the one presented in figure 4.1(b). The quantity S_0 is defined as the time average of the main component $S_x(\Omega_0, t)$. The time-frequency diagram is computed on a 10×10 cm^2 square region, close to branch 1. (b): Cut through the diagram at $40\,T_0$. The vertical dashed line on panel (a) shows the location of the cut. The frequencies Ω_0, Ω_1, Ω_2, Ω_3 and Ω_4 are given in front of their corresponding peaks.

The time-frequency diagram of a typical unstable attractor is shown in figure 4.2(a). The frequency $\Omega_0 = 0.57$ of the attractor can be seen from the beginning of the experiment. After approximately 30 periods, two frequencies raise from the noise and increase in amplitude. These are the two secondary frequencies, Ω_1 and Ω_2 created by the TRI. In this manuscript, one defines Ω_1 as the frequency located between $\Omega_0/2$ and Ω_0 while Ω_2 is the frequency located between 0 and $\Omega_0/2$. Note that this definition is the opposite of the definition taken in [139]. Figure 4.2(b) shows a cut along the frequency axis of the diagram, at $40\,T_0$. The different frequencies are relatively peaked. For this particular experiment, one has $\Omega_1 = 0.34$ and $\Omega_2 = 0.24$. Adding these two frequencies leads to $\Omega_0 = 0.58$. Thus, the frequency resonant condition expressed by equation (4.1) is verified, within experimental error bars. In figure 4.2, one can also see two other frequencies, larger than Ω_0. These frequencies are labelled Ω_3 and Ω_4 and verify the frequency resonant conditions $\Omega_3 = \Omega_0 + \Omega_1 = 0.81$ and $\Omega_4 = \Omega_0 + \Omega_2 = 0.91$.

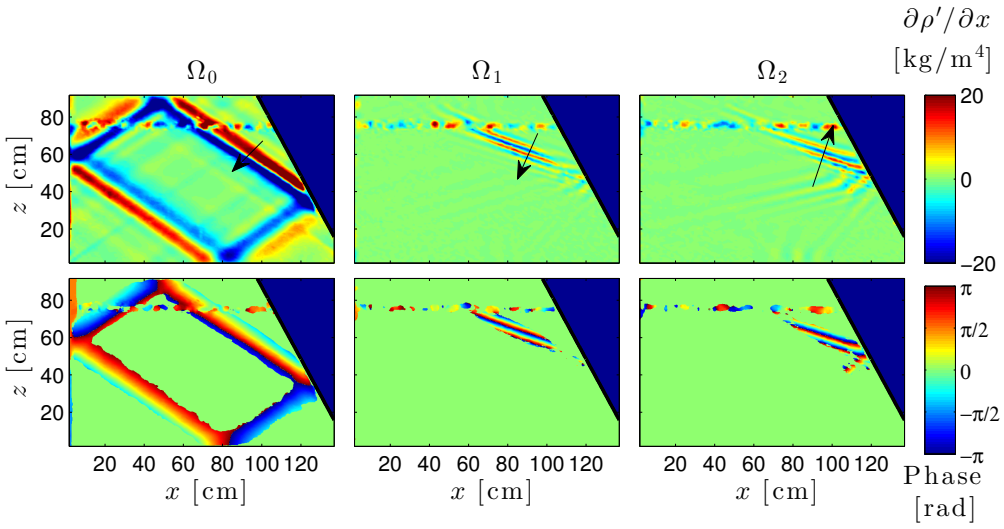


Figure 4.3: The top (respectively, bottom) row presents the real part (resp. phase) of the horizontal density gradient fields after Hilbert transform at $t = 40\,T_0$. Each column corresponds to a filtering around the following three frequencies: Ω_0, Ω_1 and Ω_2 in the first, second, and third columns, respectively. The phase is displayed only where the wave amplitude $|\partial\rho'/\partial x|$ is larger than 5% of the maximum for the first column and than 20% of the maximum for the second and third columns. There is a line with defects at $z \approx 80$ cm which is due to PIV particles that disturb the SyS measurements, along this line only.

The spatial resonant condition, expressed in equation (4.2), can be experimentally verified using a method developed in [16, 139]. Using Hilbert filtering in frequency, it is possible to separate the different wave fields at different frequencies. Figure 4.3 shows, as in [139], the real part of the horizontal density gradient fields and their phase at the different frequencies, Ω_0, Ω_1 and Ω_2. The phase is used to measure the wave-vectors, indicated by the arrows in figure 4.3. Indeed, the phase is related to the wave vector by $\vec{k} = -\vec{\nabla}\phi$. To measure precisely the wave vector, one needs to unwrap the phase in both horizontal and vertical directions, using only the region where the amplitude of the waves is the highest. This is shown on the bottom row of figure 4.3, where the phase is set to zero where the amplitude of the waves is smaller than 20% of the maximum value of the horizontal density gradient field. Then, this unwrapped phase is differentiated and one gets a value for the horizontal and vertical wave vector components for any point (x, z) in the specified region. This leads to a large set of values for k_x and k_z. Then, for each

component, a probability density function (PDF) is made, which allows us to visualize how the different values are distributed. The most probable value of the PDF gives the wave vector components and the error associated with this measure is estimated as the width of the Gaussian fit of the PDF. For the experiment presented in figure 4.3, the PDFs are shown in figure 4.4, for the horizontal and vertical components of the wave vectors. They are nicely peaked, meaning that the most probable value is well defined, even if the waves have a beam shape, instead of being plane waves. These values are presented in table 4.1, with the error bars.

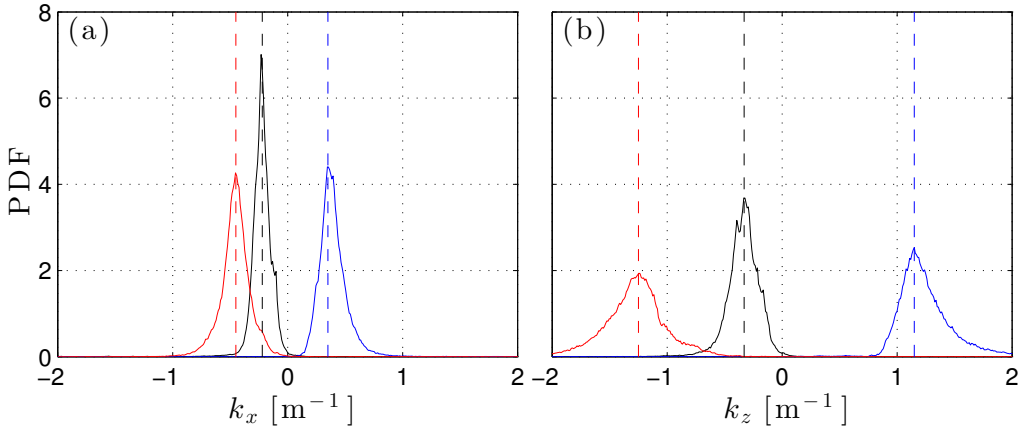


Figure 4.4: Probability density function (PDF) of the horizontal (a) and vertical (b) component of the wave vector for the three different frequencies: $\vec{k}_0$ (black), $\vec{k}_1$ (red) and $\vec{k}_2$ (blue). The vertical dashed lines indicates the maxima of the different PDFs.

Thus, the spatial resonant condition is satisfied within the experimental error bars. Comparing with the values found in [139], one can see that the values of the wave vector components are lower. For the primary waves, the wave vector is more than two times smaller. This is due to the size of the experiment. As shown in section 3.3.4, an increase of perimeter of the attractor by a factor of three leads to a increase of the width, and thus the wave length, of a stable attractor by a factor of $3^{2/3} \approx 2$. Moreover, as presented in section 4.1.2, for unstable attractors, the wave length is higher than the one for the same stable attractor. Consequently, this is fully consistent to have a larger primary wave length here. The secondary waves created here have also larger wave lengths than the ones created by the TRI in [139]. Nevertheless, the ratio between the injected scale and the smallest scale of the waves is equal to 32. Indeed, the wave-maker injects a vertical wave number of $k_{z,\mathrm{inj}} = \pi/H \approx 3.4\ \mathrm{m}^{-1}$. Thus, the horizontal wave number is $k_{x,\mathrm{inj}} = k_{z,\mathrm{inj}} \tan\theta \approx 2.4\ \mathrm{m}^{-1}$ and the wave length $\lambda_{\mathrm{inj}} \approx 1.51$ m. The angle θ is defined by $\theta = \arcsin \Omega_0$. The smallest

Subscript	Ω	k_x (m^{-1})	k_z (m^{-1})
0	0.57	-22 (± 5)	-33 (± 12)
1	0.34	-45 (± 9)	-125 (± 18)
2	0.24	$+35$ (± 9)	$+115$ (± 14)

Table 4.1: Horizontal and vertical components of the wave vector for each frequency of the TRI.

scales is given by Ω_1, whose the wave length is approximately equal to 0.05 m. Scolan *et al.* [139] have found such a ratio equal to 25. This is the same order of magnitude.

4.1.2 Consequences on the size and the amplitude of the branches

For stable attractors, the size of the beam is directly linked with the geometry and the focusing, as shown in section 3.3.4. In this section, the wave length and the amplitude of unstable attractors have been followed in time, during the growth and the steady state. Their time evolution are compared with the one of stable attractors, presented in section 3.3.4.

For this section, the same series of experiments as the ones presented in section 3.3.4 have been investigated. Nevertheless, the attractors considered in this section are unstable, because performed at higher forcing amplitude. As in section 3.3.4, the experiments have been carried out in the large tank, with the SyS visualization technique, during two consecutive days. Only the amplitude a of the wave-maker has been changed, meaning that all experiments have exactly the same geometrical parameters $(d, \tau) = (0.34, 1.81)$. Table 4.2 contains the forcing amplitude of the different experiments, their stability and the symbols used in this section to plot the data.

Experiments	a [mm]	Stability	Symbols
1	0.7	Stable	Green pentagons
2	1.5	Stable	Magenta hexagons
3	2.2	Stable	Blue circles
4	2.9	Unstable	Cyan triangles
5	3.7	Unstable	not plotted
6	4.4	Unstable	Red squares
7	5.1	Unstable	not plotted
8	5.8	Unstable	Black diamonds

Table 4.2: Experiments used for this section. All have been performed with exactly the same geometry: $H = 92.3$ cm, $L = 145.5$ cm, $\alpha = 27.4°$ and $\Omega_0 = 0.57$. Consequently, $(d, \tau) = (0.34, 1.81)$. The experiments carried out at low forcing amplitude, also used in section 3.3.4, are stable while the ones performed at high forcing amplitude are unstable. The symbols used to plot the wave length and amplitude in figure 4.5 are detailed in the right column. Note that two experiments (number 5 and 7) have not been plotted for the sake of clarity.

The wave length λ and the amplitude of branch 1 $|\partial\rho'/\partial\eta_1|$ are measured as described in section 3.3.4, after frequency and space filterings. Thus, the presence of the TRI does not disturb the measurements of the wave length and the amplitude of the attractor because the wave fields oscillating at different frequencies than Ω_0 do not appear on the filtered image. Figure 4.5(a) shows the time history of the horizontal density gradient field at one point located on the branch 1 for the unstable attractor with $a = 4.4$ mm (see Exp. 6 Table 4.2). The TRI starts around $t = 30\,T_0$. The beginning of the instability is marked by the vertical dashed lines in the three panels of figure 4.5. The wave length and the amplitude of this attractor are plotted as a function of time in figure 4.5(b) and (c), as red squares. The other symbols represent the wave lengths and the amplitudes of five other experiments at different forcing amplitude (see Table 4.2). Figure 3.30 in section 3.3.4 has shown that the three curves for the wave lengths of the stable attractors are collapsed

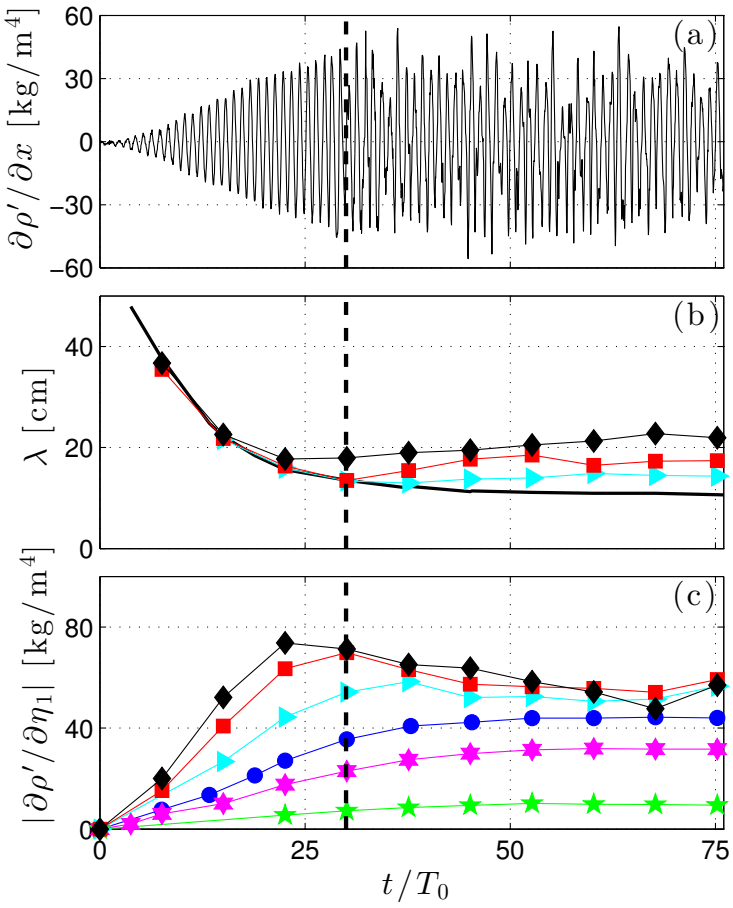


Figure 4.5: (a): Time-history of the horizontal density gradient field at one point located on branch 1 for the unstable attractor with $a = 4.4$ mm (Exp. 6 of Table 4.2). (b) and (c): Wave length and amplitude of branch 1 as a function of time for three stable and three unstable attractors (see Table 4.2). The three curves for the stable attractors are the ones presented in figure 3.30. On panel (b), for the sake of clarity, the average of the wave lengths of these three stable experiments is plotted as a solid black line. The vertical dashed line on the three panels represents the time where the experiment on panel (a) becomes unstable.

along a single curve. Thus, for the sake of clarity, only the average of the wave lengths of these three stable experiments has been plotted as a function of time in figure 4.5(b), using a solid black line. Let us focus on the Exp. 6 of Table 4.2, plotted using red squares. One can see that the wave length of this unstable attractor follows this curve until $30\,T_0$. This means that, before the start of the instability, the attractor experiences the linear geometric focusing described in section 3.3.4. After $30\,T_0$, the wave length of the unstable attractor escapes from the linear focusing curve (solid black line). In figure 4.5(c), where the amplitude of branch 1 is plotted as a function of time, one can see that the amplitude of the attractor reaches a maximum around $30\,T_0$, when the instability starts. Thus, through linear focusing, all the energy injected by the wave-maker is focused into the attractor and the amplitude increases until the TRI threshold is reached, around $t = 30\,T_0$. After $t = 30\,T_0$, when the amount of energy focused into the branch 1 is too high, the instability starts. This brings the attractor to a slightly larger wave length, which appears constant

with time beyond a transient growth, after $50\,T_0$. The amplitude of the attractor decays until it reaches a plateau, around $50\,T_0$. The instants when both the wave length and amplitude are stabilized in time seem to be the same. Consequently, the TRI balances the geometrical focusing: while the attractor is more and more focused by the reflection on the slope, the TRI acts to limit the level of energy in the branch, by transferring part of this energy into the secondary waves and by making the branch 1 wave length larger.

The two other unstable experiments (Exps. 4 and 8 with cyan triangles and black diamonds) exhibit similar characteristics than Exp. 6 (red squares). Indeed, the wave length of both these experiments follow the curve of the stable experiments, until the instability starts. This happens when the amplitude reaches a maximum. In figure 4.5(b), the higher the amplitude of the wave-maker, the earlier the wave length curve escapes from the linear focusing and the earlier the maximum of the amplitude is reached. Thus, attractors with a higher amplitude of forcing are more unstable. After, $t = 50\,T_0$, the different wave lengths are stabilized in time, but the different values reached, named as λ_f, are different. Indeed, the higher the amplitude of the wave-maker, the larger the final wave-length. In figure 4.5(c), after $t = 50\,T_0$, all the amplitudes of the unstable attractors are stabilized around the same value, independently of the amplitude of the wave-maker. This final value for the amplitude is noted $|\partial\rho'/\partial\eta_1|_f$. On the contrary, for stable experiments, the final amplitude depends on the amplitude of the wave-maker only.

The final values for the wave lengths and the amplitudes are plotted as a function of the amplitude of the wave-maker in figures 4.6(a) and (b). The values have been determined in averaging the wave lengths or the amplitudes between 50 and $75\,T_0$. For figure 4.6, the eight experiments of Table 4.2 (three stable and five unstable) have been used. Among the five unstable ones, only three have been plotted in figure 4.5, for the sake of clarity (see Table 4.2). Nevertheless, the extra-two unstable experiments (numbered 5 and 7) exhibit very similar characteristics as the ones presented in figure 4.5. Figures 4.6(a) and (b) summarize the steady states reached by the attractors. When the amplitude of the wave-maker is low, there is no TRI: the wave length is constant and independent of a while the amplitude increases with a. When the amplitude of the wave-maker is large, TRI appears: the wave length increases with a while the amplitude is constant and independent of a.

From these final wave lengths and amplitudes, one can compute the stream function ψ_0 of the attractor branch 1 as a function of the amplitude of the wave-maker a. The stream function is related to the density thanks to

$$-g\frac{\rho'}{\bar{\rho}} = \frac{-iN}{\Omega_0}\frac{\partial\psi}{\partial x}, \tag{4.4}$$

assuming that the waves are plane waves $\psi = \psi_0 \exp\big(i(\Omega_0 N t - k_x x - k_z z)\big)$. To link the stream function with the density gradient fields, one has to differentiate equation (4.4) with respect to x. This leads to

$$\psi_0 = \frac{g}{4\pi^2\bar{\rho}}\frac{\Omega_0^2}{N^2(1-\Omega_0^2)}\lambda^2\frac{\partial\rho'}{\partial\eta_1}. \tag{4.5}$$

The stream function is thus proportional to the wave length squared and the amplitude. One can compute the stream function in our case, even if the branch 1 of the attractor is clearly note a plane wave. In the final state, after $50\,T_0$, when all the wave lengths and the amplitudes appear to be constant in time, the stream function is thus constant in time. The final stream function is plotted as a function of the amplitude of the wave-maker a in figure 4.6(c), in log-log scales. It appears that the stream function depends on the amplitude of the wave-maker to the power 3/2. A linear fit gives to a good accuracy

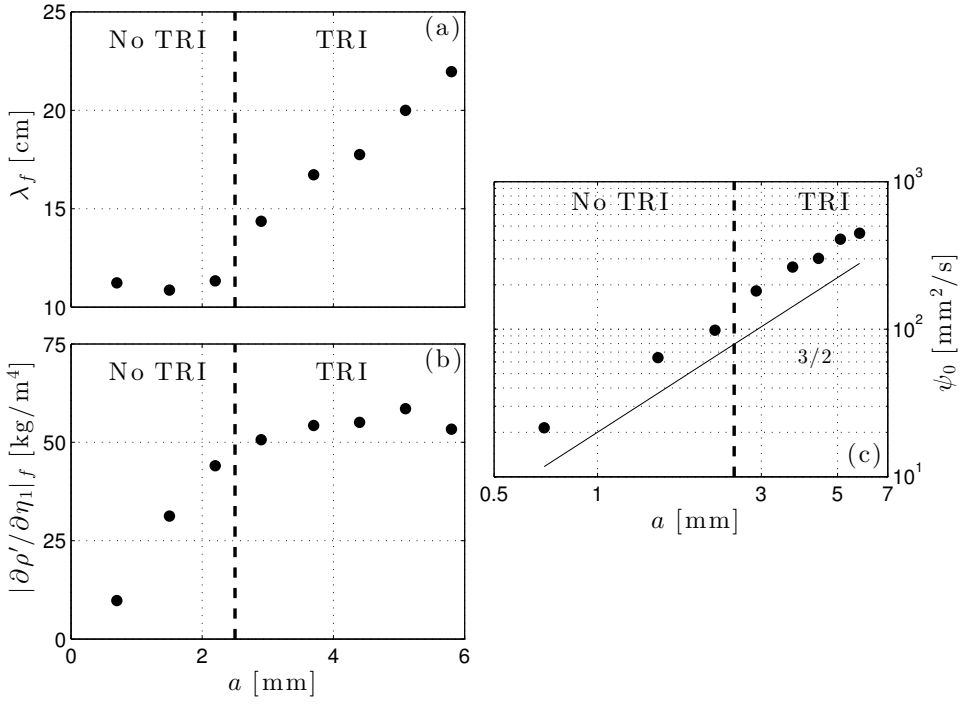


Figure 4.6: Final wave length (a), amplitude (b) and stream function (c) of the branch 1 of attractors as a function of the amplitude of the wave-maker a. The dashed lines on the three panels delimit the lowest amplitudes, where no TRI is observed, and the highest amplitudes, where TRI is observed. Note that the axis of panel (c) are both in log-scale. The solid line on panel (c) shows the 3/2 power law.

$\psi_0 \propto a^{1.44}$, with an exponent 1.44 which is very close to 3/2. This seems independent of the presence of the TRI. At low amplitudes, there is no TRI. λ is constant for geometrical reasons and the amplitudes is thus proportional to $a^{3/2}$. At high amplitudes, when the TRI is present, the final amplitudes saturates and the final wave length increases with a scaling law $a^{3/2}$. We do not have yet any explanation of such a scaling $a^{3/2}$. This is the same scaling as the self-similar scaling developed in [146, 79, 64] and in section 3.3.1 but the connections are unclear. Nevertheless, this gives an estimation of the TRI threshold, which is around $\psi_0 \approx 150$ mm^2/s. Thus the dimensionless value ψ_0/ν of the threshold, which can be assimilated to a Reynolds number, is around 150.

4.1.3 Comparison with numerical simulations

In what follows, we describe the comparison of the experimental and numerical results for the onset of the triadic resonance instability on the most energetic branch of the attractor. The 3D numerical simulations are performed using the spectral element method code described in section 3.6 and have already been validated for stable attractors. Again, these numerical simulations are compared with the experiments reported in [139].

The experimental and numerical snapshots of the horizontal density gradient fields are presented in figure 4.7. The development of TRI is clearly seen in the most energetic branch of the attractor. A very good quantitative and qualitative agreement is again observed between the experimental and numerical wave fields. The experimental and numerical time-series at a point in branch 1 of the attractor show also an excellent correspondence.

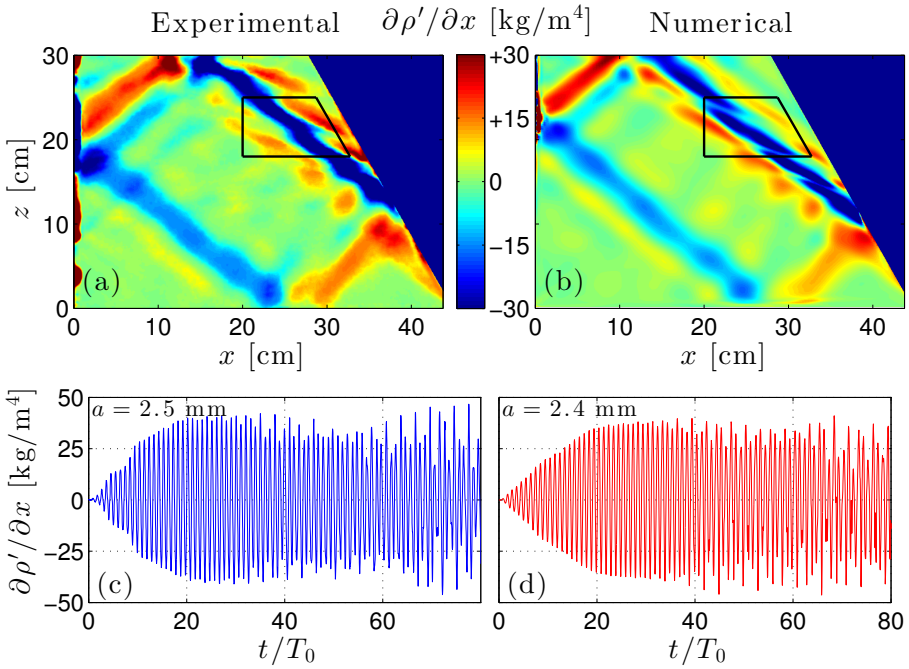


Figure 4.7: Experimental (a) and numerical (b) snapshots of the horizontal density gradient at $t = 50\,T_0$. The amplitude of the wave maker is $a = 2.5$ mm for the experiment and $a = 2.4$ mm for the numerical simulation. The wave frequency is $\Omega_0 = 0.62 \pm 0.01$. Both attractors are unstable and the instability appears first on the most energetic branch. The small black quadrilateral defines the acquisition region used for computing the time-frequency spectrum presented in figure 4.8. Experimental (c) and numerical (d) horizontal density gradients as a function of the time, for a point located on the most energetic branch within the black trapezoid depicted in panels (a) and (b). The density stratification is the same as described in caption to figure 3.37.

Let us now focus on the development of the instability in more detail to see if computations reproduce the experimentally observed triads in temporal and spatial domains. We first consider the evolution of the instability in the temporal domain. The development of the frequency spectrum of wave motion over time is presented in figure 4.8. The time-frequency diagrams are calculated from numerical and experimental data for points as in [16], with the formula presented in equation (4.3). The experimental and numerical diagrams are averaged over the trapezoidal analyzing area shown in figures 4.7(a) and (b). It can be seen that the numerical and experimental spectra agree qualitatively and quantitatively. The signal is initially entirely dominated by the forcing frequency $\Omega_0 = 0.62$: it corresponds precisely to the primary (carrier) wave. Then oscillations with frequencies Ω_1 and Ω_2, which correspond to two secondary waves generated by TRI, slowly develop with time. At $t = 50\,T_0$, these frequencies are $\Omega_1 = 0.24$ and $\Omega_2 = 0.38$. They satisfy the frequency conditions for the triadic resonance

$$\Omega_1 + \Omega_2 = \Omega_0. \tag{4.6}$$

In addition, one can see also two peaks $\Omega_3 = 0.86$ and $\Omega_4 = 1.00$ satisfying temporal conditions

$$\Omega_3 - \Omega_1 = \Omega_0 \qquad \text{and} \qquad \Omega_4 - \Omega_2 = \Omega_0. \tag{4.7}$$

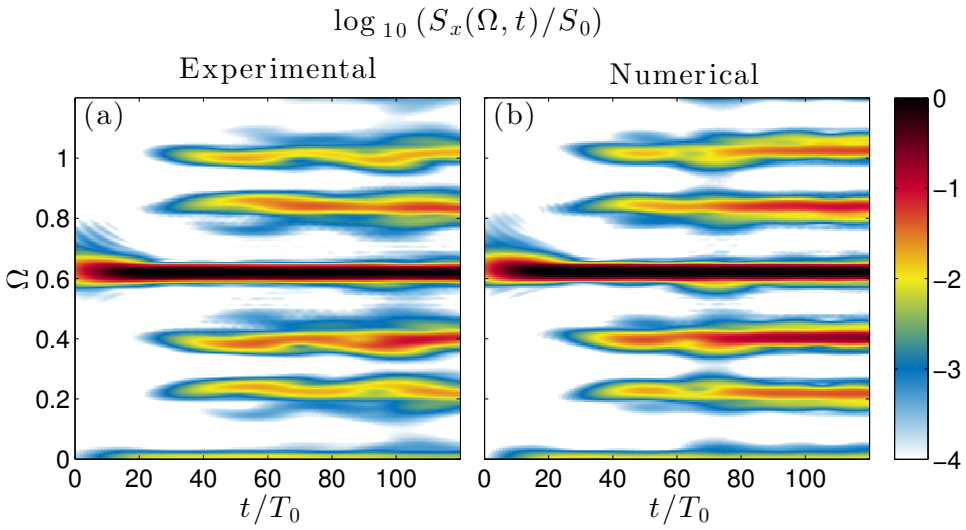


Figure 4.8: Experimental (a) and numerical (b) time-frequency diagrams of data presented in figure 4.7. Both have been computed with the same signal processing parameters, over the same area, located on the most energetic branch and depicted with a black trapezoid in figure 4.7.

To verify the fulfillment of the condition for triadic resonance in space, we apply the Hilbert transform technique [114, 16] to the numerically simulated data in the same way as it is done in experiments reported in [16, 139] or in section 4.1.1. The signal is demodulated with the Fourier transform, filtered around the three frequencies of interest, Ω_0, Ω_1 and Ω_2, and reconstructed back in real space using the inverse Fourier transform. As shown in Figure 5 of [139] or in figure 4.3, it is possible to compute amplitude and phase of each component. The latter appears as patterns of stripes, corresponding to a fixed moment of time. The wave vectors can be derived by differentiating these phases along the x and z directions.

To quantify the wave vectors involved into the triadic resonance in the numerical data, we construct probability density functions (PDFs) for the components of wave vectors, as in section 4.1.1. Using these PDFs for the components of the wave vector corresponding to the primary wave oscillating at Ω_0, we can estimate $\vec{k}_0 = (-63.5 \pm 1, -80.1 \pm 1)$ m^{-1}. The same procedure for the secondary wave oscillating at Ω_1 gives $\vec{k}_1 = (-104.8 \pm 7, -242.5 \pm 20)$ m^{-1}. The phase pattern is slightly more complicated for the component oscillating at Ω_2 as can be noticed in Figure 5 of [139] where lines of equal phase for this frequency are not completely straight and there is a larger error bar on the measurement of the wave vector. Numerically, it is possible to investigate further in the focusing branch of the attractor thanks to the PDF analysis: one realizes that there are two families of collinear wave vectors, which yield multi-peaked PDF of the wave vector components, where the main peak corresponds to $\vec{k}_2 = (46.5 \pm 3, 174.3 \pm 3)$ m^{-1}. These values of the wave vector components closely match the spatial condition of the triadic resonance. The physical interpretation of the other peaks present in the PDF of the wave vector components for the wave field filtered at Ω_1 is unclear.

The triangles of the wave vectors obtained in experiments and simulations are shown in figure 4.9. Again, we observe a good quantitative agreement between the experimental and numerical results. This validates the numerical simulations for unstable attractors. In the remainder of the manuscript, the spectral element code is used to investigate different

problems in complement to the experiments. Indeed, some physical quantities are easily accessible from the numerical point of view. Further in this chapter, the three-dimensional structure of stable and unstable attractors in the y direction is studied using both numerical simulations and experiments. In Chapter 5, the code is used to obtain long-term simulations with mixing in order to measure the evolution of the potential energy of the stratification as a function of time.

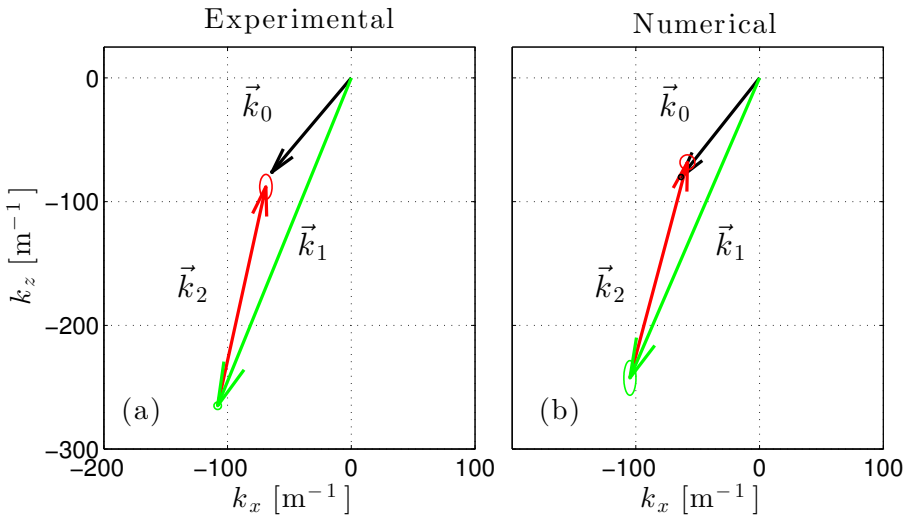


Figure 4.9: Experimental (a) and numerical (b) triads. The three wave vectors are measured from the phase of the waves after Hilbert filtering around Ω_0, Ω_1 and Ω_2. The error bars are given by of ellipses at the arrow tips.

4.2 An other type of triadic resonance instability

In this section, we discuss how the choice of the operating point in the Arnold tongue of $(1,1)$ attractors affects the observed scenario for the onset of triadic resonance instability (TRI). This part is related to section 3.2.3, where the susceptibility of the $(1,1)$ Arnold tongue is investigated for stable attractors. Figure 4.10, also located in section 3.2.3 as figure 3.18, is essential to understand the following section. In Table 4.3 are specified the experimental conditions of the three main *long-term* experiments discussed in this section represented by the symbols ♦, ■ and ★ in figure 4.10. A fourth symbol, ▲, concerns another *long-term* experiment reported in Chapter 5. It is worth to note that the experiments discussed in the section have been made in the small tank using PIV.

4.2.1 Different cases of TRI.

The case of TRI in standing waves in a rectangular domain has been studied in [110], represented by the lozenges ♦ and ◊ in figure 4.10. These cases fall on the vertical line $d = 1$ where $R = 0$. The theoretical analysis presented in [110] assumes that standing primary wave oscillating at frequency Ω_0 can feed two standing secondary waves oscillating at frequencies Ω_1 and Ω_2 provided spatial and temporal conditions of the triadic resonance are satisfied and provided the damping in the system is below a given threshold. The damping is supposed to be primarily associated with the loss of energy in boundary layers at the walls of the domain. The temporal resonance condition of the TRI amounts to $\Omega_0 = \Omega_1 \pm \Omega_2$.

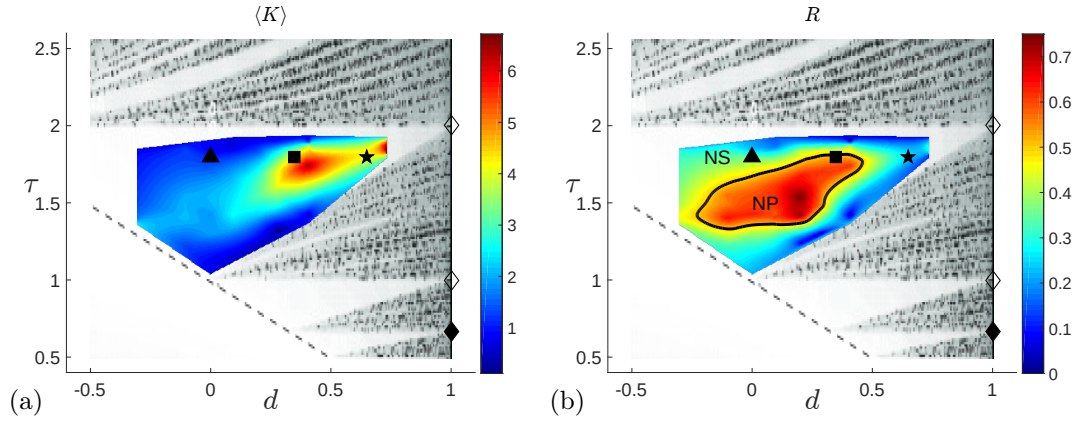


Figure 4.10: Structure of Arnold tongue of a stable $(1,1)$ attractor in terms of the mean normalized kinetic energy $\langle K \rangle$ (a) and the ratio of minimum to maximum kinetic energy R (b). The solid black line shows the contour at the value $R = 0.5$, enclosing the region with nearly propagating waves (NP), while nearly standing waves (NS) are outside this region. These data are also shown in figure 3.18. Superimposed on this picture are four different symbols corresponding to the location of the three main *long-term* experiment geometries discussed in Chapters 4 and 5 of this manuscript and of experiments reported by McEwan in [110]. ■ is for the well-focused $(1,1)$ attractor with propagating waves (section 4.2.1), ★ is for the weakly-focused $(1,1)$ attractor with standing waves (section 4.2.2) and ▲ for the strongly-focused $(1,1)$ attractor with propagating waves (section 5.3.1). ♦ and ◊ are for the case of the rectangular domain discussed by [110].

Since all the waves involved into triadic resonance are standing ones, their half-lengths in horizontal and vertical directions should be equal to L/M and H/N where M and N are integer numbers. Then, the spatial resonance condition can be written as $M_0 = M_1 \pm M_2$ and $N_0 = N_1 \pm N_2$. In practice, high energetic contents are encountered for the triads with "plus" and "minus" signs in temporal and spatial resonance conditions, respectively, i.e. with the cases where secondary waves oscillate at a smaller frequency than the primary wave, and the energy is transferred to shorter spatial scales, privileging the direct cascade. All three waves ($j = 0, 1, 2$) should satisfy the dispersion relation: $(N_j/M_j)^2(L/H)^2 = (1 - \Omega_j^2)/\Omega_j^2$. In the experiments described in [110], the forcing typically corresponded to low mode with $N_0 = 1$ and M_0 varying from 1 to 5. It has been shown experimentally that, at the laboratory scale, it is possible to transfer energy to the waves that are a few times shorter than the primary one. For example, for the low-mode forcing at $N_0 = 1$ and $M_0 = 3$, McEwan [110] observed secondary waves with $(N_1, M_1) = (6, 4)$ and $(N_2, M_2) = (3, 3)$.

The case of TRI in well-focused attractors has been described in [139] and in section 4.1.1. It is a typical scenario of instability in the central region of the Arnold tongue corresponding to $(1,1)$ attractor in (d, τ) diagram. The experiment represented by the symbol ■ in figure 4.10 is also located in the central region of the $(1,1)$ Arnold tongue, for $a = 5$ mm. It shows a similar instability, illustrated on 4.11. For this regime, $\langle K \rangle$ is large and $R \gtrsim 0.5$. Accordingly, the $(1,1)$ attractor has thin well-localised branches. Scolan *et al.* [139] have shown that the onset of instability in such a wave attractor occurs locally first in the most energetic wave beam which has the largest amplitude but the smallest width. This scenario of instability is consistent with the one discussed in [16, 17] and [80]. This is also what it is observed in figure 4.11, for the experiment represented by the symbol ■ in figure 4.10.

Reference or section	Unit	[110]	Section 4.2.1	Section 4.2.2
Symbol in figure 4.10	–	♦	■	★
H	mm	326	303	303
L	mm	377	444	444
a	mm	4.8	5	5
α	∘	90	25.4	14.3
Ω_0	–	0.655	0.61	0.60
d	–	1	0.35	0.65
τ	–	0.66	1.80	1.80
Ω_1	–	0.397	0.36	0.33
Ω_2	–	0.277	0.25	0.27
$\lvert k_{x,\mathrm{inj}}\rvert$	m^{-1}	25.0	7.8	7.8
$\lvert k_{z,\mathrm{inj}}\rvert$	m^{-1}	9.6	10.4	10.4
$\lvert k_{x,0}\rvert$	m^{-1}	25.0	33	9.5
$\lvert k_{z,0}\rvert$	m^{-1}	9.6	37	12.6
$\lvert k_{x,1}\rvert$	m^{-1}	50.0	80	25.3
$\lvert k_{z,1}\rvert$	m^{-1}	38.5	200	66.4
$\lvert k_{x,2}\rvert$	m^{-1}	25.0	45	15.8
$\lvert k_{z,2}\rvert$	m^{-1}	28.9	170	53.8

Table 4.3: Parameters for the three main and *long-term* experiments discussed in this Chapter. $k_{x,\mathrm{inj}}$ and $k_{z,\mathrm{inj}}$ are respectively the horizontal and vertical forcing wave numbers. The horizontal and vertical wave vector components are denoted $(k_{x,i}, k_{z,i})$ in which the subscript i refers to the primary ($i = 0$) or to the secondary waves ($i = 1$ and 2). Ω_i is the corresponding dimensionless frequency. In [110], we have chosen the data with the frequency triplet that is close to those considered in sections 4.2.1 and 4.2.2. The values of wave vectors are evaluated from the parameters of standing waves presented in [110].

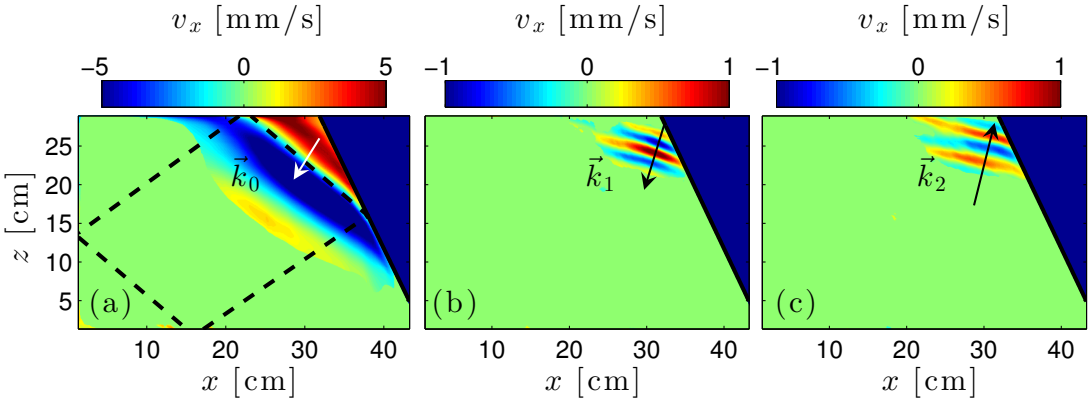


Figure 4.11: Horizontal velocity fields for the experiment indicated by the symbol ■ in figure 4.10 and Table 4.3, filtered at Ω_0(a), Ω_1(b) and Ω_2(c) in frequency and in space to keep only the relevant directions. The velocity field is displayed only where the wave amplitude is larger than 20% of the maximum. The wave vectors are represented by the arrows. The dashed line on panel (a) shows the ray tracing prediction for this geometry.

Owing to local character of instability, the confinement of fluid domain does not affect the instability directly. The focusing provides the energy transfer from the input perturbation which has the scale of vertical size of the fluid domain to the scale associated with the width of the attractor beams, which serves as a primary wave. Subsequent triadic resonance transfers energy to secondary waves. The overall efficiency of the energy transfer from large- to small-scale motions is remarkably high, even at the laboratory scale. Scolan *et al.* [139] describe the case where the typical wavelength of the primary wave represented by the beam of the attractor is roughly 9 times shorter than the wavelength of the input forcing, and one of the secondary waves has even a wavelength roughly 3 times shorter than the primary wave, leading to a reduction factor of 25! This is also visible in figure 4.11 where the primary and the two secondary waves have been disentangled using the Hilbert transform [114].

4.2.2 TRI in weakly-focused $(1, 1)$ attractors

In this section, we describe a new scenario for the onset of instability which is intermediate between those described in the previous section 4.2.1. This new scenario is typical for weak

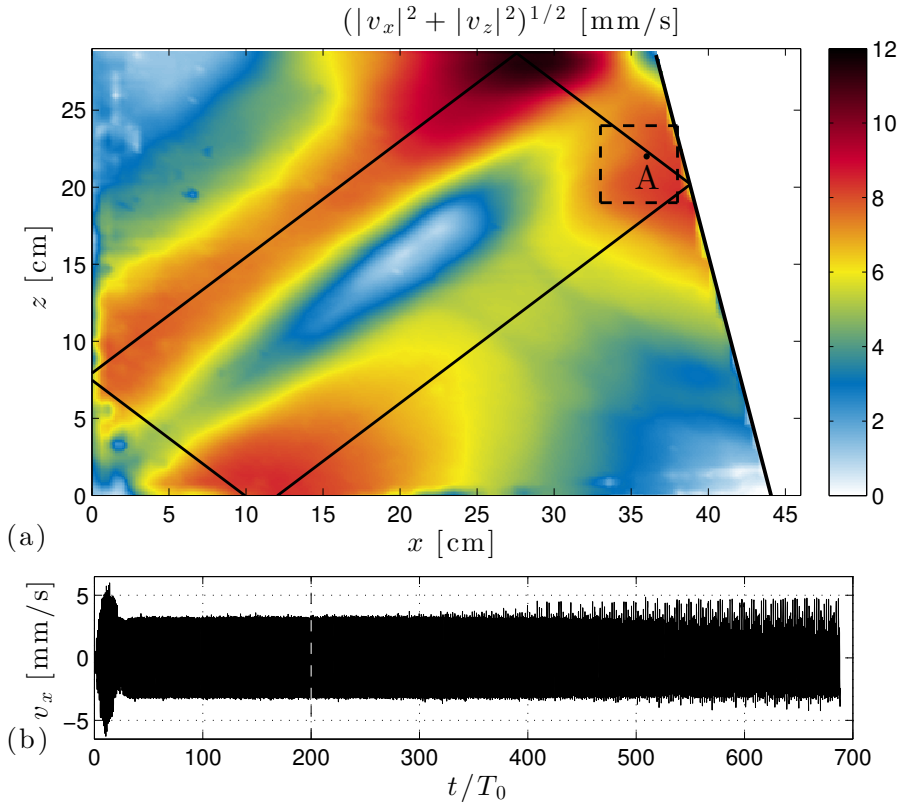


Figure 4.12: Velocity field for the experiment indicated by the symbol ★ in figure 4.10 (see Table 4.3 for the parameters). (a): Picture of internal wave field, filtered around Ω_0, $200\,T_0$ after the start of the wave maker and black lines show the billiard geometric prediction of the attractor. (b): Time-history of oscillations at the point A shown in (a). The vertical dashed line in (b) shows the instant of the picture (a) while the dashed square in (a) shows the region where the time-frequency diagram in figure 4.13 has been calculated. The initial transient is due to the setting of the attractor, while the instability is noticeable after roughly 400 periods of oscillations.

focusing. The observation of triadic resonance has been performed for $(d, \tau) = (0.65, 1.80)$ and $a = 5$ mm. This experiment is represented by the symbol ★ in figure 4.10.

The snapshot of wave pattern after 200 periods of oscillations (approximately 30 minutes of observations) is shown in figure 4.12(a). The time history of oscillations measured at the point A, defined in figure 4.12(a), is presented in figure 4.12(b). After a rather short transient of approximately 25 periods, the signal is stable: the attractor is set. Then, one can clearly see the apparent instability developing after 400 forcing periods, i.e. after more than 1 hour of observations.

Figure 4.13(a) presents the time-frequency diagram for the case illustrated in figure 4.12. It is calculated at each point in space, as in [16], with the formula presented in equation (4.3) and then averaged over the rectangle shown in figure 4.12(a) around point A. Note that, here, it is the horizontal velocity field component, v_x, which is used to compute the time-frequency diagram instead of the horizontal density gradient field, used in figure 4.2. It can be seen that, initially, the signal is entirely dominated by the forcing frequency $\Omega_0 = 0.60$ corresponding to the primary (carrier) wave. Oscillations with frequencies $\Omega_1 = 0.33$ and $\Omega_2 = 0.27$ slowly develop with time. These frequencies correspond to two secondary waves generated by TRI. They satisfy the frequency conditions for the triadic resonance

$$\Omega_1 + \Omega_2 = \Omega_0. \tag{4.8}$$

In addition, one can also see two peaks satisfying differential conditions

$$\Omega_3 - \Omega_1 = \Omega_0 \qquad \text{and} \qquad \Omega_4 - \Omega_2 = \Omega_0. \tag{4.9}$$

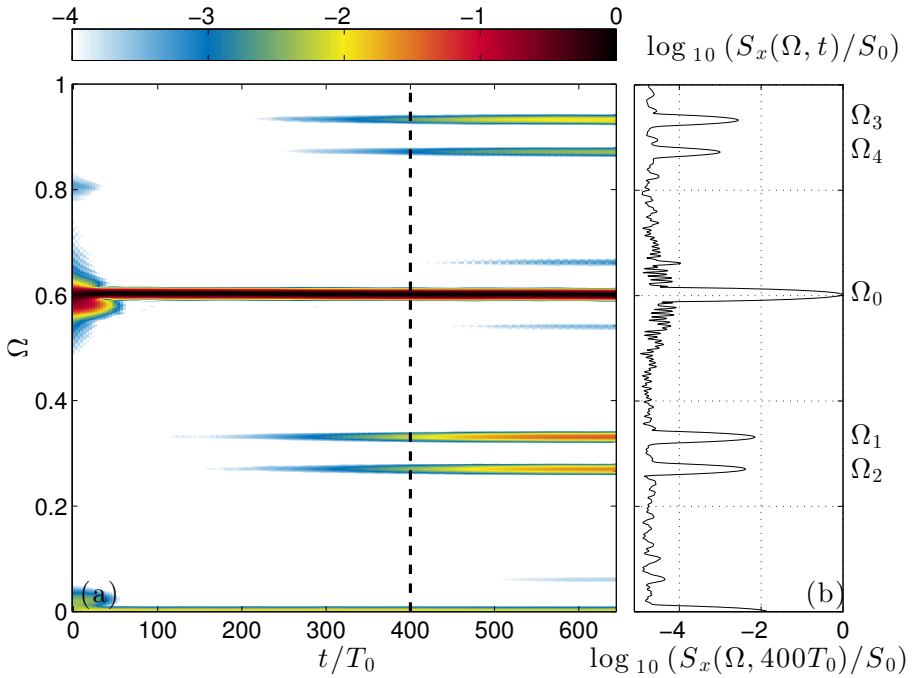


Figure 4.13: (a): Time-frequency diagram of internal-wave field, obtained from a 50 mm side square region, surrounding the point A shown in figure 4.12(a). (b): Vertical cut of the diagram along the frequency axis at $t = 400\,T_0$, indicated by the white dashed line. S_0 corresponds to the time average of the frequency component associated with the primary wave Ω_0. Results are presented for the experiment indicated by the symbol ★ in figure 4.10 (see Table 4.3 for parameters).

Figure 4.14 shows the decomposition of the wave field into the components corresponding to the primary and secondary waves. The decomposition, performed with the help of Hilbert transform [114], reveals node-antinode patterns of amplitudes of secondary waves, similar to Chladni figures. These patterns are present soon in the experiment, but their amplitude increases gradually. Thus, this is very different from TRI presented in [139] or in sections 4.1.1 and 4.2.1 where the waves are created on a very localized region of the tank. Here, the secondary waves appear directly everywhere in the tank, in a shape presented in figure 4.14. The sequences of wave profiles measured along the vertical line indicated in the images are also shown in the right panels. It can be seen that the secondary-wave motion is represented by standing waves of high vertical modes. The standing wave patterns can be further decomposed into the sums of propagating waves. All vectors satisfy the dispersion relation individually. The length of the primary wave can be estimated as $\lambda_0 = 2\pi/|\mathbf{k}_0| = 39.8$ cm with horizontal and vertical components $\lambda_{x0} = 66.1$ cm and $\lambda_{z0} = 49.7$ cm. The quantities $\lambda_{x0}/2$ and $\lambda_{z0}/2$ are reasonably close to the distances from the left top corner of the trapezoidal fluid domain to the reflection points of the attractor. The ray tracing yields the distances to the reflection points 28 and 21.6 cm in horizontal and vertical directions, respectively. Therefore, in the present case, the primary wave has a length scale associated with the global geometry of attractor. By contrast, in the case of spatially localized onset of instability with high growth rate described in [139] (see section 4.1.1 and symbol ■ in figure 4.10.), we have seen that the length of the primary wave

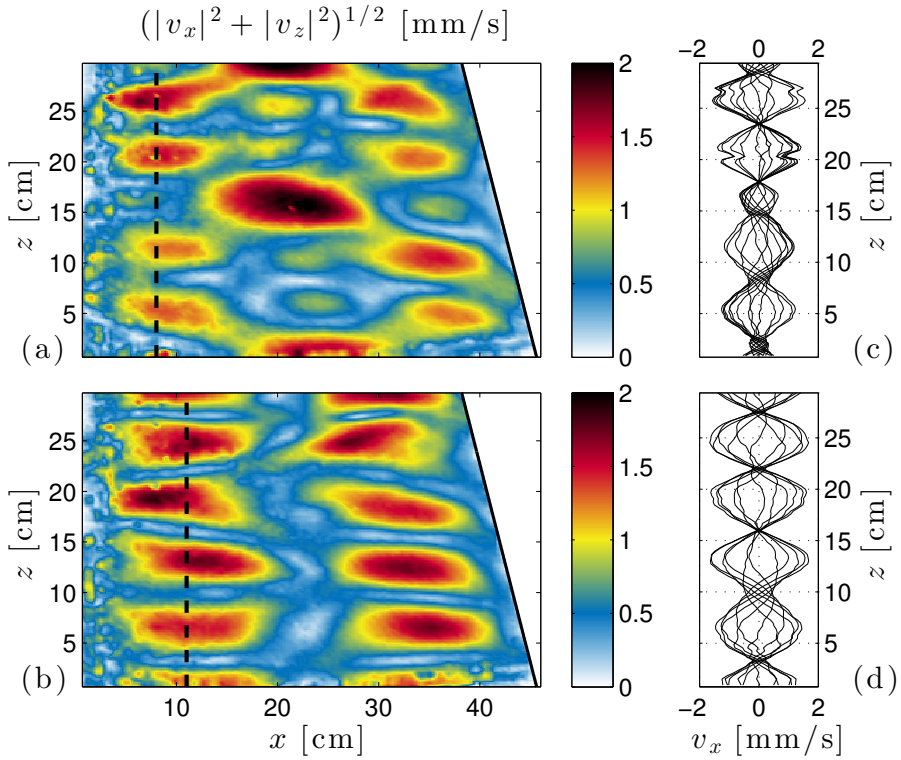


Figure 4.14: Components of the wave field corresponding to frequencies Ω_1 (a) and Ω_2 (b), obtained with the Hilbert transform centered at $t = 620\,T_0$ and using a $85\,T_0$ long Hamming window. Results are presented for the experiment indicated by the symbol ★ in figure 4.10 (see Table 4.3 for the parameters). Note that the components oscillating at Ω_1 and Ω_2 correspond to standing waves as is clearly seen on the sequences of wave profiles shown on the right of each picture (panels (c) and (d)).

is associated with the width of the attractor branch.

Horizontal cuts in figure 4.13 at Ω_1 and Ω_2 are plotted in figure 4.15. At low amplitude of secondary waves, the linear trend is obscured by the instrumental noise, while toward the end of the experiment there is a trend to saturation of amplitudes of secondary waves. The vertical logarithmic representation emphasizes a remarkably linear growth for about three decades (!) in the amplitude of secondary waves. The growth rate of the instability can be estimated to be around $\sigma = 6.5 \times 10^{-4}$ s^{-1}, which leads to a characteristic growth time of the instability around 1500 s (i.e. half an hour or $150\,T_0$).

This time has to be compared with the time scale τ_w set by the limited size of the test tank. It can be defined as the time for secondary waves to perform a horizontal return-trip in the tank: $\tau_w = 2L/c_{gx}$, where c_{gx} is the group velocity in the horizontal direction. This group velocity can be measured using the wave numbers of the secondary waves estimated via Hilbert transform and wave number filtering. It gives $\tau_w \approx 60$ s, which is very small in comparison with the instability growth time of 1500 s. It is worth to note that τ_w is a good measure of the return-trip time of secondary waves because these waves are only slightly inclined. Indeed, their propagation angle is close to 20° since Ω_1 and Ω_2 are around $\Omega_0/2 = 0.3$.

The data presented in [139] or in figure 4.11 clearly show that the triadic resonance develops first in the most energetic branch of the wave attractor, the one connecting the inclined slope to the surface. The data on the wave-vector components presented in [139] yield τ_w around 180 and 320 s for the two secondary waves involved into the triplet which is measured at time around 300 s after emergence of detectable secondary waves. Therefore, the secondary waves could make only between 1 and 2 return trips, and owing to the presence of the vertical component of the group velocity they could not return to their generation site. So, the onset of the instability described in [139] and also seen in the experiment represented by the ■ on the (d, τ) diagram is to a good approximation a spatially

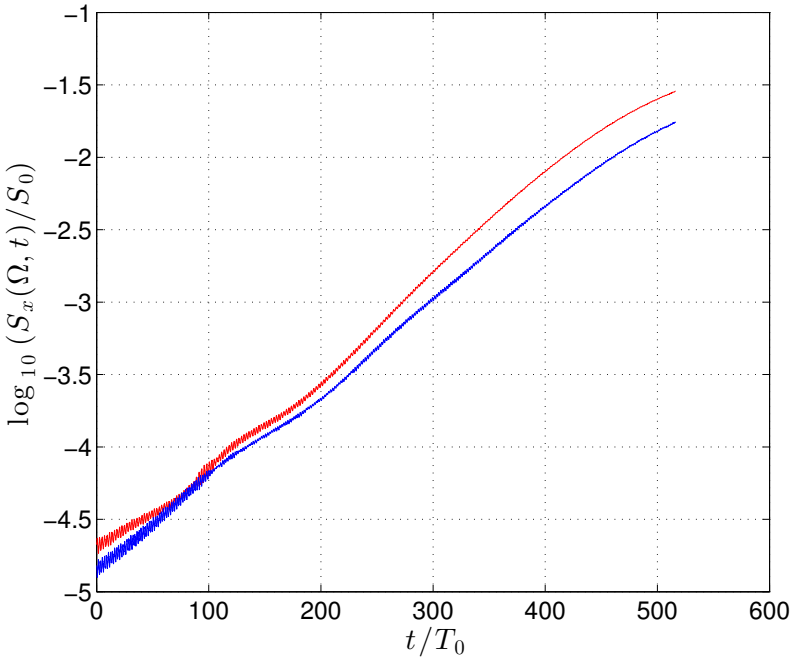


Figure 4.15: Cuts along the time-axis of the time-frequency diagram presented in figure 4.13 at frequencies Ω_1 (red line) and Ω_2 (blue line).

isolated *local* event, while the onset and subsequent development of instability described in the present section is a *global* event, which is inherently related to the confinement. This event has many common features with the instability in a rectangular domain described by McEwan [110].

4.3 Wave structure in the transversal direction: 3D effects and role of lateral walls

A remaining question for both stable and unstable attractors is if the flow in the tank is really independent of the y-coordinate. This is assumed experimentally because the SyS technique needs a bi-dimensional flow, or at least some symmetries [126]. Indeed, in this technique, the image results from the integration of the field along the transverse direction and the ray of light is expected to cross the tank through always the same density perturbation. Moreover, the PIV technique as described in this manuscript is representative of the flow only if the flow does not depend on the y direction. One can expect a bi-dimensional flow from the setup, because it has been designed on purpose. Indeed, the tank is narrow in the transverse y direction and forcing is applied via the wave-maker through almost all the width of the tank. So the flow is expected to be two-dimensional, except very close to both vertical lateral walls where the viscosity plays an important role. Nevertheless, the width is not negligible in front of the other lengths of the system and the two-dimensionality of the flow needs to be verified. This has been done in the experiments and numerical simulations presented in this section, for both stable and unstable attractors. Here, the attractors are well-focused attractors. Thus, when they are unstable, this means unstable by the local TRI, starting on branch 1. Nevertheless, the results presented here should be valid for the global TRI, because there is no so much

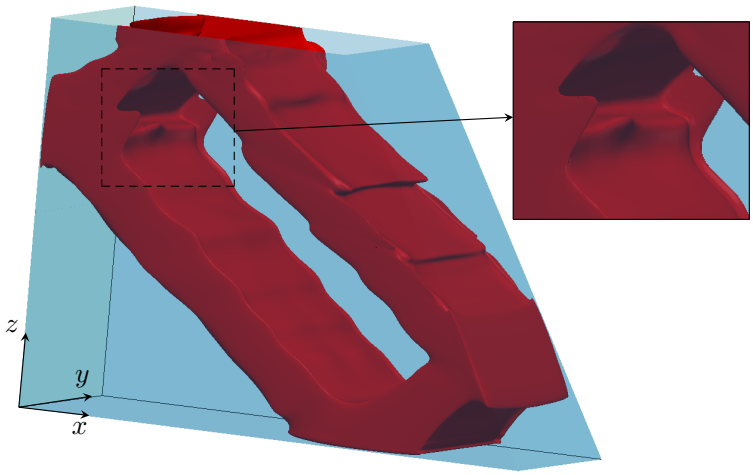


Figure 4.16: Visualization of the three-dimensional effects in the internal wave attractor. Snapshot of the instantaneous magnitude of the velocity field $(v_x^2 + v_z^2)^{1/2}$ produced by the 3D numerical simulations based on the spectral element method for $a = 2.4$ mm. The snapshot corresponds to a contour plot (level 2.5 mm/s) of the amplitude of the velocity field $(v_x^2 + v_z^2)^{1/2}$ at $t = 50\,T_0$. The inset presents a zoom to emphasize an example in which the transversal direction is curved.

differences between the different cases of TRI regarding the y-coordinate.

An overall idea of the importance of three-dimensional effects in wave attractors can be indeed drawn from figure 4.16 which represents an isosurface of the norm of the velocity vector for a 3D simulation at the onset of the instability. We can see the same features as in the vertical xOz plane view in figure 4.7 with the loop of the attractor and the secondary perturbations. However, the iso-surface of the velocity norm is not flat in the transversal direction as the fronts of the perturbations are visibly curved especially on the two top S-shape features in the focusing branch near the slope. Also, close to lateral walls, in particular in corner regions at the intersection of vertical walls, it is possible to see some three-dimensional structures. The inset of figure 4.16 is a zoom on a region where the 3D-effects are particularly visible.

4.3.1 2D visualizations in vertical plane xz at different transversal locations

To check this assumption that the flow is two-dimensional, we use experimental standard PIV technique for several vertical sections at different constant y positions of the light sheet and thus compare flow properties between the different sections. Experiments have been performed with L=43.5 cm, H=30 cm and $\alpha = 25°$, a geometry close to experiments performed in [139]. For these experiments, $(d, \tau) = (0.35, 1.85)$. Different vertical sections in the transverse direction have been illuminated with a vertical laser sheet, coming from the bottom of the tank, which is transparent. A 45° inclined mirror, located below and as long as the tank, transforms a horizontal laser sheet into a vertical one. By simply translating the mirror in the transverse direction, one can illuminate the different test sections. Three series of experiments have been performed, each one with a different amplitude of the wave maker: a = 1.5, 3 and 5 mm. For each series, between 9 to 12 vertical sections have been illuminated by simply translating the mirror in the transverse direction.

Measurements have been carried out in the stationary state of the attractor. For the lowest amplitude experiment, there is no instability of the attractor: the wave maker was stopped only at the end of the full series, once all sections have been illuminated. For the two other series, the instability takes place after a long transient: consequently, the wave maker has been stopped after performing measurements at each transversal location to avoid mixing effects that would modify the stratification and thus the attractor itself. For all series, measurements in the central section of the tank were performed twice, once at the beginning, once at the end. This gives an estimate of the errors made on these measurements and also gives the possibility to check that, after a whole series, the attractor is really unchanged. To compare the different sections of the same series, we focused only on the most energetic branch of the attractor, i.e. the branch 1. Transversal profiles are extracted through this branch, always at the same location. As the horizontal and vertical velocities are measured, it is possible to calculate the velocity along this branch inclined at the angle $\theta = \arcsin \Omega_0$ using the formula $v_{\xi_1} = -v_x \cos\theta + v_z \sin\theta$. The maximum value corresponds to the center of the branch, $\eta_1 = 0$, where η_1 is the coordinate transversal to the branch.

Numerically, with 3D simulation, it is possible to get velocity profiles in the transverse y direction. Two 3D simulations have been performed, with exactly the same geometrical parameters as in [139], and with two different amplitudes of the wave maker: $a = 1.6$ and 2.2 mm. For this experiment, $(d, \tau) = (0.18, 1.81)$. Velocity profiles in the transverse y direction were extracted from the most energetic branch and the velocity v_{ξ_1} along this branch computed as for experiments.

It is important to note that the transverse resolution is much higher in the numerical data (512 points for 17 cm) than in the PIV experimental ones (between 9 and 12 points for the same 17 cm). Moreover, the different points obtained experimentally come from different individual experiments performed at the same input parameters but not from the same unique experiment. Thus, it is difficult to synchronize the different points and we are limited to look at amplitudes of the filtered signals at Ω_0, Ω_1 and Ω_2. In contrast, various quantities can be examined numerically such as the raw signal, the whole signal filtered around Ω_0, Ω_1 and Ω_2 and the mean flow generated by the attractor.

4.3.2 Velocity profiles in transverse y direction

Figure 4.17(a) presents the different velocity profiles for the numerical simulation with $a = 1.6$ mm. For this amplitude, the attractor is stable. The raw velocity profiles for v_ξ are, as expected, very close to the two-dimensionality, except into the boundary layers where the velocity goes to zero. Moreover, it appears clearly that the amplitude of the transverse velocity v_y (represented by a dashed line) is much smaller than the velocity v_ξ along the branch. This is a clear confirmation that the attractor generated by the wave maker is two-dimensional to a good approximation. The difference between the raw velocity magnitudes measured in positive and negative ξ directions comes from the presence of slow near-wall secondary currents superposed with the fundamental monochromatic wave motion in the wave beams as discussed in more detail in the next section.

To extract only the component of the wave field oscillating at the fundamental frequency, one can do Hilbert filtering on the raw profiles around Ω_0 over $20\,T_0$. The modulus of the velocity filtered for the numerical simulation with $a = 1.6$ mm is shown with a thick dashed line in figure 4.17(b). As the raw profiles, it is also very close to two-dimensionality. By looking to the real part of the filtered signal, one can be convinced that the profiles

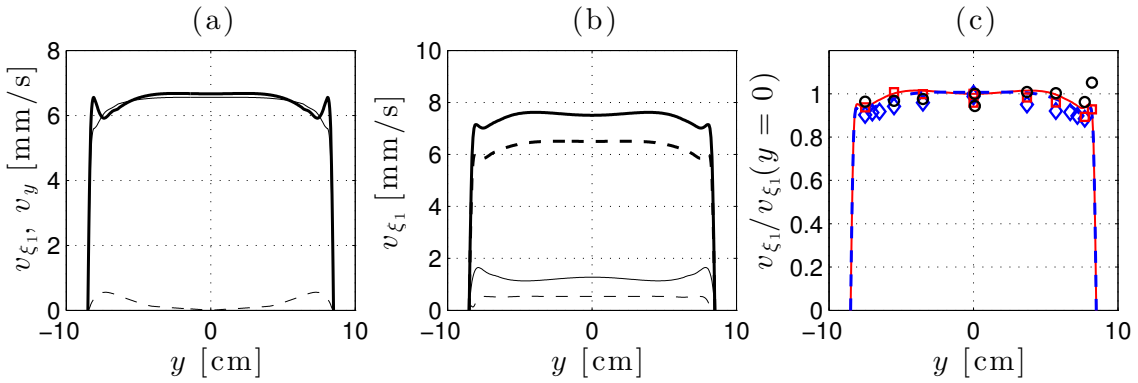


Figure 4.17: (a): Raw velocity profiles as a function of the transversal direction y for the numerical simulation with $a = 1.6$ mm. Thick solid line and thin solid line: maximum ($\max v_{\xi_1}$) and opposite of the minimum (-$\min v_{\xi_1}$) of the velocity v_{ξ_1} for each y over the time history. Dashed line: maximum of the absolute value of the transversal velocity v_y over the time history for each y. (b): Modulus of v_{ξ_1} filtered over $20\,T_0$ around Ω_0 (thick dashed line), for the numerical simulation with $a = 1.6$ mm. Modulus of v_{ξ_1} filtered over $20\,T_0$ around Ω_0 (thick solid line), Ω_1 (thin solid line) and Ω_2 (thin dashed line), for the numerical simulation with $a = 2.2$ mm. (c): Normalized profiles of v_{ξ_1} filtered around Ω_0 for the numerical simulation with $a = 1.6$ mm (thick dashed blue line) and $a = 2.2$ mm (thin solid red line). Points were obtained using PIV experiments: $a = 1.5$ mm (blue diamonds), $a = 3$ mm (red squares) and $a = 5$ mm (black circles).

for v_ξ are exactly the same for positive and negative values. Hilbert transform allows us also to investigate the two-dimensionality of the TRI. As the numerical simulation with $a = 1.6$ mm is stable, one can use the one with $a = 2.2$ mm, which is unstable. Figure 4.17(b) shows the profiles along y of the modules of v_ξ filtered around ω_0 (thick solid line), ω_1 (thin solid line) and ω_2 (thin dashed line) for this simulation. These profiles appear to be nearly constant in the y direction, except close to the edges. This ensures that the instability which develops in the tank is also two-dimensional.

To compare the numerics and the experiments, we can superimpose the experimental and numerical v_ξ profiles after Hilbert filtering around Ω_0 for the different amplitudes of the wave maker. Figure 4.17(c) shows these different profiles: the solid blue line (resp. diamonds) corresponds to numerical (resp. experimental) data for $a = 1.6$ mm (resp. $a = 1.5$ mm) while the dashed red line (resp. squares) corresponds to numerical (resp. experimental) data for $a = 2.2$ mm (resp. $a = 3$ mm). Experimental points for $a = 5$ mm are represented by black circles. All data are normalized by the velocity in $y = 0$ cm to avoid divergences in amplitude due to the location of the point where is measured the velocity along the branch and small discrepancies in wave maker amplitude. All data show again a very good two-dimensionality. The loss of amplitude on the edges, before the boundary layers is less than 10%. Moreover, numerical and experimental data for $a = 1.6$ and $a = 1.5$ mm (dashed blue line and diamonds) show a good agreement between each other. For higher amplitudes $a = 2.2$ and $a = 3$ mm (red line and squares), where the TRI is developed, the agreement is also very good. Even for the experiment with $a = 5$ mm, where TRI is well developed, the shape of the experimentally measured transverse profile is in reasonable agreement with the simulation at $a = 2.2$ mm. All numerical and experimental data collapse in a reasonable way on a curve that ensures that all waves inside the tank are reasonably invariant in the transverse y-direction.

4.3.3 Generation of mean-flows

We previously showed that the velocity field in the transverse direction for the wave attractor confirms the usual 2D approximation as a reasonable one. Nevertheless, it turns out that a closer look on the profiles of v_ξ reveals a discrepancy between profiles of the maximum (max v_ξ) and the opposite of the minimum (-min v_ξ) of the velocity v_ξ as illustrated in figure 4.17(a). Indeed, the raw profiles for the attractor are not totally symmetric: when v_ξ is positive (thick solid line), even if the profile looks two-dimensional, there are some small peaks close to boundary layers which are not present in the profiles when v_ξ is negative (thin solid line). This symmetry breaking suggests the presence of a mean flow, always in the same direction, which modifies the velocity profiles close to boundary layers. To verify this, we analyse now further the data and check for possible mean-flow generated within the tank. To extract this mean-flow from the raw data, we used Hilbert filtering around $\Omega = 0$.

The numerical simulation specially run to thoroughly study the mean-flow has been performed with the same geometrical parameters as the one with the amplitude $a = 1.6$ mm for section 4.3.2. The attractor is stable and is precisely located at the same position in the tank as in figure 3.37. To limit the size of the data saved, the three components of the velocities were recorded only for the two horizontal planes, $z = 10$ cm and $z = 20$ cm, with 0.5 second time-steps. On theses planes, the velocities were saved on a mesh with a good resolution of 128×256 points.

Hilbert filtering at $\Omega = 0$ was applied on time-series of the three velocity components for each point of the x-y plane. We consider the situation once the attractor reaches the steady state. Figure 4.18 shows the mean-flow in the two different horizontal planes,

$z = 10$ cm and $z = 20$ cm. The color represents the vertical velocity component v_z, while arrows represent the horizontal velocity components, $v_x\,\vec{x} + v_y\,\vec{y}$. The wave maker is located at $x = 0$ cm, on the left of the figure. The slope is indicated, on the right, by a vertical white line. Figure 4.7 shows the location of the attractor in the $x - z$ plane. At $z = 10$ cm, the attractor is reflecting on the slope while, at $z = 20$ cm, it is reflecting on the wave maker. These are the two intense regions in figure 4.18, close to the slope at $z = 10$ cm and close to the wave-maker at $z = 20$ cm. As reflections occur in these regions, it can be difficult to extract conclusions for the mean-flow. Nevertheless, it is still possible to examine the mean-flow in the regions where the attractor beams intersect with the planes located at $z = 20$ cm and $z = 10$ cm. These intersection regions are delimited by the dashed rectangles in figure 4.18. The flow in the branches of attractors shows a clear three-dimensional behavior, with recirculation zones where the horizontal components of the velocity vectors are forming jet-like currents close to the vertical walls of the tank to compensate the mean flow in the central part of the wave beam. It is important to emphasize that the magnitude of the mean-flow is much smaller than the velocity of the fluid due to the waves. Indeed, for this attractor, the typical amplitude of the velocity oscillations in the most energetic branch at the intersection with the plane $z = 20$ cm is about 2.5 mm/s while the typical velocities of the mean-flow are about 0.1 mm/s, thus less than 5% of the velocity due to the waves.

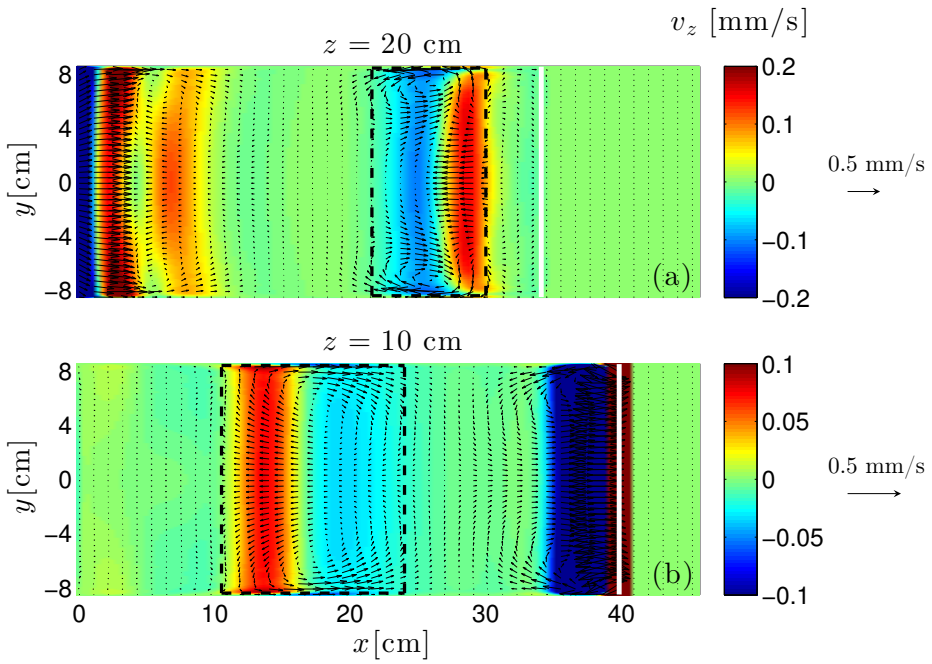


Figure 4.18: Mean-flow (Hilbert filtering analysis at $\Omega = 0$ applied on numerical data) generated in the two different horizontal planes $z = 20$ cm (panel (a)) and $z = 10$ cm (panel (b)). The color represents the vertical velocity component, v_z, while arrows represent the horizontal velocity components, $v_x\,\vec{x} + v_y\,\vec{y}$, with the arrow scale displayed at the right of the figure. The wave maker is located at $x = 0$ cm, on the left of the figure, while the slope is indicated, on the right, by a vertical white line. The dashed rectangles delimit the regions where the attractor beams intersect with the planes located at $z = 20$ cm (panel a) and $z = 10$ cm (panel b).

4.3.4 Dissipation in the bulk and in the boundary layers

To further examine the three-dimensionality of the flow, we determine the spatial distribution of the dissipation in the tank. We first compute the dissipation

$$\varepsilon(x, y, z, t) = 2\nu e_{i,j} e_{i,j} \tag{4.10}$$

where ν is the kinematic viscosity while the strain rate tensor is defined as

$$e_{i,j} = \frac{1}{2}\left(\frac{\partial v_i}{\partial x_j} + \frac{\partial v_j}{\partial x_i}\right). \tag{4.11}$$

v_i and x_i are respectively the components of the velocity field and of the position. Then, for a given y-transversal coordinate, we average on a 2×2 cm^2 square to define the locally averaged dissipation

$$\overline{\varepsilon}(y) = \langle\, \varepsilon(x, y, z, t)\, \rangle_{(x,z,t)}, \tag{4.12}$$

which has also been averaged, after 42 periods after the start of the forcing, over three time periods. This quantity is shown as an inset in figure 4.19.

However, as for example in [11], it is even more explicit to integrate this result horizontally along the transversal y-coordinate as follows

$$\tilde{\varepsilon}(y) = \int_{-W/2}^{y} \overline{\varepsilon}(y')\, \mathrm{d}y' \tag{4.13}$$

in which W is the total width of the tank.

We plot in figure 4.19 the horizontally integrated dissipation $\tilde{\varepsilon}(y)$, normalized by the total dissipation $\tilde{\varepsilon}(W/2)$ within the parallelepiped 2cm×2cm×W, in two different locations:

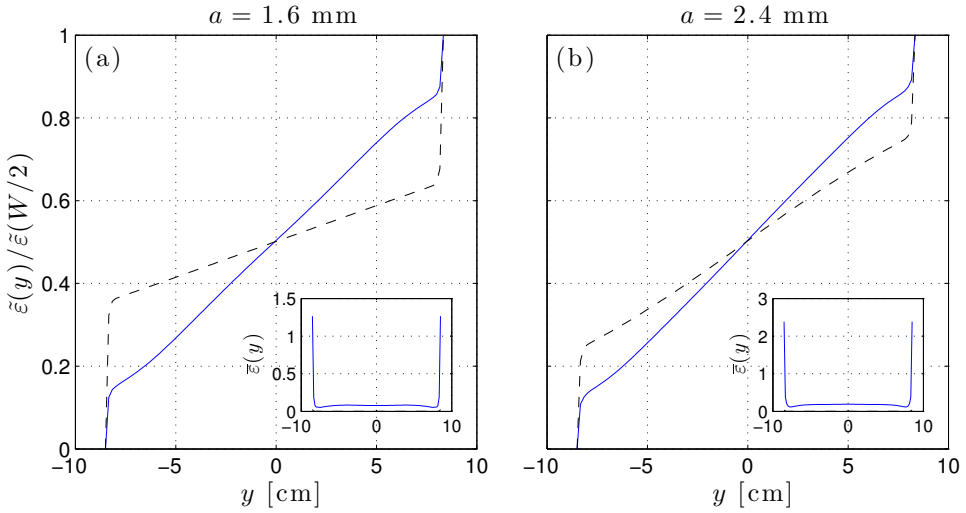


Figure 4.19: Horizontally integrated dissipation $\tilde{\varepsilon}(y)$ (see definition in Eq. 4.13), normalized by the total dissipation $\tilde{\varepsilon}(W/2)$. Panel (a) corresponds to the forcing amplitude a = 1.6 mm, while panel (b) to a = 2.4 mm. The solid blue line corresponds to a region located within the most energetic branch of the attractor, while the dashed black line corresponds to a region close to the center of the tank outside the attractor. The inset present the locally averaged dissipation $\overline{\varepsilon}(y)$ (in mm^2·s^{-3}) for both forcing amplitudes within the most energetic branch.

one in branch 1 after the focusing onto the slope (with the subscript a for attractor), the second one around the center of the tank (with the subscript c for center) and thus far from any branch of the attractor. For a weak forcing a=1.6 mm which leads to a stable attractor, one gets $\tilde{\varepsilon}_a(W/2) = 1.7$ and $\tilde{\varepsilon}_c(W/2) = 0.013$ mm^2·s^{-3}. For a larger forcing $a = 2.4$ mm leading to unstable regime, above values are typically multiplied by a factor 2, since one gets $\tilde{\varepsilon}_a(W/2) = 3.7$ and $\tilde{\varepsilon}_c(W/2) = 0.028$ mm^2·s^{-3}.

Above figure 4.19 emphasizes that, within the most energetic branch, the spatial distribution of the dissipation is only weakly changed while increasing the amplitude of the forcing, and therefore by passing from a stable to an unstable attractor. Approximately 1/4 of the dissipation is located in the boundary layers, which occupy less than 10% of the total width. The three remaining quarters are within the bulk of the flow. The dissipation outside the attractor is significantly altered by the amplitude of the forcing. This is presumably because TRI has generated secondary waves which propagate, outside the attractor and more precisely toward the center of the tank. However, it is important not to overestimate this result since the total dissipation in the center of the tank is more than 100 times smaller than its counterpart within the most energetic branch of the attractor. It was of course expected, since this is where waves, and therefore energy, are trapped.

4.3.5 Synthetic Schlieren test

Using the numerically computed density gradients in the transversal direction, we can provide an estimation of the error made on experimentally measured density gradients by assuming that the flow is two-dimensional inside the tank. We use the simulation for $a = 2.2$ mm as in section 4.3.2, by considering the density gradients instead of velocity fields. These data were available on a point located on branch 1, for all y. Figure 4.20(a) shows the time history of the horizontal density gradient in $y = 0$ cm. TRI occurs after $35\,T_0$ in this simulation.

Dalziel *et al.* [29] have shown that the angle of deflection of a light ray crossing the tank in the i-direction is

$$\alpha_i = \frac{1}{n}\frac{\mathrm{d}n}{\mathrm{d}\rho} W \frac{\partial \rho'}{\partial i}, \tag{4.14}$$

i being x or z. Here W is the width of the tank and n the optical index of water. The quantity $\mathrm{d}\rho/\mathrm{d}n$ is essentially constant and equal to 4.1×10^3 kg/m^3. Equation (4.14) assumes that the flow is two-dimensional and that the density gradients do not depend on the y-direction. This deflection induces displacement of the dots on the camera CCD from which we can measure the density gradients.

With the numerical simulations, one can proceed in the inverse way. Knowing the density gradients and especially their dependence in y, one can compute the displacement that these gradients would have caused on a CCD camera placed at typical experimental distances. For density gradients depending slightly on y, one has to integrate over the width of the tank to get the deflection

$$\alpha_i = \frac{1}{n}\frac{\mathrm{d}n}{\mathrm{d}\rho} \int_{-W/2}^{W/2} \frac{\partial \rho'}{\partial i} \mathrm{d}y. \tag{4.15}$$

This integration assumes that the deflection of the ray is small in x and z directions, so the ray remains more or less at (x, z) constant. That is why one can use only a line profile in y for density gradients. In typical experimental conditions, the CCD camera is placed at 1.75 m of the tank and at 2.25 m of the random dot pattern. The camera has a lens of 25 mm. Considering these experimental parameters, simple geometrical calculations

then allows us to convert the angle deflection α_i into the displacement on the camera Δ_i. Displacements are indicated in figures 4.20(b) and (c) by the red squares, before the onset of TRI (panel b) and after the onset of TRI (panel c). The order of magnitude of these displacements is of few micrometers, while the pixel size of the two different cameras used are equal to 3.45 and 4.65 μm. Thus, the displacements are of few pixels and sufficient for data treatment. Interestingly, one can also compute the displacements as if the flow was strictly two-dimensional, by assuming that, once given (x, z), the density gradients in $y = 0$ are the same for all y in the tank. The deflection is thus as in equation (4.14). These displacements are indicated in figure 4.20(b) and (c) by the blue circles, before the onset of TRI (panel b) and after the onset of TRI (panel c). The difference between blue circles and red squares is very small in both situations, before and after the onset of TRI. This shows that the two-dimensional assumption for the flow is robust and the error using it is very small. One can see in figure 4.20(b) and (c) that the displacements of blue circles are slightly larger than those for red squares. This shows that the density gradients in the center plane xOz are slightly underestimated in the experimental measurements performed with the synthetic schlieren technique, typically by a factor of 5% without TRI and by a factor of 7% with TRI. This combined experimental-numerical check is a nice confirmation of the validity of the SyS technique that justifies the comparisons performed in sections 3.6.3 and 4.1.3 of this manuscript.

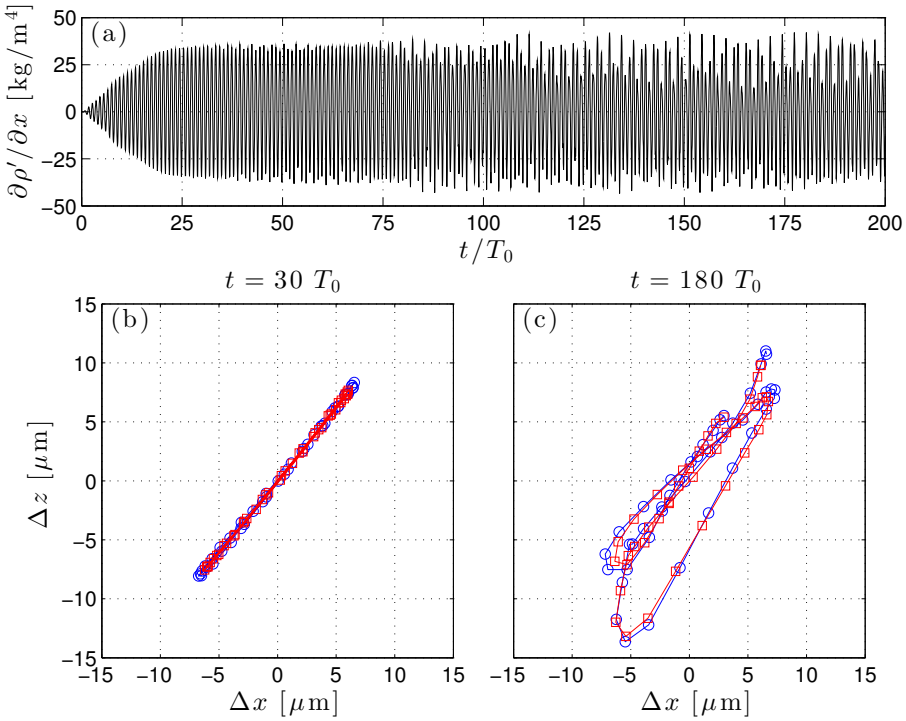


Figure 4.20: (a): Time history of horizontal density gradient in $y = 0$ cm for the numerical simulation with $a = 2.2$ mm. (b): Displacement of the dots on the CCD camera that the simulation would have caused if the density gradients have been measured using Synthetic Schlieren technique at $t = 30\,T_0$, before the onset of TRI. (c): Same as panel b) after the onset of TRI ($t = 180\,T_0$). The blue circles indicated the displacement caused if the flow is assumed to be 2D, while the red squares show the displacement caused without this assumption. The displacements are plotted for two periods of the wave-attractor around the time indicated above the figures.

Conclusion

In this Chapter, I discussed the different triadic resonant instability (TRI) occurring in internal-wave attractors and its consequences on the attractor itself and on the flow inside the tank.

First, I have observed that TRI can appear from the most energetic branch of the attractor and therefore has a *local* character, as previously mentioned in [139]. This *local* TRI can be observed in well-focused attractors. Numerical simulations are in very good agreement with the experiments when TRI is developing. Moreover, I have also shown that TRI has consequences on the amplitude and the wave-length of the attractor branches. Before TRI, as described in Chapter 3, the wave length of the branches is only set by the geometry of the basin and the amplitude increases with the forcing amplitude. When the forcing is too high, TRI is triggered and the amplitude of the attractor becomes independent of the forcing amplitude while the wave length increases. Thus, the TRI can balance the geometrical focusing.

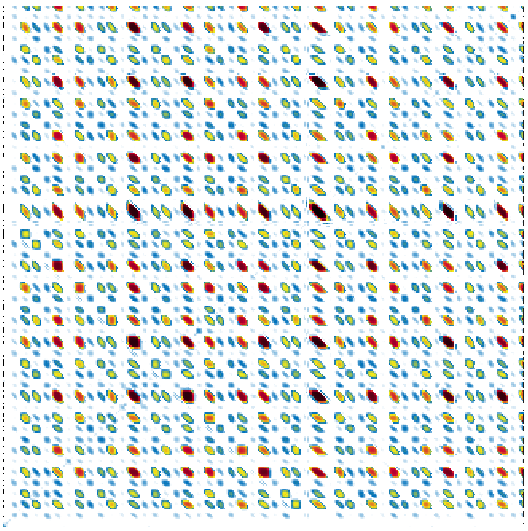
Then, I have shown that the geometry of the attractor can influence the TRI. Indeed, for weakly-focused attractors, I observed a TRI growing *globally*, in all the basin, with a very low growth rate. The secondary waves are found to be standing waves, with a characteristic time to propagate in all the tank much smaller than the growth rate. Thus, it worths to investigate TRI in long-term experiments. This is done in the next chapter.

Finally, I have investigated the three-dimensional aspects of the flow in the tank, using experiments and numerical simulations. The numerically simulated distribution of wave amplitudes across the tank is in good agreement with the experimental data, for both stable and unstable attractors. These data show, as expected, that the flow is quasi independent of the y-coordinate, with or without TRI. Moreover, in the most energetic branch of the attractor, I have shown that approximately 25% of the total dissipation occurs within the boundary layers which occupy less than 10% of the total width.

Three-dimensional calculations allow to estimate the error introduced in conventional SyS technique which assumes two-dimensionality of the flow (or given symmetries) and considers spanwise integrated optical distorsions. The validation of three-dimensional spectral element code in a present nominally two-dimensional problem represents a necessary step for future exploration of fully 3D problems in the spirit of Maas *et al.* [104, 95, 35], which can shed light on the occurrence of attractors in oceanographic problems.

Chapter 5

Non-linear energy cascade and mixing in internal wave attractors



In the previous chapter, we have seen that internal wave attractors are prone to TRI if the amplitude of the forcing is sufficiently large. TRI can be localized on branch 1, as described in section 4.1.1 and in [139], or more global as described in section 4.2.2. Moreover, to capture all the dynamics, the duration of the experiments must be much larger than the time for the secondary waves to propagate in all the tank. Consequently, in this chapter, we describe the long-term behavior of unstable attractors. They are forced at high amplitude and this leads to a triadic cascade of energy. The secondary waves, created by TRI, are also unstable via triadic resonant interactions and more secondary waves appear. The energy at the forcing frequency, localized in the attractor, is thus transferred towards the secondary waves via a cascade mechanism. There are strong signatures of internal wave turbulence.

Wave-turbulence (or weak-turbulence) is a regime where waves have an amplitude sufficiently high that there is a transfer of energy through different spatial scales via wave-interactions. Thus, the energy cascades through a large range of scales from an injected scale towards a small dissipative one. Wave-turbulence has already been observed or described at the surface of liquid with gravity waves [66] or capillary waves [45], in inertial waves in rotating fluids [151], in elastic plates [14, 117, 37], in plasmas... In the oceans, Lvov and Tabak [94] have explained the observed spectra of Garrett and Munk [57] by internal wave turbulence. One can do some analogies with the 3D turbulence, but they are limited. The wave turbulence is a statistical theory of weakly non-linear wave interactions, developed initially by [66, 153, 154]. Let us consider a wave, with its wave vector $\vec{k}$ and its frequency ω. The energy is given by:

$$E_{\vec{k}} = n_{\vec{k}}\omega, \tag{5.1}$$

where $n_{\vec{k}}$ is the wave action. The time evolution of the wave action is given by the wave-turbulence theory, which predicts an out-of-equilibrium solution for the inertial range, in between the injected and dissipate scales. In this range, the energy flux ε is conserved and one has a scaling law for the energy:

$$E_{\vec{k}} \propto \varepsilon^{1/(n-1)} k^{-r}, \tag{5.2}$$

where $r > 1$ and n is the index of the wave interactions. Typically for internal waves, $n = 3$: we talk about three-wave interactions or triadic resonant interaction (TRI). This out-of-equilibrium solution is called the Zakharov spectrum [121]. These spectra have been computed for various systems with wave-turbulence. They also can be found simply by dimensional analysis of the relevant parameters of the systems.

If the forcing amplitude is sufficiently strong, all the waves present in the tank are able to partially mix the fluid. Thus, this is a retro-action of waves on the linearly stratified fluid that carries them. As the stratification is modified, the wave propagation is also modified. The amount of mixing is related to extreme events, caused by the random summation at one point of different waves with different frequencies propagating in the tank. This can cause locally overturns which disrupt the stratification once they are sufficiently intense.

Energy cascade in long-term experiments

An experiment is qualified of "long" when its duration is greater than the time necessary for the secondary waves created by TRI to explore the tank. In section 4.2.2, we have demonstrated the effect of the ratio between the typical growth time of the primary instability τ_* and the duration of the horizontal return-trip τ_w of secondary waves in the tank. If $\tau_* \ll \tau_w$, the onset of instability is local, while for $\tau_* \gg \tau_w$ the secondary waves are more likely to appear in form of standing waves. However, τ_* and τ_w do not form an exhaustive set of time scales. The evolution of the system to saturated state where the energy injection is in balance with dissipation may have a very long time-scale τ_{sat}. Over the time span $0 < t < \tau_{sat}$, the system may experience a cascade of triadic resonance instabilities generating new time-scales of the return trips τ_w. For the full study of dynamics, the system should be observed during the time $\tau_{obs} > \tau_{sat} \gg \tau_w$. Thus, long-term experiments with $\tau_{obs} \gg \tau_w$ can reveal the effects of confinement for the system with $\tau_* \ll \tau_w$ similar to the one described in [139] or in section 4.1.1. In this chapter, we analyze the long-term evolution of the spectrum in the case of unstable attractors and present for the first time the evidence of the effects due to confinement. Thus, most of the experiments presented in this chapter are called long-term experiments. Typically, these experiments are two hour long, which is approximately 700 periods of the attractor. In the two previous chapters, the short-term experiments only last between 100 and $150\,T_0$. During these two hour experiments, data are recorded continuously. Long-term experiments have been only performed in the small tank, with the PIV visualization technique. Stratification is measured with the conductivity probe before and after each experiment in order to evaluate the amount of mixing generate by the waves.

This chapter is centered around two types of long-term experiments, presented in Table 5.1. The first type is composed of experiments at intermediate forcing amplitude (case B), typically $a = 5$ mm while the second type represents experiments with high forcing amplitude $a = 10$ mm (case C). The first category of experiments leads to an energy cascade of discrete frequencies with strong signatures of internal wave turbulence. The second type causes also a cascade in frequencies, which has a discrete part embedded into a more continuous part. Moreover, in the last case, the waves are enough strong to cause partial mixing in the tank. A stable attractor (case A) is used to highlight the differences between a stable linear case and the two unstable ones. As case A is stable, the experiment is short-term only. The geometry of these three experiments is the same and corresponds to the case of well-focused attractors (■). The (d, τ) parameters are approximately equal to $(0.35, 1.80)$.

Case	Type	Ω	H cm	L cm	α °	a mm	t_{max} T_0
A	Stable attractor	0.59	30.0	45.0	27.3	1.5	149
B	Discrete cascade	0.61	30.3	44.4	25.4	5	693
C	Mixing cascade	0.60	30.1	44.2	24.8	10	651

Table 5.1: Typical experiments representative of different cases: low forcing (case A, stable), intermediate forcing (case B, unstable) and high forcing (case C, unstable with mixing).

Examples of experimental velocity fields for case B are shown in figure 5.1 at different stages. During the two first stages, the attractor is growing and is stable. Almost all the

energy is localized around the ray tracing prediction, shown as dashed black lines. On panel (c), the TRI starts and two secondary waves are created, but the energy is still well localized around the ray tracing prediction. At a later stage, on panel (d), the instability is well developed and the attractor is slightly deformed by the secondary waves that seems present in all the tank because one can see some energy which is not localized on the ray tracing prediction. The observations for figure 5.1(d) are also true but amplified several hundreds of periods after the start of TRI. The experimental velocity field is shown for case B at a much larger stage in figure 5.2. The attractor is still visible, but branches are deformed by the presence of secondary waves. As it will be clear below, the internal wave frequency spectrum which was initially a Dirac function has been progressively enriched to give rise to a very complex spectrum, through a cascade of central interest.

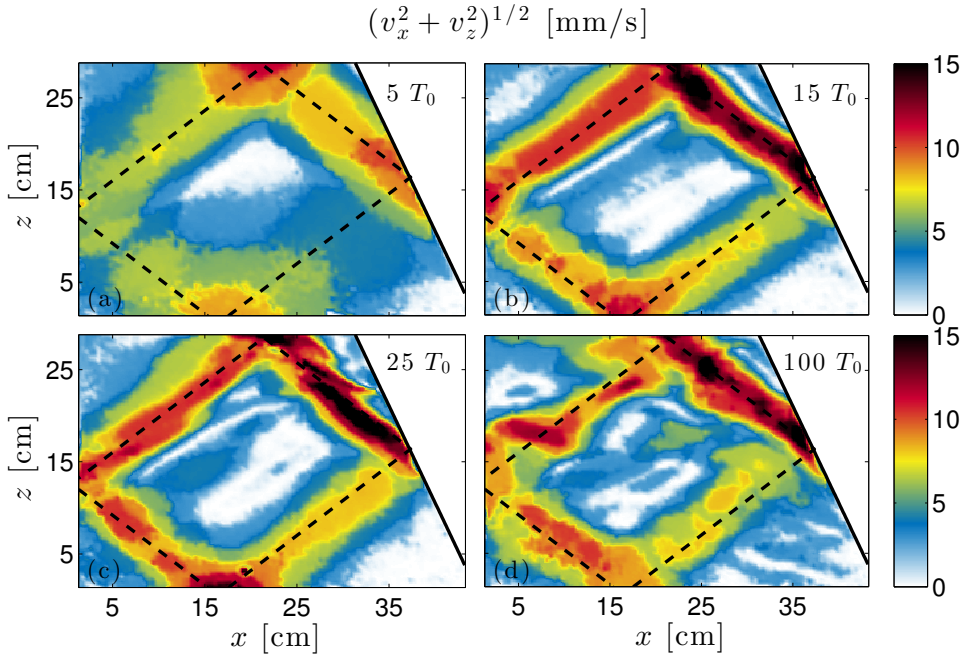


Figure 5.1: Magnitude of the experimental two-dimensional velocity fields for case B (see Table 5.1) at $t = 5\,T_0$(a), $15\,T_0$(b), $25\,T_0$(c) and $100\,T_0$(d). Black dashed lines show the billiard geometric prediction of the attractor, which is fully recovered when considering small forcing amplitude (see Chapter 3) or at an earlier time when considering larger forcing.

The different experiments of Table 5.1 can be analyzed using a time-frequency representation [53] calculated at each spatial point. More precisely, we compute the quantity given in equation (4.3) for the horizontal velocity fields. To increase the signal to noise ratio, the data are averaged over the square represented in figure 5.2 by the white dashed line. We present only the analysis of the horizontal velocity field, but the results are similar for the vertical one. Figure 5.3 presents the basic types of the newly observed cascades, with progressively increasing complexity: a simply monochromatic spectrum (case A of Table 5.1), and rich multi-peak spectra (cases B and C).

The appropriate choice of the length of the Hamming window h allows us to tune the resolution in frequency and time. A large (resp. small) window provides a high (resp. low) resolution in frequency and a weak (resp. good) resolution in time. In order to separate the different frequencies in the cases B and C, a good resolution in frequency is necessary. The three panels have been obtained with a 15 min long Hamming window ($\simeq 80\,T_0$). As

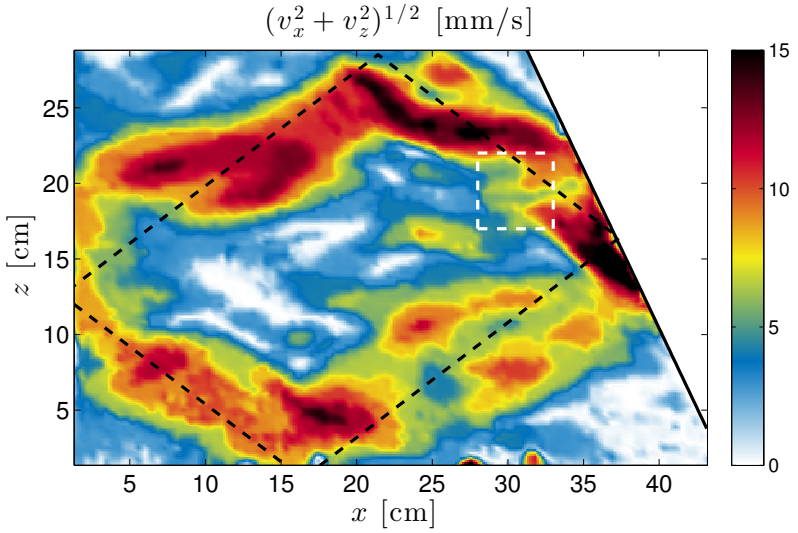


Figure 5.2: Magnitude of the experimental two-dimensional velocity field for case B (see Table 5.1) at $t = 400\,T_0$. Black dashed lines show the billiard geometric prediction of the attractor.

the size of the Hamming window is on the order of the duration of the experiments, some edge problems appear at the beginning and end of the time-frequency diagrams. This can be clearly seen in figure 5.3, at the beginning of all diagrams, around Ω_0, where the peak is wider than in the rest of the experiments. This problem is not visible at the end because we deliberately cut off diagrams just before. The size of the Hamming window is also responsible of the wrong impression that the continuous spectrum can be seen right at the start of the experiment in figure 5.3(c). We checked that a time-frequency diagram with a shorter Hamming window emphasizes that the continuous spectrum does appear gradually like for the secondary frequency peaks in figure 5.3(b). However, with such a choice, the frequency resolution would not be sufficient to discriminate the frequencies.

The richness of the frequency spectrum increases with the amplitude of the wave-maker a. Internal wave attractors in the large amplitude regime present therefore a nice cascade, transferring energy from large-scale monochromatic input to many discrete internal wave frequencies. Moreover, comparing figure 5.3(b) with figure 5.3(c), we note that the frequency spectrum remains qualitatively similar: a “discrete" part, with well-defined peaks, and a “continuous" part (not visible in figure 5.3(b) but really present). However, in case C, the magnitudes of peaks in the “discrete" part of the spectrum fluctuate in time, and the energy content of the “continuous" part is significantly higher (two orders of magnitude), as is clearly visible from the background color. This cascade thus presents features reminiscent of wave turbulence, worth to explore. Moreover, for case C, by measuring the stratification before and after the experiments, a partial mixing of the initial stratification has been found. For the two first cases A and B, no change in the stratification has been observed. The different stratifications are shown further in this Chapter, in section 5.2.3.

In this chapter, we describe the different processes responsible for the discrete cascade in section 5.1 and for the mixing in section 5.2, using cases B and C. Finally, in section 5.3, we discuss the role in the cascade process of the geometry and of the choice of the operating point in the Arnold tongue. Cases B and C, being for well-focused attractors (■), are compared with weakly- or strongly-focused attractors (★ or ▲, see figure 4.10), also forced at large amplitude ($a = 5$ or 10 mm).

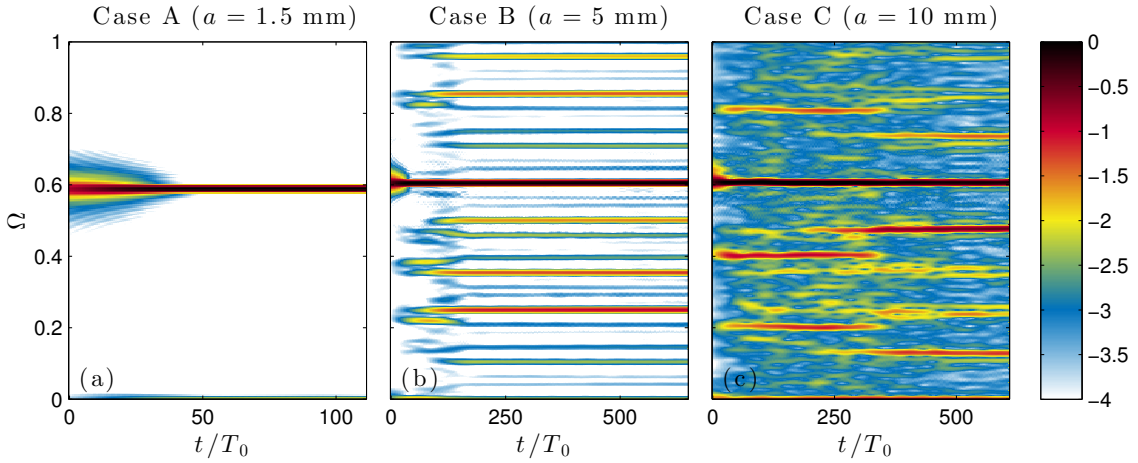


Figure 5.3: Time-frequency diagrams: $\log_{10}\left(S_x(\Omega,t)/S_0\right)$, defined in equation (4.3), for three different forcing amplitudes a. The quantity S_0 is defined as the time average of the main component $S_x(\Omega_0,t)$. The time-frequency diagrams are calculated on the 5×5 cm^2 square region, located on branch 1 and indicated by the white dashed line in figure 5.2 for case B. These three experiments have very close geometries (see Table 5.1), with $(d,\tau)\approx(0.35,1.80)$.

5.1 Discrete TRI cascade

In this section, the case of the discrete cascade is investigated using the experiment presented in case B of Table 5.1. Different tools to highlight the signatures of the internal wave turbulence are developed. First, the signal is analyzed using bispectrum or bicoherence to see the three-wave interactions. Then, the energy spectra is computed in order to see if all the energy follows the dispersion relation of internal waves and spatial spectra are exhibited.

5.1.1 Time-frequency diagram

The time-frequency diagram of case B presented in figure 5.3(b) is also plotted in figure 5.4(a). One can identify at least eight couples of secondary waves. On the cut made through the frequency axis at $t=400\,T_0$ in figure 5.4(b), the four most energetic couples in the spectrum are labelled. The secondary frequencies are named using two indices as follows. The first index i indicates the position in the couple, $i=1$ for frequencies higher than $\Omega_0/2$ or $i=2$ for frequencies smaller than $\Omega_0/2$. The second index n corresponds to the number of the couple. Thus, n varies from 1 to 8, as one can identify at least eight different couples. For each couple n, one has

$$\Omega_{1,n}+\Omega_{2,n}=\Omega_0=0.605, \tag{5.3}$$

with a very large precision of the order of 10^{-3}. The index n classifies the different couples from the most intense ($n=1$) to the less intense ($n=8$). The different values of the frequencies are given in Table 5.2.

The first couple is generated by the attractor itself, as a standard TRI described in [139] or in section 4.2.1. This is shown in figure 4.11, where the different wave fields have been separated. The wave vectors are measured using the method explained in section 4.1.1 and are contained in Table 4.3. One finds $\vec{k}_0=(-33\pm4,-37\pm5)$ m^{-1}, $\vec{k}_1=(-80\pm18,-200\pm$

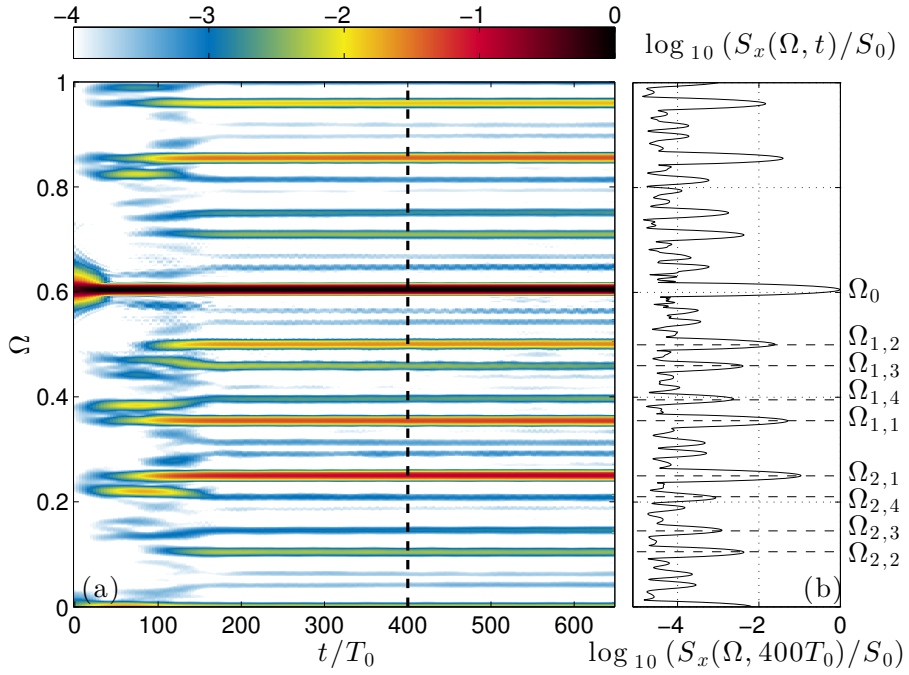


Figure 5.4: (a): Time-frequency diagram of internal wave field, obtained from a 5×5 cm^2 side square region defined in figure 5.2. (b): Vertical cut of the diagram along the frequency axis at $t = 400\,T_0$, indicated by the black dashed line. S_0 corresponds to the time average of the frequency component associated with the primary wave Ω_0. The different frequency peaks corresponding to the four first couples are labelled.

Couple n	1	2	3	4	5	6	7	8
$\Omega_{1,n}$	0.355	0.500	0.460	0.397	0.565	0.312	0.544	0.418
$\Omega_{2,n}$	0.250	0.105	0.146	0.209	0.042	0.293	0.062	0.189
$\Omega_{1,n} + \Omega_{2,n}$	0.605	0.605	0.606	0.606	0.607	0.605	0.606	0.607

Table 5.2: Secondary dimensionless frequencies Ω present on the time-frequency diagram of case B in figure 5.4.

23) m^{-1} and $\vec{k}_2 = (+45 \pm 22, +170 \pm 38)$ m^{-1}. Thus, the spatial resonant condition is fulfilled within the experimental errors. This is the start of the non-linear cascade.

Then, other couples appear and one can note that all the frequencies in the tank are linked by three-wave interactions. The different frequencies of the cascade can be generated as follows. Once the first couple has been created by the attractor, the two frequencies of this couple interact together to create the second couple

$$\Omega_{1,1} - \Omega_{2,1} = \Omega_{2,2}, \tag{5.4}$$
$$\Omega_{2,1} + \Omega_{2,1} = \Omega_{1,2}. \tag{5.5}$$

Thus, the second couple is complete. Now, several interactions are possible between the different frequencies. An interaction between the first and the second couples leads to a third one

$$\Omega_{1,2} - \Omega_{1,1} = \Omega_{2,3}, \tag{5.6}$$
$$\Omega_{1,1} + \Omega_{2,2} = \Omega_{1,3}, \tag{5.7}$$

and an interaction between the frequencies of the second couple creates a forth couple

$$\Omega_{1,2} - \Omega_{2,2} = \Omega_{1,4}, \tag{5.8}$$
$$\Omega_{2,2} + \Omega_{2,2} = \Omega_{2,4}. \tag{5.9}$$

Here, one has four different couples, so eight frequencies. The reader can easily continue to create other frequencies by combining the different frequencies of the different couples. This mechanism leads to an infinite set of discrete frequencies and the first eight couples are at least visible in figure 5.4. At the end, each frequency is linked with a large number of other frequencies by a three-wave interaction

$$\Omega_{m,n} = \Omega_{m',n'} \pm \Omega_{m'',n''}, \tag{5.10}$$

where m, m' and m'' stand for 1 or 2 while n, n' and n'' are the indexes of the couples with $n > n' > n''$. It worths to note that, for all three-wave interactions, one has $n = n' + n''$. Moreover, the larger n is, the less energy is present in the n-th couple as one can noticed in figure 5.4. Note that all the couples interact also with the attractor frequency Ω_0 (see equation (5.3)).

From the attractor frequency and the first couple frequencies, it is very easy to find the other secondary frequencies in the diagram. Nevertheless, in order to prove that all the frequencies really interact between each other, one needs to be more precise and see if the phases of the waves are connected. To do that, the bispectral analysis is used in the next section.

5.1.2 Bispectrum and bicoherence

To detect the frequency triplets, we use the bispectral analysis. The bispectrum is the Fourier Transform of the third-order cumulant function and it measures the extent of statistical dependence among three spectral components (Ω_k, Ω_i, Ω_j) satisfying the frequency resonant condition $\Omega_k = \Omega_i + \Omega_j$. The bispectrum can be normalized and considered in form of bicoherence which is 0 for triplets with random phases and 1 for triplets with perfect phase coupling, as in [46].

The bispectra or bicoherences presented in this manuscript are obtained using the HOSA Matlab toolbox. The data, composed of the time history of the horizontal or vertical velocity fields at one spatial point, is segmented into 16 different records, 50% overlapping between each other. The mean is removed from each record, and the Fast Fourier Transform (FFT) computed. The bispectrum of the k-th record is computed as, $M_k(\Omega_i, \Omega_j) = F_k(\Omega_i)F_k(\Omega_j)F_k^*(\Omega_i+\Omega_j)$, where F_k denotes the FFT of the k-th record and $*$ denotes the complex conjugate. The power spectrum is defined by $P_k(\Omega_i) = |F_k(\Omega_i)|^2$. The spectral and bispectral estimates are averaged across records, and the bicoherence is then estimated as

$$B(\Omega_i, \Omega_j) = \frac{|M(\Omega_i, \Omega_j)|^2}{P(\Omega_i)P(\Omega_j)P(\Omega_i + \Omega_j)}, \tag{5.11}$$

where $M(\Omega_i, \Omega_j)$ is the final estimate of the bispectrum, and $P(\Omega_i)$ is the final estimate of the power spectrum. We also perform a spatial average over the same square region used for the time-frequency analysis. Moreover, the bispectrum and bicoherence obtained for the horizontal and vertical velocity fields are also averaged.

In order to test this tool, one can use it on a simple TRI first. The unstable weakly-focused attractor (★) with the global TRI presented in section 4.2.2 is perfect to test the bicoherence and the bispectrum tools. Indeed, this experiment is a long-term one and

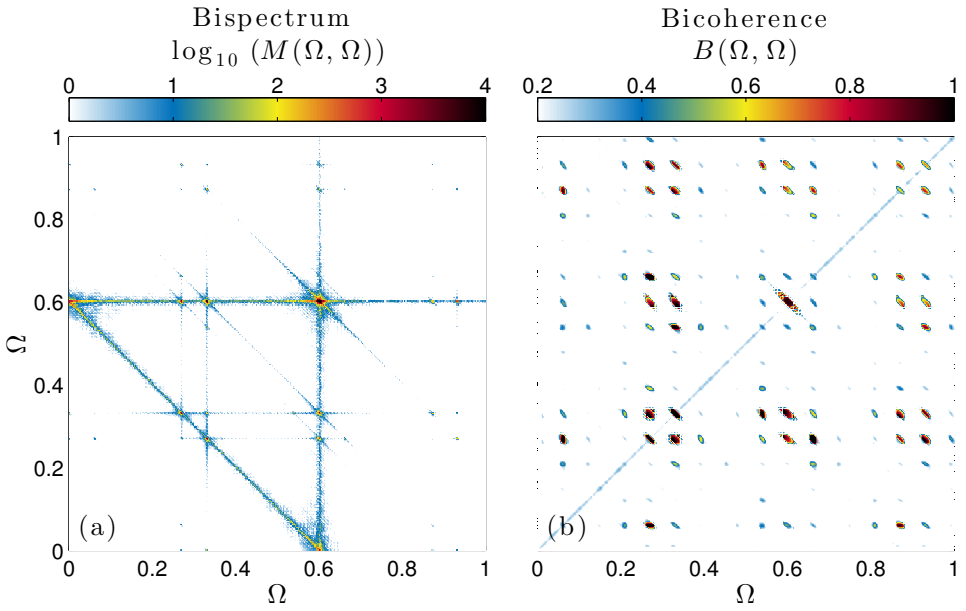


Figure 5.5: Bispectrum (a) and bicoherence (b) for the weakly-focused attractor (★) presented in section 4.2.2.

it exhibits only one couple of secondary frequencies over a very long time. Morever, the growth rate is very small, as shown in figure 4.15. Figures 5.5(a) and (b) show the bispectrum and the bicoherence of this experiment. The signal used to compute the bispectrum and the bicoherence is taken between $200\,T_0$ and $700\,T_0$. First, the bispectrum and the bicoherence in figures 5.5(a) and (b) are symmetric with respect to the bisector. This is consistent with their definitions, where Ω_i and Ω_j can be exchanged. Then, on both figures, one can note different peaks. A peak located at (Ω_x, Ω_y) shows the strength of the interaction between the frequencies Ω_x, Ω_y and $\Omega_x + \Omega_y$. The most intense peak is located at $(\Omega_0, \Omega_0) = (0.61, 0.61)$. Then, in figure 5.5(a), one can distinguish different lines which are horizontal, vertical or oblique. The horizontal and vertical lines are at Ω_0. The oblique line is in between the points $(0, \Omega_0) = (0, 0.61)$ and $(\Omega_0, 0) = (0.61, 0)$. This oblique line shows the interaction between the frequency Ω_x, Ω_y and Ω_0 because, on this line, $\Omega_x + \Omega_y = \Omega_0$. Thus, the three-wave interaction between the attractor and the couple of secondary waves created by TRI is on this line. This interaction corresponds to the two peaks located on this line at the points $(\Omega_1, \Omega_2) = (0.33, 0.27)$ and $(\Omega_2, \Omega_1) = (0.27, 0.33)$. These peaks are also present in the bicoherence in figure 5.5(b), but without the oblique line at Ω_0 because the bicoherence is normalized. On both figures, we also have other peaks at different locations: $(\Omega_0, \Omega_1) = (0.61, 0.33)$, $(\Omega_0, \Omega_2) = (0.61, 0.27)$ and the symmetric ones with respect to the bisector. They show the three-wave interactions between the attractor, one of the two secondary waves and a third frequency, higher than the forcing frequency. Other interactions are also present, between the different harmonics of Ω_0 and the secondary waves. Finally, there is also two peaks, close to the x- or y-axis. They are located at $(\Omega_1 - \Omega_2, \Omega_2) = (0.06, 0.27)$ and $(\Omega_2, \Omega_1 - \Omega_2) = (0.27, 0.06)$. They are visible on the bicoherence but very weak on the bispectrum. They testify of a three-wave interactions between the two secondary waves and a third frequency, created by them. Thus, one can guess the beginning of a cascade, in this experiment too. By looking more carefully the time-frequency diagram in figure 4.13, one can see this third frequency and

its complementary to Ω_0 at the end of the experiment. Thus, the three-wave interactions are easily visible using bispectrum or bicoherence.

To validate completely the use of bicoherence of bispectrum, one can follow the intensity of the $(\Omega_2, \Omega_1) = (0.27, 0.33)$ peak (or the $(\Omega_1, \Omega_2) = (0.33, 0.27)$ peak by symmetry) as a function of time and plot it to compare with the growth rate extracted from the time-frequency diagram in figure 4.13. To do that, the bispectrum has been computed on different time intervals, having the length of the Hamming window used in the computation of the time-frequency diagram. For each bispectrum, the intensity of the secondary wave peaks is normalized by the intensity of the (Ω_0, Ω_0) peak and plotted as a function of time. Figure 5.6 shows the normalized intensity and the comparison with the growth rate, also plotted in figure 4.15 in Chapter 4. The amplitude of the secondary frequencies from the time-frequency diagram and the intensity of the secondary waves peak have similar behavior and show the same growth rate. This validates definitely the use of the bispectrum and bicoherence tools to investigate the three-wave interactions in the tank.

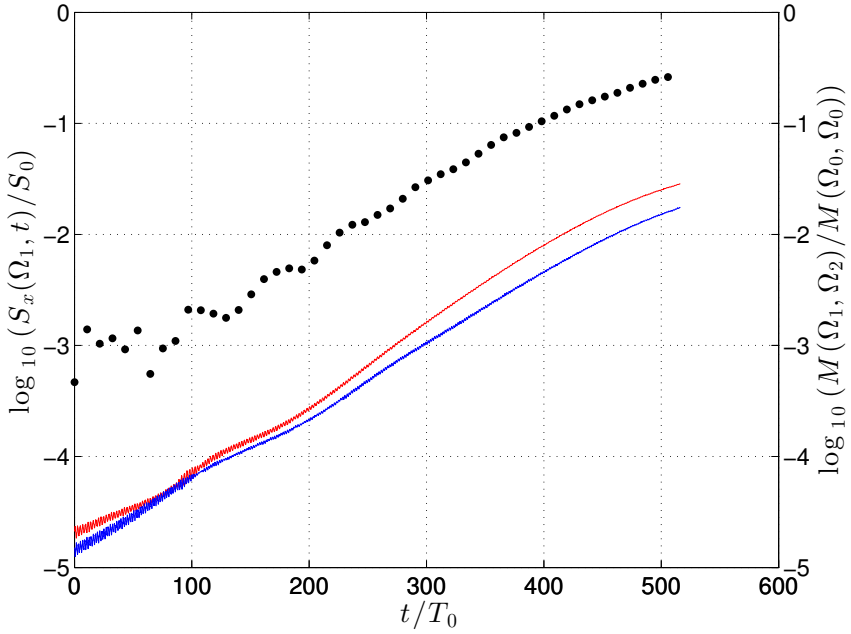


Figure 5.6: Cuts along the time-axis of the time-frequency diagram presented in figure 4.13 at frequencies Ω_1 (solid red line) and Ω_2 (solid blue line). The black dots show the intensity of the secondary wave peak (Ω_1, Ω_2) of the bispectrum normalized by the (Ω_0, Ω_0) peak as a function of time.

To conclude, bicoherence and bispectrum are very convenient tools to see the three-wave interactions between the frequencies in the tank. With one simple TRI experiment, different peaks are present. In the case of a strong TRI cascade, this will lead to a very rich pattern.

5.1.3 Frequency resonant condition

Once one has tested the bicoherence and the bispectrum, one can choose one of these two related tools to examine the three-wave interactions in the cascade experiments. The bicoherence exhibits well localized peaks and the signal-over-noise ratio appears larger as weak peaks are more visible. Thus, only the bicoherence is used in the remainder

of the manuscript. Nevertheless, the description on the three-wave interactions in the discrete cascade experiment (case B) made below with the bicoherence is similar using the bispectrum.

The bicoherence shown in figure 5.7 for case B is obtained in averaging over the same square region used for the time-frequency analysis and in the time interval $[200, 690]\ T_0$. The thick black line is the bisector. The bicoherence is symmetric with respect to this line. The three thin solid lines (horizontal, vertical and oblique) are associated with Ω_0. In addition to the strong peak $(\Omega_0, \Omega_0) = (0.61, 0.61)$ corresponding to the forcing frequency, at the crossing of the horizontal and vertical solid lines, the possible triplets satisfying the definition of triadic resonance at $\Omega_k = \Omega_0$ can be found on the solid oblique line with slope -1 connecting the points $(0, \Omega_0) = (0, 0.61)$ and $(\Omega_0, 0) = (0.61, 0)$. This emphasizes that the mechanism at play is triadic. Other peaks are also visible corresponding to other choices of Ω_k revealing that the instability mechanism is repeated and leads to a cascade. One horizontal, one vertical and one oblique lines are associated to each of the first secondary frequencies: $\Omega_{1,1}$ (dashed) and $\Omega_{2,1}$ (dashed dotted). These lines intersect three times in the diagram and a peak is present at each intersection. These peaks show that, at each intersection, there is a three-wave interaction between the two frequencies of the first couple and an other frequency. The two first intersections of the dashed and dashed dotted lines are symmetric with respect to the bisector and located at $(\Omega_{2,1}, \Omega_{1,1} - \Omega_{2,1}) = (\Omega_{2,1}, \Omega_{2,2}) = (0.25, 0.105)$ (or the symmetric). Thus, $\Omega_{1,1}$ and $\Omega_{2,1}$ are combined to get $\Omega_{2,2}$. The other intersection is on the bisector at $(\Omega_{2,1}, \Omega_{2,1}) = (0.25, 0.25)$. The peak at this intersection shows the second harmonics of $\Omega_{2,1}$ which is equal to $\Omega_{1,2} = 0.500$. Thus, the interactions between the two frequencies of the first couple generate the second couple. By the cascade

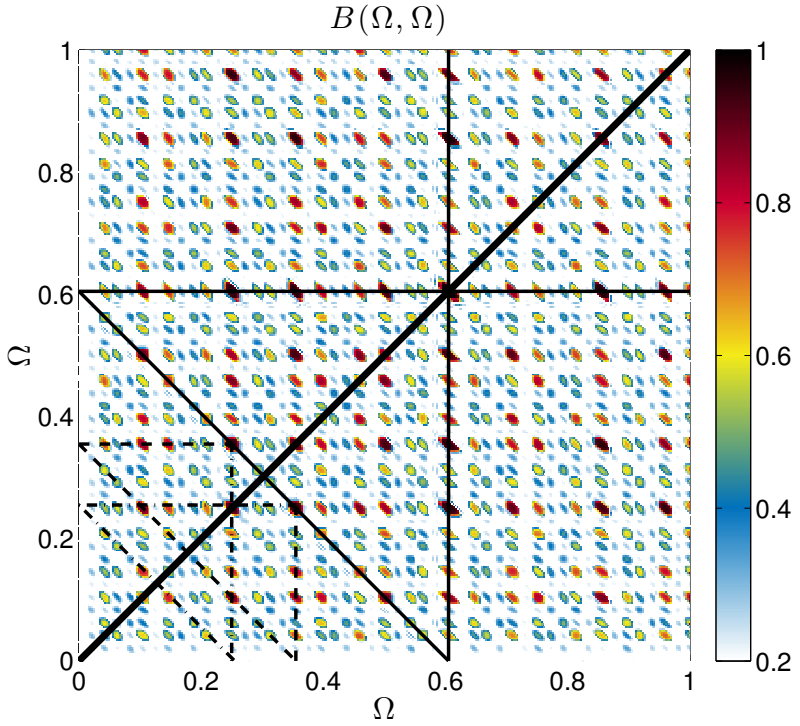


Figure 5.7: Bicoherence for case B. The thick solid line is the bisector. The horizontal, vertical and oblique lines are associated to the different frequencies: Ω_0 (solid), $\Omega_{1,1}$ (dashed) and $\Omega_{2,1}$ (dashed dotted).

mechanism described above, all the couples appear. All the three-wave interactions in the basin are shown by the peaks, in figure 5.7.

The set of discrete frequencies obtained experimentally is very easy to reproduce mathematically, without taking into account of the energy transfer between the waves. One starts with three frequencies, the forcing one and the two of the first couple. At stage 0, there is only the attractor frequency Ω_0. At stage 1, it creates the first couple of secondary frequencies, by simple TRI on branch 1. At stage 2, the fist couple creates the second one. At stage 3, the two first couples lead to the third and fourth couples, etc... This process is illustrated in figure 5.8(a), showing the different frequencies present at each stage. The set of frequencies increases with the stage number: the number of frequencies is equal to two to the power the stage number. Thus, at stage 4, there are $2^4 = 16$ frequencies and eight couples. These couples are the ones visible in the time-frequency diagram in figure 5.4. Using the set of frequencies, one can mimic a bicoherence diagram. One has to look at all the three-wave interactions in the set of frequencies and put a black dot at the location of these interaction in a (Ω, Ω) plane. This "simulated" bicoherence diagram, computed for the set of frequencies at stage 4, is shown in figure 5.8(b), superimposed on the experimental bicoherence diagram shown in figure 5.7, for Ω in the range $[0, 0.7]$. All the most intense peaks of the experimental bicoherence peaks are covered by the black dots coming from the cascade process model. The weakest peaks are not covered here but they would be if the bicoherence is calculated with the set of frequencies at stage 5. This shows that the frequencies predicted by the model are in a very good agreement with the

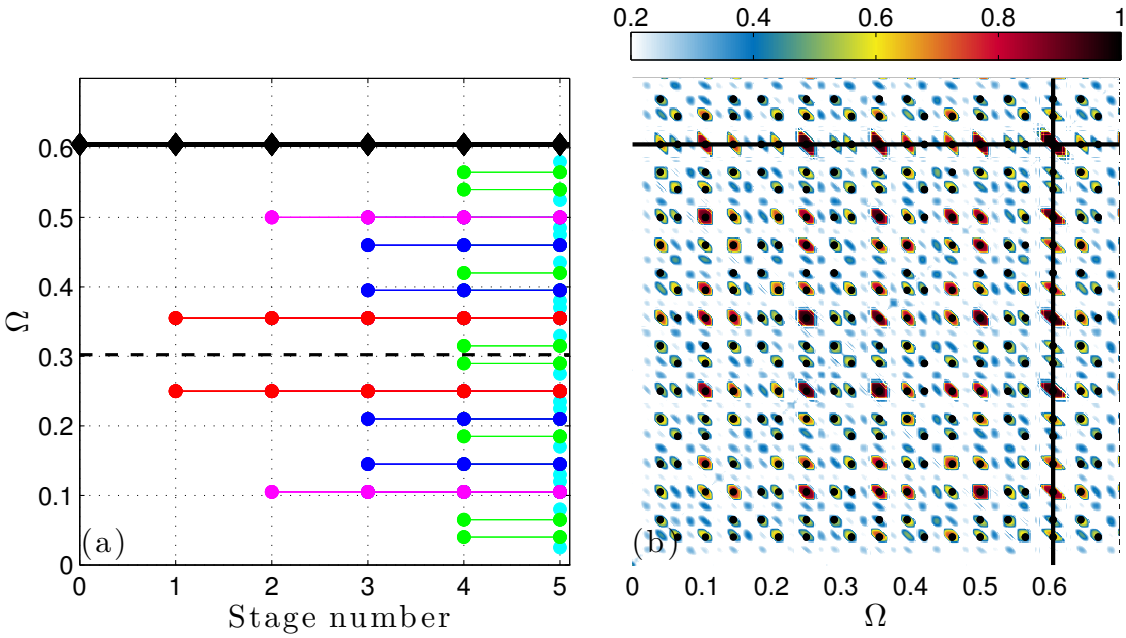


Figure 5.8: (a): Sketch of the cascade process: frequencies as a function of the stage number. The attractor frequency is represented by the black diamonds. The frequencies created at one stage have the same color: red for stage 1, magenta for stage 2, blue for stage 3, green for stage 4 and cyan for stage 5. At stage 4, the eight couples described in that manuscript are present. (b): Experimental bicoherence superimposed with the three-wave interactions obtained by the cascade process at stage 4. One point represents a three-wave interaction between three frequencies present in the model. The black lines show Ω_0.

experimentally observed ones. Moreover, all the frequencies that can interact between each others are really interacting. If it is not the case, we would have black dots superposed on the white background of the experimental bicoherence.

5.1.4 Energy-spectrum

The previous section has shown that the frequency resonant conditions for the triadic cascade were fulfilled. One has also shown in section 5.1.1 that the spatial resonant condition for the first triadic interaction, between the attractor and the first couple is verified. Nevertheless, once the two first secondary waves are created on branch 1, they can travel through all the basin, being reflected on the different walls. As they reflect on the slope, these waves can be focused or defocused and thus, their initial wave vectors can be changed. Moreover, for the other couples, we did not find any localized generation as for the first one. Thus, it seems that these couples are created more globally, like for TRI in the case of weakly-focused attractors (see section 4.2.2). Consequently, it is impossible to verify that the spatial resonant conditions are fulfilled by all the waves. Nevertheless, all these waves interact together as shown by the bicoherence. Thus, the computation of a wave-energy spectrum will allow us to verify that all the energy lies on the dispersion relation and that we have signatures of wave-turbulence. The wave energy spectrum has already been used as a diagnostic tool by Yarom and Sharon [151] in the case of inertial-waves.

The wave energy spectrum is computed using the following procedure. Horizontal and vertical velocity fields $v_x(x,z,t)$ and $v_z(x,z,t)$ are obtained with 2D PIV measurements in the entire trapezoidal domain, on a grid with 0.36 cm $\times$ 0.36 cm spatial resolution and 0.5 s temporal resolution. As the x (respectively z) direction length is around 45 cm (resp. 30 cm) and as we used 80 T_0 to compute each energy spectrum, the total data grid size is thus $125 \times 80 \times 1600$ points. A three-dimensional (two dimensions for space, one for time) Fourier transform of these fields leads to $\hat{v_x}(k_x,k_z,\Omega)$ and $\hat{v_z}(k_x,k_z,\Omega)$. For the Fourier transform, we padded the velocity fields with zeros to increase the resolution in wave number and frequency. The final data grid used for $E(k_x,k_z,\Omega)$ is $400 \times 400 \times 2000$. The resolution in wave number is thus $\Delta k_x = \Delta k_z = 0.043$ rad/cm and the frequency resolution is $N\Delta\Omega = 6.28 \times 10^{-3}$ rad/s. One can thus define the 2D energy spectrum by

$$E(k_x,k_z,\Omega) = \frac{|\hat{v_x}(k_x,k_z,\Omega)|^2 + |\hat{v_z}(k_x,k_z,\Omega)|^2}{2ST}, \tag{5.12}$$

where $S = 45 \times 30$ cm^2 is the area of the PIV measurement and $T = 80\,T_0$ its duration. The spatio-temporal resolution of our measurements leads to upper bounds in wave numbers and frequency. We thus have $k_{max} = 8.6$ rad/cm and $N\Omega_{max} = 6.28$ rad/s.

In the dispersion relation for internal waves, $\Omega = \sin\theta$, the wave vector $\vec{k}$ and its components do not appear directly but they are linked with the angle θ by $\sin\theta = k_x/\sqrt{k_x^2+k_z^2}$. To compute the energy spectrum as a function of the variable θ, one can interpolate the energy spectrum $E(k_x,k_z,\Omega)$ to get $E(k,\theta,\Omega)$, where k is the norm of the wave vector. For this interpolation, we define Δk as the smallest wave vector that has data points in the Cartesian coordinates. Here, $\Delta k = 0.043$ rad/cm and we chose $k_{min} = 5\Delta k \approx 0.22$ rad/cm to have a good interpolation at low wave numbers. We chose to take 200 points for k between 0 and k_{max} and 300 points for θ between $-\pi$ and π. Then, one can integrate over the entire range of wave vectors $[k_{min}, k_{max}]$ as follows

$$E(\theta,\Omega) = \int_{k_{min}}^{k_{max}} E(k,\theta,\Omega) k \mathrm{d}k, \tag{5.13}$$

or on any range of wave vectors between k_{min} and k_{max}. Then, because all the frequencies in the TRI cascade case have very different levels of energy, one can normalize $E(\theta, \Omega)$ by the energy as a function of Ω only,

$$E(\Omega) = \int_{-\pi}^{+\pi} E(\theta, \Omega) \mathrm{d}\theta. \tag{5.14}$$

Consequently, the relevant quantity, plotted as a function of θ and Ω is the dimensionless ratio $E(\theta, \Omega)/E(\Omega)$.

First, one tests this method on a stable attractor (case A of Table 5.1), to see what one can visualize. Figure 5.9 shows the energy spectrum of the stable attractor (case A), with the spatial integration range being the whole range accessible by the experiment. The dispersion relation of internal waves is plotted using a dashed line in figure 5.9. On this figure, there are different spots at $\Omega = \pm\Omega_0 = \pm 0.61$ and located on the dispersion relation. These spots correspond to the attractor. The two main spots, one for $\Omega = 0.61$ and $\theta \in [0; \pi/2]$ and one for $\Omega = -0.61$ and $\theta \in [-\pi; -\pi/2]$, represent the branch 1, which is the most energetic. Indeed, as the convention for the wave phase is $\phi = \Omega N t - k_x x - k_z z$, the wave vector of branch 1 has $\theta \in [-\pi; -\pi/2]$ for negative frequencies. The other spots represent the other branches, as indicated in figure 5.9.

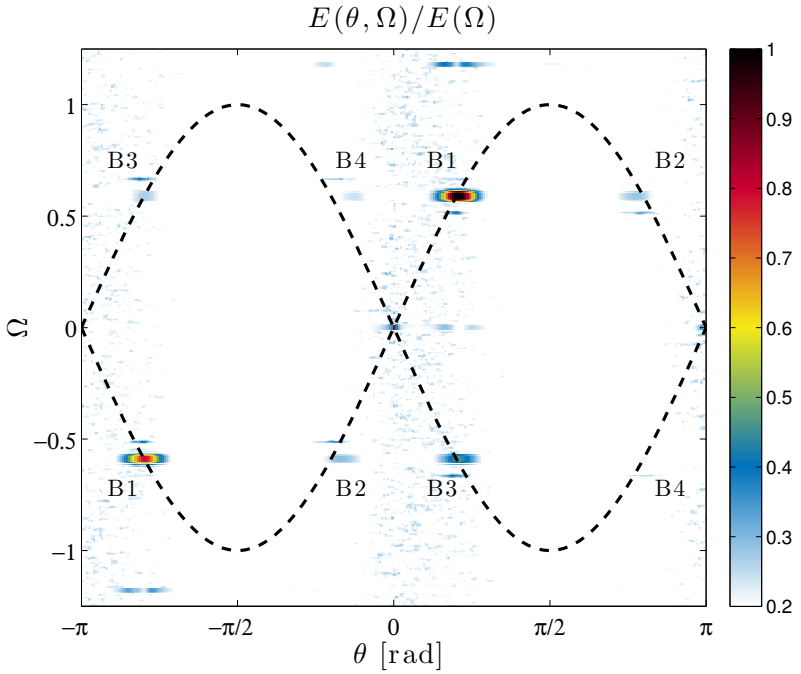


Figure 5.9: $E(\theta, \Omega)/E(\Omega)$ for a stable attractor (case A of Table 5.1) as a function of θ and Ω. The integration range in wave vector is the full range accessible with the acquisition parameters: 0.22 to 8.6 rad/cm (i.e. wave lengths between 28.5 to 0.75 cm). Colors indicate the levels of energy spectrum. The black dashed lines correspond to the dispersion relation $\Omega = \pm \sin\theta$. The different branches represented by the spots are indicated on the figure.

The energy spectrum us allows to visualize the repartition in θ and Ω of the energy. For a stable attractor, one has only spots around $\pm\Omega_0$ and on the dispersion relation. The energy spectra for the TRI cascade experiment is expected to be richer, due to all the secondary waves created by the cascade.

Figure 5.10 shows the energy spectrum for the TRI cascade experiment (case B). The spatial integration range is the whole range accessible by the acquisition parameters. It is much richer than the one presented in figure 5.9 for a stable experiment. In addition to the attractor spots, one has a lot of energy at different frequencies. Almost all this energy lies on the dispersion relation, plotted as dashed lines. This means that every frequency in the tank correspond to an internal wave. Moreover, one can see that it is well distributed within the four branches, or direction of propagation. Thus, the secondary waves propagate in all directions as they reflect on the walls of the basin.

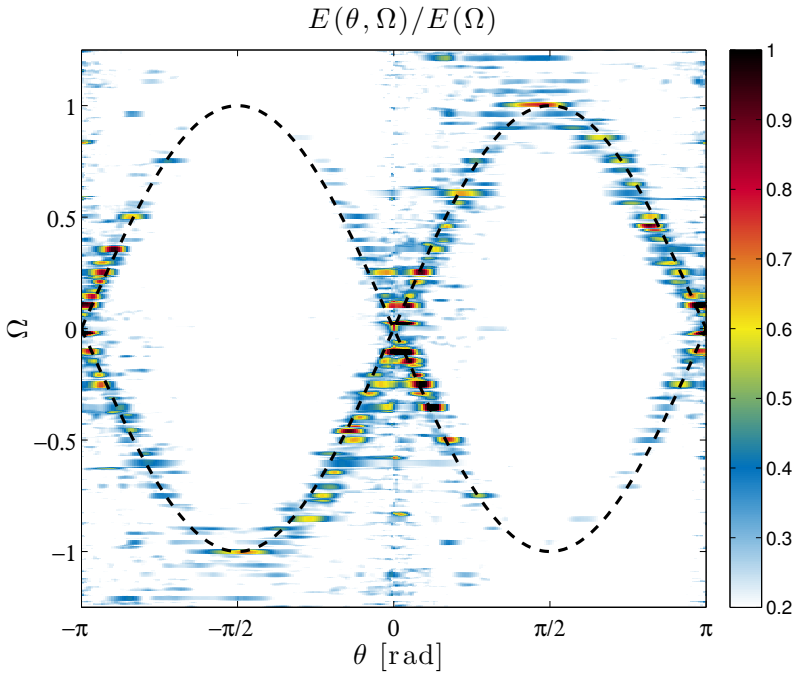


Figure 5.10: $E(\theta,\Omega)/E(\Omega)$ for a TRI cascade experiment (case B) as a function of θ and Ω. The integration range in wave vector is the full range accessible with the acquisition parameters: 0.22 to 8.6 rad/cm (i.e. wave lengths between 28.5 to 0.75 cm). Colors indicate the levels of energy spectrum. The black dashed lines correspond to the dispersion relation $\Omega = \pm \sin\theta$.

To investigate more the energy spectrum for the TRI cascade, one can separate the scales to see where the motions take place within the different scales. This is what has been done in figure 5.11 where the two integration ranges are $[0.22, 1]$ rad/cm for panel (a) (large scales) and $[1, 1.86]$ rad/cm for panel (b) (small scales). The first integration range represents 84% of the energy in the entire range $[k_{min}, k_{max}]$ while the second represents 11% of this energy. Thus, only 5% of the energy is left in the scales between 1.86 rad/cm and $k_{max} = 8.6$ rad/cm. Figure 5.11(a) seems similar to figure 5.10 except that there is less noise while figure 5.11(b) shows a strong difference. Indeed, in panel (b), the spots corresponding to the attractor at $\Omega = \Omega_0$ have disappeared. This is normal because the small scales are taken between 3.4 and 6.3 cm. Thus, the attractor whose the typical wave length is 15 cm is located in the large scales, taken between 6.3 and 28.5 cm. Thus, the energy at the small scales is only carried by the secondary waves. Nevertheless, figure 5.11(a) shows that there are also secondary waves present in at large scales. All the waves follow the dispersion relation because all the energy on both panels lies on the dashed lines. Thus, even

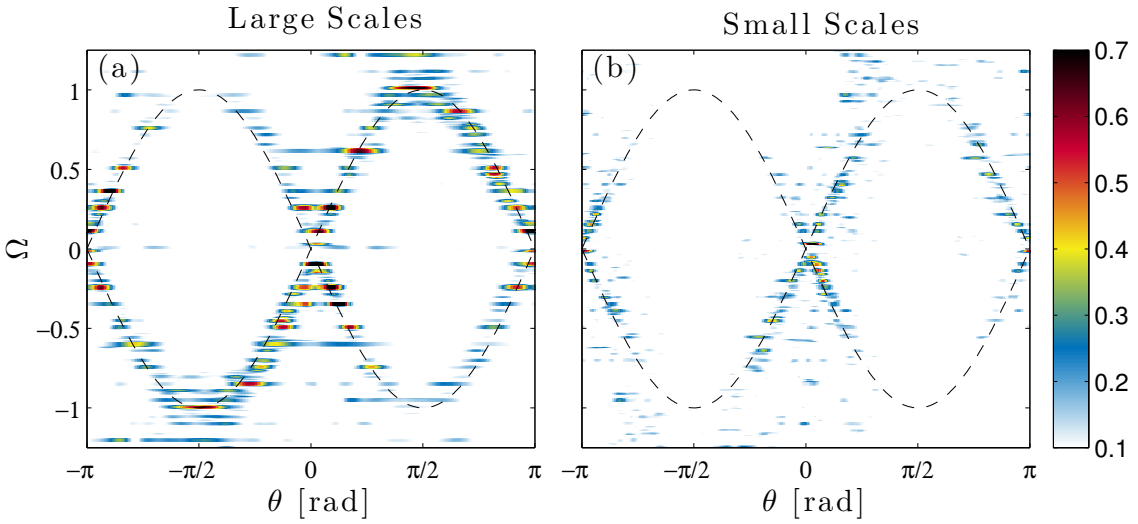


Figure 5.11: Ratio $E(\theta,\Omega)/E(\Omega)$ for the TRI cascade experiment and two length scale intervals: 0.22 to 1 rad/cm for (a); 1 to 1.86 rad/cm for (b) (i.e. wave lengths 28.5 cm to 6.3 cm, for left panel, while 6.3 cm to 3.4 cm for right one). Colors indicate the levels of energy. The black lines correspond to the dispersion relation $\Omega = \pm \sin\theta$.

at different scales, the dispersion relation rules. This means that all the energy present in the TRI cascade experiment is carried by internal waves. These waves interact non-linearly between each other, via three-wave interactions or TRI as shown with the bicoherence. All these considerations are very strong signatures of a wave-turbulence framework for the TRI cascade experiment. This wave-turbulence is discrete, because the set of frequencies is discrete, but energy is exchanged between internal waves via a three-wave interaction mechanism.

5.1.5 Spatial spectrum

As strong signatures of internal wave turbulence have been highlighted in this section, it is interesting to look at the spatial spectra of the TRI cascade experiment (case B). Indeed, spatial spectra are very commun tools in fully 3D isotropic turbulence as in the wave-turbulence framework [28, 14, 151].

To compute the spatial spectrum, only a 2D Fourier transform on space has to be done. From the horizontal and vertical velocity fields $v_x(x,z,t)$ and $v_z(x,z,t)$, this leads to the spatial spectrum

$$E(k_x,k_z) = \left\langle \frac{|\hat{v_x}(k_x,k_z,t)|^2 + |\hat{v_z}(k_x,k_z,t)|^2}{2S} \right\rangle_t , \tag{5.15}$$

where $S = 45 \times 30$ cm^2 is the surface of the PIV measurement and $\langle\rangle_t$ means an average in time over $40\,T_0$. This average is performed during the stationary state of the experiment. The spatial resolution of the 2D PIV measurements being 0.36 cm in both directions, the maximum accessible wave number is the same as the one for the energy spectra: $k_{max} = 8.6$ rad/cm. Nevertheless, the signal has been padded using 1000 points, which increases the wave number resolution with respect to the energy spectrum: $\Delta k_x = \Delta k_z = 0.0172$ rad/cm. The final data grid used for $E(k_x,k_z)$ is 1000×1000. As in the general

framework for turbulence, one can expect a power law for the energy spectra as a function of $|k_x|$ and $|k_z|$. Thus, the four quadrants where k_x and k_z are positive or negative are averaged in order to get the energy spectrum as a function of $|k_x|$ and $|k_z|$. Then, one integrate over $|k_x|$ or $|k_z|$:

$$E(|k_x|) = \int_{k_{min}}^{k_{max}} E(|k_x|,|k_z|)\mathrm{d}|k_z|, \tag{5.16}$$

$$E(|k_z|) = \int_{k_{min}}^{k_{max}} E(|k_x|,|k_z|)\mathrm{d}|k_x|. \tag{5.17}$$

The energy spectra are plotted as a function of $|k_x|$ or $|k_z|$ in figure 5.12. Both exhibit for large values of $|k_x|$ or $|k_z|$ a power law with a -3 exponent, as highlighted by the dashed lines on both panels. The forcing injected scales is $k_{z,\mathrm{inj}} = 0.1$ rad/cm and $k_{x,\mathrm{inj}} = 0.08$ rad/cm. Thus, the injected scales are located on the left side of both panels. The two vertical dashed dotted lines show the horizontal and vertical wave numbers of the attractor measured using figure 4.11. Because the energy transfer is made from the attractor scale to the smaller scales of the secondary waves, the attractor scale marks the beginning of the triadic energy cascade. This cascade exhibits a decay of the spectrum with a -3 exponent.

Using a Hamiltonian to describe internal wave turbulence in a three-dimensional infinite space, Lvov and Tabak [94] predict theoretically a $-3/2$ power law for k_z and k_H, the modulus of the horizontal wave vector (which is two-dimensional because the set-up is three-dimensional). This prediction is relevant with the observations of Garrett and Munk [57] for the oceans. Nevertheless, our -3 exponent is much larger that the Lvov and Tabak exponent. The discrepancy can be due to several reasons. In our experimental set-up, the flow has been proved to be quasi independent of the y-coordinate, for both stable and unstable attractors in section 4.3. Thus, our set-up can be considered as a two-dimensional set-up, meaning that the wave-interactions are 2D while the waves in the oceans or in the Lvov and Tabak model are 3D. Moreover, in the basin, the waves are really confined. This has been shown in section 4.2.2 where the TRI appears at the global scale. Thus, the waves feel the boundaries of the basin while they are less confined in the oceans. Reflexions on the slope can also change the wave length of the waves, via focusing or defocusing. Consequently, the size of the basin can limit and disrupt the spatial spectra because the wave-turbulence theory assumes that the injected and dissipative scales are well-separated.

Even if our set-up is far from being ideal to match with the theoretical hypotheses made for the predictions, one can play with the spectra using dimensional analysis. Nazarenko [121] gives the Zakharov spectra predictions for any waves

$$E \propto c_0^{\beta} \varepsilon^{1/(n-1)} k^{\delta}, \tag{5.18}$$

where the dispersion relation of the waves is $\omega = c_0 k^q$ and

$$\beta = 2 - \frac{3}{n-1}, \tag{5.19}$$

$$\delta = D - 6 + 2q + \frac{5 - D - 3q}{n-1}. \tag{5.20}$$

The dimension of the set-up is D and the number of wave interactions is n. The internal wave dispersion relation is

$$\Omega = \frac{\omega}{N} = \sin\theta = \frac{k_x}{\sqrt{k_x^2 + k_z^2}} = \frac{k_x}{k}. \tag{5.21}$$

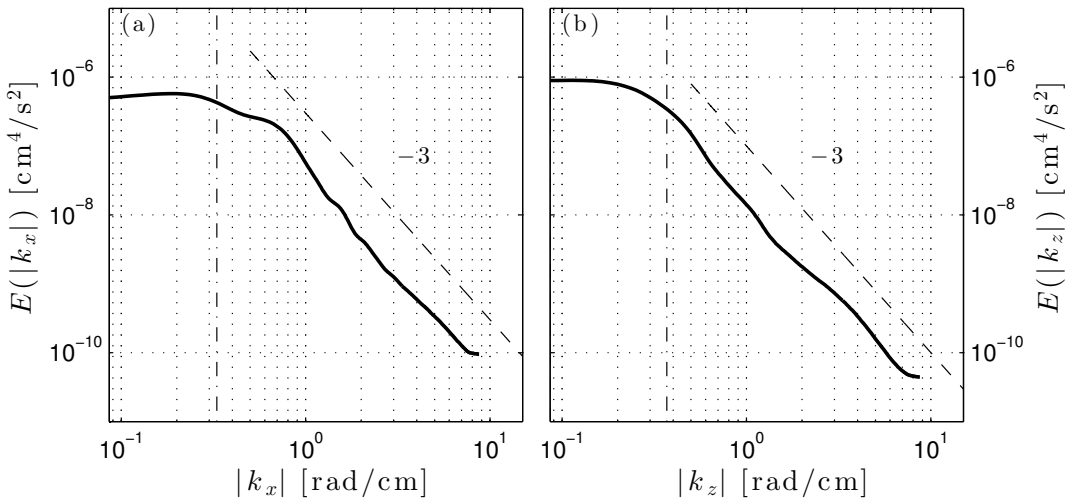


Figure 5.12: Spatial energy spectra as a function of $|k_x|$ (a) and $|k_z|$ (b). The vertical dashed dotted lines show the horizontal or vertical wave numbers of the attractor. The dashed lines show a -3 slope.

Thus, the main difficulty comes from the dispersion relation, which does not depend directly on the modulus of the wave vector. One has to choose between k_x, k_z or k to know the value of q. For internal waves, n is equal to 3 and D can be equal to 2 in our set-up or 3 for [94, 57]. If we assume that the waves are isotropic, $k_x \approx k_z$ and $q = 0$. As a consequence, Ω is fixed around 0.7. Let see what happens when one varies the dimension of the set-up D:

- if $D = 3$, using equation (5.18), one obtains $E \propto N^{1/2}\varepsilon^{1/2}k^{-2}$. The -2 exponent is the one observed by [57] and is close to the one predicted by [94]
- if $D = 2$, this leads to $E \propto N^{1/2}\varepsilon^{1/2}k^{-5/2}$, which is closer to what we find.

Nevertheless, one can also consider than the waves are not isotropic because the secondary waves have lower frequency than $\Omega_0 = 0.6$. Thus, k_z is greater than k_x and $q = 1$:

- if $D = 3$, this brings to $E \propto N^{1/2}\varepsilon^{1/2}k_z^{-3/2}$. This corresponds to the prediction made by Lvov and Tabak [94]
- if $D = 2$, one has $E \propto N^{1/2}\varepsilon^{1/2}k_z^{-3}$, which corresponds to the power law in figure 5.12, for the vertical wave number. Nevertheless, one also observes such a scaling for k_x and both horizontal and vertical components of the wave vectors are linked by the dispersion relation.

One needs here to improve the theoretical predictions, for example, by reproducing the calculus of [94] for a 2D set-up. Another option can be to quantify the dependance of the spectra in ε, as in [117].

Above results are convincing signatures of a discrete wave turbulence framework for internal waves in the intermediate forcing amplitude regime (case B of Table 5.1), even if the theoretical predictions for the spatial spectrum are difficult to applicate on our system. Nevertheless, this is the first experimental evidence of internal wave turbulence. For the largest amplitude, we have indications that a system is beyond the wave turbulence-like

regime and has reached a mixing regime. This is developed in the next section, for case C of Table 5.1.

5.2 Mixing induced by TRI cascade

In this section, case C of Table 5.1 is discussed. This experiment is performed with a very high forcing amplitude ($a = 10$ mm) and with the same geometry as case B (well-focused attractor ■, see figure 4.10). It is characterized by a partial mixing of the linear stratification. First, one investigate this experiment as what has been done for case B in section 5.1. The time-frequency, bicoherence, energy and spatial spectra are discussed. Then, one focuses particularly on the extreme events responsible for the mixing in the tank.

5.2.1 Time-frequency diagram and bicoherence

Figure 5.13(a) shows the time-frequency diagram of the high forcing amplitude experiment, case C of Table 5.1, also presented in figure 5.3(c). A cut at $t = 400\,T_0$ of this diagram is plotted in figure 5.13(b). The time-frequency diagram is computed with exactly the same method as the other ones presented in this chapter. It exhibits also a energy cascade, from the attractor frequency Ω_0 to other frequencies. Similarly to case B and figure 5.4, one can see several pairs of discrete peaks. These pairs verify the frequency resonant condition but appear to be not stationary in time. Indeed, the couple of frequency around $(0.4, 0.2)$ is first present before it vanishes and the couple around $(0.45, 0.15)$ dominates at the end of the experiment. This shows that the dynamics of the flow, inside the tank, is not stationary

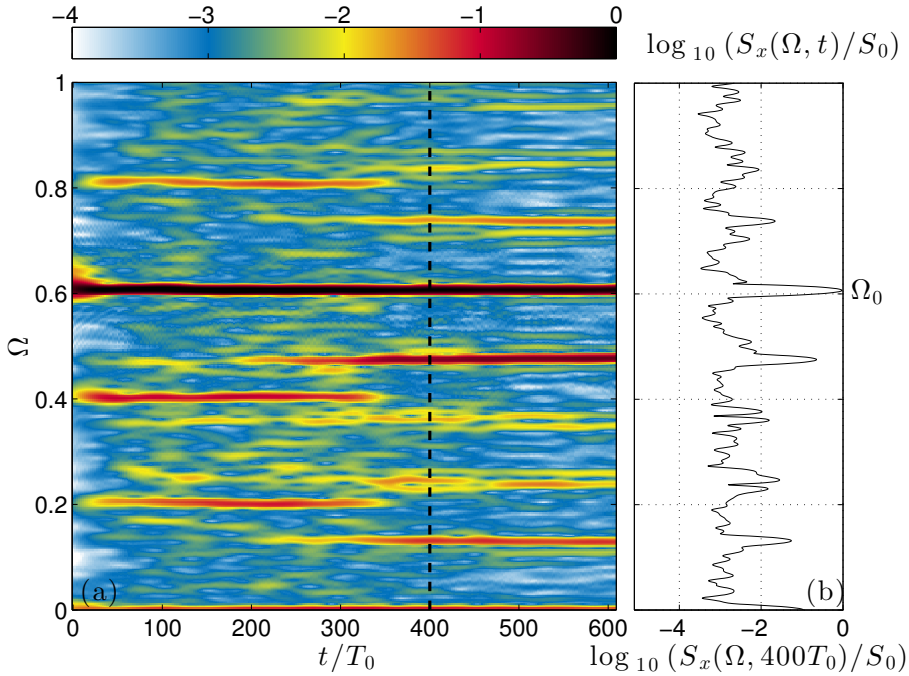


Figure 5.13: (a): Time-frequency diagram of internal wave field for case C, obtained from a 5×5 cm^2 side square region on branch 1. (b): Vertical cut of the diagram along the frequency axis at $t = 400\,T_0$, indicated by the black dashed line. S_0 corresponds to the time average of the frequency component associated with the primary wave Ω_0.

at all. Moreover, below these pairs of peaks, there is a "continuous" part, revealed by the blue color in figure 5.13(a) and on the cut of figure 5.13(b). The background is much higher for case C, more than one order of magnitude, than the one for case B. Pairs of discrete peaks with weak intensity are not really visible, above this high background.

Similar characteristics can be seen on the bicoherence of case C, plotted in figure 5.14. The bicoherence is also computed with the same method as the one for case B. The two couples of discrete peaks are visible on the oblique line between the points $(\Omega_0, 0)$ and $(0, \Omega_0)$. Few other peaks, showing the beginning of the cascade as described for case B, can be also observed. Nevertheless, the background is higher than the one for case B and hides partially the weakest peaks. Thus, the discrete frequency peaks visible on the time-frequency diagram fulfill the frequency resonant condition for TRI but the weakest peaks are embedded in a "continuous" part of the background.

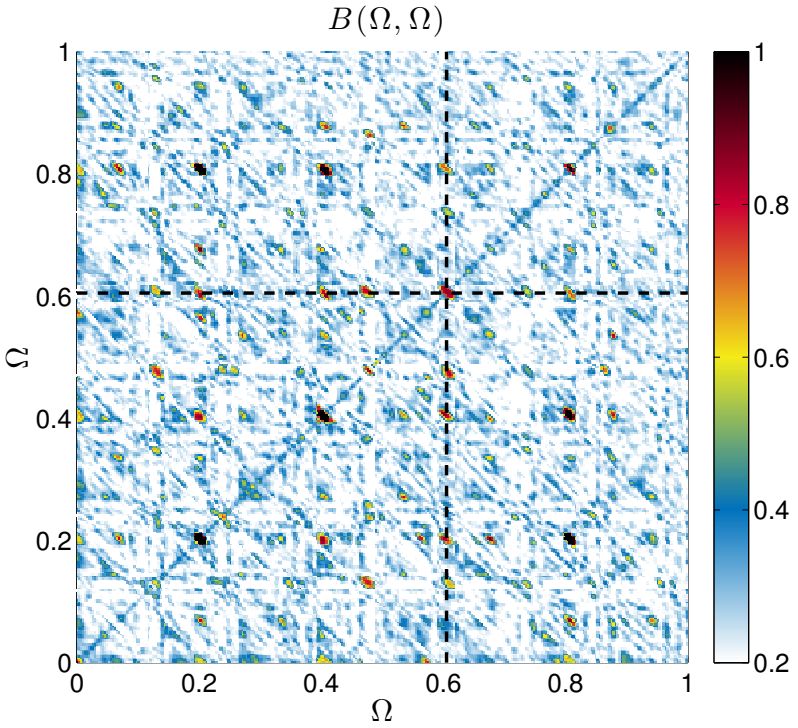


Figure 5.14: Bicoherence for case C. The horizontal and vertical lines are associated to Ω_0.

In this experiment, the cascade seems to present higher levels in energy at all frequencies. Using the energy spectrum, one can investigate if all this energy has a wave shape or not.

5.2.2 Energy and spatial Spectra

Figure 5.15 shows the energy spectrum $E(\theta, \Omega)/E(\Omega)$ as a function of the angle of propagation θ and the dimensionless frequency Ω. It has been obtained by integrating on all range of wave numbers accessible by the experiment. The dispersion relation for internal waves is plotted as dashed black lines. One can distinguish different peaks that are present on the dispersion relation, for the attractor at $\Omega_0 = 0.6$ but also for secondary waves. However, there is also some energy which is localized around $\theta = 0$ or $\pm\pi$ for all frequencies. This energy clearly escapes from the dispersion relation, meaning that there is not only waves

propagating in the tank. The different angles θ where this energy is localized correspond to a wave propagation at the horizontal or to horizontal motions. This could be the signature of the stratification of the fluid. Indeed, as the fluid in the tank is initially linearly vertically stratified in density, the horizontal motions are favored while the vertical ones are more difficult. Thus, the background noise, higher in case C than in case B appears here to be correlated horizontally.

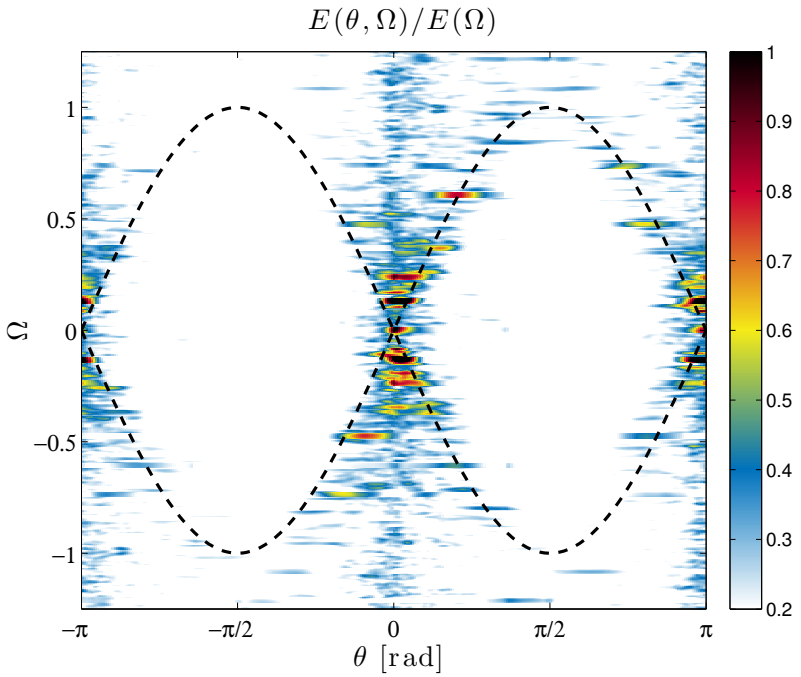


Figure 5.15: $E(\theta,\Omega)/E(\Omega)$ for the mixing experiment (case C) as a function of θ and Ω. The integration range in wave vector is the full range accessible with the acquisition parameters: 0.22 to 8.6 rad/cm (i.e. wave lengths between 28.5 to 0.75 cm). Colors indicate the levels of energy spectrum. The black dashed lines correspond to the dispersion relation $\Omega = \pm \sin\theta$.

To investigate further, one can split the energy spectrum within two different scales, as for case B. The large scales are between the basin scale and 6.3 cm while the small scale are taken to be between 6.3 and 3.4 cm. For case C, the first range of wave numbers has 82% of the total energy and the second one has 11%. Thus, in proportion, the energy in the second range is slightly higher than the one in case B. Figure 5.16 shows the energy spectra, for these two different ranges of scales. In panel (a), at large scales, one find something similar as for case B, where almost all the energy lies on the dispersion relation. There are different peaks, even weak, located on the dashed black lines. However, for small scales, in panel (b), all the energy is localized around $\theta = 0$ or $\pm\pi$ for all frequencies. Thus, the motion at small scales seems to be quasi-horizontal. Consequently, the energy out of the dispersion relation for the total energy spectrum in figure 5.15 comes from the small scales, essentially. This could be a signature of the mixing, which is probably localized at small scales. Indeed, the short-scale perturbations are expected to be due to extreme events, natural precursors to mixing. Note that the energy away from the dispersion relation can also be due to different reasons. Indeed, one can be reserved on the two-dimensionality of the flow with such very high forcing. Thus, the mixing process may not be completely

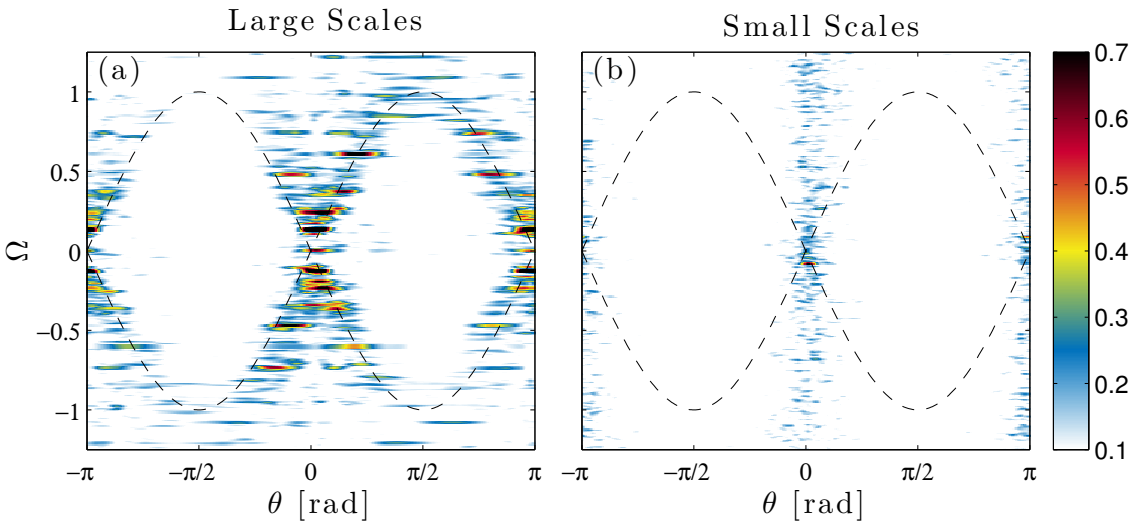


Figure 5.16: Ratio $E(\theta,\Omega)/E(\Omega)$ for the mixing experiment (case C) and two length scale intervals: 0.22 to 1 rad/cm for (a); 1 to 1.86 rad/cm for (b) (i.e. wave lengths 28.5 cm to 6.3 cm, for left panel, while 6.3 cm to 3.4 cm for right one). Colors indicate the levels of energy. The black lines correspond to the dispersion relation $\Omega = \pm \sin\theta$.

independent of the y-coordinate. Moreover, very strong motions are created by the flow. The motions can lead to Doppler shifts on the energy spectrum if the waves propagates through a moving stratified fluid.

The spatial spectra as a function of $|k_x|$ and $|k_z|$ computed for case C are plotted in figure 5.17. As for case B, they exhibit also a -3 power law, although it is less convincing. As the wave turbulence regime is changed in case C into a mixing regime, one can consider that we are in a strong wave turbulence regime or in a stratified regime, as defined in [121].

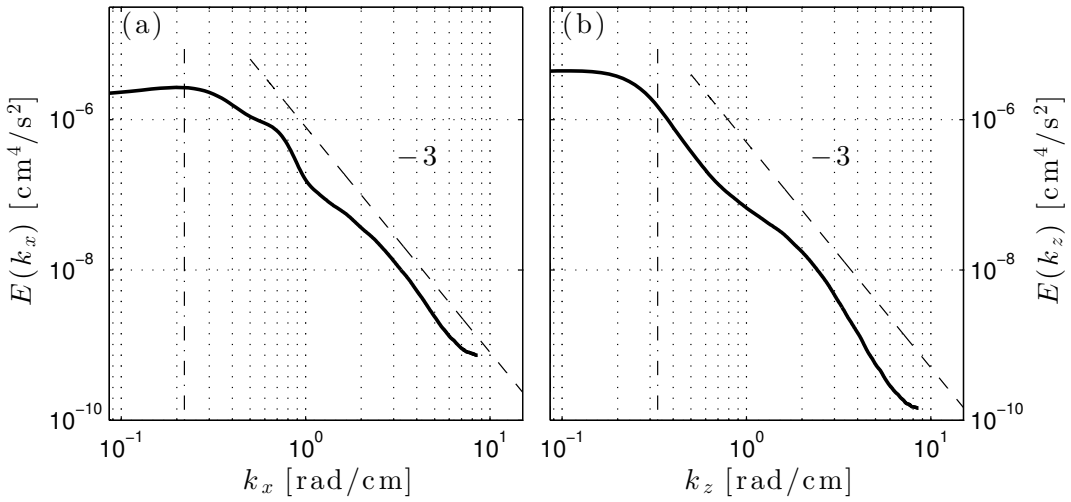


Figure 5.17: Spatial energy spectra as a function of $|k_x|$ (a) and $|k_z|$ (b) for case C. The vertical dashed dotted lines show the horizontal or vertical wave numbers of the attractor. The dashed lines show a -3 slope.

This is a regime where the weak wave amplitude hypothesis does not hold any more. This assumes that k_z is much greater than k_x and that the spatial spectra depends only on N, the buoyancy frequency and on k_z. A dimensional analysis gives $E \propto N^2 k_z^{-3}$, which is the same exponent as the one found for case B in a weak wave turbulence regime. Nevertheless, this is consistent with our spectra and the predictions of [10, 33]. Note that the power law is less clear than the one for case B. Moreover, one also has the same power law for the horizontal wave number $|k_x|$.

5.2.3 Mixing inferred from vorticity distribution

An important issue is whether or not sufficiently energetic internal wave motion can produce an irreversible energy contribution to mixing. Figure 5.18(a) presents the comparison between density profiles measured before and after experiments: while no modification of the density (within experimental error) can be observed in case B, one gets a clear evidence of mixing in case C.

Differences between the regimes corresponding to low and high mixing are clearly seen in statistics of extreme events. This statistic is obtained by the calculation of probability density functions (PDFs), a widely used tool for describing turbulence [6]. Since we are interested in small-scale events destabilizing the stratification, we take the horizontal y-component of vorticity

$$\xi_y(x,z,t) = \frac{\partial v_x}{\partial z} - \frac{\partial v_z}{\partial x}, \tag{5.22}$$

measured in the vertical midplane of the test tank as a relevant quantity and consider the PDF of the dimensionless quantity $\Xi_y = \xi_y/N$. In figure 5.18(b), we present the vorticity PDFs corresponding to different wave regimes in the attractor. Note that the area under each PDF is equal to unity, what allows a meaningful comparison between the probabilities of extreme events in the cases A, B and C. In a stable attractor (see case A), extreme events are completely absent and the wave motion is concentrated within the relatively narrow branches of the attractor while the rest of the fluid is quiescent. Accordingly, the PDF has a sharp peak at zero vorticity and is fully localized between well-defined maximum and minimum values of vorticity. In cases B and C, the development of TRI increases the probability of extreme events due to summation of primary and secondary wave components. The occurrence of local destabilizing events can be viewed as a competition between stratification and vorticity. In a two-dimensional flow, a relevant stability parameter is a version of the Richardson number, which can be introduced as

$$\mathrm{Ri}_\xi = \left(\frac{N}{\xi_y}\right)^2 = \left(\frac{1}{\Xi_y}\right)^2. \tag{5.23}$$

For a horizontal stratified shear flow this parameter reduces to the conventional gradient Richardson number $\mathrm{Ri} = N^2/(\mathrm{d}v_x/\mathrm{d}z)^2$, where $\mathrm{d}v_x/\mathrm{d}z$ is the velocity shear. Flows with large Ri are generally stable, and the turbulence is suppressed by the stratification. The classic Miles-Howard necessary condition for instability requires that $\mathrm{Ri}<1/4$ somewhere in the flow [116, 72]. If this condition is satisfied, the destabilizing effect of shear overcomes the effect of stratification, and some mixing occurs as a result of overturning. The threshold value $|\Xi_y| = 2$ is marked on the plot of vorticity PDFs. It can be seen that data corresponding to cases B and C have "tails" extending into the domains $|\Xi_y| > 2$. The area under the tails represents the probability of event of strength $|\Xi_y| > 2$. In case C, this probability is an order of magnitude greater than in case B, in qualitative agreement with much higher mixing in case C as compared to case B.

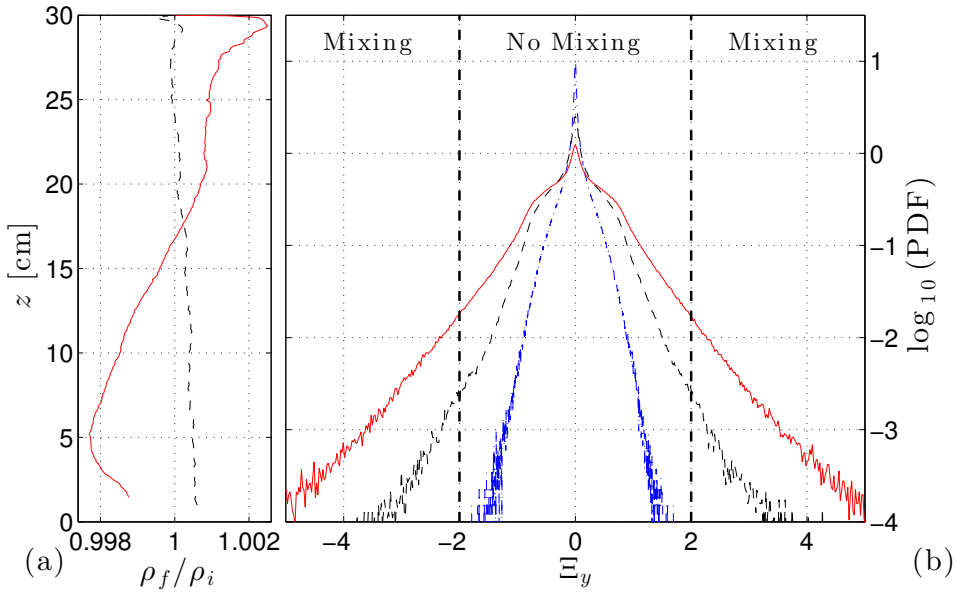


Figure 5.18: (a): Ratio between the density profiles measured after and before the experiments for cases B (dashed black line) and C (solid red line). (b): Experimental probability density functions (PDFs) of the dimensionless vorticity Ξ_y in the tank, calculated on the grid from experimental image for cases A (dashed dotted blue line), B (dashed black line) and C (solid red line). Samples are taken using 400 images close to the end of the experiment, when the wave regime is fully developed. The individual PDFs are averaged over roughly 8×10^3 equally spaced points covering the whole wave field.

The measure of the mixing can be defined as the normalized potential energy

$$A(t) = \frac{E_p(t) - E_p(0)}{E_p^* - E_p(0)}, \tag{5.24}$$

in which $E_p = \int \mathrm{d}x\mathrm{d}z\, \rho(x,z,t) gz$ stands for the potential energy and $*$ stands for its final value for the fully mixed system. It worths to note that this potential energy is a linear potential energy: one has to multiply E_p by the width of the tank W to get the right dimension of an energy, as the mixing is assumed independent of the y-coordinate. This has no influence of the value of A. For case C (see figure 5.18(a)), one attains a final value $A \approx 25\%$. Mixing is therefore remarkably strong: two hours of experiment in case C are equivalent to the action of molecular diffusion on a time scale of several weeks.

The density profiles measured before and after the experimental runs do not allow monitoring the time evolution of the mixing dynamics. However, these dynamics are nicely revealed in numerical calculations as shown in figure 5.19. The numerical set-up has been described in section 3.6.2 of this manuscript and it has been validated comparing the simulations with both stable and unstable attractors in sections 3.6.3 and 4.1.3. For this mixing part, only 2D numerical simulations have been used. Indeed, as in experiments, long-term simulations are necessary to investigate the TRI cascade and the mixing characteristics. Thus, to decrease the computational time, we choose to perform 2D simulations only. Nevertheless, as the lateral walls are not present in the 2D numerical set-up, the amplitude of the forcing can not be directly compared with the one of the experimental wave-maker. In figure 5.19, the dramatic effect of the amplitude of oscillations on the mixing (with other

parameters being fixed) is clearly seen, ranging from slow erosion of initial stratification to violent mixing. The three numerical experiments have been carried out with different forcing amplitudes: $a = 1$ mm (green), $a = 5$ mm (magenta) and $a = 9$ mm (black). Their geometry is close to the one of the three experiments A, B and C, presented in Table 5.1. The weakest amplitude causes only a slight mixing because the gain of potential energy A stays close to zero. However, the two highest forcing amplitudes induce significant mixing, in the same order as in the case C. This illustrates also the discrepancies between the forcing amplitude in 2D numerical simulations: no mixing has been observed in experiment with $a = 5$ mm (case B) while important mixing is present in 2D numerical simulations with the same forcing amplitude. Nevertheless, the numerical simulations are very useful to investigate the mixing dynamics as a function of time.

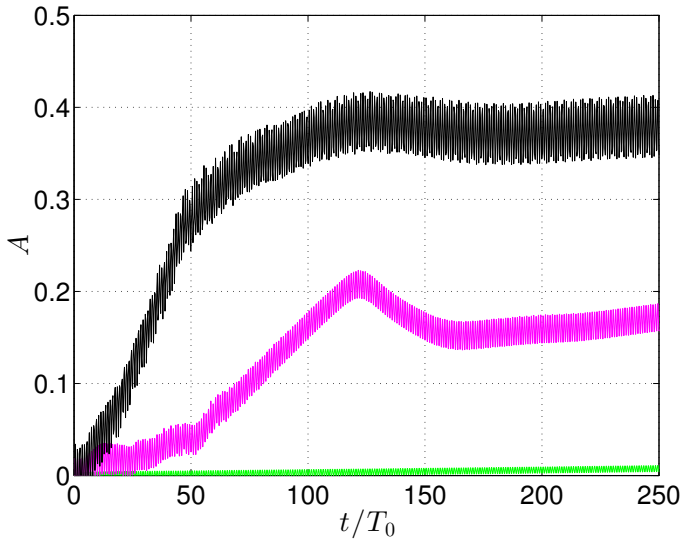


Figure 5.19: Time evolution of the normalized potential energy for three different forcing amplitudes: green ($a = 1$ mm), magenta ($a = 5$ mm) and black ($a = 9$ mm).

An other option can be experimental. Indeed, recently, in our group, the development of a PIV/PLIF combination technique has been performed. PLIF stands for Planar Laser Induced Fluorescence, which is a technique used for density measurements. A dye is put in the fluid, and its concentration is directly related to the density of the fluid. Thus, one can have access to the density in all the tank. Usually, this technique has been used the measure the mixing of two fluids of different densities. I participated in the development of this technique in a linearly stratified fluid and we are able to quantify the mixing through the turbulent diffusivity coefficient K_t, caused by TRI in vertical mode-1 of high amplitude [34]. This technique can be applied to internal wave attractors in order to follow the mixing and the relevant quantities as K_t as a function of time.

5.3 Comparison with other long-term experiments

The two previous sections have described typical cases of discrete triadic cascades (case B) and mixing experiments (case C). However, the typical scenarios can be slightly modified by the choice of the (d, τ) parameters, i.e. the operating point in the Arnold tongue. Indeed, sections 3.2.3 and 4.2.2 have shown that these parameters can change the susceptibility of the attractors and the onset of the TRI. Thus, this can have an influence on the typical cases presented in sections 5.1 and 5.2. First, in section 5.3.1, we compare the case B (well-

focused attractor ■) with similar experiments at the same forcing amplitude ($a = 5$ mm) but with different d values: weakly-focused attractor ★ or strongly-focused attractor ▲. Then, in section 5.3.2, one does the same thing for case C (well-focused attractor ■), with $a = 10$ mm. Only another experiment has been performed with $a = 10$ mm, with a geometry such that there is a weakly-focused attractor ★. The precise location of the different experiments in the Arnold tongue can be found in figure 4.10.

5.3.1 Other discrete TRI cascade experiments

Case B is a typical case of a triadic energy cascade, with strong signatures of wave-turbulence. In the (d, τ) diagram, this experiment is located on the most susceptible region with high $\langle K \rangle$ and R values (see section 3.2.3). It corresponds to the case of well-focused attractors (■) with the onset of TRI is local. The case of weakly-focused attractors (★) has already been described in section 4.2.2, with exactly the same amplitude $a = 5$ mm. The TRI is triggered globally and the secondary waves corresponds to global quasi-resonances of the trapezoidal basin. For this experiment, $\langle K \rangle$ is still high but R is low. One can only consider a last case, of strongly-focused attractors (▲), with low values of $\langle K \rangle$ and R. Figures 5.20 shows the time-frequency diagrams for these three cases: panel (a) for the weakly-focused attractor of section 4.2.2, panel (b) for the new case of strongly-focused attractor and panel (c) for case B of section 5.1.

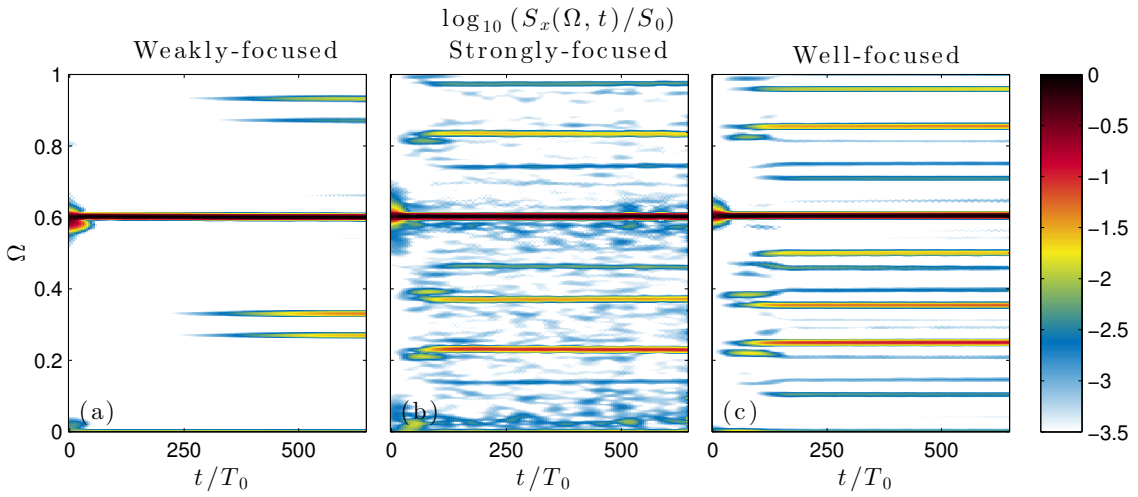


Figure 5.20: Time-frequency diagrams: $\log_{10}\left(S_x(\Omega,t)/S_0\right)$, defined in equation (4.3), for three different focused attractors with the forcing amplitudes $a = 5$ mm: weakly-focused ★ (a), strongly-focused ▲ (b) and well-focused ■ (c). The quantity S_0 is defined as the time average of the main component $S_x(\Omega_0, t)$. The time-frequency diagrams are calculated on a 5×5 cm^2 square region, on branch 1.

Contrary to what one can expect, the TRI cascade is weaker in the strongly-focused attractor (▲) than in case B, the well-focused attractor (■). From panels (a) to (c) of figure 5.20, one can see a graduation in the richness of the pattern. For panel (a), there is only one couple of secondary waves, with a very low growth rate. The onset of TRI is global. For panel (b), there are two couples of secondary waves. One can check that the first one is created by local TRI on branch 1 and the second couple is the product of the triadic interaction of the first couple. This is the first step of the triadic cascade. For panel (c), the cascade is fully developed, as one has at least eight couples of secondary

waves. One can explain that the strongly-focused attractor (▲) is less unstable than the well-focused attractor (■) because of the susceptibility. Indeed, $\langle K \rangle$ is smaller for the strongly than for the well-focused attractor. Thus, tuning the (d, τ) parameters of the experiments allows us to control the development of the cascade, from one couple only to several pairs.

Although the instability starts and evolves differently in strong-, weak- or well-focused attractors, they can exhibit some common features. Figure 4.14 shows in section 4.2.2 that the secondary waves generated by the weakly focused attractor (★) are standing waves. Some frequencies created by well- or strongly-focused attractors (■ or ▲) in long-term experiments can also be standing waves. For example, figure 5.21 shows that, for the well-focused attractor, the two frequencies $\Omega_{2,1}$ and $\Omega_{2,2}$ are standing waves as it is clear from the wave patterns filtered at these frequencies. Note that not all the frequencies present in figure 5.4 correspond to standing waves.

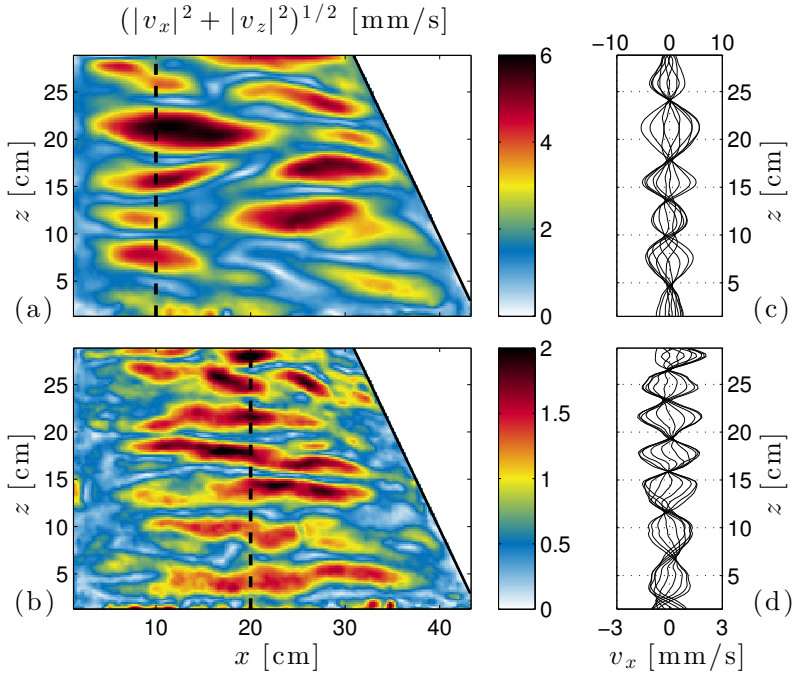


Figure 5.21: Components of the wave field for case B (■) corresponding to frequencies $\Omega_{2,1}$ (a) and $\Omega_{2,2}$ (b), obtained with the Hilbert transform centered at $t = 620\ T_0$ using a $85\,T_0$ long Hamming window. Note that the components oscillating at $\Omega_{2,1}$ and $\Omega_{2,2}$ correspond to standing waves as is clearly seen on the sequences of wave profiles shown on the right of each picture (panels (c) and (d)).

With the frequencies corresponding to the peaks of the spectrum shown in figure 5.20, one can compute the values of parameters τ associated to these waves. These frequencies are shown by points in the diagram (d, τ) in figure 5.22. The symbols for the secondary waves are the same than the one for the attractor: ■ stands for the well-focused attractor, ★ for the weakly-focused attractor while the ▲ is for the strongly-focused attractor. The symbols are white for secondary waves whose frequencies are lower than Ω_0 (so larger τ) and are black when the frequencies are larger than Ω_0 (so smaller τ). The size of the symbol is smaller for secondary waves than for the attractor. It can be seen that the τ parameters for the standing secondary waves are close to black zones in the (d, τ) diagram. Thus, at least some frequencies created by the weakly-, strongly- and well-focused attractors

could correspond to quasi-resonant modes. In absence of commonly accepted terminology, we can tentatively call the dark regions as geometric quasi-resonances. Previously quasi-resonances have been discussed assuming non-zero resonance width (see [121]). Here we refer to possibility of global quasi-resonances assuming that the Lyapunov exponent can take very small negative non-zero value. In a realistic system with weak viscous dissipation, we can expect that some of the quasi-resonances can exhibit a seiche-like behavior similar to exact seiche modes discussed in [97, 104]. Therefore, at the conceptual level, the key driving processes in long-term experiments with unstable wave attractors can be considered as a combination of "local" and "global-scale" TRI events, with long-term transients between the two.

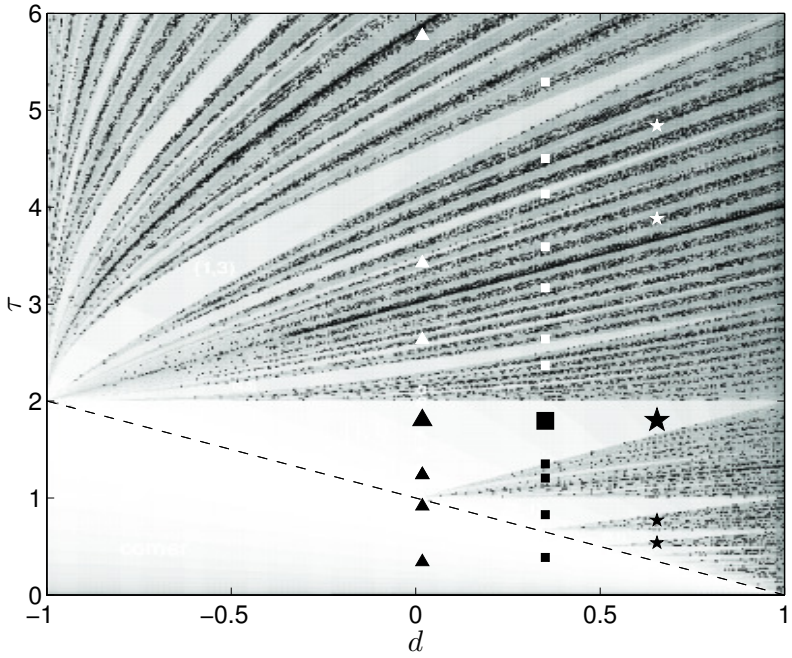


Figure 5.22: (d, τ) diagram with the different frequencies present in the tank for the weakly-focused attractor (★), the well-focused attractor (■) and the strongly-focused attractor (▲). The symbols are white for secondary waves whose the frequencies is lower than Ω_0 (so larger τ) and are black when the frequencies are larger than Ω_0 (so smaller τ). When τ is larger than 6, the symbols are not plotted.

Interesting parallels can be found in the dynamics of rotating fluids. For instance, Duguet *et al.* [36] show rich multi-peak spectra for inertial oscillations in a compressible fluid confined in a rotating cylindrical vessel. They relate the frequencies associated with the observed peaks to global modes of the fluid motion. Similarly, Favier *et al.* [46] analyze the frequency spectrum of fluid motion generated by libration-driven elliptic instability in a rotating ellipsoid and show the presence of the eigenfrequencies of linear and quadratic inertial modes.

5.3.2 Other mixing experiments

In this section, case C is compared to another mixing long-term experiment, caused by a weakly-focused attractor (★) forced at the same amplitude ($a = 10$ mm). In Chapter 4, we have shown that the onset of TRI in wave attractors and the parameters of wave triplets involved into resonant interactions strongly depend on the choice of the operating points

in (d, τ) plane. However, one can expect a certain level of universality when the energy input into the continuously stratified confined system is large and the system is given a sufficiently long time to reach a quasi-steady state with fully developed energy cascade. This cascade can operate via the hierarchy of triadic wave-wave interactions transferring energy to small-scale internal waves and ultimately to mixing events as it is experimentally shown in section 5.2.3. The confinement of the system requires the global balance between the injection and dissipation of energy at the steady state [125, 79]. A true steady state cannot be reached in a density stratified fluid: a certain portion of available kinetic energy induces mixing which in turn produces a slow erosion of the mean background stratification. If the time-scale of this erosion is long, we observe a quasi steady state behaviour. Below, we compare the case C of Table 5.1, which is a well-focused $(1, 1)$ attractor (■) with the case of a weakly-focused $(1, 1)$ attractor (★). Both attractors are forced at an amplitude equal to $a = 10$ mm.

The time-frequency diagrams of the two unstable attractors at different operating points are shown in figure 5.23. Panel (a) shows the time-frequency diagrams of case C (■), also presented in figures 5.3(c) and 5.13(a), while panel (b) exhibits the time-frequency diagram of a weakly-focused attractor (★). Both have a forcing amplitude of $a = 10$ mm. Obtained in regimes with measurable mixing (high forcing amplitude), it can be seen that both diagrams have qualitatively similar features. Several discrete frequency peaks of large magnitude are embedded into a continuous spectrum, which has significantly smaller magnitude. These peaks fluctuate in time and the background is high in both cases. The bicoherence of the weakly-focused case, not presented in this manuscript, also shows very similar features with the one of case C.

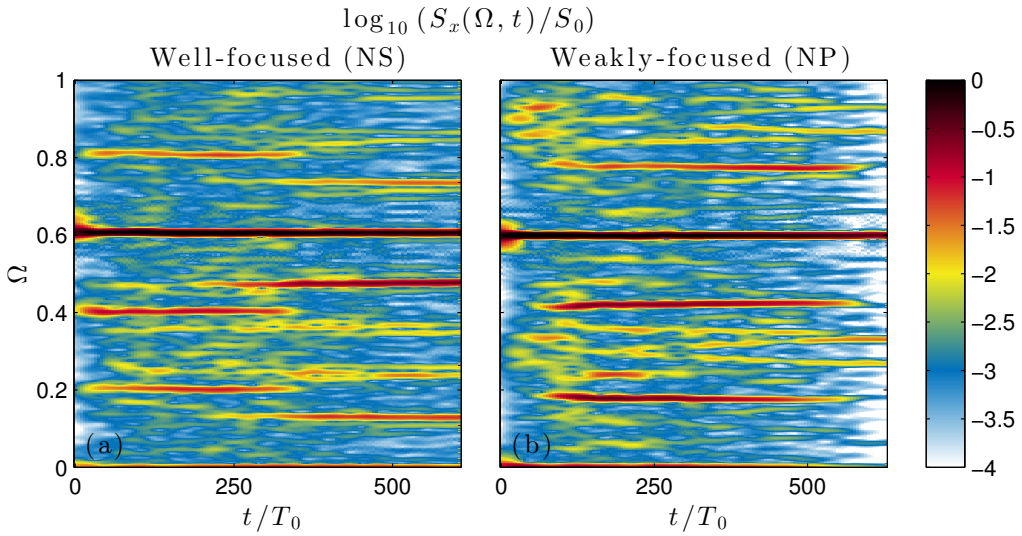


Figure 5.23: Time-frequency diagrams of two signals recorded in unstable wave attractors corresponding to different operating points. Both attractors are unstable and the wave regime is such that it induces significant mixing. The left panel corresponds to the experiment indicated by the symbol ■ while the right one by the ★ (see figure 4.10 and Table 4.3 for the parameters). Note that the forcing amplitude for these two experiments is $a = 10$ mm.

5.3.3 Probability density functions of the horizontal vorticity

Section 5.2.3 shows that the probability density function (PDF) of the dimensionless horizontal y-component of the vorticity field, $\Xi_y = \xi_y/N$, represents a relevant quantity for consideration of statistics of extreme events in the experimental system. This quantity has a clear physical meaning as a ratio of the destabilizing effect of vorticity to the stabilizing effect of stratification. Obviously, we can expect some mixing in the system when significant statistics of events with high values of $|\Xi_y|$ are encountered.

Figures 5.24(a) and (b) represents the PDFs of Ξ_y for weak- and well- focused $(1, 1)$

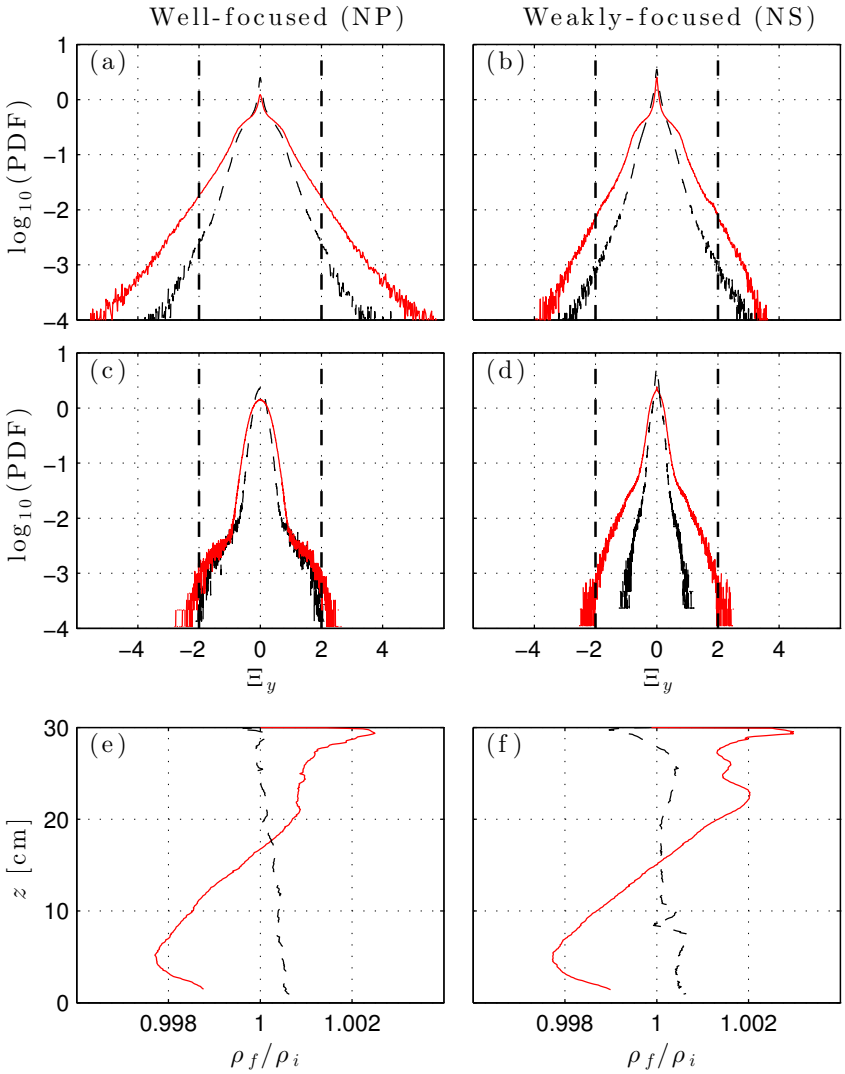


Figure 5.24: Probability density functions of the dimensionless vorticity Ξ_y in the tank, calculated from all images between 480 and 500 T_0, for the two well-focused (propagating) ■ (a) or weakly-focused (standing) ★ (b) wave experiments presented in figure 5.23. Probability density functions of the vorticity in the tank, filtered at Ω_0, for the two propagating (c) or standing (d) wave experiments. Ratio between the final and the initial stratifications for the two well-focused (propagating) (e) or weakly-focused (standing) (f) wave experiments. The red color is associated with experiments with $a = 5$ mm and the black color is associated with experiments performed at $a = 10$ mm.

attractors for two different values of the forcing amplitude a. The left column is for well-focused attractors (■) while the right column is for weakly-focused attractors (★). On each row, the red curves represent the data for attractors with $a = 5$ mm while the black ones are for attractors with $a = 10$ mm. It can be seen that if a is fixed, the system with weak focusing (characterized by high values of $\langle K \rangle$ and low values of R in a stable regime) shows consistently lower statistics of extreme events. At the same time, at sufficiently high values of the forcing amplitude a, the shape of vorticity PDFs in attractors with high and low focusing is qualitatively similar. Indeed, the qualitative behaviour of two systems at high a is similar as attested by their time-frequency diagrams (figure 5.23). Moreover, the long-term effect on stratification is also similar since we observe a well-measurable mixing when comparing the initial and final density distributions in figures 5.24(e) and (f). We believe that the significant statistics of extreme events with high horizontal vorticity arises from the spontaneous summation of the frequency components of the wave field. The primary wave alone cannot produce events with sufficiently high vorticity. This is attested by figures 5.24(c) and (d) that represents the PDFs of Ξ_y for the primary wave field filtered at Ω_0 for the well-focused (■) and weakly-focused attractors (★). It can be seen that these PDFs have no tails extending to the domains with $|\Xi_y| > 2$. The threshold value $|\Xi_y| > 2$ has been suggested in section 5.2.3 as extension of the classic Miles-Howard criterion for stability of horizontal shear flows of continuously stratified fluid [72, 116]. In fact, some physical considerations suggesting a wider range of applications of the Miles-Howard criteria can be found in classic works, for example in [132]. The threshold value of $|\Xi_y| = 2$ allows us to make some useful qualitative conclusions on the mixing efficiency. The probability of having an extreme event with intensity $|\Xi_y| > 2$ is given by the integral over the corresponding tails of the PDF. The cases with measurable mixing depicted in figure 5.24(e) and (f) correspond to drastically increased probability of extreme events. It increases from 2‰ for $a = 5$ mm to 19‰ for $a = 10$ mm in the "propagating waves" case (■), and from 0.7‰ for $a = 5$ mm to 5.6‰ for $a = 10$ mm in the "standing waves" case (★). We observe a comparable increase of probability, by factor 10 and 8, in both cases. Although the statistics of high-vorticity events seems to represent a kinematic indicator for the occurence of mixing, at the present stage it is difficult to relate this statistics directly to the overall mixing efficiency. Additional parameters should be measured, most importantly, the typical scale of overturning structures. As an alternative, one can make an attempt to estimate the turbulent diffusion coefficient in the experimental system using the PIV/PLIF technique [34].

Conclusions

In this Chapter, I discussed essentially *long-term* experiments and triadic energy cascade in unstable regimes. I have shown that, for a given geometry, the forcing amplitude can tune the amount of instabilities in the system. For low forcing, the attractor remains stable. For an intermediate forcing, the attractor is unstable and leads, after a long transient period, to a cascade of triadic interactions. Several couples of secondary waves are created: they all exchange energy through three-wave interactions. This is the first experimental signatures of internal wave turbulence. For high forcing, a cascade is also present but the waves are sufficiently strong to partially mix the fluid. The mixing process is linked with high vorticity events, created by the combination of the different waves. This set-up can thus be taken as a "mixing-box".

Then, I studied the influence of the geometry on the triadic cascades. For a given forcing amplitude, the choice of the operating point in the (d, τ) diagram (so the geometry of the attractor) allows us to control the intensity of the cascade, limiting the number of secondary wave couples. Some secondary frequencies are found to be quasi-resonant geometrical modes. Nevertheless, if the forcing amplitude is sufficiently high, the geometry does not matter anymore and different attractors can lead to comparable amounts of mixing.

This work can explain, partially, the cascade processes at play in the abyss. Guo and Holmes-Cerfon [65] have found that, on a 2D realistic topography, the probability to get an wave attractor is of 10 attractors per 1000 km. Interestingly, this study shows that in the case of small-scale bathymetry the attractors with very elongated loops represent the most probable configuration, justifying our interest to attractors with a “degenerated” geometry. Thus, the presence of attractors in seas and lakes is not to exclude. They are likely to be in a non-linear regime due to focusing. Consequently, one can expect that they are responsible for energy cascade and mixing in their neighborhood. The relevance of such a scenario in a three-dimensional topography [105, 35] is still to explore.

Conclusion

The main objectives of my PhD were to understand the linear and non-linear cascade processes at play in idealized experiments of internal wave attractors. First, in Chapter 3, we have investigated internal wave attractors in the linear regime, at low forcing amplitude.

1. We explored the structure of the Arnold tongue corresponding to a simple attractor. We have shown that the kinetic energy of the confined fluid system represents an appropriate global variable that allows us to classify the observed wave regimes. A typical Arnold tongue is shown to have a central region corresponding to "classical" well focused wave attractors with thin branches where the wave energy is concentrated. These attractors typically have a large total kinetic energy, and the wave motion in the attractor branches is represented by a propagative wave. The behaviour of "classical" wave attractors has been studied in great detail, both in linear [98, 97, 138, 125, 70, 64, 69, 38, 65] and non-linear [125, 139, 79] regimes. The central region of Arnold tongue is surrounded by border regions corresponding to zones of geometric degeneracy which can be of two types: one in which attractors collapse onto a line representing a diagonal of the trapezoid and the other which the system itself does not support effective focusing. The latter case corresponds to well-studied configuration of standing internal waves in a rectangular domain filled with uniformly stratified fluid [110]. For the intermediate case of an elongated attractor in the domain with weak focusing, the wave motion in the attractor represents a nearly standing wave which, however, has increased energy concentration at the loop predicted by the ray tracing which indicates that the propagative component of the wave field does matter.

2. We have investigated the influence of the geometry of the basin on the different characteristics of the attractor such as its wave length, width and amplitude. In the linear regime and for a fixed geometry, the wave length and width of the attractor are totally independent of the forcing amplitude while the amplitude of the wave attractor increases with it. Moreover, the scaling of the ratio width-over-perimeter has been tested using the two tanks of different sizes. This shows a very good correspondence with the theoretical predictions of Grisouard *et al.* [64]. This leads to the conclusion that, in the ocean, linear attractors have too narrow branches to be stable. Thus, TRI is very likely in the oceanic context for wave attractors and it is worthwhile to study this instability in wave attractors.

3. Different forcings have been investigated using the wave-maker described in [115, 63]. The experimental wave fields obtained have been compared with the theoretical

stream function computed following [86, 98, 97]. For a forcing on the total height of the basin, the experiments are in a very good agreement with the vanishing viscosity prediction. For a forcing on a primary fundamental interval only, the scale is too small in the small tank to allow the waves to reach the ray tracing prediction. Nevertheless, in the large tank experiments, one observes rays converging towards the attractor, with decreasing wave length when approaching the closed loop. This is in agreement with the predicted theoretical stream function. This kind of experiment constitutes the simplest investigation to understand the convergence of internal wave rays towards the attractor.

As the linear focusing very likely leads to the instability of internal wave attractors in the oceans, it is worthwhile to study the start of the triadic resonant instability (TRI) from an experimental point of view. This has been done in Chapter 4.

1. Scolan *et al.* [139] have reported the local character of TRI, growing from the most energetic branch of the attractor. We have shown that the start of TRI can be global, depending on the choice of the operating point at the Arnold tongue. Such global TRI occurs when the attractor is of large amplitude and close to a standing wave, so in the right tip of the Arnold tongue. The growth characteristic time of this global instability is found to be much larger than the return-trip time of the secondary frequencies in the tank. Thus, it is necessary to observe global TRI through long-term experiments. The secondary frequencies are quasi-standing waves. This global instability thus represents an intermediate case between the local TRI [139] and the TRI in purely standing waves [110].

2. We investigated the influence of local TRI on the wave length and on the amplitude of the attractor. When the attractor grows, it undergoes linear focusing up until the point that the instability starts. The attractor then escapes from the linear focusing and its wave length remains larger than in the linear case, due to the instability. The amplitude of the attractor is limited by the instability, because of the energy transfer to secondary waves. The dissipation reaches a steady state, as mentioned in [79].

3. We also developed a collaboration with Ilias Sibgatullin, to perform numerical simulations of internal wave attractors with exactly the same configuration as in the experiments. Ilias Sibgatullin wrote the code and carried out the simulations while I performed most of the data analysis. The numerically simulated and experimental attractors are in very good agreement for both stable and unstable cases. Experiments and numerical simulations have also shown that the attractor flow is quasi invariant in the transversal direction. Some three-dimensional effects have been investigated but appear to be small: TRI is also quasi independent of the transversal coordinate and the mean-flow induced by the attractor remains small with respect to the wave velocity field. The SyS technique, based on integration of the density gradient field over the tank width, has been validated using numerical simulations, for both stable and unstable cases. The main three-dimensional effect is that around 25% of the total dissipation in the width occurs in the viscous boundary layers of the lateral walls of the tank.

Finally, we explored the triadic energy cascade in internal wave attractors, using long-term experiments in Chapter 5.

1. We studied energy cascade of unstable attractors for large forcing. These experiments show convincing signatures of discrete internal wave turbulence, observed

experimentally for the first time. We used the bicoherence as a relevant tool to visualize the three-wave interactions of such an energy cascade. Almost all the energy in the tank follows the dispersion relation showing the presence of only waves in the experiments. We have computed the spatial spectra which exhibit a -3 power law. Note that this exponent is different from the one predicted by the wave turbulence theory [94]. Moreover, we have shown that the choice of the operating point at the Arnold tongue allows us to tune the intensity of the discrete cascade, from only one couple of secondary waves to more than eight pairs. In the oceanic context, the Garrett and Munk measured spectra in the ocean [57] are close to the internal wave turbulence predictions of Lvov and Tabak [94]. Thus, following our experiments, one can expect that internal wave attractors in oceans are unstable and lead to internal wave turbulence. This may explain a route for the energy cascade in oceans, where the topography can enhance some attractors. Moreover, as attractors transfer a large amount of their energy to the secondary waves, this can be difficult to observe them directly.

2. For very high forcing, we show that some mixing can be induced by the energy cascade of an internal wave attractor. Thus, the experimental set-up represents an "internal wave mixing box". The mixing is caused by extreme vorticity events, higher than the Miles-Howard threshold for vorticity defined by the Richardson number. The extreme events are due to the random summations of the wave fields of the different frequencies present in the tank. The attractor alone cannot cause mixing, even at very high amplitude. Moreover, under sufficiently large forcing, the cascade does not depend any more on the geometry of the attractor in the mixing regime. This is a common fate for wave attractors with strong and weak focusing, with qualitatively similar statistics of extreme events leading to mixing. Thus, this regime appears to be universal. The choice of the operating point at the Arnold tongue and the amplitude of the input perturbation provide extreme flexibility to control the parameters of the energy cascade in the system. We believe that this "mixing box" configuration has a strong potential to mimic many aspects of the energy cascade in confined geophysical systems both experimentally and numerically.

3. We have shown that some frequencies in the spectrum of wave motions correspond to standing and nearly-standing waves with high vertical modes. These observations may have an important consequence on the dynamics of large stratified geophysical systems. Lakes, for example, may be subject to very complex forcing. The cascade of triadic instabilities that develops as a response to forcing may effectively transfer energy to standing and nearly-standing waves of high vertical modes. When the forcing stops, the attractor-like components of the internal wave motion quickly disappear as described in [70, 64]. In absence of energy injection, at low wave numbers, the spectrum of wave motions in attractors quickly shifts toward large wave numbers due to focusing, and the large wave numbers quickly decay due to viscosity. In contrast, the normal vertical (global resonance) modes conserve their length scale and decay at a much longer time-scale owing to purely viscous mechanism. Similar dynamics is expected for quasi-resonant modes characterized by vanishingly weak focusing. Such a scenario can explain the presence of high vertical modes in limnological observations.

Perspectives

In Chapter 2, I have shown interesting results about tidal conversion at finite and infinite depths. The affine similitude theory for a square-shaped cylinder in a stratified fluid of infinite depth is in good agreement with the measured added mass despite the waves perturbating the pendulum after reflecting on the edges of the tank. This causes non-reliable measurements at low frequencies. For a circular-shaped cylinder in a stratified fluid of finite depth, the results are consistent with the ones reported in [39, 42]. The measurements are less perturbed by the wave reflections. Moreover, at very small depths, the damping coefficient is found to be larger than 1 in the low-frequency limit, relevant for tidal conversion. This means that the damping coefficient at finite depth is larger than the one at infinite depth, as predicted by Llewellyn Smith and Young [92]. I have also shown that some topographies can exhibit a lack of tidal conversion at finite depth [96]. Nevertheless, more pendulum experiments are necessary to completely verify the affine similitude theory and the predictions for tidal conversion made by Llewellyn Smith and Young [92]. Indeed, the vertical flat plate oscillating horizontally in a stratified fluid of limited depth is of particular interest since a theoretical prediction exists in [93, 122]. Moreover, the topography lacking of tidal conversion exhibited by Maas [96] merits being completed by experiments at very small or large depths.

For the internal wave attractors, many questions remain open. In particular, this work may be continued and our knowledge in the attractor cascade may be improved by the following points.

First, as we performed idealized laboratory experiments, it it necessary to keep in mind the main differences between the oceans and our experiments.

- Guo and Holmes-Cerfon [65] pointed out that more complex attractors than the $(1, 1)$ attractor are more likely to be present in the ocean. Thus, it is worth considering the energy cascade in more complicated attractors, like the $(2, 1)$ for example. These attractors can be obtained using the same basin geometry as for the experiments reported in this manuscript.

- A very large part of the studies on attractors in the oceans [65, 38] and in the experiments [139, 70, 69, 68], including our studies, is performed in a bi-dimensional set-up. As the oceans are three-dimensional and not bi-dimensional, it is necessary to perform 3D attractor experiments. This is the objective of Grimaud Pillet, who started his PhD on three-dimensional attractors in our group in September 2015.

- In the oceans, the Earth's rotation also plays a very important role, being responsible for inertial waves. The rotation is not expected to modify the linear processes of wave attractors, but it vastly complicates the appearance and the behavior of the triadic instability. Thus, the triadic cascade may be modified due to this rotation. Paco Maurer, who started his PhD in our group in September 2014, is working on TRI in gravito-inertial plane wave beams [109]. Note that the set-up he uses cannot support wave attractors.

- The forcing made with the wave-maker on all the height of the fluid is very specific to the experiments and is not realistic for the oceans. Tidal forcing may be important to test, as in the experiment reported in [38].

- In order to consider all the differences between the ocean and the idealized experiments, the non-linear stratification of the ocean should also be taken into account.

Then, in this manuscript, the mixing process has been discussed qualitatively using vorticity PDFs and the Miles-Howard criteria on the Richardson number. Nevertheless, it is possible to investigate further mixing in stratified fluid. Indeed, Yvan Dossmann, who started a post-doc in our group in September 2014, is working on the PIV/PLIF experimental technique. This allows us, by measuring simultaneously the velocity and density fields, to get access to the turbulent diffusivity [34]. Preliminary experiments in attractor configurations have shown that the turbulent diffusivity is much higher in the case of a trapezoidal basin with an attractor than for a rectangular tank, with similar forcing. Note that long-term experiments are of crucial importance to observe and study quantitatively the mixing processes. Moreover, it is worthwhile to investigate the mixing in the experiments from the Lagrangian point of view, which is a tool widely used for example in atmospherical data [77, 32] or in turbulence [18].

From a more fundamental point of view, the attractor set-up may be used to study internal wave turbulence. Indeed, one has demonstrated that attractors lead to triadic energy cascade for high forcing and long-term experiments. Thus, we have at our disposal a very convenient and useful set-up to explore internal wave turbulence and the cascade associated with it. Developing PIV in the large tank will allow us to increase the size of the experimental set-up, in order to decrease the confinement effects and to increase the separation between the injected and dissipative scales. Thus, the basic hypothesis of the wave-turbulence framework [121] will be further confirmed. Moreover, it may be possible to use two cameras with this set-up: one, focused on the flow at large scales and one dedicated to a given smaller region of the basin, in order to better resolve the small scales of the spatial spectra. Note that, in addition, the discrete wave-turbulence obtained in some experiments may be connected with the theoretical work of Kartashova [81].

Publications in relation to the manuscript

- **Energy cascade in internal wave attractors.**
  C. Brouzet, E. V. Ermanyuk, S. Joubaud, I. N. Sibgatullin and T. Dauxois
  Published in *Europhysics Letters* (2016), vol. 113:44001

- **Internal wave attractors examined using laboratory experiments and 3D numerical simulations.**
  C. Brouzet, I. N. Sibgatullin, H. Scolan, E. V. Ermanyuk and T. Dauxois
  Published in *Journal of Fluid Mechanics* (2016), vol. 793:109-131

- **Mixing by internal waves quantified using combined PIV/PLIF technique.**
  Y. Dossmann, B. Bourget, C. Brouzet, T. Dauxois, S. Joubaud, and P. Odier
  Submitted to *Experiments in Fluids* (January 2016)

- **Internal wave attractors: Arnold tongue's structure and its implications for the instability scenario.**
  C. Brouzet, E. V. Ermanyuk, S. Joubaud, G. Pillet and T. Dauxois
  Submitted to *Journal of Fluid Mechanics* (April 2016)

- **Added mass: a sidekick to tidal conversion.**
  C. Brouzet, E. V. Ermanyuk, M. Moulin, and T. Dauxois
  In preparation.

- **Internal wave attractors at different laboratory scales.**
  C. Brouzet, E. V. Ermanyuk, S. Joubaud and T. Dauxois
  In preparation.

Bibliography

[1] M. H. Alford. Observations of parametric subharmonic instability of the diurnal internal tide in the south china sea. *Geophysical Research Letters*, 35(L15602), 2008.

[2] M. H. Alford, J. A. MacKinnon, Z. Zhao, B. Pinkel, J. Klymak, and T. Peacock. Internal waves across the pacific. *Geophysical Research Letters*, 34(L24601), 2007.

[3] M. P. Baldwin, L. J. Gray, T. J. Dunkerton, K. Hamilton, P. H. Haynes, W. J. Randel, J. R. Holton, M. J. Alexander, I. Hirota, T. Horinouchi, D. B. A. Jones, J. S. Kinnersley, C. Marquardt, K. Sato, and M. Takahashi. The Quasi-Biennial Oscillation. *Reviews of Geophysics*, 39(2):179–229, 2001.

[4] F. K. Ball. Energy transfer between external and internal gravity waves. *Journal of Fluid Mechanics*, 374:117–144, 1998.

[5] G. K. Batchelor. Small-scale variation of convected quantities like temperature in turbulent fluids. *Journal of Fluid Mechanics*, 5:113–133, 1959.

[6] G. K. Batchelor. *The Theory of Homogeneous Turbulence.* Cambridge University Press, 1982.

[7] T. H. Bell. Lee waves in stratified flows with simple harmonic time dependence. *Journal of Fluid Mechanics*, 67:705–722, 1975.

[8] D. Benielli and J. Sommeria. Excitation and breaking of internal gravity waves by parametric instability. *Journal of Fluid Mechanics*, 374:117–144, 1998.

[9] M. V. Berry. Regularity and chaos in classical mechanics, illustated by three deformations of a circular billiard. *European Journal of Physics*, 2:91–102, 1981.

[10] P. Billant and J.-M. Chomaz. Self-similarity of strongly stratified inviscid flows. *Physics of Fluids*, 13(6), 2001.

[11] T. Bonometti, S. Balachandar, and J. Magnaudet. Wall effects in non-Boussinesq density currents. *Journal of Fluid Mechanics*, 616:445–475, 2008.

[12] G. Bordes. *Interactions non-linéaires d'ondes et tourbillons en milieu stratifié ou tournant.* PhD thesis, ENS de Lyon, 2012.

[13] G. Bordes, F. Moisy, T. Dauxois, and P.-P. Cortet. Experimental evidence of a triadic resonance of plane inertial waves in a rotating fluid. *Physics of Fluids*, 24(014105), 2012.

[14] A. Boudaoud, O. Cadot, B. Odille, and C. Touzé. Observation of wave turbulence in vibrating plates. *Physical Review Letters*, (234504), 2008.

[15] B. Bourget. *Ondes internes, de l'instabilité au mélange. Approche expérimentale.* PhD thesis, ENS de Lyon, 2014.

[16] B. Bourget, T. Dauxois, S. Joubaud, and P. Odier. Experimental study of parametric subharmonic instability for internal plane waves. *Journal of Fluid Mechanics*, 723:1–20, 2013.

[17] B. Bourget, H. Scolan, T. Dauxois, M. Le Bars, P. Odier, and S. Joubaud. Finite-size effects in parametric subharmonic instability. *Journal of Fluid Mechanics*, 759:739, 2014.

[18] M. Bourgoin, J.-F. Pinton, and R. Volk. Lagrangian Methods in Experimental Fluid Mechanics. In T. von Larche and P. D. Williams, editors, *Modeling Atmospheric and Oceanic Flows: Insights from Laboratory Experiments and Numerical Simulations*, Geophysical Monograph Series, chapter 15. John Wiley & Sons, 2014.

[19] P. Bouruet-Aubertot, J. Sommeria, and C. Staquet. Breaking of standing internal gravity waves through two-dimensional instabilities. *Journal of Fluid Mechanics*, 285:265–301, 1995.

[20] C. E. Brennen. A review of added mass and fluid inertial forces. Technical Report CR 82.010, Naval Civil Engineering Laboratory, 1982.

[21] C. Brouzet, E. V. Ermanyuk, S. Joubaud, G. Pillet, and T. Dauxois. Internal wave attractors: Arnold tongue's structure and its implications for the instability scenario. *Submitted to Journal of Fluid Mechanics*, 2016.

[22] C. Brouzet, E. V. Ermanyuk, S. Joubaud, I. N. Sibgatullin, and T. Dauxois. Energy cascade in internal wave attractors. *Europhysics Letters*, 113(44001), 2016.

[23] C. Brouzet, I. N. Sibgatullin, H. Scolan, E. V. Ermanyuk, and T. Dauxois. Internal wave attractors examined using laboratory experiments and 3D numerical simulations. *Journal of Fluid Mechanics*, 793:109–131, 2016.

[24] K. A. Buch Jr and W. J. A. Dahm. Experimental study of the fine scale structure of conserved scalar mixing in turbulent shear flows. Part 1. Sc>1. *Journal of Fluid Mechanics*, 317:21–71, 1996.

[25] O. Bühler and C. J. Muller. Instability and focusing of internal tides in the deep ocean. *Journal of Fluid Mechanics*, 588:1–28, 2007.

[26] G. F. Carnevale, M. Briscolini, and P. Orlandi. Buoyancy- to inertial-range transition in forced stratified turbulence. *Journal of Fluid Mechanics*, 427:205–239, 2001.

[27] D. Clarke. Calculation of the added mass of elliptical cylinders in shallow water. *Ocean Engineering*, 28:1361–1381, 2001.

[28] P. Cobelli, P. Petitjeans, A. Maurel, V. Pagneux, and N. Mordant. Space-time resolved wave turbulence in a vibrating plate. *Physical Review Letters*, (204301), 2009.

[29] S. B. Dalziel, G. O. Hughes, and B. R. Sutherland. Whole-field density measurements by 'synthetic schlieren'. *Experiments in Fluids*, 28(4):322–335, 2000.

[30] T. Dauxois and W. R. Young. Near-critical reflection of internal waves. *Journal of Fluid Mechanics*, 390:271–295, 1999.

[31] R. E. Davis and A. Acrivos. The stability of oscillatory internal waves. *Journal of Fluid Mechanics*, 30(04):723–736, 1967.

[32] A. De La Cámara, A. M. Mancho, K. Ide, E. Serrano, and C. R. Mechoso. Routes of Transport across the Antarctic Polar Vortex in the Southern Spring. *Journal of Atmospherical Science*, 69:741–752, 2012.

[33] M. Dewan. Saturated-cascade similitude theory of gravity wave spectra. *Journal of Geophysical Research*, 102(D25):29,799–29,817, 1997.

[34] Y. Dossmann, B. Bourget, C. Brouzet, T. Dauxois, S. Joubaud, and P. Odier. Mixing by internal waves quantified using combined PIV/PLIF technique. *Submitted to Experiments in Fluids*, 2016.

[35] S. Drijfhout and L. R. M. Maas. Impact of channel geometry and rotation on the trapping of internal tides. *Journal of Physical Oceanography*, 37:2740–2763, 2007.

[36] Y. Duguet, J. F. Scott, and L. Le Penven. Oscillatory jets and instabilities in a rotating cylinder. *Physics of Fluids*, 18(104104), 2006.

[37] G. Düring, C. Josserand, and S. Rica. Weak Turbulence for a Vibrating Plate: Can One Hear a Kolmogorov Spectrum? *Physical Review Letters*, 97(025503), 2006.

[38] P. Echeverri, T. Yokossi, N. J. Balmforth, and T. Peacock. Tidally generated internal-wave attractors between double ridges. *Journal of Fluid Mechanics*, 669:354–374, 2011.

[39] E. V. Ermanyuk. The use of impulse response functions for evaluation of added mass and damping coefficient of a circular cylinder oscillating in linearly stratified fluid. *Experiments in Fluids*, 28:152–159, 2000.

[40] E. V. Ermanyuk. The rule of affine similitude for the force coefficients of a body oscillating in a uniformly stratified fluid. *Experiments in Fluids*, 32:242–251, 2002.

[41] E. V. Ermanyuk, J.-B. Flor, and B. Voisin. Spatial structure of first and higher harmonic internal waves from a horizontally oscillating sphere. *Journal of Fluid Mechanics*, 671:364–383, 2011.

[42] E. V. Ermanyuk and N. V. Gavrilov. Force on a body in a continuously stratified fluid. Part 1. Circular cylinder. *Journal of Fluid Mechanics*, 451:421–443, 2002.

[43] E. V. Ermanyuk and N. V. Gavrilov. Oscillations of cylinders in a linearly stratified fluid. *J. Appl. Mech. Tech. Phys.*, 43(4):503–511, 2002.

[44] E. V. Ermanyuk and N. V. Gavrilov. Force on a body in a continuously stratified fluid. Part 2. Sphere. *Journal of Fluid Mechanics*, 494:33–50, 2003.

[45] E. Falcon, C. Laroche, and S. Fauve. Observation of gravity-capillary wave turbulence. *Physical Review Letters*, 98(094503), 2007.

[46] B. Favier, A. M. Grannan, M. Le Bars, and J. M. Aurnou. Generation and maintenance of bulk turbulence by libration-driven elliptical instability. *Physics of Fluids*, 27:066601, 2015.

[47] H. J. S. Fernando. Turbulent mixing in stratified fluids. *Annual Review of Fluid Mechanics*, 23:455–493, 1991.

[48] R. Ferrari and C. Wunsch. Ocean circulation kinetic energy: Reservoirs, sources, and sinks. *Annual Review of Fluid Mechanics*, 41:253–282, 2009.

[49] A. Fincham and G. Delerce. Advanced optimization of correlation imaging velocimetry algorithms. *Experiments in Fluids*, Suppl.:S13–S22, 2000.

[50] P. F. Fischer. An overlapping Schwarz method for spectral element solution of the incompressible Navier-Stokes equations. *J. Comput. Phys.*, 133:84–101, 1997.

[51] P. F. Fischer and J. S. Mullen. Filter-based stabilization of spectral element methods. *C.R. Acad. Sci. Paris. Ser. I - Analyse Numer.*, 332:265–270, 2001.

[52] P. F. Fischer and E. Ronquist. Spectral element methods for large scale parallel Navier-Stokes calculations. *Comp. Methods in Appl. Mech. and Engineering*, 116 (1-4):69–76, 1994.

[53] P. Flandrin. Time-Frequency/Time-Scale Analysis, Time-Frequency Toolbox for Matlab. *Academic*, 1999.

[54] J. M. H. Fortuin. Theory and application of two supplementary methods of constructing density gradient columns. *Journal of Polymer Science*, 44(144):505–515, 1960.

[55] C. Garrett. Internal tides and ocean mixing. *Science*, 301(5641):1858–1859, 2003.

[56] C. J. R. Garrett and E. Kunze. Internal tide generation in the deep ocean. *Annual Review of Fluid Mechanics*, 39:57–87, 2007.

[57] C. J. R. Garrett and W. H. Munk. Space time scales of internal waves. *Geophysical Fluid Dynamics*, 3:225–264, 1972.

[58] B. Gayen and S. Sarkar. Turbulence during the generation of internal tide on a critical slope. *Physical Review Letters*, 104(218502), 2010.

[59] B. Gayen and S. Sarkar. Degradation of an internal wave beam by parametric subharmonic instability in an upper ocean pycnocline. *Journal of Geophysical Research*, 118:4689–4698, 2013.

[60] T. Gerkema and Zimmerman J. T. F. *An introduction to Internal Waves.* Lecture notes. Royal NIOZ, 2008.

[61] V. A. Gorodtsov and E. V. Teodorovich. Energy characteristics of harmonic internal wave generators. *J. Appl. Mech. Tech. Phys.*, 27:523–529, 1986.

[62] H. Görtler. Über eine Schwingungserscheinung in Flüssigkeiten mit stabiler Dichteschichtung. *Journal of Applied Mathematics and Mechanics*, 23(2):65–71, 1943.

[63] L. Gostiaux, H. Didelle, S. Mercier, and T. Dauxois. A novel internal waves generator. *Experiments in Fluids*, 42(1):123–130, 2007.

[64] N. Grisouard, C. Staquet, and I. Pairaud. Numerical simulation of a two-dimensional internal wave attractor. *Journal of Fluid Mechanics*, 614:1–14, 2008.

[65] Y. Guo and M. Holmes-Cerfon. Internal wave attractors over random, small-amplitude topography. *Journal of Fluid Mechanics*, 787:148–174, 2016.

[66] K. Hasselmann. On the non-linear energy transfer in a gravity-wave spectrum. Part 1. General theory. *Journal of Fluid Mechanics*, 481, 1962.

[67] K. Hasselmann. A criterion for nonlinear wave instability. *Journal of Fluid Mechanics*, 30(04):737–739, 1967.

[68] J. Hazewinkel, N. Grisouard, and S. B. Dalziel. Comparison of laboratory and numerically observed scalar fields of an internal wave attractor. *European Journal of Mechanics B/Fluids*, 30:51–56, 2011.

[69] J. Hazewinkel, C. Tsimitri, L. R. M. Maas, and S. B. Dalziel. Observations on the robustness of internal wave attractors to perturbations. *Physics of Fluids*, 22:107102, 2010.

[70] J. Hazewinkel, P. van Breevoort, S. Dalziel, and L. R. M. Maas. Observations on the wavenumber spectrum and evolution of an internal wave attractor. *Journal of Fluid Mechanics*, 598:373–382, 2008.

[71] E. Horne Iribarne. *Transport properties of internal gravity waves.* PhD thesis, ENS de Lyon, 2015.

[72] L. N. Howard. Note on a paper of John W. Miles. *Journal of Fluid Mechanics*, pages 509–512, 1961.

[73] R. X. Huang. *Encyclopedia of Energy*, volume 4, chapter Ocean, Energy Flows in. Elsevier, 2004.

[74] D. G. Hurley. The generation of internal waves by vibrating elliptic cylinders. Part 1. Inviscid solution. *Journal of Fluid Mechanics*, 351:105–118, 1997.

[75] D. G. Hurley and G. Keady. The generation of internal waves by vibrating elliptic cylinders. Part 2. Approximate viscous solution. *Journal of Fluid Mechanics*, 351:119–138, 1997.

[76] G. N. Ivey, K. B. Winters, and J. R. Koseff. Density Stratification, Turbulence, but How Much Mixing? *Annual Review of Fluid Mechanics*, 40:169–184, 2008.

[77] J. A. Jiménez Madrid and A. M. Mancho. Distinguished trajectories in time dependent vector fields. *Chaos*, 19(013111), 2009.

[78] S. Joubaud, J. Munroe, P. Odier, and T. Dauxois. Resonant triad instability in stratified fluids. *Physics of Fluids*, 24(041703), 2012.

[79] L. Jouve and G. I. Ogilvie. Direct numerical simulations of an inertial wave attractor in linear and nonlinear regimes. *Journal of Fluid Mechanics*, 745:223–250, 2014.

[80] H. H. Karimi and T. R. Akylas. Parametric subharmonic instability of internal waves: locally confined beams versus monochromatic wave trains. *Journal of Fluid Mechanics*, 757:381–402, 2014.

[81] E. Kartashova. Discrete wave turbulence. *Europhysics Letters*, 87(44001), 2009.

[82] B. King, H. P. Zhang, and H. L. Swinney. Tidal flow over three-dimensional topography in a stratified fluid. *Physics of Fluids*, 21(116601), 2009.

[83] A. I. Korotkin. *Added Masses of Ship Structures.* Springer, 2010.

[84] E. Kunze and S. G. Llewellyn Smith. The Role of Small-Scale Topography in Turbulent Mixing of the Global Ocean. *Oceanography*, 17(1):55–64, 2004.

[85] R. Y. S. Lai and L. Cheng-Ming. Added mass of a spheroid oscillating in a linearly stratified fluid. *International Journal of Engineering Science*, 19(11):1411–1420, 1981.

[86] F. P. A. Lam and L. R. M. Maas. Internal wave focusing revisited; a reanalysis and new theoretical links. *Fluid Dynamics Research*, 40:95–122, 2008.

[87] K. G. Lamb. Internal wave breaking and dissipation mechanisms on the continental slope/shelf. *Annual Review of Fluid Mechanics*, 46:231–254, 2014.

[88] G. Lesur and P.-Y. Longaretti. On the relevance of subcritical hydrodynamic turbulence to accretion disk transport. *Astronomy and Astrophysics*, 444:25–44, 2005.

[89] G. Lesur and P.-Y. Longaretti. Impact of dimensionless numbers on the efficiency of magnetorotational instability induced by turbulent transport. *Mon. Rot. R. Astron. Soc.*, 378:1471–1480, 2007.

[90] G. Lesur and G. I. Ogilvie. On the angular momentum transport due to vertical convection in accretion disks. *Mon. Rot. R. Astron. Soc.*, 404:64–68, 2010.

[91] S. G. Llewellyn Smith and W. R. Young. Conversion of the barotropic tide. *Journal of Physical Oceanography*, 33:1554–1566, 2002.

[92] S. G. Llewellyn Smith and W. R. Young. Tidal conversion at a very steep ridge. *Journal of Fluid Mechanics*, 495:175–191, 2003.

[93] J. Lockwood Taylor. Some hydrodynamics inertia coefficients. *Phil. Magazine*, 9(55):161–183, 1930.

[94] Y. V. Lvov and E. G. Tabak. Hamiltonian Formalism and the Garrett-Munk Spectrum of Internal Waves in the Ocean. *Physical Review Letters*, 87(16), 2001.

[95] L. R. M. Maas. Wave attractors: linear yet nonlinear. *International Journal of Bifurcation and Chaos*, 15(9):2757–2782, 2005.

[96] L. R. M. Maas. Topographies lacking tidal conversion. *Journal of Fluid Mechanics*, 684:5–24, 2011.

[97] L. R. M. Maas, D. Benielli, J. Sommeria, and F. P. A. Lam. Observation of an internal wave attractor in a confined stably stratified fluid. *Nature*, 388:557–561, 1997.

[98] L. R. M. Maas and F. P. A. Lam. Geometric focusing of internal waves. *Journal of Fluid Mechanics*, 300:1–41, 1995.

[99] L. R. M. Maas, A. Paci, and B. Yuan. Experiments on topographies lacking tidal conversion. In *NewWave: New challenges in internal wave dynamics*, 2015.

[100] J. A. MacKinnon. Mountain waves in the deep ocean. *Nature*, 501:321–322, 2013.

[101] J. A. MacKinnon and K. B. Winters. Subtropical catastrophe: Significant loss of low-mode tidal energy at 28.9 °. *Geophysical Research Letters*, 32(L15605), 2005.

[102] L. Magaard. Zur Berechnung interner Wellen in Meeresräumen mit nicht-ebenen Böden bei einer speziellen Dichteverteilung. *Kieler Meeresforschungen*, 18:161–183, 1962.

[103] L. Magaard. Ein Beitrag zur Theorie der internen Wellen als Störungen geostrophischer Strömungen. *Deutsche Hydrogr. Zeitschr.*, 21:241–278, 1968.

[104] A. M. M. Manders and L. R. M. Maas. Observations of inertial waves in a rectangular basin with one sloping boundary. *Journal of Fluid Mechanics*, 493:59–88, 2003.

[105] A. M. M. Manders and L. R. M. Maas. On the three-dimensional structure of the inertial wave field in a rectangular basin with one sloping boundary. *Fluid Dynamics Research*, 35:1–21, 2004.

[106] A. M. M. Manders, L. R. M. Maas, and T. Gerkema. Observations of internal tides in the Mozambique Channel. *Journal of Geophysical Research*, 109(C12034), 2004.

[107] J. Marshall, A. Adcroft, C. Hill, L. Perelman, and C. Heisey. A finite volume incompressible Navier-Stokes model for studies of the ocean in parallel computers. *Journal of Geophysical Research*, 102:5753–5766, 1997.

[108] M. Mathur and T. Peacock. Internal wave beam propagation in non-uniform stratifications. *Journal of Fluid Mechanics*, 639:133–152, 2009.

[109] P. Maurer, S. Joubaud, and P. Odier. Generation and stability of gravito-inertial waves. *Submitted to JFM*, 2016.

[110] A. D. McEwan. Degeneration of resonantly-excited standing internal gravity waves. *Journal of Fluid Mechanics*, 50:431–448, 1971.

[111] A. D. McEwan, D. W. Mander, and R. K. Smith. Forced resonant second-order interaction between damped internal waves. *Journal of Fluid Mechanics*, 55(4):589–608, 1972.

[112] A. D. McEwan and R. A. Plumb. Off-resonant amplification of finite internal wave packets. *Dynamics of Atmospheres and Oceans*, 2(1):83–105, 1977.

[113] L. F. McGoldrick. Resonant interactions among capillary-gravity waves. *Journal of Fluid Mechanics*, 21(2):305–331, 1965.

[114] M. J. Mercier, N. B. Garnier, and T. Dauxois. Reflection and diffraction of internal waves analyzed with the hilbert transform. *Physics of Fluids*, 20(8):086601, 2008.

[115] M. J. Mercier, D. Martinand, M. Mathur, L. Gostiaux, T. Peacock, and T. Dauxois. New wave generation. *Journal of Fluid Mechanics*, 657:308–334, 2010.

[116] J. W. Miles. On the stability of heterogeneous shear flows. *Journal of Fluid Mechanics*, pages 496–508, 1961.

[117] N. Mordant. Are there waves in elastic wave turbulence? *Physical Review Letters*, 100(234505), 2008.

[118] E. G. Morozov. Semidiurnal internal wave global field. *Deep Sea Research: Part I*, 42:135–148, 1995.

[119] D. E. Mowbray and B. S. H. Rarity. A theoretical and experimental investigation of the phase configuration of interal waves of small amplitude in a density stratified liquid. *Journal of Fluid Mechanics*, 28(1):1–16, 1967.

[120] W. H. Munk and C. Wunsch. Abyssal recipes II: energetics of tidal and wind mixing. *Deep sea research part I*, 45:1977–2010, 1998.

[121] S. Nazarenko. *Wave Turbulence*. Springer, Lecture Notes in Physics edition, 2011.

[122] J. N. Newman. Lateral motion of a slender body between two parallel walls. *Journal of Fluid Mechanics*, 39(1):97–115, 1969.

[123] M. Nikurashin and R. Ferrari. Overturning circulation driven by breaking internal waves in the deep ocean. *Geophysical Research Letters*, 40:3133–3137, 2013.

[124] M. Nikurashin and G. Vallis. A theory of the interhemispheric meridional overturning circulation and associated stratification. *Journal of Physical Oceanography*, 42:1652–1667, 2012.

[125] G. I. Ogilvie. Wave attractors and the asymptotic dissipation rate of tidal disturbances. *Journal of Fluid Mechanics*, 543:19–44, 2005.

[126] K. Onu, M. R. Flynn, and B. R. Sutherland. Schlieren measurement of axisymmetric internal wave amplitudes. *Experiments in Fluids*, 35:24–31, 2003.

[127] G. Öster and M. Yamamoto. Density gradient techniques. *Chemical Reviews*, 63(3):257–268, 1963.

[128] N. Otobe, S. Sakai, S. Yoden, and M. Shiotani. Visualization and WKB analysis of the internal gravity wave in the QBO experiment. *Japan Soc. Fluid Mech.*, 17, 1998.

[129] J. Pedlosky. *Waves in the Ocean and Atmosphere.* Springer, 2003.

[130] M. Perlin, W. Choi, and Z. Tian. Breaking waves in deep and intermediate waters. *Annual Review of Fluid Mechanics*, 45:115–145, 2013.

[131] S. Perrard, M. Le Bars, and P. Le Gal. Experimental and Numerical Investigation of Internal Gravity Waves Excited by Turbulent Penetrative Convection in Water Around Its Density Maximum. In M. Goupil, K. Belkacem, C. Neiner, F. Lignières, and J. J. Green, editors, *Studying Stellar Rotation and Convection.*, volume 865 of *Lecture notes in Physics*, chapter 12, pages 239–257. Springer, 2013.

[132] O. M. Phillips. *The dynamics of the Upper Ocean.* Cambridge University Press, 1966.

[133] O. M. Phillips. On flows induced by diffusion in a stably stratified fluid. *Deep Sea Research*, 17:435–443, 1970.

[134] R. A. Plumb and A. D. McEwan. The instability of a forced standing wave in a viscous stratified fluid: a laboratory analogue of the Quasi-Biennal Oscillation. *Journal of Atmospherical Science*, 35:1827–1839, 1978.

[135] K. L. Polzin, J. M. Toole, J. R. Ledwell, and R. W. Schmitt. Spatial variability of turbulent mixing in the abyssal ocean. *Science*, 276(5309):93–96, 1997.

[136] M. Rahmani, B. Seymour, and G. Lawrence. The evolution of large and small-scale structures in Kelvin-Helmholtz instabilities. *Environmental Fluid Mechanics*, 14:1275–1301, 2014.

[137] L. Rainville and R. Pinkel. Propagation of Low-Mode Internal Waves through the Ocean. *Journal of Physical Oceanography*, 36:1220–1236, 2006.

[138] M. Rieutord, B. Georgeot, and L. Valdettaro. Inertial waves in a rotating spherical shell: attractors and asymptotic spectrum. *Journal of Fluid Mechanics*, 435:103–144, 2001.

[139] H. Scolan, E. Ermanyuk, and T. Dauxois. Nonlinear fate of internal waves attractors. *Physical Review Letters*, 110:234501, 2013.

[140] B. Semin, G. Facchini, F. Pétrélis, and S. Fauve. Une expérience modèle de l'oscillation quasi-biennale. In *Rencontre du Non-Linéaire*, 2015.

[141] J. Sommeria. Uvmat toolbox for Matlab.

[142] I. V. Sturova. Oscillations of a circular cylinder in a linearly stratified fluid. *Fluid Dynamics*, 36(3):478–488, 2001.

[143] B. R. Sutherland, S. B. Dalziel, G. O. Hughes, and P. F. Linden. Visualization and measurement of internal waves by 'synthetic schlieren'. Part 1. Vertically oscillating cylinder. *Journal of Fluid Mechanics*, 390:93–126, 1999.

[144] B. R. Sutherland and P. F. Linden. Internal wave excitation by a vertically oscillating elliptical cylinder. *Physics of Fluids*, 14(2):721–739, 2002.

[145] W. Tang and T. Peacock. Lagrangian coherent structures and internal wave attractors. *Chaos*, 20(017508), 2010.

[146] N. H. Thomas and T. N. Stevenson. A similarity solution for viscous internal waves. *Journal of Fluid Mechanics*, 54:495–506, 1972.

[147] C. Tropea, A. Yarin, and J. F. Foss, editors. *Handbook of Experimental Fluid Mechanics*. Springer, 2007.

[148] V. Vlasenko, N. Stashchuk, and K. Hutter. *Baroclinic tides. Theoretical Modeling and Observational Evidence*. Cambridge University Press, 2005.

[149] B. Voisin, E. V. Ermanyuk, and J.-B. Flor. Internal wave generation by oscillation of a sphere, with application to internal tides. *Journal of Fluid Mechanics*, 666:308–357, 2011.

[150] C. Wunsch. On oceanic boundary mixing. *Deep Sea Research*, 17:293–301, 1970.

[151] E. Yarom and E. Sharon. Experimental observation of steady inertial wave turbulence in deep rotating flows. *Nature Physics*, 10:510, 2014.

[152] C. S. Yih. *Hydrodynamics*. Cambridge University Press, 1950.

[153] V. E. Zakharov and N. N. Filonenko. Energy spectrum for stochastic oscillations of a fluid surface. *Sov. Phys. Dokl.*, 11:881–884, 1967.

[154] V. E. Zakharov and N. N. Filonenko. Weak turbulence of capillary waves. *J. Appl. Mech. Tech. Phys.*, 4(506), 1967.

Abstract

A question of paramount importance in the dynamics of oceans is related to the energy cascade from large to small scales and its contribution to mixing. Internal wave attractors may be one of the possible mechanisms responsible for such a cascade. In this manuscript, we study experimentally internal wave attractors in a trapezoidal test tank filled with linearly stratified fluid. In such a geometry, the waves can form closed loops called attractors.

We show that the attractor formation is purely linear: small scales are thus created by wave focusing. The attractor characteristics are found to only depend on the trapezoidal geometry of the tank. At the ocean scale, we show that attractors are very likely to be unstable. Indeed, internal wave attractors are prone to a triadic resonance instability, which transfers energy from the attractor to a pair of secondary waves. This instability and its main characteristics are described as a function of the geometry of the basin.

For long-term experiments, the instability produces several pairs of secondary waves, creating a cascade of triadic interactions and transferring energy from large-scale monochromatic input to multi-scale internal-wave motion. We reveal, for the first time, experimental convincing signatures of internal wave turbulence. Beyond this cascade, we have a mixing regime, which appears to be independent of the trapezoidal geometry and, thus, universal.

This manuscript is completed by a study on added mass and wave damping coefficient of bodies oscillating horizontally in a stratified fluid, with applications to tidal conversion.

Résumé

La cascade d'énergie qui a lieu dans les océans, depuis les grandes vers les petites échelles, est capitale pour comprendre leur dynamique et le mélange irréversible associé. Les attracteurs d'ondes internes font partie des mécanismes conduisant potentiellement à une telle cascade. Dans ce manuscrit, nous étudions expérimentalement les attracteurs d'ondes internes, dans une cuve trapézoïdale remplie d'un fluide stratifié linéairement en densité. Dans cette géométrie, les ondes peuvent être focalisées vers un cycle limite : l'attracteur.

Nous montrons que la formation de l'attracteur est purement linéaire : des petites échelles sont donc créées grâce à la focalisation des ondes. Les principales caractéristiques de l'attracteur dépendent uniquement de la géométrie trapézoïdale de la cuve. A l'échelle de l'océan, nous montrons que les attracteurs d'ondes internes sont très probablement instables. En effet, ceux-ci sont sujets à une instabilité de résonance triadique, qui transfère de l'énergie depuis l'attracteur vers un couple d'ondes secondaires. Cette instabilité et ses principales caractéristiques sont décrites en fonction de la géométrie du bassin.

Pour des expériences de longue durée, l'instabilité produit plusieurs paires d'ondes secondaires, créant une cascade d'instabilités triadiques et transférant l'énergie injectée à grandes échelles vers des échelles plus petites. Nous montrons, pour la première fois de façon expérimentale, de très fortes signatures de turbulence d'ondes internes. Au delà de cet état, la cascade atteint un régime de mélange partiel du fluide stratifié. Cet ultime régime apparait indépendant de la géométrie trapézoïdale du bassin, et donc, universel.

Cette thèse est complétée par une étude sur la masse ajoutée et l'amortissement par émission d'ondes d'objets oscillant horizontalement dans un fluide stratifié en densité. Cela a des applications concernant la conversion de l'énergie des marées en ondes internes.